Single Photon and Entangled Photon Light Sources towards Quantum Sensing with Optical Resonators

Callum Huw Jones

Supervisors:

Professor Frank Vollmer
Professor Jolly Xavier P

Submitted by Callum Huw Jones to the
University of Exeter as a thesis for the degree of
Doctor of Philosophy in Physics,
September 2023.

I certify that all material in this thesis which is not my own work has been identified and that any material that has previously been submitted and approved for the award of a degree by this or any other University has been acknowledged.

Abstract

Quantum optical sensors exploiting properties such as entanglement offer the potential to make enhanced measurements of physical parameters with a higher precision per photon used than achievable with coherent states of light. This thesis is on building sources of single photons and entangled photon pairs, towards developing quantum optical sensors using whispering gallery mode (WGM) resonators. These optical interferometers are used as highly sensitive optical sensors, including as biosensors which can detect single molecules when combined with localised surface plasmon resonances. Therefore, developing WGM sensors which use quantum optical states of light could enable measurements on biological samples and even single molecules with higher precision using fewer photons.

This thesis has three parts. First, we discuss some motivations for quantum sensing schemes using WGM resonators, and compare with previous quantum biosensing experiments. Theoretical modelling results are shown for WGM optical resonators coupled to one arm of a Mach-Zehnder interferometer (MZI). This setup is predicted to produce an interesting double resonance dip when an indistinguishable photon pair is incident on the two input ports; a variation on the behaviour of N00N states in an MZI but now also with an optical resonance. Using a computational model, an example of a WGM measurement scheme is shown that can achieve a factor of two enhancement in signal-to-noise ratio (SNR) by using entangled photon pairs.

In the second part we discuss single photon emitters in hexagonal boron nitride (hBN). Atomic vacancy defects in hBN have been demonstrated as room temperature single photon sources. These single photon emitters are characterised with a view to sensing applications and the fluorescence blinking behaviour is studied. The intensity stability of the single photon emission is measured using the time-dependent Mandel Q parameter. Although these sources can produce nonclassical states of light, it was found that a source of entangled photons would be more versatile for sensing experiments.

The final part is on building a source of entangled photon pairs using the spontaneous parametric down-conversion (SPDC) nonlinear optical process in a periodically-poled KTP crystal (PPKTP). Polarisation entangled states are generated using a PPKTP Sagnac loop setup, and characterised using quantum state tomography and Hong-Ou-Mandel (HOM) interference. We show an example of this source being applied to a refractive index sensor by using HOM interference of photon pairs coupled to a tapered optical fibre sensor. Tapered fibres can provide a means to couple entangled photon pairs to WGM resonators, and to close the thesis we discuss the potential for realising the experiment investigated in the theory chapter: using entangled photon pairs for quantum optical sensing with WGM sensors. The main challenge is achieving narrow bandwidth and wavelength-tuneable entangled photon pairs, however using cavity-enhanced down conversion sources this is possible in future work.

Acknowledgements

It has been a pleasure to work with so many inspiring people and brilliant scientists over the four years of this project. First I would like to thank my supervisors, Frank Vollmer and Jolly Xavier. I am very grateful to Frank Vollmer for the opportunity to work on this project, for all his support and for his encouragement to be ambitious and focused. The experimental work on quantum optics presented in this thesis was all begun in our lab by my supervisor Jolly Xavier. I will always be grateful for his guidance, his kindness, and for teaching me so much about experimental optics and about being a scientist.

The experiments in this thesis were also thanks to the work of Samir Vartabi Kashanian. I would like to thank him for being so generous with his time among other projects, and for his advice on all things quantum optics and coding. Many thanks to the University of Exeter physics workshop team for fabricating custom components for our experimental setups. I thank our collaborators at University of Technology Sydney, Minh Nguyen and Igor Aharonovich, for enabling us to study single photon emitters in hexagonal boron nitride and for their valuable input to our manuscript. Thanks also to Alessandro Fedrizzi for essential information on the PPKTP Sagnac loop experiment and guidance on future experiments. My pastoral tutor, Tim Naylor, gave me some advice and encouragement I'm really grateful for during the middle two years when things weren't looking so good.

Working in the Living Systems Institute has been an opportunity to meet so many great colleagues and friends. Thank you first to Aneeth Kakkanattu Arunkumar for being a great friend and lab mate in B02.20, and thank you also to Rithvik Gutha, Christina Sharp, Alice Attenborough, Kalani Perera, Matt Houghton, Sam Crowther, and Shahin Ghamari for your friendship and great company. To those who went before, thank you for the wisdom you can only get from another student: Katya Zossimova, Narima Eerqing, Serge Vincent, Simona Frustaci, and Sivaraman Subramanian. To the postdocs in our group, thank you all for your advice and help: Deshui Yu, Gema Cabello, Hsin-Yu Wu, Monika Pietrzyk, Nikita Toropov, Srikanth Pedireddy, and Thomas Derrien.

I am ever grateful for my parents Mandi and Rob, and my big brother Ben. Thank you for always being there for me and supporting me to follow whatever I'm interested in.

I fy nghariad, diolch am popeth. Thank you most of all for your love and encouragement, and your contagious passion for science.

"You can do anything
...with a LASER!"

Ray Davies

in memoriam

Director, Photonics Academy
of Wales @ Bangor (PAWB)

Contents

List of Figures

List of Tables

List of Abbreviations

EMCCD	Electron-multiplying charge coupled device
FSR	Free spectral range
hBN	Hexagonal boron nitride
HBT	Hanbury Brown and Twiss
HOM	Hong-Ou-Mandel
MZI	Mach-Zehnder interferometer
NTC	Negative temperature coefficient (thermistor)
OSA	Optical spectrum analyser
PC	(Fibre) Polarisation controller
PDMS	Polydimethylsiloxane
PID	Proportional-integral-derivative
PLA	Polylactic acid
PPKTP	Periodically-poled potassium titanyl phosphate
SNL	Shot-noise limit
SNR	Signal-to-noise ratio
SPDC	Spontaneous parametric down-conversion
SPAD	Single photon avalanche diode
SPoD	Single photon on demand
WGM	Whispering gallery mode

Publications

C. Jones, J. Xavier, S. Vartabi Kashanian, M. Nguyen, I. Aharonovich, and F. Vollmer, "Time-dependent Mandel Q parameter analysis for a hexagonal boron nitride single photon source," Optics Express, vol. 31, no. 6, pp. 10794–10804, 2023.

J. Xavier, D. Yu, **C. Jones**, E. Zossimova, and F. Vollmer, "Quantum nanophotonic and nanoplasmonic sensing: towards quantum optical bioscience laboratories on chip," Nanophotonics, vol. 10, no. 5, pp. 1387–1435, 2021.

Part I - Motivation for Introducing Quantum Optics to WGM Interferometric Biosensors

1 Introduction

Optical measurements are key to probing natural phenomena across practically all areas of physical and life sciences. The limitations of resolution, phase precision, intensity noise etc. in such measurements are fundamentally determined by quantum mechanics, specifically the description of light as photons: quantum optics. As research efforts turn increasingly from fundamental studies of quantum mechanics to applications in quantum technologies, one of the main areas is developing measurement techniques that push towards the fundamental limits on precision. This area is known as quantum metrology or quantum sensing.

Quantum sensing techniques use exotic states of light such as single photons, entangled photon pairs, and squeezed light and associated measurement setups to achieve a precision advantage per photon over measurements using classical light. These techniques are applied to a wide range of measurements. For this thesis I focus on applications to biosensing: detecting and studying small molecules, proteins, viruses etc. which are relevant to biological processes. Studying these objects individually is challenging since they are much smaller than visible wavelengths of light. However, detection at the single molecule level is possible and essential, for example: in developing ultra-sensitive measurements for disease biomarkers, and in fundamental studies into molecular processes which have heterogeneity that is hidden in ensemble measurements.

One method of single molecule sensing uses whispering gallery mode (WGM) optical resonators combined with optoplasmonic enhancements. These sensors enable label-free detection of small molecules and direct detection of the function of individual enzymes. Quantum sensing techniques have not yet been introduced to these sensors, nor has any quantum-enhanced biosensing experiment reached single molecule sensitivity to date. This thesis aims to develop sources of single photon states and entangled photon pairs required for quantum sensing experiments, and to investigate how we could improve on the sensitivity of single molecule WGM sensors using such states in the future.

The following sections introduce the key topics and literature on quantum sensing, WGM single molecule biosensors, and the state-of-the-art in combining quantum sensing with biological measurements. This is followed by an outline of the thesis and a summary of our research approach.

1.1 Quantum sensing

Optical phase measurements using classical light are limited in their precision by the shot-noise limit. This is the noise introduced due to the photon number distribution of

the light being used to measure the phase. Classical light is described by the coherent state and its photon number distribution (measured by counting photons over some time interval) is the Poisson distribution [1].

The derivation of limits to measurement precision uses estimation theory [2, 3, 4]. We need the error in a parameter ϕ in the case of a general measurement on a quantum system using an N-partite probe state (i.e. an N-photon state in an optical measurement), denoted $\Delta\phi$. This measurement can be repeated to reduce the error; let it be repeated M times. For a separable probe state (i.e. not in an entangled state) the relevant limit is, up to a constant factor $k \sim 1$ [5]:

$$\Delta\phi \geq \frac{k}{\sqrt{M}} \left(\frac{1}{\sqrt{N}} \right). \tag{1}$$

This is the **shot-noise limit** (SNL) which ultimately limits measurements using classical probe states. The same result is obtained from the Central Limit Theorem by combining N independent Gaussian distributed errors across M independent measurements [6]. If instead the probe state is allowed to be entangled the lower bound becomes, again up to a constant factor $k \sim 1$ [5]:

$$\Delta\phi \geq \frac{k}{\sqrt{M}} \left(\frac{1}{N} \right). \tag{2}$$

The scaling of error with $1/N$ is the **Heisenberg limit** and represents the fundamental limit to the error in a general measurement on a quantum system using an N-partite probe state: a factor of $\sqrt{N}$ below the SNL. In quantum sensing the aim is to achieve a lower measurement error per photon used than the SNL. This is done by choosing suitable N-photon input states and measurement schemes.

Quantum sensing experiments can be grouped into two broad approaches which are analogous to approaches in quantum optical computing: photon counting experiments and continuous variables. These approaches generally need different experimental setups and technologies for photon detection. Photon counting experiments use quantum optical states with few photons such as entangled states or single photons, which are detected as discrete signals on single photon detectors or photon number resolving detectors. Continuous variables approaches generally use higher power quantum optical states (such as Gaussian states) which are detected with a continuous photocurrent signal, often using homodyne or heterodyne detection methods.

The main approach to continuous variables quantum sensing to overcome the SNL is to use squeezed light [7]. While coherent states have equal uncertainties in field quadratures (or intensity and phase), the uncertainties in squeezed states are redistributed such that one quadrature is below shot noise and the other is above [8, 9]. Squeezed states are typically generated in nonlinear optical interactions [10, 11]. By using squeezing in intensity, for example, the error in a measurement of optical intensity can be made below

the SNL.

Caves first proposed a phase measurement in the Mach-Zehnder interferometer (MZI) which can beat the SNL [12]. This method uses a squeezed vacuum field as one of the input states to the interferometer, and a coherent state at the other input. This is the principle behind the advanced LIGO (Laser Interferometer Gravitational wave Observatory) experiment, which uses squeezed light in an interferometer to enhance its sensitivity to strain in the interferometer arms by 2.3 dB beyond the SNL [13].

Using photon counting experiments, another approach to quantum sensing is to use entangled photon states. For example, in the MZI the N00N state is in principle capable of reaching the Heisenberg limit. This state is the superposition of N photons in each arm of the interferometer [14]. Sub-shot noise phase measurements using N00N states have been made with $N = 4$ photons [15, 16]. Making large N00N states however is very challenging and generally involves using many photons to post-selectively detect a few photons in the desired N00N state [14].

Multiple phase estimation schemes have achieved Heisenberg scaling uncertainty. Daryanoosh et al. have made a phase measurement with a variance within 4% of the absolute Heisenberg limit [17]. Higgins et al. have shown that an entangled probe state is not necessarily required for Heisenberg scaling uncertainty, using heralded single photon probes and adaptive measurement techniques [18].

To beat the SNL while accounting for all intensity passing through the phase element in the photon resources N requires a system with high quantum efficiency. Slussarenko et al. demonstrated this for the first time using an $N = 2$ N00N state [19]. This was made possible by using high efficiency superconducting nanowire single photon detectors, resulting in a total intensity transmission coefficient - including detector efficiency - of $\eta = 0.8$ in each interferometer arm.

Overall, optical measurements with errors below the SNL can be made using probe states such as heralded single photons, entangled photon states, and squeezed states. Optical measurements have even been made very close to the absolute Heisenberg limit on phase precision. However, it is important to note that the comparative SNL depends on how the photon number in the measurement is counted. Making measurements which are below the SNL while taking all the photons used in the measurement into account is challenging due to photon losses.

When talking about practical quantum sensing advantages it is important to ask whether a better precision could be achieved by increasing the optical power used in a comparable

classical measurement. Increasing the optical power for a laser source will typically be far easier than for a source of single or entangled photons which will generally provide significantly less than MHz rates of photons. Squeezed light can be used with μW-mW optical power [20] but will still typically be more limited in power than classical light sources. Quantum sensing finds applications in those situations where the optical power used in a measurement is limited, for example because increasing the power would introduce new noise sources or cause damage to the sample under study. The LIGO experiment is an excellent example of a practical advantage in quantum sensing. This was possible because the experiment had been engineered to eliminate other noise sources - resulting in a measurement limited by shot noise at the optimum optical power - and this noise could only be reduced further by introducing squeezed light.

1.2 WGM single molecule biosensors

WGM resonators such as silica microspheres are a versatile platform for high precision sensors [1]. These are spherical optical cavities (typically fabricated by melting optical fibre tips with a high power IR laser) which support optical resonances with an evanescent field extending into the surrounding medium [21, 22]. Light can be coupled to the resonator via frustrated total internal reflection from a prism, or by bringing the evanescent field around a tapered optical fibre close to the sphere.

Changes in the environment of the sensor such as temperature or refractive index changes are transduced into changes in the WGM resonance wavelength, resonance width or mode splitting, see Figure 1(b). The ultra-high Q factors achievable in these resonators (typically $\sim 10^{6-7}$ [25]) result in narrow resonances which can be tracked with high precision - on the order of fm shifts [21] - allowing very small changes in the sensor environment to be detected. Applications include sensing temperature, pressure, electric and magnetic fields, and biosensing [22].

The sensitivity of WGM sensors can be enhanced by combining them with plasmonics. Plasmonic biosensing is a field in its own right; shifts in surface plasmon resonances can detect changes in the optical environment with high sensitivity due to the mode volume confinement and E-field enhancement provided near plasmonic nanoparticles (commonly gold nanoparticles of various geometries) [25]. In plasmonic nanostructures Q factors are significantly lower ($\sim 10-100$ [25]) than expected for WGM resonators, however optical modes are confined to nanoscale volumes. A combination of WGM and plasmonic techniques as hybrid optoplasmonic sensors [26, 27, 28] have enabled the observation of

[1] The name originates from the whispering gallery in St Paul's Cathedral, London, which supports acoustic resonances around the perimeter of the circular gallery. This phenomenon can also be heard in many other buildings around the world.

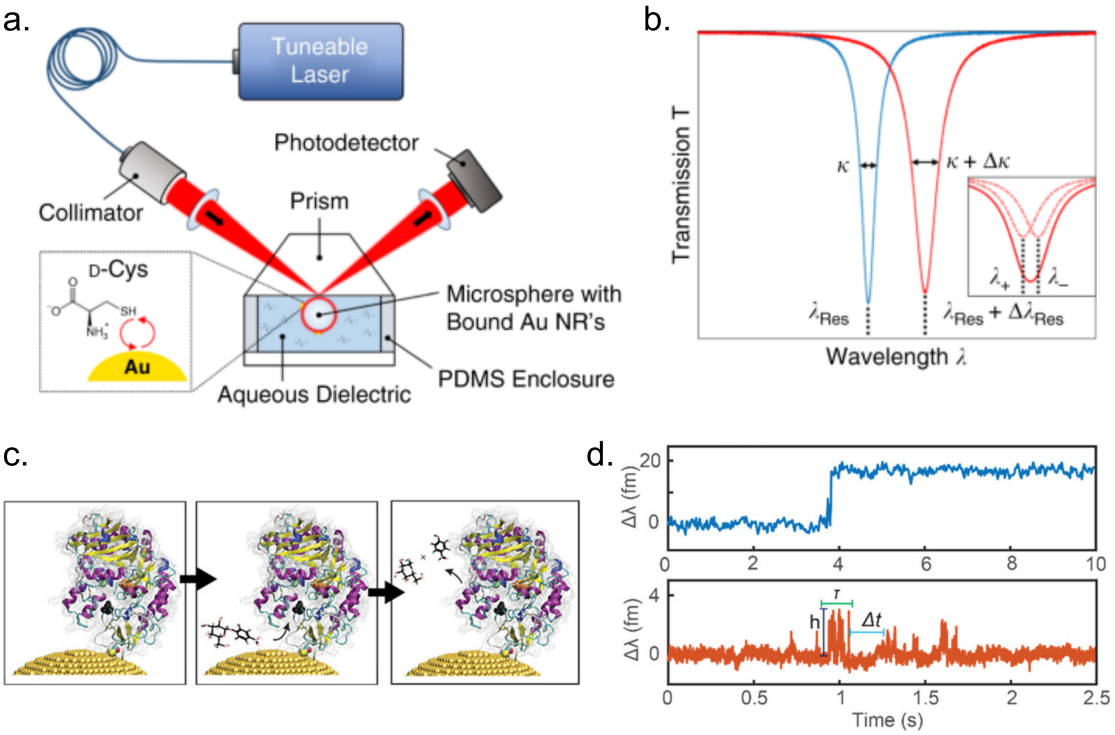

Figure 1: Examples of WGM single molecule biosensing. (a) A prism-coupled WGM optoplasmonic sensing setup showing detection of cysteine binding to gold nanorods. (b) Schematic of WGM resonance spectrum showing shifts in the resonance wavelength and linewidth which are read off as the sensing signal. Adapted from Vincent et al. [23] under CC-BY 4.0 license. (c) Schematic of enzyme turnover bound to a gold nanorod and studied on a WGM sensor. (d) Examples of WGM resonance shift signals. Top: step due to enzyme binding to the sensor, bottom: spikes due to enzyme turnover events. Adapted from Subramanian et al. [24] under CC-BY 4.0 license.

signals due to single molecules interacting with plasmonic nanoparticles [29].

Optoplasmonic WGM sensors typically use gold nanorods attached to WGM resonators, and the nanorod surface can be functionalised with receptor molecules to allow specific detection of a target molecule. These sensors have been used to detect small molecules and proteins binding and undergoing chemical reactions [29, 23], the binding of enzymes and turnover events of individual enzymes [30, 24, 31], and the detection of single Zn^{2+} and Hg^{2+} ions [32].

In terms of improvements to the capabilities of WGM single molecule sensors, signals from small molecules are often close to the noise level [29, 23]. Increasing the signal-to-noise ratio (SNR) could enable more confident detection of smaller signals, increasing the number of detections in an experiment and improving statistics, but could also reveal more detail in current signals. For example, in experiments detecting conformational changes of enzymes there can be information in the number and duration of signal spikes during a detection event which can be obscured by noise [24, 33]. The magnitude of the single molecule signal is proportional to the polarisability change [25], therefore a higher SNR could also enable the detection of even smaller conformational changes of biomolecules which have smaller associated polarisability changes. The detection limits of bare WGM microsphere sensors [34] were improved dramatically with the introduction of plasmonic enhancements using plasmonic nanoparticles [28], but there are still noise sources which could be mitigated (e.g. laser noise, thermorefractive noise) in order to improve on the SNR of these measurements, as discussed by Subramanian [33].

1.3 State-of-the-art in quantum-enhanced biosensing

In the past decade, there have been many demonstrations of biosensing and bioimaging experiments using quantum sensing to achieve enhancements in SNR or spatial resolution, and there are now a number of reviews in this area [35, 36, 37]. As described in the quantum sensing section, quantum optical sensing schemes can offer practical advantages over equivalent classical measurements when the measurement is shot-noise-limited and when there is a limit on the optical power which can be used. In the case of biosensing a strong argument for using quantum optical enhancements is that many biological samples are prone to photodamage when exposed to high optical power and/or long measurements [38, 39]. Therefore, quantum sensing strategies can improve the SNR of biosensing experiments beyond what would be possible using classical light due to the two constraints of shot noise and photodamage (as shown schematically in Figure 2). In principle, the SNR is bounded by the Heisenberg limit at the maximum optical power before reaching the photodamage threshold, although that is far beyond current experimental capabilities: we can see this by comparing typical photodamage thresholds observed for focused beams of

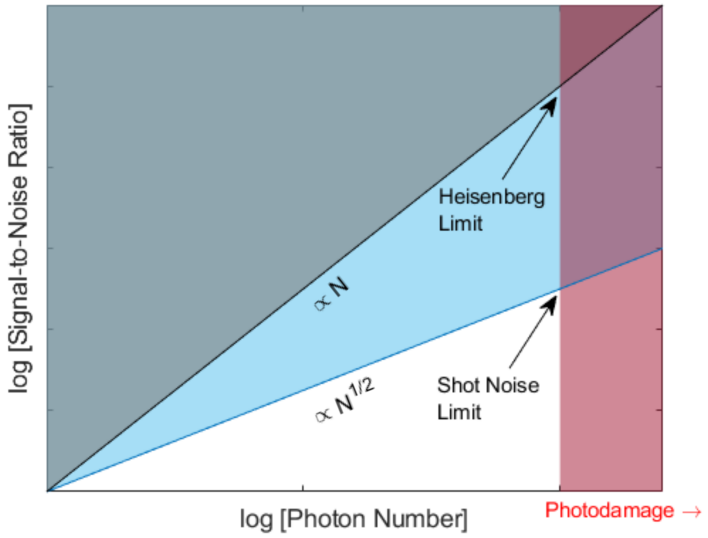

Figure 2: Schematic of SNR against photon number used per measurement (proportional to optical power) in a general biosensing measurement. This is to show how the SNR can be bounded by the SNL and photodamage threshold (red area), so that measurements with classical light are constrained to the white region. Quantum sensing experiments have the potential to increase the maximum SNR into the blue region, and in principle are instead bounded by the Heisenberg limit and photodamage thresholds.

$\sim$ 100 mW [38, 39] to the low photon count rates used in quantum sensing measurements achieving Heisenberg-scaling uncertainties [17, 18].

Quantum-enhanced biosensing experiments include entangled photon pairs used to detect protein concentration in MZIs [40] and plasmonic sensors [41], entangled photons used with tapered optical fibre sensors [42, 43], and many imaging techniques using entangled photon pairs [44, 36]. Squeezed light has been used in particle tracking experiments [45, 46], enhanced sensitivity in plasmonic sensors [47, 48], magnetometry using WGM microresonators [49], Raman microscopy [20, 50], and other microscopy techniques such as dark field [51] and stimulated Brillouin microscopy [52]. Although this may not be a complete list, we can see that the majority of experiments in this area are using squeezed light in order to reach optical powers which are comparable to the power required for classical biosensors. As an example of this, Casacio et al. [20] demonstrate a SNR enhancement in Raman microscopy at the point where shot noise and photodamage constrain the classical SNR (as shown in Figure 2). By using squeezed light, they demonstrate a 13% improvement in SNR which could not be achieved by increasing the power of a classical probe due to the photodamage threshold in the yeast cells being studied.

Although a large range of biosensing experiments have been adapted to use quantum

sensing methods, these methods have not yet been applied to single molecule experiments such as single molecule detection using WGM optoplasmonic sensors. So far, single molecule detection of bovine serum albumin (BSA) protein molecules has reached the SNL [53]. That experiment used dark field illumination with classical light and heterodyne detection in a tapered optical fibre sensor. As discussed in Ref. [53], using quantum correlated photons as probe states in this experiment could enable sub-shot noise precision in the future.

Due to the ability of WGM optoplasmonic sensors to detect signals from small molecules and conformational changes in individual enzymes, there is a great motivation to push towards the noise limits of these sensors and to investigate the potential for enhancing their sensitivity using quantum optics. The current limits to WGM single molecule sensors and the potential benefits of improving their SNR were summarised at the end of the previous section. From Ref. [49], we can see that sensing enhancements are possible using squeezed light in WGM microresonator magnetometers using acoustic resonances; similar quantum optics routes to enhanced precision measurements with WGM biosensors could enable new biosening and even single molecule detection capabilities in the future.

1.4 Research approach and thesis outline

The focus of this thesis is to build and characterise sources of quantum optical states suitable for quantum biosensing experiments, and to investigate the potential for sensitivity enhancements in WGM biosensors using quantum sensing schemes. Two approaches were chosen to developing light sources with quantum correlations: the first was to use bright room temperature single photon emitters in hexagonal boron nitride (hBN), with the aim to build up entangled photon pairs for sensing by two-photon interference; the second approach was to generate entangled photon pairs directly using a nonlinear optical process in the second order nonlinear crystal periodically-poled potassium titanyl phosphate (PPKTP). Entangled photon pairs would enable proof-of-principle quantum sensing schemes in the photon counting regime.

One of the challenges in this project was to develop the tools for making quantum optical measurements in our laboratory, based on setups built and designed by Professor Jolly Xavier. We aimed to build up from single photon sources to entangled photon pairs to develop a set of quantum optics experiments which would enable us to study quantum biosensing. This effort is motivated by the ultimate aim of combining quantum sensing with WGM biosensors and investigating how to make quantum-enhanced measurements at the single molecule level.

Throughout the project, the theory of quantum optics with WGM resonators was being

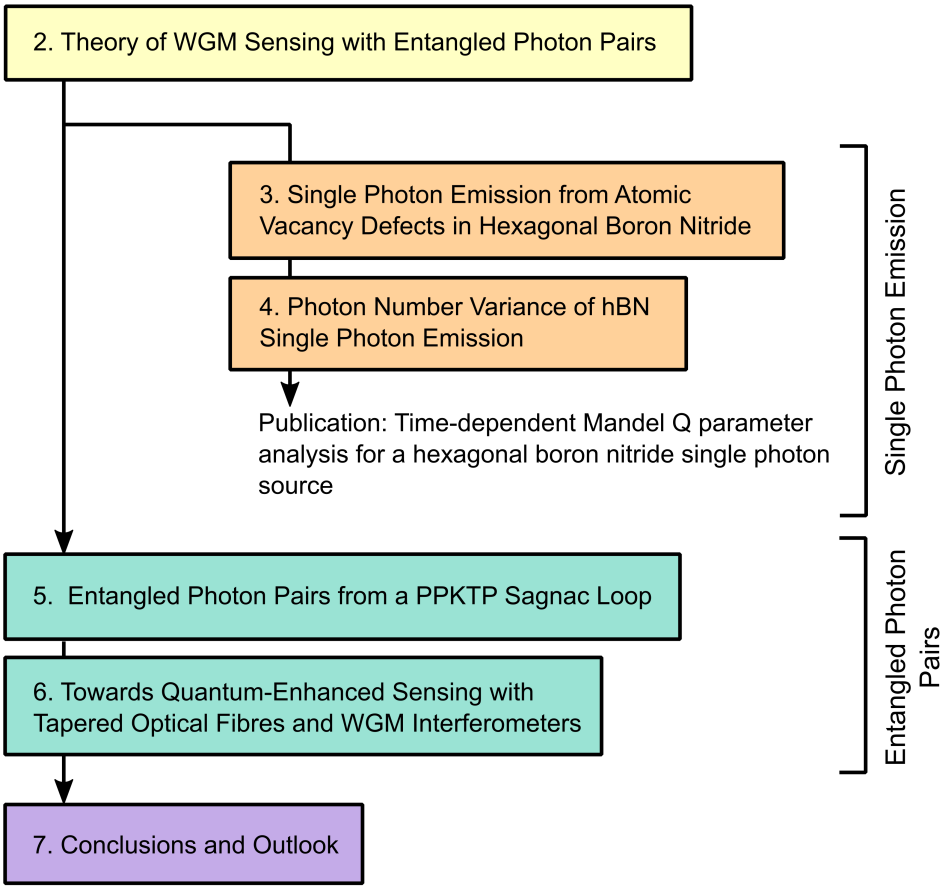

Figure 3: Thesis outline.

investigated to find potential quantum sensing schemes using entangled photon pairs coupled to WGM resonators. The chosen sensing scheme for the theoretical study was a MZI with an entangled photon input state and a WGM resonator coupled to one interferometer arm by tapered fibre coupling. This is similar to existing quantum sensing schemes using the MZI [40, 19]. However, adding an optical resonance as the phase shift in the interferometer results in a far more complex behaviour as an entangled photon input state modifies the classical WGM transmission spectrum depending on the coupling conditions.

The structure of this thesis is shown in Figure 3. **Chapter 2** introduces the necessary quantum optics theory and a model for WGM resonators within quantum optics. This model is used to predict the signal spectrum for a MZI with a WGM resonator in one arm, and with entangled photon pairs as the input state. Finally the SNR enhancement is investigated using a computational model to compare the classical and entangled photon WGM spectra.

Chapter 3 describes the development and characterisation of single photon sources in hBN, including $g^{(2)}$ measurements and Hong-Ou-Mandel (HOM) interference, which

could not be observed due to the spectral diffusion of these single photon emitters.

Chapter 4 continues with a study of the intensity stability of hBN single photon emitters and its relevance to sensing applications. Since it was not possible to build entangled photon pairs by HOM interference, we turn to sensing applications where the low photon number variance of single photon states could potentially be used. Fluorescence blinking and bleaching are investigated, and the photon number variance in the emission from these sources is studied over a range of timescales using the time-dependent Mandel Q parameter. Part of this chapter was based on a publication (Ref. [54]): the supplementary information is attached in Appendix A.

Chapter 5 introduces the nonlinear optical process spontaneous parametric down-conversion (SPDC) for producing entangled photon pairs. Then I describe the building and characterisation of a polarisation entangled photon pair source based on a PPKTP crystal in a Sagnac loop. Chapter 5 finishes with results on HOM interference using the polarisation entangled photon pairs.

Chapter 6 looks towards quantum biosensing experiments using our PPKTP entangled photon pair source. Tapered optical fibres are introduced as sensors, and HOM measurements are shown with a tapered fibre before the HOM beamsplitter. The HOM dip position is sensitive to the refractive index around the tapered fibre and I show results on sensing refractive index changes using entangled photon pairs. Finally I show how tapered optical fibres can couple photons to WGM resonators and discuss the experimental challenges in realising the WGM coupled MZI with entangled photon pairs, as shown theoretically in Chapter 2.

Chapter 7 concludes the thesis and gives an outlook on future work towards quantum-enhancements in biosensing with tapered fibres and WGM sensors.

2 Theory of WGM Sensing with Entangled Photon Pairs

2.1 Introduction

Quantum sensing schemes which measure a linear phase change in an interferometer are very well discussed in the literature [15, 40, 19]. In this work, we are interested in quantum sensing schemes which can be applied to a WGM optical resonator, in order to monitor shifts in ultra-narrow ($\sim$100 MHz linewidth) resonances and detect signals such as single molecule binding events. Quantum sensing schemes involving optical resonances are less common in the literature. We need a theoretical model of coupling entangled photon pairs to a WGM resonator to motivate and inform future experiments. For example, what sensitivity enhancements can be gained by using entangled photon pairs and in what sensing scheme? What are the optimum coupling conditions to the WGM resonator? What are the critical experimental parameters for developing a source of entangled photons as the input state?

In this chapter I will discuss models of coupling light to a single WGM resonance in both classical and quantum optics regimes. The chapter begins by introducing the concepts from quantum optics that will be used in the following sections.

A widely used result in quantum sensing schemes is the N-fold enhancement of the phase shift in a Mach-Zehnder interferometer (MZI) when the state inside the interferometer is an N-photon path entangled state [15]. Using an existing quantum optics model for WGM coupling I will present some predictions for the behaviour of a WGM resonator in one arm of a MZI, with an entangled photon pair at the input. The resonance spectrum of the output coincidence count rate has a double dip feature and points with enhanced sensitivity to shifts in the resonance wavelength.

Finally, I will present a computational study of the noise in a measurement of the WGM resonance position, using a Monte Carlo approach to generate random noise. The SNR will be compared between sensing schemes using classical light and entangled photon pairs. Under certain coupling conditions and when the sensor is operated in the shot-noise-limited regime, it is possible to see approximately a factor of two enhancement in the SNR using entangled photon pairs compared to a classical transmission measurement. This investigation is intended to demonstrate one potential approach to quantum-enhanced sensing in WGM resonators and give some insight into the challenges in realising it experimentally.

2.2 Quantum Optics Concepts

2.2.1 Representing quantum states of light

In quantum optics the electromagnetic field is quantised and can be treated as a set of harmonic oscillators for each momentum $\mathbf{k}$ and polarisation s mode. Photons with momentum $\mathbf{k}$ and polarisation s are excited states of these harmonic oscillators. This leads to the concept of the photon number state $|n\rangle$, which is a single mode of the electromagnetic field in the n^{th} excited state, i.e. with n photons. The lowest energy state of the electromagnetic field is then the $n = 0$ number state; the vacuum state $|0\rangle$.

This section follows 'Optical Coherence and Quantum Optics' by Mandel and Wolf [55]. We can describe general states of the electromagnetic field using a set of annihilation and creation operators: $\hat{a}_{\mathbf{k}s}$ and $\hat{a}^{\dagger}_{\mathbf{k}s}$. The creation operator acts on a number state to add one photon to the field and the annihilation operator removes one photon in the following way:

$$\begin{aligned} \hat{a}_{\mathbf{k}s}|n\rangle_{\mathbf{k}s} &= \sqrt{n}\,|n-1\rangle_{\mathbf{k}s} \\ \hat{a}^{\dagger}_{\mathbf{k}s}|n\rangle_{\mathbf{k}s} &= \sqrt{n+1}\,|n+1\rangle_{\mathbf{k}s}. \end{aligned} \tag{3}$$

The annihilation and creation operators satisfy the following bosonic commutation relations:

$$\begin{aligned} [\hat{a}_{\mathbf{k}s}, \hat{a}^{\dagger}_{\mathbf{k}'s'}] &= \delta^{3}_{\mathbf{k}\mathbf{k}'}\delta_{ss'} \\ [\hat{a}_{\mathbf{k}s}, \hat{a}_{\mathbf{k}'s'}] &= 0 \\ [\hat{a}^{\dagger}_{\mathbf{k}s}, \hat{a}^{\dagger}_{\mathbf{k}'s'}] &= 0. \end{aligned} \tag{4}$$

The combination $\hat{a}^{\dagger}_{\mathbf{k}s}\hat{a}_{\mathbf{k}s}$ is the number operator $\hat{n}$ since the number states are eigenstates of this operator with eigenvalues n:

$$\hat{a}^{\dagger}_{\mathbf{k}s}\hat{a}_{\mathbf{k}s}|n\rangle_{\mathbf{k}s} = n\,|n\rangle_{\mathbf{k}s}. \tag{5}$$

The Hamiltonian of the free electromagnetic field is expressed in terms of the number operator as:

$$\hat{H} = \sum_{\mathbf{k}}\sum_{s}\hbar\omega\left[\hat{a}^{\dagger}_{\mathbf{k}s}\hat{a}_{\mathbf{k}s} + \frac{1}{2}\right] \tag{6}$$

where each photon contributes an energy $\hbar\omega$ and the contribution $\hbar\omega/2$ per mode is the vacuum energy.

Now I will describe some states of light that will be useful for this thesis using this formalism of creation and annihilation operators.

Single photon state. A single photon state is a single mode number state with exactly one photon:

$$|1\rangle_{\mathbf{k}s} = \hat{a}^{\dagger}_{\mathbf{k}s}|0\rangle. \tag{7}$$

Ideally this state has zero variance in the photon number. However, for heralded single photons from nonlinear interactions for example, in reality there is some contribution to the state from the vacuum state and two or higher photon number states. At sufficiently low average photon number, the higher photon number contributions are negligible and these sources are good approximations to the single photon state.

Coherent state. Coherent states are eigenstates of the annihilation operator and behave analogously to classical optical fields. In terms of creation operators, the coherent state is:

$$|\alpha\rangle_{\mathbf{k}s} = \exp\left(-\frac{|\alpha|^2}{2}\right)\sum_{n=0}^{\infty}\frac{\alpha^n}{n!}(\hat{a}^\dagger_{\mathbf{k}s})^n|0\rangle. \tag{8}$$

The prefactor in this expression is a Poisson distribution: the photon number distribution for the coherent state $|\alpha\rangle$ is a Poisson distribution with both mean and variance $|\alpha|^2$.

Photon pair state. A description for a pair of photons in separate modes 1, 2 (e.g. separate spatial modes) with frequencies ω, ω' will be needed for describing entangled photon pairs generated by a nonlinear optical process. A time-dependent representation of a photon pair with joint spectral amplitude $\phi(\omega,\omega')$ is:

$$|\psi(t)\rangle = \left(\frac{\delta\omega}{2\pi}\right)\sum_{\omega}\sum_{\omega'}\phi(\omega,\omega')\hat{a}^\dagger_1(\omega)\hat{a}^\dagger_2(\omega')\mathrm{e}^{i(\omega-\omega')t}|0,0\rangle_{1,2}. \tag{9}$$

The sums can be replaced by integrals by taking the limit $\delta\omega \to 0$, with integration limits $(-\infty,\infty)$.

However, to simplify the calculations I will assume the two photons are in single frequency modes at ω (i.e. monochromatic), so the following time-independent representation can be used:

$$|\psi(\omega)\rangle = \hat{a}^\dagger_1(\omega)\hat{a}^\dagger_2(\omega)|0,0\rangle_{1,2}. \tag{10}$$

Although this gives no information on the spectrum and temporal distribution of the photon pair, it will be sufficient to demonstrate effects that depend on indistinguishable photon pairs.

2.2.2 Entangled states

Quantum mechanics allows solutions to the Schrödinger equation which are superposition states, i.e. a given particle can be in a superposition of multiple states in some degree of freedom. When this is extended to multiple particles, entangled states become possible - states which describe the joint state of multiple particles in a superposition which cannot be described completely in terms of each particle individually [56, 57].

Entangled states have been introduced in the previous chapter as essential tools for quantum sensing schemes. The entangled states I will consider here are non-separable states of two photons, i.e. for some degree of freedom they cannot be expressed in the form of a product state:

$$|\psi_{entangled}\rangle \neq |\text{Photon 1}\rangle|\text{Photon 2}\rangle. \tag{11}$$

The following are the two entangled states used in this thesis: polarisation and path entangled states. Some different kinds of entangled photon states are reviewed by Kwiat [58].

Polarisation entangled state. A pair of photons in two spatial modes 1, 2, which are in an entangled state in the polarisation degree of freedom (horizontal, H or vertical, V), for example:

$$\begin{aligned} |\psi_{polarisation}\rangle &= \frac{1}{\sqrt{2}}\left(\hat{a}^{\dagger}_{1H}\hat{a}^{\dagger}_{2V} + \hat{a}^{\dagger}_{1V}\hat{a}^{\dagger}_{2H}\right)|0,0\rangle_{1,2} \\ &= \frac{1}{\sqrt{2}}\left(|H,V\rangle_{1,2} + |V,H\rangle_{1,2}\right). \end{aligned} \tag{12}$$

The notation $|H\rangle$, $|V\rangle$ is used to represent one photon number states in the H or V polarisations. Note that this is one of the four Bell states: maximally entangled states of two qubits.

Path entangled state. A pair of photons in an entangled state between two spatial modes 1, 2, such that either both photons are in mode 1 or mode 2:

$$\begin{aligned} |\psi_{path}\rangle &= \frac{1}{2}\left(\hat{a}^{\dagger 2}_{1} + \hat{a}^{\dagger 2}_{2}\right)|0,0\rangle_{1,2} \\ &= \frac{1}{\sqrt{2}}\left(|2,0\rangle_{1,2} + |0,2\rangle_{1,2}\right). \end{aligned} \tag{13}$$

Entangled states of this form are often called N00N states for the general case in which there is a superposition of N photons in each mode [14]. This is the two-photon N00N state [2].

A useful representation for characterising entangled states in experiment is in terms of the density matrix $\hat{\rho}$, which for a pure state is the outer product of the state vector $|\psi\rangle$:

$$\hat{\rho} = |\psi\rangle\langle\psi|. \tag{14}$$

The diagonal elements of the density matrix are real and correspond to the probabilities of observing each possible state in the chosen basis. Off-diagonal elements are in general complex and represent correlations: entangled states will have off-diagonal elements that are non-zero.

[2] These states are named N00N after the general N-photon state: $|N0\rangle + |0N\rangle$.

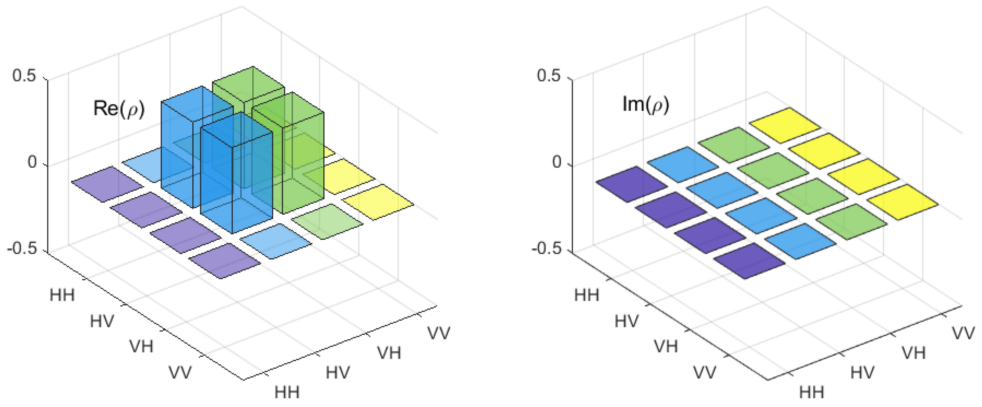

Figure 4: Real and imaginary parts of the density matrix $\hat{\rho}$ for the polarisation entangled state $|\psi_{polarisation}\rangle$ in the main text.

The density matrix can be determined experimentally as described in Chapter 5. One way to quantify the degree of entanglement of a state produced in experiment is to measure its density matrix $\hat{\rho}_{expt}$ and find its Fidelity F with respect to the target entangled state $|\psi_{target}\rangle$:

$$F = \langle \psi_{target} | \hat{\rho}_{expt} | \psi_{target} \rangle. \tag{15}$$

An example of the theoretical density matrix for the polarisation entangled state $|\psi_{polarisation}\rangle$ is shown in Figure 4.

2.2.3 HOM interference

The Hong-Ou-Mandel (HOM) effect is another essential tool in quantum optical sensing. This effect is shown schematically in Figure 5. When indistinguishable photon modes are combined simultaneously on a beamsplitter, interference between the two modes causes both photons to exit via the same output mode [59]. Indistinguishability here refers to the photons sharing the same spectral and polarisation modes, and having zero time delay at the beamsplitter.

Using the photon pair description introduced above, we can take the input state to be:

$$|\psi_{in}\rangle = \hat{a}_1^\dagger \hat{a}_2^\dagger |0,0\rangle_{1,2}. \tag{16}$$

The beamsplitter transforms the input creation operators in the following way [57]:

$$\hat{a}_1^\dagger = \frac{1}{\sqrt{2}}(\hat{a}_3^\dagger + i\hat{a}_4^\dagger); \;\; \hat{a}_2^\dagger = \frac{1}{\sqrt{2}}(i\hat{a}_3^\dagger + \hat{a}_4^\dagger). \tag{17}$$

Therefore the output state is given by substituting for the transformed creation operators

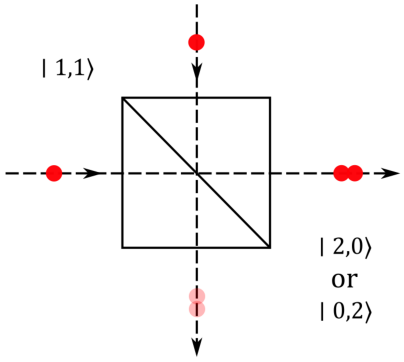

Figure 5: Schematic of HOM interference between two indistinguishable photons arriving simultaneously on a beamsplitter.

[3]:

$$\begin{aligned}
|\psi_{out}\rangle &= \frac{1}{2}(\hat{a}_3^\dagger + i\hat{a}_4^\dagger)(i\hat{a}_3^\dagger + \hat{a}_4^\dagger)|0,0\rangle_{3,4} \\
&= \frac{1}{2}(i\hat{a}_3^{\dagger 2} + \hat{a}_3^\dagger\hat{a}_4^\dagger - \hat{a}_4^\dagger\hat{a}_3^\dagger + i\hat{a}_4^{\dagger 2})|0,0\rangle_{3,4} \\
&= \frac{1}{2}(i\hat{a}_3^{\dagger 2} + i\hat{a}_4^{\dagger 2})|0,0\rangle_{3,4} \\
|\psi_{out}\rangle &= \frac{i}{\sqrt{2}}(|2,0\rangle_{3,4} + |0,2\rangle_{3,4}).
\end{aligned} \tag{18}$$

The result is a path entangled state (the two-photon N00N) state. Note that the terms with one photon in each output mode cancelled (this is possible because $\hat{a}_3^\dagger$ and $\hat{a}_4^\dagger$ commute). Therefore, we would expect to measure no coincidence detections in the output modes 3, 4: this produces the so-called 'HOM dip' in the coincidence counts when the delay between the two input photons is varied about zero.

This method for modelling beamsplitters in quantum optics will be used extensively through this chapter to describe interferometers. In the next section I will show how HOM interference is used in the MZI to make phase measurements with enhanced precision.

2.2.4 Quantum optics model of the MZI

The MZI can be used to make enhanced phase measurements using indistinguishable pairs of photons at the input. This section briefly gives the quantum optical description of an MZI with a linear phase shift introduced into one arm, shown schematically in Figure 6(a). This will be useful later for comparison to an MZI with a WGM resonator in one arm. The input modes to the MZI are $\hat{a}_1$, $\hat{a}_2$, and we consider an indistinguishable photon pair as the initial state:

$$|\psi_{in}\rangle = \hat{a}_1^\dagger\hat{a}_2^\dagger|0,0\rangle. \tag{19}$$

[3]By transforming the operators and acting on a constant vacuum state, we are working in the *Heisenberg picture*. Conversely in the *Schrödinger picture* the operators are constant and the state vector changes.

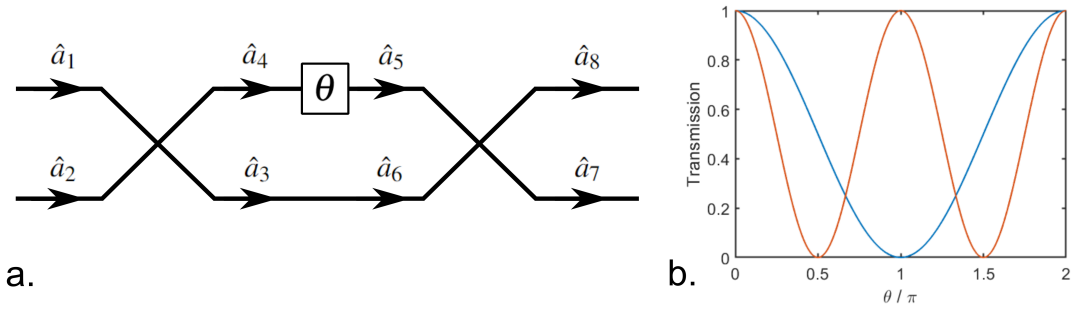

Figure 6: Schematic of MZI in quantum optics. (a) MZI with mode amplitudes labelled as described in the main text. A phase shift θ is introduced to one interferometer arm. (b) Transmission as a function of phase difference θ for: an entangled photon pair input state measuring the coincidence detections in both output modes (orange, corresponding to $P_{1,1}$), and a coherent input state measuring the transmitted intensity at one output mode (blue).

Operation of first beamsplitter transforming to modes $\hat{a}_3$, $\hat{a}_4$:

$$\hat{a}_1^\dagger = \frac{1}{\sqrt{2}}(\hat{a}_3^\dagger + i\hat{a}_4^\dagger);\ \ \hat{a}_2^\dagger = \frac{1}{\sqrt{2}}(i\hat{a}_3^\dagger + \hat{a}_4^\dagger). \tag{20}$$

State after the first beamsplitter is a two-photon N00N state; the $|1,1\rangle$ state destructively interferes by the HOM effect:

$$|\psi_{BS1}\rangle = \frac{i}{2}(\hat{a}_3^{\dagger 2} + \hat{a}_4^{\dagger 2})|0,0\rangle. \tag{21}$$

The phase shift operator acts only on mode $\hat{a}_4$, introducing a θ phase difference between the two arms:

$$\hat{a}_5^\dagger = \hat{U}_\theta^\dagger \hat{a}_4^\dagger \hat{U}_\theta = \hat{a}_4^\dagger e^{i\theta}. \tag{22}$$

State after the phase shift, note that the phase shift is doubled for a two-photon N00N state in the interferometer:

$$|\psi_\theta\rangle = \frac{i}{2}(\hat{a}_5^{\dagger 2} e^{2i\theta} + \hat{a}_6^{\dagger 2})|0,0\rangle. \tag{23}$$

Operation of the second beamsplitter transforming to output modes $\hat{a}_7$, $\hat{a}_8$:

$$\hat{a}_5^\dagger = \frac{1}{\sqrt{2}}(\hat{a}_7^\dagger + i\hat{a}_8^\dagger);\ \ \hat{a}_6^\dagger = \frac{1}{\sqrt{2}}(i\hat{a}_7^\dagger + \hat{a}_8^\dagger). \tag{24}$$

State after the second beamsplitter (output state):

$$|\psi_{BS2}\rangle = \left(\frac{i}{4}(e^{2i\theta} - 1)\hat{a}_7^{\dagger 2} + \frac{i}{4}(1 - e^{2i\theta})\hat{a}_8^{\dagger 2} - \frac{1}{2}(e^{2i\theta} + 1)\hat{a}_7^\dagger \hat{a}_8^\dagger\right)|0,0\rangle. \tag{25}$$

After acting with the creation operators (note the factor $\sqrt{2}$ when the creation operator acts twice):

$$|\psi_{BS2}\rangle = \frac{i\sqrt{2}}{4}(e^{2i\theta} - 1)|2,0\rangle + \frac{i\sqrt{2}}{4}(1 - e^{2i\theta})|0,2\rangle - \frac{1}{2}(e^{2i\theta} + 1)|1,1\rangle. \tag{26}$$

The probabilities of measuring both photons on the same detector (single count, $P_{2,0}, P_{0,2}$), and one photon on each detector (coincidence count, $P_{1,1}$) oscillate with twice the phase shift θ:

$$P_{2,0} = P_{0,2} = |\langle 2,0|\psi_{BS2}\rangle|^2 = \frac{1}{4}(1-\cos 2\theta) \tag{27}$$

$$P_{1,1} = |\langle 1,1|\psi_{BS2}\rangle|^2 = \frac{1}{2}(1+\cos 2\theta). \tag{28}$$

If a coherent state (e.g. a single laser mode) was used at the input to the MZI, the output intensities would oscillate with θ, therefore the interference fringes using photon pair inputs oscillate at twice the frequency compared to the classical case (as shown in Figure 6(b)). This allows the phase to be measured with enhanced sensitivity at points on the interference signal where the gradient is maximum. In the next section we will replace the linear phase shift in one arm with a WGM resonator, which has a more complicated behaviour introducing both losses and phase shift which depend on the detuning from resonance.

2.3 Quantum Optics Model for WGM Sensing

2.3.1 Classical model for WGM resonator

First, let us describe the amplitude and phase change in a single optical mode coupled to a WGM resonator using a classical model. The situation is shown in Figure 7. The input and output mode labels are named anticipating the quantum optical model in the next section. Parameters are: coupling reflection coefficient r, coupling transmission coefficient κ, transmission amplitude per round trip α, phase accumulated per round trip $\theta(\omega)$, refractive index n, resonator radius R, and resonance frequency ω_0. Following the derivation in Refs. [60, 61], the input-output relation for the optical electric field amplitude is:

$$E_{out} = E_{in}\sqrt{\eta}\mathrm{e}^{i\Theta}. \tag{29}$$

Intensity transmission coefficient η:

$$\eta = \frac{\alpha^2 + r^2 - 2r\alpha\cos\theta}{1 - 2r\alpha\cos\theta + r^2\alpha^2}. \tag{30}$$

Phase of transmitted mode Θ:

$$\Theta = \pi + \theta + \arctan\left(\frac{r\sin\theta}{\alpha - r\cos\theta}\right) + \arctan\left(\frac{r\alpha\sin\theta}{1 - r\alpha\cos\theta}\right) \tag{31}$$

where $\theta(\omega)$ is the phase accumulated per round trip:

$$\theta(\omega) = \frac{2\pi Rn}{c}\delta_\omega = \frac{2\pi Rn}{c}(\omega - \omega_0). \tag{32}$$

Note that the coupling transmission coefficient κ does not appear in the expressions above; they can all be written in terms of r using the relation $|\kappa|^2 + |r|^2 = 1$ which is required by energy conservation. An example of the WGM transmission spectrum is shown

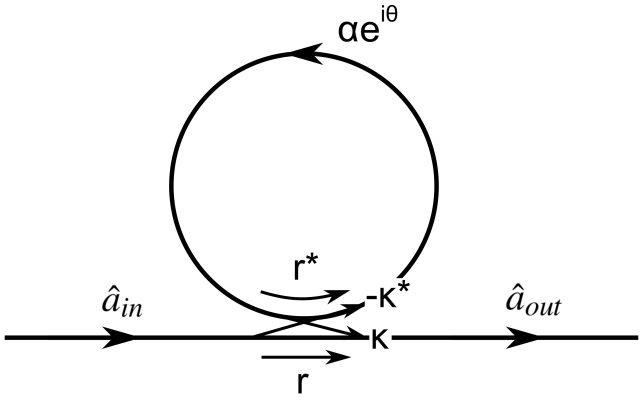

Figure 7: Diagram of a WGM resonator coupled to a waveguide. This general model could describe any kind of WGM resonator such as a ring resonator, toroid, or sphere. The input and output mode amplitude operators are shown as used in the quantum optics model for this system. The parameters are coupling reflection coefficient r, coupling transmission coefficient κ, amplitude transmission per round trip α, and phase change per round trip θ.

in Figure 8, with $\alpha = 0.9997$ and varying the coupling reflection coefficient r. There are three regimes for the coupling conditions: overcoupling ($r < \alpha$), critical coupling ($r = \alpha$), and undercoupling ($r > \alpha$). At critical coupling in an ideal resonator all the input power is coupled to the resonator on resonance and the transmission is zero. Figure 8 shows the linewidth increases going from under- to overcoupling.

As well as the transmission properties of the output mode from the resonator, we also need to consider the effect of the resonator on the arrival time of coupled photons, since this will be important for photon counting experiments. Photons coupled to the resonator will be delayed by an interval depending on the number of round trips they make. We can write down the probability of a photon making integer m round trips.

Amplitudes for m round trips:

$$\begin{aligned} &m = 0 : r\hat{a}_{in} \\ &m = 1 : -\kappa^*\kappa\alpha e^{i\theta}\hat{a}_{in} \\ &m = 2 : -\kappa^*\kappa\alpha^2 r^* e^{2i\theta}\hat{a}_{in} \\ &m = 3 : -\kappa^*\kappa\alpha^3 r^{*2} e^{3i\theta}\hat{a}_{in} \\ &\quad\ldots \\ &\quad -|\kappa|^2\left(\alpha e^{i\theta}\right)^m (r^*)^{m-1}\hat{a}_{in}. \end{aligned} \tag{33}$$

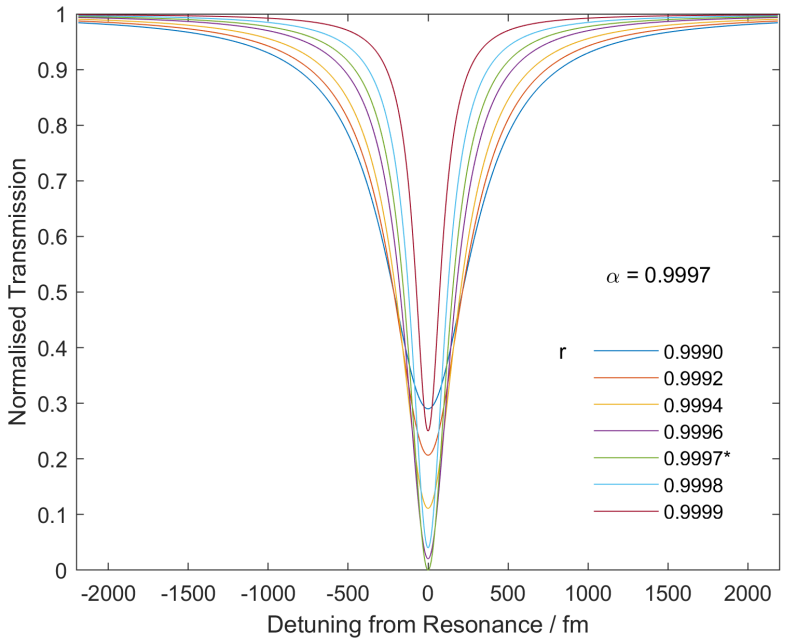

Figure 8: WGM resonances for varying coupling parameter r. The transmission per round trip α is fixed at 0.9997 to produce a FWHM of $\sim$100 fm typical for microsphere sensors. As the coupling parameter is varied from undercoupling ($r > \alpha$) to overcoupling ($r < \alpha$), the WGM linewidth increases.

Expressing amplitudes as probabilities and using $|r|^2 + |\kappa|^2 = 1$:

$$P_m = \left(\frac{1-|r|^2}{|r|}\right)^2 |\alpha r|^{2m}. \tag{34}$$

Since $\alpha, r < 1$, this is an exponential decay. The round trip time t_0 relates the number of round trips m to time delay t:

$$t = t_0 m = \frac{2\pi R n}{c} m. \tag{35}$$

The probability density function for the time delay t is derived from P_m using Equation 35 but must be normalised. Let the normalisation factor be B.

$$P(t) = B|\alpha r|^{(c/\pi n R)t} \tag{36}$$

Normalisation:

$$B\int_0^\infty dt\, |\alpha r|^{(c/\pi n R)t} = 1 \tag{37}$$

$$B\int_0^\infty dt \exp\left(\ln|\alpha r|^{(c/\pi n R)t}\right) = 1 \tag{38}$$

$$B\int_0^\infty dt \exp\left(\frac{c}{\pi n R} t \ln|\alpha r|\right) = 1 \tag{39}$$

$$B = -\frac{c}{\pi n R}\ln|\alpha r|. \tag{40}$$

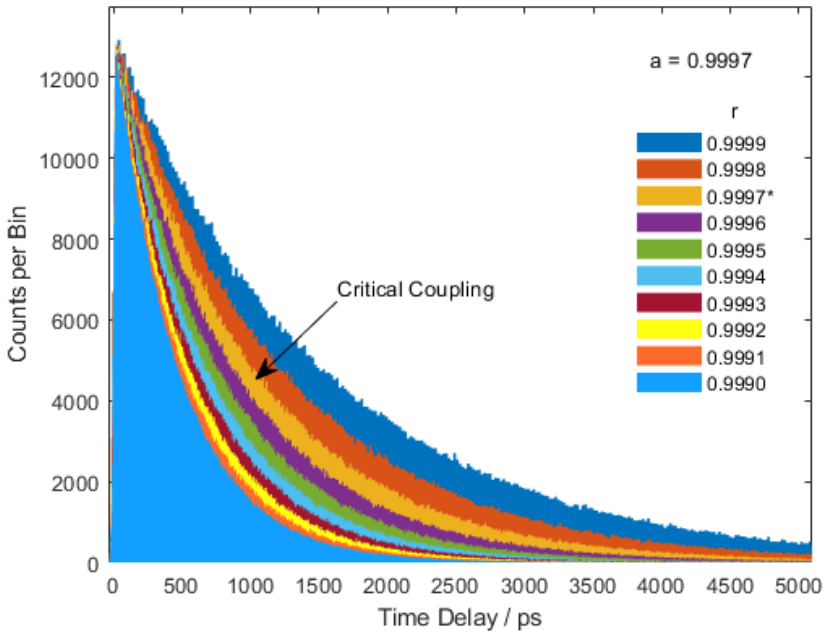

Figure 9: Distribution of photon delays induced by a WGM resonator under different coupling conditions. The data were generated with pseudo-random samples from the delay distribution $P(t)$. As the coupling parameter is varied from undercoupling ($r > \alpha$) to overcoupling ($r < \alpha$), the mean delay decreases.

The normalised probability distribution for the photon delay time is:

$$P(t) = -\frac{c}{\pi n R}\ln|\alpha r| \cdot |\alpha r|^{(c/\pi n R)t}. \tag{41}$$

Figure 9 shows this distribution plotted for $\alpha = 0.9997$ and varying coupling conditions r, from undercoupled to overcoupled. The delay is shortest in the overcoupling regime, and mean delays are typically ~ 1 ns for these parameters.

From the exponential decay distribution in Equation 34, we can derive some useful properties of the WGM resonator in terms of α and r. The $1/e$ lifetime of the decay (the cavity ring-down time) is τ:

$$\tau = -\frac{t_0}{\ln|\alpha r|} = -\frac{2\pi R n}{c\ln|\alpha r|}. \tag{42}$$

By equating this with the decay time calculated from the cavity linewidth we get a relation between the linewidth $\Delta\lambda$ and the coupling parameters α, r (at resonance wavelength λ_0):

$$\begin{aligned} \tau &= \frac{n\lambda_0^2}{2\pi c\Delta\lambda} = -\frac{2\pi R n}{c\ln|\alpha r|} \\ \implies \Delta\lambda &= -\frac{\lambda_0^2\ln|\alpha r|}{4\pi^2 R}. \end{aligned} \tag{43}$$

This relation is important because it relates the coupling and loss parameters of the resonator r and α to the resonance linewidth $\Delta\lambda$, which is a more typical value to quote for a WGM resonator. We can also relate these parameters to the Q-factor of the resonator via $Q = \lambda_0/\Delta\lambda$.

The free spectral range FSR (in units of frequency ν) is the reciprocal of the round trip time:

$$FSR_\nu = \frac{1}{t_0} = \frac{c}{2\pi Rn}. \tag{44}$$

The linewidth in units of frequency is proportional to the reciprocal of the cavity ring-down time τ:

$$\Delta\nu = \frac{1}{2\pi\tau}. \tag{45}$$

Using these two relations, the WGM cavity finesse can also be expressed in terms of α and r:

$$\mathscr{F} = \frac{FSR_\nu}{\Delta\nu} = \frac{2\pi\tau}{t_0} = -\frac{2\pi}{\ln|\alpha r|}. \tag{46}$$

2.3.2 Quantum optics model for WGM resonator with losses

Now, to describe coupling to the WGM resonator using a quantum optics approach we need a relation between input and output field amplitudes expressed as annihilation operators. Following the derivation in Alsing et al. [62], this is a little more complicated than the classical derivation because now the losses that occur in the resonator have to be included explicitly using noise operators.

The input-output relation from Ref. [62] is:

$$\hat{a}_{out} = t(\omega)\hat{a}_{in} + \hat{F}(\omega) \tag{47}$$

where the transmission amplitude $t(\omega)$ is:

$$t(\omega) = \left(\frac{r - \alpha e^{i\theta}}{1 - r^*\alpha e^{i\theta}}\right) \tag{48}$$

and the noise operator $\hat{F}(\omega)$ is:

$$\hat{F}(\omega) = -i|\kappa|^2\sqrt{\Gamma(\omega)}\sum_{n=0}^{\infty}(r^*)^n\int_0^{(n+1)L} dz\, e^{i\xi(\omega)[(n+1)L-z]}\hat{s}(z,\omega). \tag{49}$$

For real r, taking the modulus squared of $t(\omega)$ returns the classical intensity transmission coefficient η. The noise operator is derived using Loudon's beamsplitter model for losses in quantum optics [63]. By considering a continuous series of beamsplitters around the circumference of the resonator, photons are lost from the resonator with an

attenuation constant $\Gamma(\omega)$ (per unit distance around the circumference). At the same time, these beamsplitters couple photons into the resonator from the optical modes of the environment. These modes have amplitudes $\hat{s}(z,\omega)$ at position z around the resonator circumference $L = 2\pi R$. The factor $\xi(\omega) = n(\omega)(\omega/c) + i\Gamma(\omega)/2$ is the complex optical propagation constant inside the resonator.

The expectation values of the noise amplitudes coupled into the resonator $\hat{s}(z,\omega)$ are:

$$\langle \hat{s}(z,\omega) \rangle = 0 \tag{50}$$

$$\langle \hat{s}^{\dagger}(z,\omega)\hat{s}(z',\omega') \rangle = F_N(\omega)\delta(z-z')\delta(\omega-\omega') \tag{51}$$

where $F_N(\omega)$ is the mean flux of noise photons entering the resonator mode from the environment at angular frequency ω. As discussed by Loudon [63], for a system in thermal equilibrium with the environment $F_N \ll 1$.

The flux of noise photons coupled into the optical mode from the environment via losses is typically negligibly small at optical frequencies. However, the noise operators are essential for maintaining the correct commutation relations for the input and output modes. The input and output annihilation operators must obey:

$$[\hat{a}_{in}(\omega), \hat{a}_{in}^{\dagger}(\omega')] = \delta(\omega-\omega') \tag{52}$$

$$[\hat{a}_{out}(\omega), \hat{a}_{out}^{\dagger}(\omega')] = \delta(\omega-\omega'). \tag{53}$$

As shown in [62], the commutator for $\hat{a}_{out}$ is only satisfied if the noise operators are included in the input-output relation. We also have the following commutators for the noise operators:

$$[\hat{s}(z,\omega), \hat{s}^{\dagger}(z',\omega')] = \delta(z-z')\delta(\omega-\omega') \tag{54}$$

$$[\hat{a}_{in}(\omega), \hat{s}(z',\omega')] = [\hat{a}_{in}(\omega), \hat{s}^{\dagger}(z',\omega')] = 0. \tag{55}$$

As an example of how this model behaves, we can take an input coherent state with complex amplitude β and find the expectation of the output photon number at angular frequency ω, $\hat{N}(\omega)$, using the input-output relation.

$$\hat{a}_{in}|\beta\rangle = \beta|\beta\rangle; \;\; \langle\beta|\hat{a}_{in}^{\dagger} = \beta^*\langle\beta| \tag{56}$$

The number operator expectation value and input-output relation are:

$$\langle \hat{N}(\omega) \rangle = \langle\beta|\hat{a}_{out}^{\dagger}(\omega)\hat{a}_{out}(\omega)|\beta\rangle \tag{57}$$

$$\hat{a}_{out}(\omega) = t(\omega)\hat{a}_{in}(\omega) + \hat{F}(\omega). \tag{58}$$

Substituting for $\hat{a}_{out}$ we get:

$$\begin{aligned}\langle \hat{N}(\omega) \rangle = t^*(\omega)t(\omega)\langle\beta|\hat{a}_{in}^{\dagger}(\omega)\hat{a}_{in}(\omega)|\beta\rangle + t^*(\omega)\langle\beta|\hat{a}_{in}^{\dagger}(\omega)\hat{F}(\omega)|\beta\rangle \\ + t(\omega)\langle\beta|\hat{F}^{\dagger}(\omega)\hat{a}_{in}(\omega)|\beta\rangle + \langle\beta|\hat{F}^{\dagger}(\omega)\hat{F}(\omega)|\beta\rangle\end{aligned} \tag{59}$$

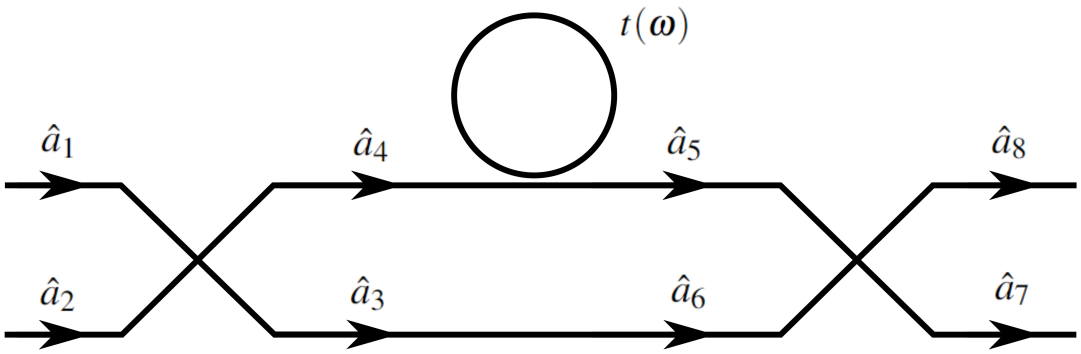

Figure 10: Diagram of the model for a WGM resonator coupled to one arm of a MZI. The resonator is characterised by a complex amplitude transmission spectrum $t(\omega)$. Mode amplitudes are labelled according to the derivation in the main text.

Since $\langle \hat{F}(\omega) \rangle = \langle \hat{s}(\omega) \rangle = 0$, the middle two terms are zero. Then:

$$\langle \hat{N}(\omega) \rangle = t^*(\omega)t(\omega)\beta^*\beta + \langle \beta | \hat{F}^\dagger(\omega)\hat{F}(\omega) | \beta \rangle. \tag{60}$$

The first term is the input photon number expectation value $|\beta|^2$ times the intensity transmission past the WGM resonator $T(\omega) = t^*(\omega)t(\omega)$, the second term has $\langle \hat{F}^\dagger(\omega)\hat{F}(\omega) \rangle \propto \langle \hat{s}^\dagger(z,\omega)\hat{s}(z',\omega) \rangle = F_N(\omega)\delta(z-z')$. The second term is the photon number coupled into the output mode from the environment. This term introduces additional noise: since there are losses in the resonator this noise is a consequence of the fluctuation-dissipation theorem. From the argument above the second term is negligible in most situations.

2.3.3 Entangled photons coupled to a WGM resonator in the MZI

Now we put the quantum optical model for the WGM resonator into a MZI as shown in Figure 10. For the input state we again take a simple expression for a photon pair at the input ports of the first beamsplitter:

$$|\psi_{in}\rangle = \hat{a}_1^\dagger \hat{a}_2^\dagger |0,0\rangle_{1,2} \otimes |0\rangle_{env} \tag{61}$$

where $|0\rangle_{env}$ is the vacuum state for the environment, or a thermal bath of oscillators, which is acted on by the noise operators in the quantum WGM model. First we find the state in modes 5 and 6 after coupling to the WGM resonator.

Operation of first beamsplitter transforming to modes $\hat{a}_3$, $\hat{a}_4$:

$$\hat{a}_3 = \frac{1}{\sqrt{2}}(\hat{a}_1 + i\hat{a}_2); \;\; \hat{a}_4 = \frac{1}{\sqrt{2}}(i\hat{a}_1 + \hat{a}_2). \tag{62}$$

Coupling mode $\hat{a}_4$ to the WGM resonator to transform to modes $\hat{a}_5$, $\hat{a}_6$:

$$\begin{aligned}\hat{a}_5 &= \frac{1}{\sqrt{2}} t(\omega)\,(i\hat{a}_1 + \hat{a}_2) + \hat{F}(\omega) \\ \hat{a}_6 &= \frac{1}{\sqrt{2}}(\hat{a}_1 + i\hat{a}_2)\end{aligned} \tag{63}$$

where the WGM coupling term and noise operators are given by:

$$\begin{aligned}t(\omega) &= \left(\frac{r - \alpha e^{i\theta}}{1 - r^* \alpha e^{i\theta}}\right) \\ \hat{F}(\omega) &= -i|\kappa|^2\sqrt{\Gamma}\sum_{n=0}^{\infty}(r^*)^n \int_0^{(n+1)L} dz\, e^{i\xi(\omega)[(n+1)L - z]}\hat{s}(z,\omega).\end{aligned} \tag{64}$$

Writing the relation between input and output modes in terms of a transfer matrix $\mathbf{M}$:

$$\begin{pmatrix}\hat{a}_5 \\ \hat{a}_6\end{pmatrix} = \frac{1}{\sqrt{2}}\begin{pmatrix}it(\omega) & t(\omega) \\ 1 & i\end{pmatrix}\begin{pmatrix}\hat{a}_1 \\ \hat{a}_2\end{pmatrix} + \begin{pmatrix}\hat{F}(\omega) \\ 0\end{pmatrix} \tag{65}$$

$$\hat{\mathbf{a}}_{out} = \frac{1}{\sqrt{2}}\mathbf{M}\hat{\mathbf{a}}_{in} + \hat{\mathbf{F}}(\omega). \tag{66}$$

Then

$$\hat{\mathbf{a}}_{in} = \sqrt{2}\mathbf{M}^{-1}\left(\hat{\mathbf{a}}_{out} - \hat{\mathbf{F}}(\omega)\right) \tag{67}$$

where

$$\mathbf{M}^{-1} = \frac{1}{2t(\omega)}\begin{pmatrix}-i & t(\omega) \\ 1 & -it(\omega)\end{pmatrix}. \tag{68}$$

Finally, we have the input annihilation operators in terms of the output mode amplitudes $\hat{a}_5, \hat{a}_6$:

$$\begin{aligned}\hat{a}_1^\dagger &= \frac{\sqrt{2}}{2t^*(\omega)}\left(i\hat{a}_5^\dagger + t^*(\omega)\hat{a}_6^\dagger - i\hat{F}^\dagger(\omega)\right) \\ \hat{a}_2^\dagger &= \frac{\sqrt{2}}{2t^*(\omega)}\left(\hat{a}_5^\dagger + it^*(\omega)\hat{a}_6^\dagger - \hat{F}^\dagger(\omega)\right).\end{aligned} \tag{69}$$

The output state in modes 5 and 6 after coupling to the WGM is given by substituting for $\hat{a}_1^\dagger, \hat{a}_2^\dagger$ in the initial input state:

$$|\psi_{5,6}\rangle = \frac{1}{2(t^*(\omega))^2}\left(i\hat{a}_5^\dagger + t^*(\omega)\hat{a}_6^\dagger - i\hat{F}^\dagger(\omega)\right)\left(\hat{a}_5^\dagger + it^*(\omega)\hat{a}_6^\dagger - \hat{F}^\dagger(\omega)\right)|0,0\rangle_{5,6} \otimes |0\rangle_{env} \tag{70}$$

$$\begin{aligned}|\psi_{5,6}\rangle = \frac{1}{2(t^*(\omega))^2}\Big(&i\hat{a}_5^{\dagger 2} - t^*(\omega)\hat{a}_5^\dagger\hat{a}_6^\dagger - i\hat{a}_5^\dagger\hat{F}^\dagger(\omega) + t^*(\omega)\hat{a}_6^\dagger\hat{a}_5^\dagger + i(t^*(\omega))^2\hat{a}_6^{\dagger 2} - \\ &t^*(\omega)\hat{a}_6^\dagger\hat{F}^\dagger(\omega) - i\hat{F}^\dagger(\omega)\hat{a}_5^\dagger + t^*(\omega)\hat{F}^\dagger(\omega)\hat{a}_6^\dagger + i\hat{F}^{\dagger 2}(\omega)\Big)|0,0\rangle_{5,6} \otimes |0\rangle_{env}.\end{aligned} \tag{71}$$

Terms in $\hat{a}_5^\dagger\hat{a}_6^\dagger$ and $\hat{a}_6^\dagger\hat{F}^\dagger(\omega)$ cancel:

$$\begin{aligned}|\psi_{5,6}\rangle = &\frac{\sqrt{2}i}{2(t^*(\omega))^2}|2,0\rangle_{5,6} \otimes |0\rangle_{env} + \frac{\sqrt{2}i}{2}|0,2\rangle_{5,6} \otimes |0\rangle_{env} \\ &- \frac{i}{(t^*(\omega))^2}|1,0\rangle_{5,6} \otimes \hat{F}^\dagger(\omega)|0\rangle_{env} + \frac{i}{2(t^*(\omega))^2}|0,0\rangle_{5,6} \otimes \hat{F}^{\dagger 2}(\omega)|0\rangle_{env}\end{aligned} \tag{72}$$

Now, we see that the probabilities for the states $|2,0\rangle_{5,6}, |1,0\rangle_{5,6}, |0,0\rangle_{5,6}$ depend on $1/|t(\omega)|^4$, which diverges at zero detuning for critical coupling with no loss. In any case, these probabilities are much greater than one near resonance. Therefore, we need to normalise the output state, but we also know that the probability of the state $|0,2\rangle_{5,6}$ should always be $1/2$ so that term must remain unchanged. If we separately normalise the other three terms with normalisation factor $A(\omega)$:

$$A^2(\omega)\left[\frac{1}{2|t(\omega)|^4}+\frac{1}{|t(\omega)|^4}|_{env}\langle 0|\hat{F}\hat{F}^\dagger|0\rangle_{env}|^2+\frac{1}{4|t(\omega)|^4}|_{env}\langle 0|\hat{F}^2\hat{F}^{\dagger 2}|0\rangle_{env}|^2\right]=\frac{1}{2}. \tag{73}$$

From Alsing et al., the expectation values of the noise operators can be calculated using:

$$\begin{aligned} {}_{env}\langle 0|\hat{F}\hat{F}^\dagger|0\rangle_{env} &= {}_{env}\langle 0|[\hat{F},\hat{F}^\dagger]+\hat{F}^\dagger\hat{F}|0\rangle_{env} \\ &= [\hat{F},\hat{F}^\dagger]. \end{aligned} \tag{74}$$

This commutator is found by using the commutation relation for the output mode amplitudes $\hat{a}_5, \hat{a}_6$ and using Equation 65:

$$\begin{aligned} &[\hat{a}_5(\omega),\hat{a}_6^\dagger(\omega)]=\delta(\omega-\omega') \\ \implies &[\hat{F}(\omega),\hat{F}^\dagger(\omega')]=\left(1-|t(\omega)|^2\right)\delta(\omega-\omega'). \end{aligned} \tag{75}$$

The expectation for the squared noise operators is given by:

$$\begin{aligned} {}_{env}\langle 0|\hat{F}^2\hat{F}^{\dagger 2}|0\rangle_{env} &= 2[\hat{F}(\omega),\hat{F}^\dagger(\omega')]^2 \\ &= \left(1-|t(\omega)|^2\right)^2\delta(\omega-\omega'). \end{aligned} \tag{76}$$

Then the normalisation constant is:

$$\begin{aligned} A(\omega) &= \left[\frac{1}{|t(\omega)|^4}+\frac{2}{|t(\omega)|^4}\left(1-|t(\omega)|^2\right)^2+\frac{2}{|t(\omega)|^4}\left(1-|t(\omega)|^2\right)^4\right]^{-1/2} \\ A(\omega) &= |t(\omega)|^2\left[1+2\left(1-|t(\omega)|^2\right)^2+2\left(1-|t(\omega)|^2\right)^4\right]^{-1/2}. \end{aligned} \tag{77}$$

The normalised output state is:

$$\begin{aligned} |\psi_{5,6}\rangle &= \frac{\sqrt{2}i}{2(t^*(\omega))^2}A(\omega)|2,0\rangle_{5,6}\otimes|0\rangle_{env}+\frac{\sqrt{2}i}{2}|0,2\rangle_{5,6}\otimes|0\rangle_{env} \\ &-\frac{i}{(t^*(\omega))^2}A(\omega)|1,0\rangle_{5,6}\otimes\hat{F}^\dagger(\omega)|0\rangle_{env}+\frac{i}{2(t^*(\omega))^2}A(\omega)|0,0\rangle_{5,6}\otimes\hat{F}^{\dagger 2}(\omega)|0\rangle_{env}. \end{aligned} \tag{78}$$

Now the probabilities of all the possible output states sum to one for all values of detuning from the resonance. We also see that the photon pairs in mode 6 have no dependence on the WGM coupling conditions, and the terms with photons in mode 5 have a $1/(t^*(\omega))^2$ dependence. This is where the double phase shift due to the two-photon N00N state comes in, because now the phase difference between photons in modes 5 and 6 is twice the usual phase shift from coupling to a WGM resonator.

The next stage is to act on this state with the output beamsplitter to interfere modes 5 and 6 which have a phase difference equal to double the WGM phase shift. Transforming back to creation operators:

$$|\psi_{5,6}\rangle = \left(\frac{i}{2(t^*(\omega))^2} A(\omega)\hat{a}_5^{\dagger 2} + \frac{i}{2}\hat{a}_6^{\dagger 2} - \frac{i}{(t^*(\omega))^2} A(\omega)\hat{a}_5^{\dagger}\hat{F}^{\dagger}(\omega) + \frac{i}{2(t^*(\omega))^2} A(\omega)\hat{F}^{\dagger 2}(\omega) \right) |0,0\rangle_{5,6} \otimes |0\rangle_{env}. \quad (79)$$

At the output beamsplitter the mode operators transform as:

$$\hat{a}_5^{\dagger} = \frac{1}{\sqrt{2}}(\hat{a}_7^{\dagger} + i\hat{a}_8^{\dagger}); \;\; \hat{a}_6^{\dagger} = \frac{1}{\sqrt{2}}(i\hat{a}_7^{\dagger} + \hat{a}_8^{\dagger}). \quad (80)$$

Substituting into the state $|\psi_{5,6}\rangle$ gives the final output state:

$$\begin{aligned} |\psi_{out}\rangle = {} & \frac{i\sqrt{2}}{4}\left(\frac{A(\omega)}{(t^*(\omega))^2} - 1 \right) |2,0\rangle_{7,8} \otimes |0\rangle_{env} + \frac{i\sqrt{2}}{4}\left(1 - \frac{A(\omega)}{(t^*(\omega))^2} \right) |0,2\rangle_{7,8} \otimes |0\rangle_{env} \\ & + \frac{1}{2}\left(\frac{A(\omega)}{(t^*(\omega))^2} + 1 \right) |1,1\rangle_{7,8} \otimes |0\rangle_{env} - \frac{iA(\omega)}{\sqrt{2}(t^*(\omega))^2} |1,0\rangle_{7,8} \otimes \hat{F}^{\dagger}(\omega)|0\rangle_{env} \\ & - \frac{A(\omega)}{\sqrt{2}(t^*(\omega))^2} |0,1\rangle_{7,8} \otimes \hat{F}^{\dagger}(\omega)|0\rangle_{env} + \frac{iA(\omega)}{2(t^*(\omega))^2} |0,0\rangle_{7,8} \otimes \hat{F}^{\dagger 2}(\omega)|0\rangle_{env}. \quad (81) \end{aligned}$$

Figure 11 shows the sum of coincidence $\{P(1,1)\}$ and single $\{P(0,1), P(1,0), P(0,2), P(2,0)\}$ detection probabilities as a function of detuning from resonance for WGM parameters $a = 0.9997, r = 0.9990$, i.e. overcoupling. 'Single' detections refer to all measurement outcomes where only one single photon detector (not a photon number resolving detector) detects photons. The sum of all detection probabilities is one showing the output state is correctly normalised.

Both the single detection and coincidence spectra have a double peak/dip structure which is very different from the typical Lorentzian dip in the WGM transmission spectrum. This seems to be the consequence of the double phase shift for the two photon N00N state coupled to the WGM resonator. As for the linear phase shift MZI, there are points in the interference signal with a higher gradient and hence higher sensitivity to changes in the detuning, than in the classical transmission signal. It may be possible to make measurements with enhanced sensitivity to the WGM resonance shift using entangled photon pairs. This is explored further in the next section.

Figures 12 and 13 show the coincidence rate and the ratio between the singles and coincidence rate, respectively. Over a range of coupling conditions we can see that the double dip in the coincidence spectrum emerges as the coupling approaches critical coupling. The visibility of the double dip spectral shape has the highest visibility for overcoupling. The singles to coincidence ratio instead has a sharp double peak. Measuring this ratio would allow both the single and coincidence counts to be used.

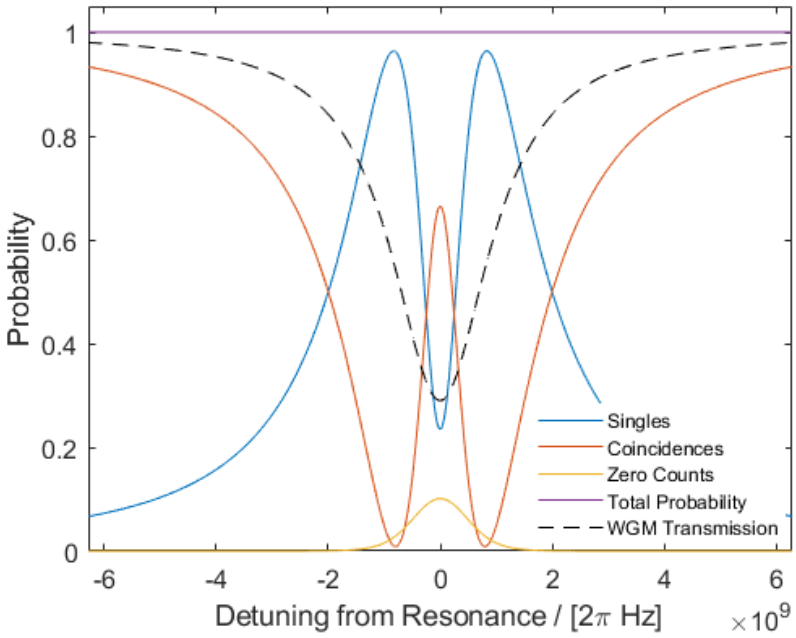

Figure 11: Detection probability spectrum for entangled photon pairs at the input to a WGM coupled MZI. Coupling parameters for the WGM resonator were $\alpha = 0.9997$ and $r = 0.9990$ (overcoupling). The three measurement outcomes single detections, coincidence detections, and no detections (zero counts) are plotted along with the total probability to show the output state is correctly normalised. The black dotted line shows the transmission spectrum for a waveguide coupled to a WGM resonator with the same α and r parameters.

2.4 Sensitivity Enhancement for a WGM coupled MZI with Entangled Photon Input

In the previous section I showed that the transmission spectrum for a WGM resonator coupled to one arm of a MZI has a double dip (peak) in the coincidence (singles) count rate, when the input state is an indistinguishable pair of photons. This spectrum is a consequence of the double phase shift introduced by an N=2 N00N state produced inside the interferometer and is not seen when considering classical input fields. A clear feature of the entangled transmission spectra is that they have sharp features with higher gradients than seen in the classical spectra for the same coupling conditions. In this section I will investigate the potential sensitivity enhancements that these spectral features might allow in the detection of shifts in the WGM resonance wavelength.

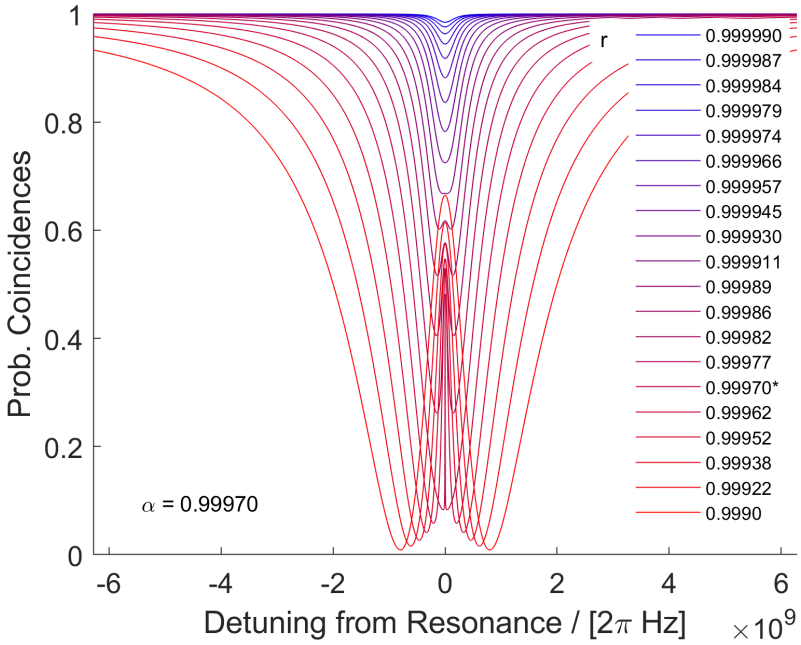

Figure 12: Transmission spectra for entangled photon WGM coupled MZI for coincidence detections. The WGM coupling parameter r is varied from undercoupling (blue) to overcoupling (red). α is fixed at 0.9997.

2.4.1 Computational model for classical and quantum WGM sensing

For comparison I will consider three cases: **1. 'Classical transmission'** The transmission spectrum for a single mode classical input field coupled to a WGM resonator, i.e. the 'conventional' WGM sensing experiment. **2. 'Classical MZI'** The transmission spectrum for a WGM resonator coupled to one arm of a MZI, with a classical field in one input mode, and monitoring one of the MZI output modes. **3. 'Entangled MZI'** The transmission spectrum for a WGM resonator coupled to one arm of a MZI, with indistinguishable photon pairs in the two input modes, and measuring coincidence detections in the two output modes.

The transmission spectra for these three cases use the equations presented in the previous section. The classical transmission spectrum:

$$I_{class} = |t(\omega)|^2 = \left| \frac{r - \alpha e^{i\theta(\omega)}}{1 - r^* \alpha e^{i\theta(\omega)}} \right|^2 . \tag{82}$$

The classical MZI spectrum (normalised such that the transmission spectrum in one output mode spans [0,1]):

$$I_{class,MZI} = |1 + t(\omega)|^2 . \tag{83}$$

The entangled MZI spectrum, which is the coincidence probability as a function of de-

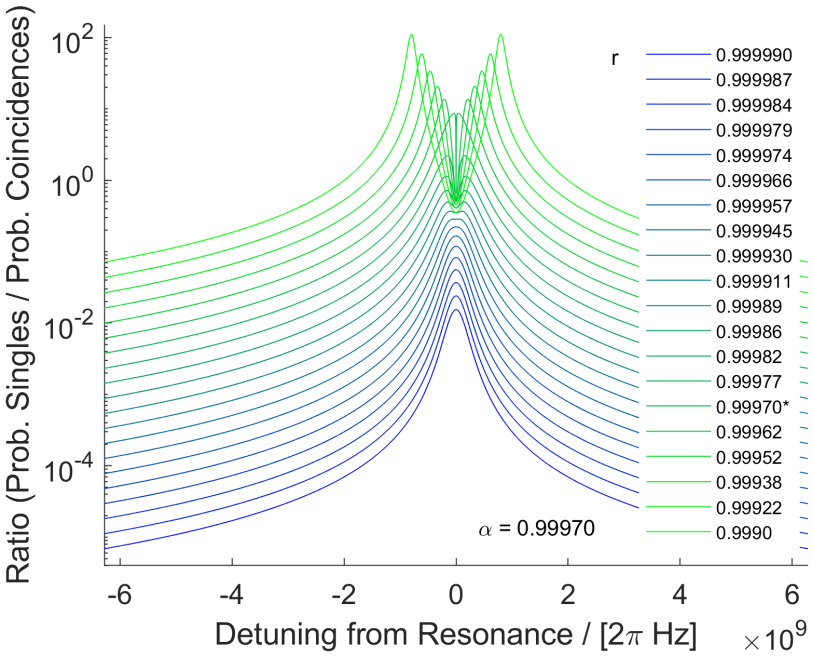

Figure 13: Transmission spectra for entangled photon WGM coupled MZI for ratio between single and coincidence detections. The WGM coupling parameter r is varied from undercoupling (blue) to overcoupling (green). α is fixed at 0.9997.

tuning from resonance from the previous section:

$$P_{coinc} = \left| \frac{1}{2} \left(\frac{A(\omega)}{(t^*(\omega))^2} + 1 \right) \right|^2. \tag{84}$$

The change we would like to detect for sensing experiments is a shift in the WGM resonance wavelength λ_o. Typically, this is measured by repeatedly scanning the input laser wavelength across the resonance and extracting the resonance wavelength and linewidth using a centroid fitting algorithm (see supplementary information of Ref. [32]). To simplify the experiment and avoid the need to rapidly tune the entangled photon wavelength we can instead consider an intensity measurement at a single point in the transmission spectrum with maximum gradient, i.e. at fixed detuning from resonance. This could be achieved experimentally either by locking the input beam wavelength to the resonance or ensuring the resonance wavelength is stable over the duration of a measurement. For each of the three cases introduced above, we can model the sensitivity of an intensity measurement to changes in the resonance wavelength (or linewidth), and the effects of randomly generated noise in the model signal.

Three examples of transmission spectra for the classical and entangled cases are shown in Figure 14, with overcoupling, near-critical coupling, and undercoupling conditions. On the right hand side the gradient $dI/d\omega$ is shown. In the entangled case, the narrow peak at the centre of the transmission spectrum has sharp gradients, with the gradient being

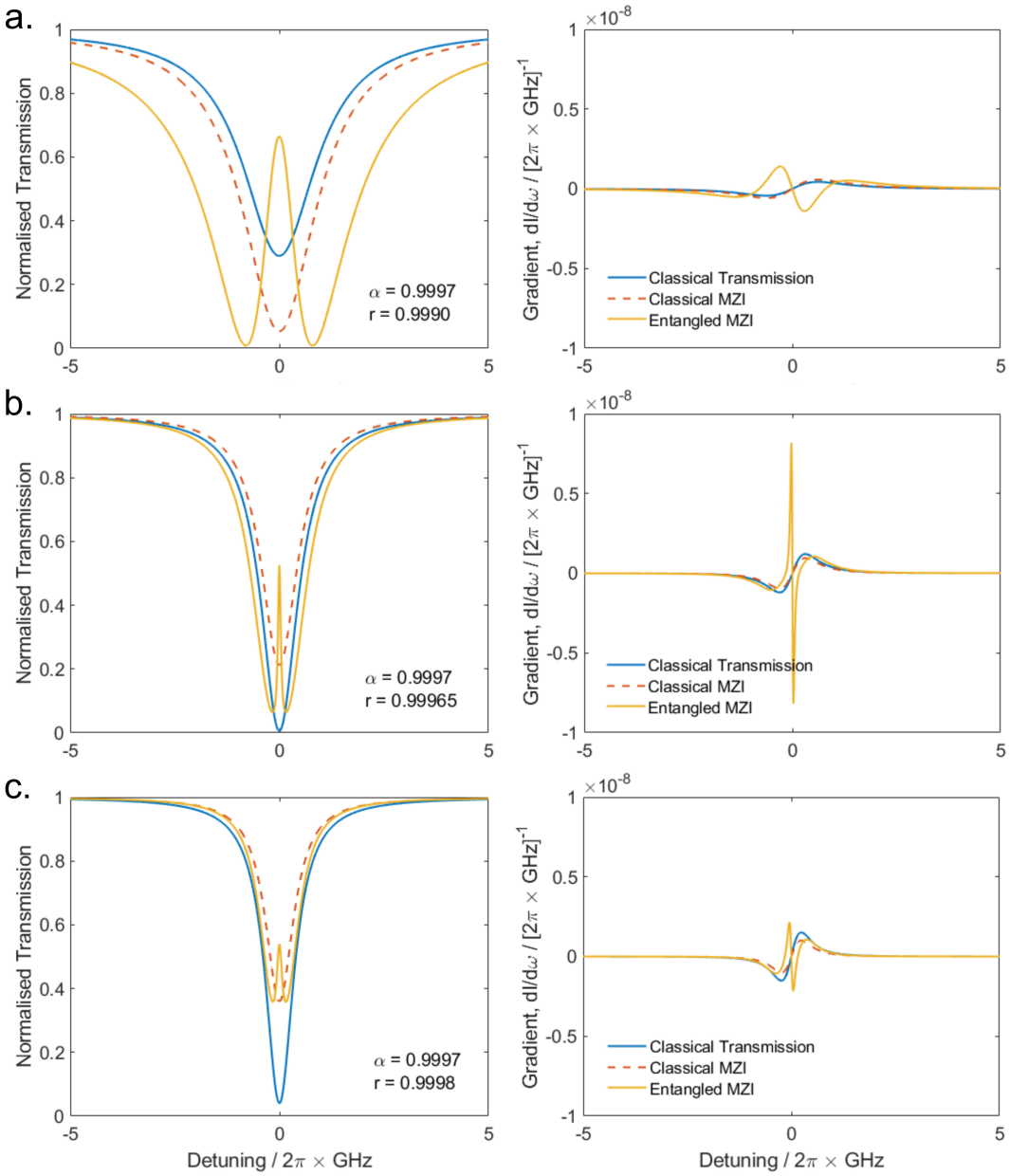

Figure 14: Classical and entangled photon transmission spectra. Transmission spectra for a WGM resonator coupled to a waveguide with classical light (blue), a WGM coupled MZI with classical input state (orange, dashed), and a WGM coupled MZI with entangled photon pair input state (yellow). The left column shows the transmission spectra (entangled photon spectrum is for coincidence detections), right column shows the gradients of the spectra. Three WGM coupling conditions are shown: (a) overcoupled ($\alpha = 0.9997$, $r = 0.9990$), (b) near critical coupled ($\alpha = 0.9997$, $r = 0.99965$), and (c) undercoupled ($\alpha = 0.9997$, $r = 0.9998$).

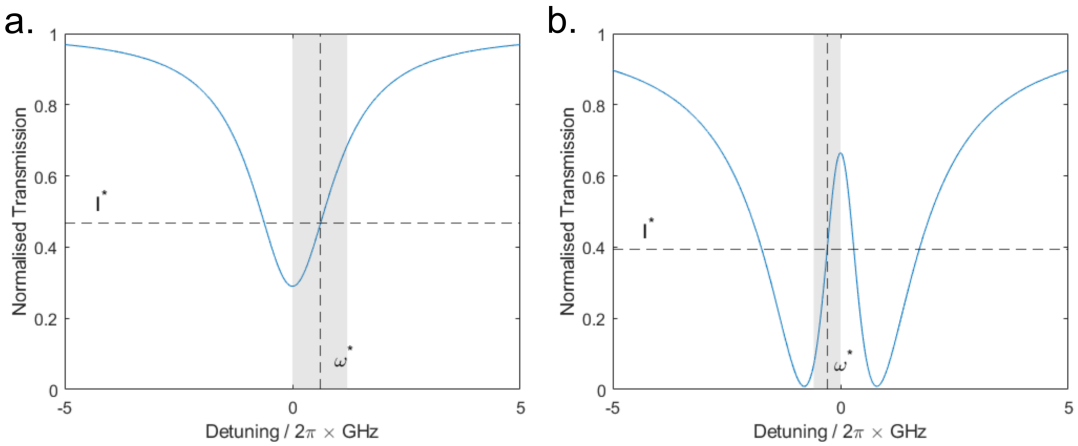

Figure 15: Illustration of maximum gradient points used for sensing model. (a) Classical transmission spectrum ($\alpha = 0.9997$, $r = 0.9990$) showing the maximum gradient point $\omega*$. The noise model uses a measurement of the intensity $I*$ to track changes in the resonance position. (b) Entangled MZI transmission spectrum ($\alpha = 0.9997$, $r = 0.9990$), here the maximum gradient point is on the sharp central peak of the coincidence spectrum. Grey areas show the maximum frequency change before the transmission spectrum reaches a maximum/minimum. This it the frequency range taken as the dynamic range of the measurement in Figure 19.

maximum near critical coupling. This suggests there is a highly sensitive point in the entangled coincidence spectrum where small changes in ω are translated into relatively large changes in the intensity I. Examples of the maximum gradient points ω^* which are tracked for each coupling condition are shown in Figure 15.

From the maximum gradient point, we can read off the change in the resonance frequency ω_o and linewidth Γ in the combined frequency change $\Delta\Omega$, via the change in transmission intensity ΔI:

$$\begin{aligned} \Delta I &= \frac{dI}{d\omega}\Delta\Omega \\ \Delta\Omega &= \Delta\omega_o + \frac{1}{2}\Delta\Gamma. \end{aligned} \tag{85}$$

We now need to make a time series of intensity measurements and add randomly generated noise to the signal to investigate the sensitivity of resonance shift measurements in each of our three cases. Typically $N_{steps} = 10^3$ time steps were used. For each time step, two types of noise are added to the transmission spectrum. The first is a random change in the resonance frequency ω_o. This is to model noise sources affecting the WGM resonator such as thermorefractive noise, changes in the coupling conditions, or fluctuations in the laser wavelength. We assume this noise is dominated by thermal sources so it can be modelled by a Gaussian distribution. The second noise source is photon shot noise due to counting small numbers of photons per time bin. This is modelled with a Gaussian

distribution with standard deviation $\sqrt{N}$ (where N is the number of photons counted per time bin) to approximate the Poisson distribution for the photon number in a coherent state.

The resonance frequency noise and shot noise are both generated using the MATLAB function *randn()* which draws pseudo-random samples from a Gaussian distribution. The final 3σ uncertainty in the combined frequency change $\Delta\Omega$ was calculated from the standard deviation of the measured intensity over 10^3 time steps, using the gradient $dI/d\omega$ to convert from intensity change ΔI to $\Delta\Omega$.

An important thing to consider is how to fairly compare the number of photons per time bin between the three different cases. A fair comparison should have the same photon rate at the sample being detected, so in our case the same photon rate coupled to the WGM resonator. The photon number expectation value for the two photon N00N state in one arm of the MZI is $\langle\hat{N}\rangle = 1$ per photon pair at the input. Let the photon pair rate be P. For the classical transmission case the same photon rate at the sample is achieved with an input photon rate $R = P$. For the classical MZI, an input rate of $R' = 2P$ at one of the MZI inputs results in an equal photon rate at the sample.

To calculate the shot noise in the photon number per time bin for each measurement, the detected photon rate is relevant. The maximum (off-resonance) detection rates are P coincidence rate for the entangled MZI case, P singles rate for the classical transmission case, and P singles rate for the classical MZI case since photons are detected at one of the MZI outputs. Therefore the shot noise per time bin is calculated using the same detected coincidence/singles rate in all three cases.

The following plots use parameters which were chosen to be roughly comparable to typical WGM sensing experiments to give some intuitive link to real experiments. For the noise in the resonance wavelength, a standard deviation of 1 fm was used throughout the following investigation, and all noise values are given in fm for comparison to experiments which typically quote wavelength shifts. A MATLAB script used to calculate these results is included in Appendix B.

2.4.2 Modelling results - sensitivity enhancements

Figure 16 shows the 3σ uncertainty $\Delta\Omega$ for classical transmission, classical MZI, and entangled MZI as a function of detected photon count rate at a fixed time bin width of $\Delta t = 100$ ms, i.e. increasing the optical power used in the measurement. The coupling conditions are set to slightly overcoupled: $\alpha = 0.9997$ and $r = 0.9996$. There are two main regimes: for photon count rates $> 10^6$ Hz, the resonance frequency noise dominates

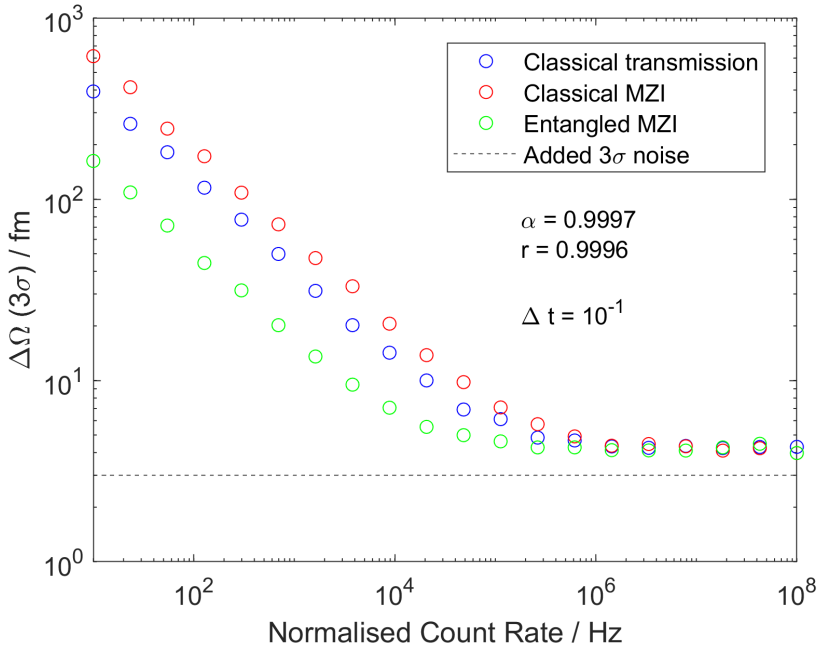

Figure 16: Noise in WGM frequency shift measurement as a function of detected photon count rate. The 3σ level noise in the combined frequency shift $\Delta\Omega$ was calculated from a Monte Carlo model with 10^3 measurements per point. The integration time per measurement was $\Delta t = 10^{-1}$ s, so the photon number per measurement is $R\Delta t$, where R is the detected count rate on the x axis. The dotted line shows the 3σ level for the noise that was added to the resonance position (3 fm) to simulate classical noise sources. This noise dominates at high photon count rates, but at low count rates the measurement is shot-noise-limited.

and the noise is constant as the optical power increases, slightly above 3 fm expected from the $1\sigma = 1$ fm noise which was added. This is the regime in which typical WGM sensing experiments will operate. For count rates $< 10^4$ Hz, shot noise begins to dominate and the uncertainty in the wavelength shift increases as $\sqrt{N}$ as the number of photons per time bin N decreases.

From Figure 16, we see that the entangled MZI has reduced noise in the wavelength shift in the shot-noise-limited region compared to the two classical cases. We can understand this to come from the higher gradient $dI/d\omega$ at the point being monitored in the entangled MZI spectrum, since the intensity noise ΔI is scaled down by this factor when converting to $\Delta\Omega$. The ratio between the noise in the three cases reaches a constant at low count rates.

The reduced noise in the entangled MZI case illustrates there could be a sensing advantage to using entangled photon pairs, but only in the shot-noise-limited regime - at low optical power. The absolute noise in the measurement is still minimised by increasing the optical power and reaching the noise floor due to the thermorefractive noise, laser noise etc. that affects the WGM resonance frequency. However, if the measurement is limited to low optical power then the entangled photon MZI setup clearly provides an advantage in sensitivity to WGM wavelength shifts. Next, we would like to investigate the noise level over a range of coupling conditions to the WGM resonator to find the coupling regime which offers the best sensitivity enhancement.

In Figure 17, the 3σ noise level is plotted as a function of the coupling reflection coefficient r, from overcoupled ($r = 0.9990$) to undercoupled ($r \to 1$). These plots were all with a photon number per bin $R\Delta t = 380$, which was chosen because it is at the edge of the shot-noise-limited regime (see Figure 16). Figure 17 shows the same data but plotted relative to $\Delta\Omega$ for the classical transmission case as the ratio $\Delta\Omega_{classtrans}/\Delta\Omega$, which is the factor by which the noise is reduced compared to the conventional classical WGM transmission measurement. The factor $\Delta\Omega_{classtrans}/\Delta\Omega$ is also the enhancement factor of the SNR, compared to the SNR for a measurement with the classical transmission setup.

A clear feature from Figure 17 is the behaviour around the critical coupling point ($r = \alpha = 0.9997$), where the gradient of the entangled MZI transmission spectrum diverges. This produces a sharp peak in the enhancement factor for the entangled MZI noise. We also see that the entangled MZI measurement has the lowest noise level across the overcoupled regime, and for undercoupling with $r \lesssim 0.99978$.

To see the noise behaviour across the full range of photon count rate shown in Figure 16 we can plot the entangled MZI enhancement factor $\Delta\Omega_{classtrans}/\Delta\Omega$ for different pho-

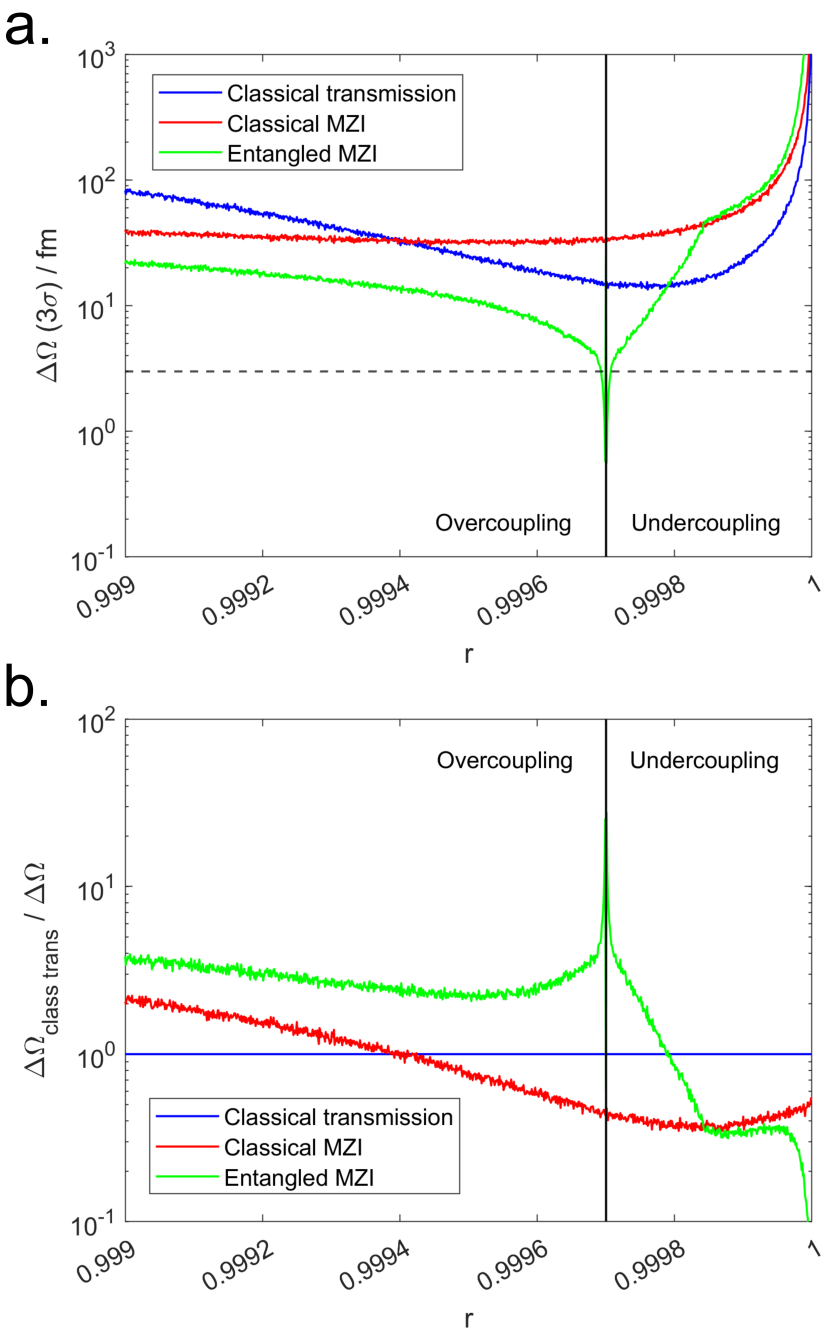

Figure 17: Noise in WGM frequency shift measurement as a function of WGM coupling parameter r. (a) The parameter α was fixed at 0.9997 and r was varied from under- to overcoupling, critical coupling is shown by the black vertical line. $\Delta\Omega$ is shown for the three experimental cases at a fixed photon number per measurement of $R\Delta t = 3.8 \times 10^2$. The dotted line shows the 3σ noise level of the classical noise. (b) Ratio between noise in the classical transmission case $\Delta\Omega_{class\,trans}$ and the two MZI cases, i.e. showing the enhancement factor in the SNR compared to the classical transmission case.

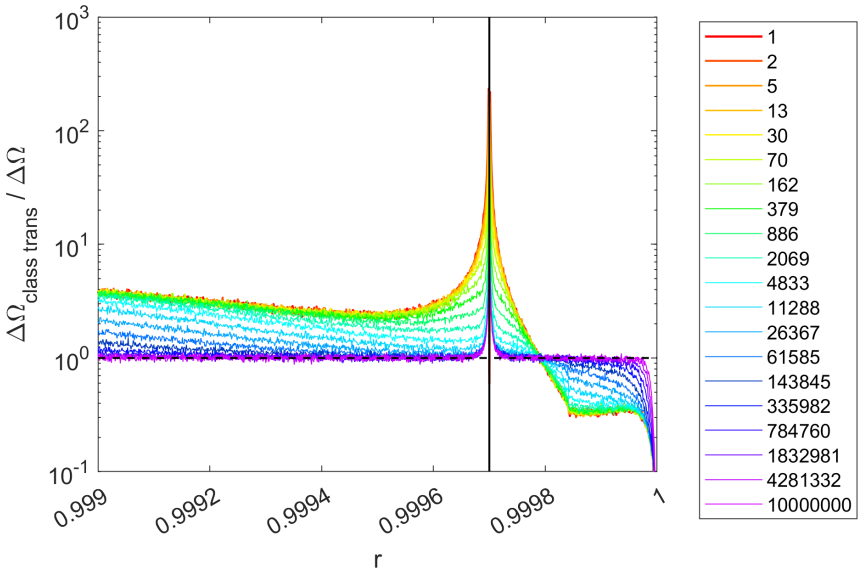

Figure 18: Noise in WGM frequency shift measurement as a function of WGM coupling parameter r and photon number per measurement. Ratio between $\Delta\Omega_{class\,trans}$ and the noise in the entangled photon MZI model for fixed $\alpha = 0.9997$ and varying r. Colours show changing photon number per measurement, i.e. moving along the x axis in Figure 16.

ton count rates, see Figure 18. As expected from Figure 16, the sensitivity enhancement is greatest and roughly constant in the shot-noise-limited regime (photon number per time bin $N \lesssim 10^3$).

It would seem like the best sensing performance for the entangled MZI case is achieved with the WGM resonator as close as possible to critical coupling. However, close to critical coupling the sharp peak in the entangled MZI spectrum becomes extremely narrow (see Figure 14). This will ultimately limit the dynamic range of the sensor since the spectrum can easily shift away from the region with the highest sensitivity. Here the dynamic range will be taken to be the region from the maximum gradient point to the nearest maximum/minimum in the spectrum, as illustrated in Figure 15. If the noise level becomes higher than this dynamic range then no signals can be detected.

The dynamic range is shown in Figure 19 as the grey area. The dynamic range $\Delta\lambda_{DR}$ was calculated for the entangled MZI spectrum over the full range of coupling conditions, then plotted as $\Delta\Omega_{classtrans}/\Delta\lambda_{DR}$ to compare to the entangled MZI SNR enhancement ratio. All the points within the grey area have a 3σ noise level greater than or equal to the dynamic range, so cannot be used effectively for sensing. This excludes the large peak near critical coupling, and shows that the highly overcoupled regime provides the best performance.

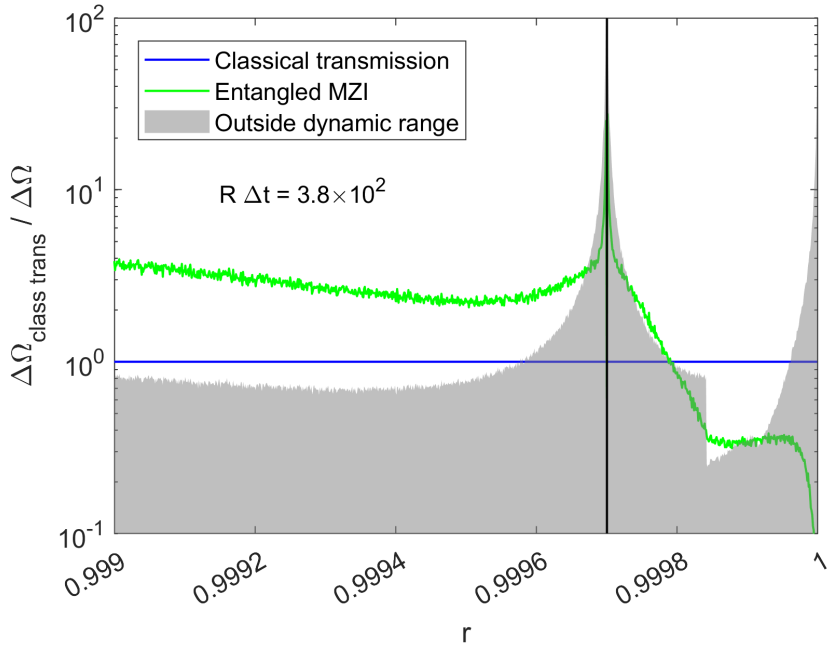

Figure 19: Effect of dynamic range on SNR enhancements achievable with the entangled photon MZI model. The classical transmission and entangled MZI models are compared with the same data as in Figure 17. The grey area shows where the entangled MZI 3σ noise level is greater than or equal to the dynamic range of the edge-of-resonance intensity measurement, so these regions of the parameter space cannot be used for a measurement of the resonance shift.

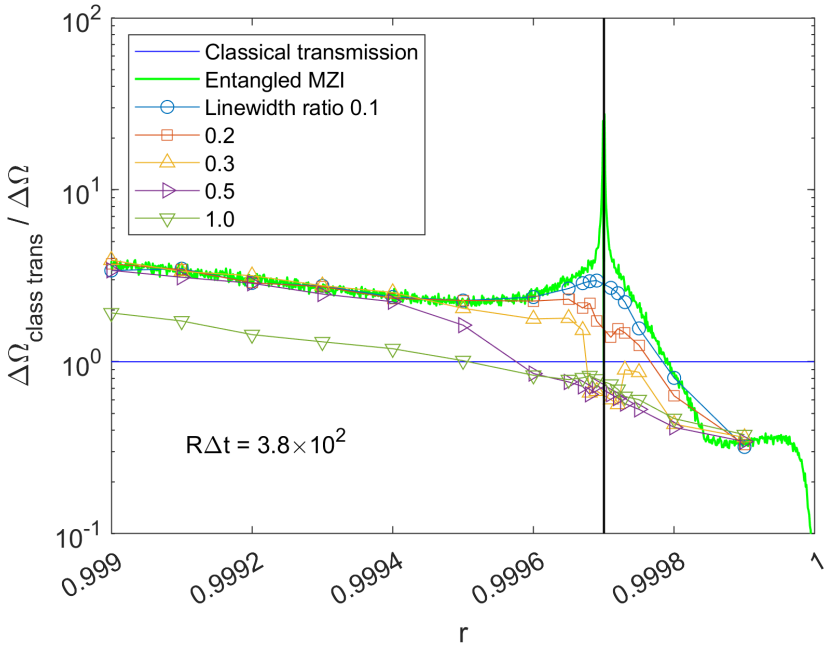

Figure 20: Effect of input linewidth on SNR enhancements achievable with the entangled photon MZI model. The classical transmission and entangled MZI models are compared with the same data as in Figure 17. The green line shows the entangled MZI noise for a monochromatic entangled photon state, points show the noise as the spectral linewidth of the entangled photon state is changed. Linewidths are given as ratios with the WGM linewidth in the classical transmission case, from 0.1 to 1.0 times the WGM linewidth.

A further consideration is the spectrum of the input light to the WGM resonator. So far it has been assumed that while the WGM resonance has a linewidth, the input light is monochromatic. For a more realistic treatment the linewidth of the input light should be included, since a laser or photon pair source will not generally have a linewidth that is much less than the WGM linewidth. To model this effect, the transmission spectra for each case were convolved with a Gaussian function, then the convolution was used instead of the normal spectrum to model the noise $\Delta\Omega$ from a time series of 10^3 points.

Figure 20 shows the entangled MZI noise level relative to the classical transmission case, including the linewidth of the input light. The ratio between the input linewidth and the WGM linewidth was varied between 0.1 and 1.0. As the input linewidth increases, first we see the peak near critical coupling disappears. This is expected since the spectral features near critical coupling become very narrow and will not be resolved if the input spectrum is wider than these features. In the strongly overcoupled regime, the SNR enhancement remains high up to a linewidth ratio of around 0.5. For an input linewidth equal to the WGM linewidth, there is no longer any sensitivity enhancement across most of the range of coupling conditions.

Overall, to achieve the best sensitivity enhancement the WGM resonator should be strongly overcoupled, and the input linewidth should be less than around 0.3 times the WGM linewidth. Under these conditions we see approximately a factor of two enhancement in the SNR of the resonance shift measurement, when the photon number per time bin $R\Delta t = 380$. This enhancement is compared to the conventional WGM transmission measurement, with a classical light source and an equal input photon count rate. For lower photon count rates, the enhancement factor is expected to stay approximately constant based on Figure 16. As the count rate is increased, the enhancement factor will decrease until the noise becomes limited by the conventional resonance frequency noise introduced earlier.

2.5 Conclusions

This chapter introduced a model for describing WGM resonances in quantum optics from Alsing et al. [62]. The model was applied to a WGM resonator coupled to one arm of a MZI. For a classical input state, the transmission spectrum is similar to the transmission spectrum of a single optical mode coupled to a WGM resonator. However, with an entangled photon pair as the input state, the transmission spectrum in terms of coincidence detections at the interferometer outputs has a double dip feature which is most visible for an overcoupled WGM resonator.

Using the feature that the entangled transmission spectrum has points with higher gradients than the classical spectra, I showed a computational study into a simple WGM resonance shift measurement by monitoring the transmission at the highest gradient point in the spectrum. With this model, I showed an example where the entangled photon input state can provide up to a factor of two enhancement in the SNR of this measurement compared to a classical transmission measurement without the MZI (the classical measurement with the MZI had a lower SNR than this). The best enhancement was achieved for a strongly overcoupled WGM resonator, and in the low photon number regime ($\sim$100 photons per time bin) where the measurement is shot-noise-limited. It also requires that the spectral width of photons is narrower than the WGM linewidth ($\sim$0.1 times the linewidth).

This was intended as one example of how a SNR could be achieved using entangled photons, with some consideration of realistic experimental parameters. Considering optical losses in the components and detectors in this measurement scheme will have a large impact on the enhancements which are actually achievable.

The entangled transmission spectrum result is interesting for the physics of WGM resonators in itself. The enhanced phase shift experienced by path-entangled photons

in a MZI is now being applied to the phase shift from an optical resonance, rather than a linear phase change which has been more commonly studied in previous work. The resonator produces a much more complex behaviour as the form of the entangled photon transmission spectrum depends strongly on the coupling condition of the WGM resonator.

This model also serves to motivate the following chapters which follow the building of single photon and entangled photon sources for quantum sensing applications. Chapters 6 and 7 will revisit applying quantum sensing schemes to WGM resonators and give some further discussion of how to realise these experimentally.

Part II - Investigating Single Photons from hBN Defects with sub-Poissonian Statistics for Applications in Biosensing

3 Single Photon Emission from Atomic Vacancy Defects in Hexagonal Boron Nitride

3.1 Introduction

Single photon states have been introduced as a fundamental concept in quantum optics, as an $n = 1$ photon number state $|n\rangle$ (or Fock state). One approach to preparing light to use in a sensing experiment, a 'bottom-up' approach, would be to generate single photons in order to build more complex quantum optical states. For example, by combining indistinguishable single photons via HOM interference to produce entangled photon states. The state made by HOM interference of pairs of single photons is a two-photon N00N state, which has found many applications in quantum-enhanced interferometry.

An ideal single photon source for this application would have a high brightness (single photon count rate), high single photon state purity (indicated by a low $g^{(2)}(0)$ value), and would produce stable emission over long time periods. To observe HOM interference, the single photons would also have to have high indistinguishability; requiring a narrow optical spectrum which is sufficiently stable over time, and emission into a single polarisation mode. A further advantage would be a source operating at room temperature. For applications to sensing with biological samples, a room temperature photon source could be brought close to the sample or even integrated in a lab-on-chip device in the future.

Single photon sources include quantum dots [64, 65, 66, 67], trapped ions [68], single fluorescent molecules [69, 70], and atomic vacancies in crystals. In the last category, well known systems are NV-centres in diamond crystals [71, 72], and vacancy defects in 2D crystals such as transition metal dichalcogenides (TMDs) [73, 74]. TMDs including $MoSe_2$, MoS_2, WSe_2 and WS_2 host single photon emitters and, being 2D materials, have the potential for integration into compact heterostructure devices. However, these materials must be used at cryogenic temperatures to produce high quality single photon emission. In this thesis I will focus on an alternative 2D material: hexagonal boron nitride (hBN). hBN also hosts single photon emitters but maintains its high quality single photon emission up to room temperature [75, 76].

Recently, commercially available single photon sources have been developed based on quantum dots in micropillar cavities [67] and photonic crystal cavities [66]. Both these sources require cryogenic temperatures to operate and produce single photons in the near-infrared (780 nm - 980 nm). The photon indistinguishability is extremely high: up to 98%, and the single photon purity (measured using the second order correlation function, described later in this chapter) is in the range $g^{(2)}(0) = 0.01 - 0.04$. Although these sources have excellent performance, the cost and the need for cryogenic systems

is still a barrier to their use. hBN single photon emitters are more readily accessible for experiments in our lab.

In this chapter I will briefly describe the properties of atomic vacancy defects in single crystals of hBN, then detail the development and characterisation of single photon sources using these defects. The concept of building entangled states from single photons combined by HOM interference was not successful using this source due to its low coherence time. Besides entanglement, a property of single photons which could potentially be applied to sensing in biological systems is their low photon number variance. Towards this end, in the next chapter I will present experiments on stabilising the hBN crystal temperature in order to improve the intensity stability of single photon emission. I will also present measurements and modelling of the Mandel Q parameter. These studies demonstrate some important considerations when finding sensing applications for single photon emitters such as hBN.

3.2 Single Photon Emission from Hexagonal Boron Nitride

hBN is an insulating material with a 2D layered structure. It has found applications as an insulating layer in 2D heterostructure devices and in combination with conductive graphene monolayers. In its bulk form, boron nitride is also known as white graphite due to the similarities in structure between BN and graphite. For single photon emission, the relevant property of hBN is its atomic vacancy defects. These defects are missing atoms and sometimes substitutions in the crystal structure, that introduce energy levels within the wide hBN bandgap (6 eV). Optical transitions between these levels are well isolated from thermal excitation; this allows excitation of individual transitions resulting in single photon emission, even at room temperature. Not requiring cryogenic cooling systems for single photon emission makes hBN significantly more accessible than other 2D single photon emitters such as TMDs.

Chemical structure. Many possible chemical structures have been proposed for hBN defects, such as a nitrogen vacancy or an anti-site nitrogen vacancy (a missing nitrogen atom with an adjacent boron atom replaced by nitrogen) [75]. There may also be other dopant elements involved in the defect structure, including additional carbon or oxygen atoms. The exact structures of hBN defects are still under much discussion, and there are even some suggestions that some types of single photon emitters in hBN are single organic molecules trapped under hBN layers [77].

Native defects include V_N (a nitrogen vacancy), V_N^{-1} (negatively charged nitrogen vacancy), and $V_N N_B$ (nitrogen vacancy with an adjacent boron substituted by nitrogen). Some of these structures are shown in Figure 21. Computational studies using density functional theory (DFT) have estimated the transition energies for these and many

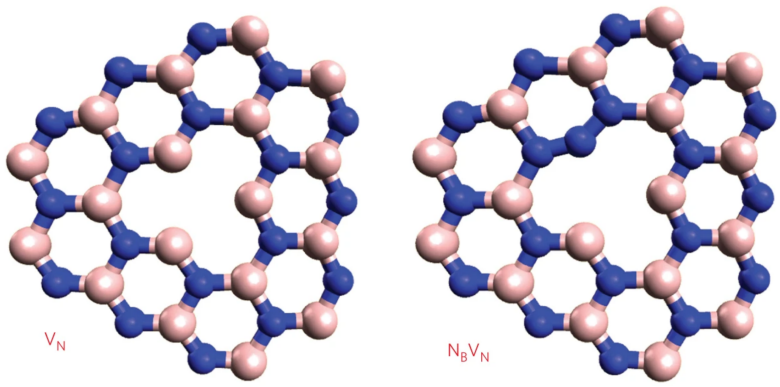

Figure 21: Schematic of two proposed structures for defects in a single layer of hBN. Blue atoms are nitrogen and pink atoms are boron. Figure adapted with permission from [75].

other defects [78, 79], with carbon containing defects attracting particular attention as researchers try to pin down the identities of single photon emitters in the visible range.

The $V_N C_B$ defect was found by Ref. [80] to match very closely to the properties of hBN emitters emitting near 2 eV (620 nm). In Ref. [81] the concentration of hBN emitters was conclusively shown to depend on the concentration of dopant carbon atoms. In that work, the negatively charged $V_B C_N^-$ defect is proposed as the most likely candidate for transitions around 585 nm, based on DFT calculations. Defects may even involve larger structures such as clusters of substituted carbon atoms. DFT simulations in Ref. [82] show that trimers of three substituted carbon atoms produce transitions in the visible range (around 750-760 nm) with spectra consistent with experiment. Carbon dimers in hBN have been identified with narrow transitions often observed at 4.1 eV (300 nm) [83] due to emitters excited under UV illumination. Some hBN emitters in the visible range have also been attributed to oxygen containing defects, such as the $O_{2B} V_N$ vacancy [84].

With so many candidates for single photon emitters in hBN, it is likely that our samples host several different types of defects. However, it is not necessary to know the exact chemical composition in order to characterise the single photon emission. Instead, a simplified energy level structure, which ignores details of the emitter's structure, is sufficient to describe the photodynamics of single photon emission.

Energy Level Structure. Most models for the energy level structure of hBN single photon emitters suggest three or four levels are needed. The simplest emitter would have a two-level structure, with transitions between the ground and excited states being responsible for antibunched photon emission. In addition to these, metastable shelving states can be added which provide non-radiative decay paths from the excited to the ground state and cause bunching in the photon emission. A three or four-level structure is supported by fitting a model to second order correlation function $g^{(2)}(\tau)$ data [85, 86].

The dynamics of photoemission may be modelled using a set of coupled differential

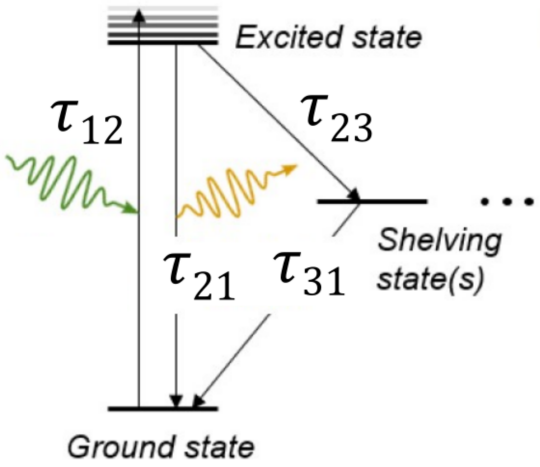

Figure 22: Three-level model for the hBN atomic defect system. The transitions are characterised by four timescales τ_{12}, τ_{21}, τ_{23}, and τ_{31}.

equations for the populations of the levels $\rho_i(t)$ at time t, as described by Boll et al. [85]:

$$\dot{\rho}_1(t) = -k_{12}\rho_1(t) + k_{21}\rho_2(t) + k_{31}\rho_3(t) \tag{86}$$

$$\dot{\rho}_2(t) = k_{12}\rho_1(t) - k_{21}\rho_2(t) - k_{23}\rho_2(t) \tag{87}$$

$$\dot{\rho}_3(t) = k_{23}\rho_2(t) - k_{31}\rho_3(t). \tag{88}$$

Here k_{ij} are the transition rates between levels i, j. In this case a three-level system is shown, but additional shelving states may be added if required to describe the $g^{(2)}(\tau)$ function. A possible energy level structure for a three-level system is shown in Figure 22. The normalised second order correlation function is derived from these equations as [87]:

$$g^{(2)}(\tau) = \frac{\rho_2(\tau)}{\rho_2(t \to \infty)}. \tag{89}$$

The initial condition for solving the differential equations is the emitter in the ground state: $\rho_1(0) = 1$, $\rho_{2,3\ldots}(0) = 0$. Then, in order to fit to experimental data for $g^{(2)}(\tau)$, the differential equations are solved for ρ_2 using the transition rates k_{ij} as fitting parameters.

The origin of this long-lived shelving state may be due to conversion between different charge states of the emitter. As discussed in [88] we can consider a model in which the emitter enters the shelving state via excitation into the conduction band by a two-photon excitation process. This causes the emitter to become more positively charged in the shelving ('dark') state, and must re-capture an electron from the conduction band to return to the radiative ('bright') state. Evidence for this model is provided by re-pumping the emitter into the bright state: for example excitation at 532 nm / re-pumping at 450 nm [88], and excitation at 675 nm / re-pumping at 532 nm [89]. In both cases, introducing the re-pumping beam enhances the emission rate and reduces the photon bunching of the

emission.

Wavelength. The emission spectrum of a typical hBN quantum emitter excited at 532 nm features a sharp zero phonon line (ZPL) with a centre wavelength in the range 540-800 nm [90, 84] and a linewidth at room temperature ∼nm [75, 90, 91]. However, hBN emission in the UV region has also been reported using short wavelength excitation [92].

There is significant heterogeneity in the ZPL wavelength between different emitters, reflecting the variety of possible defect structures and variation in the environment around a defect. For example, the layer in which an emitter is found could vary, as well as its location on a hBN single crystal and the local strain around the emitter.

Fabrication. Monolayer or multilayer flakes of hBN are obtained from bulk hBN single crystals by mechanical or solvent exfoliation. To increase the density of vacancy defects in the material, hBN layers must then be activated. For the experiments presented here, the hBN samples are provided by the group of Professor Igor Aharonovich at the University of Technology, Sydney. These samples are multilayer hBN flakes which have been activated by annealing at 850°C in a tube furnace under an argon atmosphere, according to the method described in Ref. [75].

Alternative activation methods include oxygen plasma etching [93] and irradiation with ion or electron beams [94]. Emitters with a narrow range of ZPL wavelengths have been produced by growing hBN films by low-pressure chemical vapour deposition (LPCVD) [95]. More recently, ion beams have been used to induce defects deterministically at chosen points on a hBN crystal [92].

Applications. Single photon emitters in hBN are beginning to reach the stage of being applied to quantum technologies. For example, hBN quantum emitters have been developed as pulsed single photon sources for quantum key distribution (QKD) operating at room temperature [96, 97].

Using spin defects in hBN, in particular the V_B^- vacancy, magnetic field dependence of the photoluminescence was shown in Ref. [98]. These spin defects have been manipulated using optically detected magnetic resonance (ODMR) [99, 100]. This work on magnetic field sensitive quantum emitters in hBN could lead to magnetic field sensors or even spin-based qubits.

hBN emitters can be integrated with cavities; it is even possible to fabricate photonic crystal cavities from single flakes of hBN as shown in Ref. [101]. Of particular relevance to this project is the integration of hBN emitters with WGM resonators. Ref. [102] demonstrates a hBN/TiO_2 ring resonator hosting V_B^- spin defects. An ensemble of defects are excited by the cavity mode which enhances the photoluminescence intensity via the Purcell effect. Since the emission spectrum of the defects is much broader than the WGM profile the resulting emission spectrum is a comb of WGMs within a broad envelope due

to the photoluminescence spectrum.

In Ref. [103] single quantum emitters in a hBN flake are coupled to a SiN ring resonator using CMOS fabrication processes. The input and output light from the resonator is coupled via a waveguide. By coupling single emitters to the cavity modes it was possible to demonstrate single photon emission and, as for the previous paper, the emission spectrum is a comb of narrow WGM lines within the envelope of the emitter's ZPL.

A distinct advantage of using an on-chip microring resonator system in [103] is that an emitter could be located on the hBN flake, then the resonator fabricated on top so as to overlap the emitter in a controlled way. The same procedure would not be applicable to coupling a hBN emitter to a microsphere resonator. With a microsphere, hBN would have to be attached non-deterministically and the probability of overlapping an emitter with the WGM around the equator would be very low.

3.3 Experimental Setup

Individual atomic vacancy defects in multilayer hBN single crystals were located and studied using a custom-built confocal microscope setup. Professor Jolly Xavier designed and built the setup. I was involved in building the setup, particularly the later modifications and making the LabVIEW control software, which was done with Dr Samir Vartabi Kashanian. In this custom microscope setup, the single photon emission was separated from the pump laser at 532 nm and detected on two single photon avalanche diodes (SPADs). The following sections detail the characterisation methods used to study the photon statistics of these single photon sources.

Solvent-exfoliated multilayer hBN nanoflakes (Graphene Supermarket) were provided by our collaborators Dr Minh Nguyen and Professor Igor Aharonovich, stored in a suspension of 50:50 water:ethanol. These crystals were already activated by thermal annealing at 850°C under an Ar atmosphere to increase the density of atomic vacancy defects. In order to use the sample, 10 μl amounts were drop-cast onto 5×5 mm silicon substrates, then annealed further at 500°C for 30 minutes to remove the solvent and any organic impurities. Drop-casting was done gradually with the substrate at 50°C, allowing each drop to dry partially before adding the next. The result was a visible white residue of hBN deposited in rings over the surface of the substrate, as shown in Figure 23.

Both CW and pulsed lasers at 532 nm were used as pump lasers, so lifetime measurements could also be performed on the same setup. The CW laser (Prometheus, Coherent Inc.) is very narrow linewidth: $<$ 1 kHz. The pulsed laser (PicoQuant) has both CW and pulsed modes, with a linewidth $<$ 1 nm, pulse length 72 ps, and repetition rate tuneable up to 80 MHz.

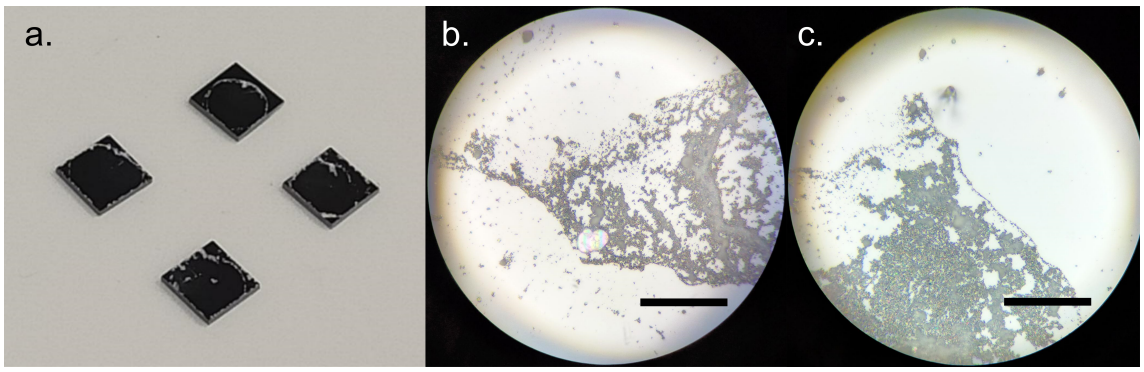

Figure 23: hBN samples drop-cast on silicon substrates. (a) Four 5×5 mm silicon substrates with hBN multilayer flakes drop-cast from a suspension in water/ethanol. (b, c) Micrographs of hBN nanoflakes deposited on the substrate. Scale bars are 100 μm.

A schematic of the setup is shown in Fig. 24. The pump beam at 532 nm from either the CW or pulsed lasers is steered by two scanning mirrors (Thorlabs Inc.) which are used to align the beam to the centre of the objective back aperture. They can also be used to steer the beam over the sample surface with high precision and very quickly, however the scanning range is limited by the back aperture of the objective blocking the beam. A scan lens ensures the spot size is roughly uniform as it moves across the image plane. The pump beam is focused by a 100x objective with numerical aperture (NA) 0.9 to a spot on the sample surface $\sim$1 μm in diameter. The sample itself is mounted on a custom aluminium sample holder on top of an *xyz* piezo translation stage (Nanocube, PI Ltd.). Using the piezo stage in closed loop operation the sample can be moved over a 100 μm range with 2 nm precision. The stage is controlled with a LabVIEW virtual instrument (VI) so the sample position can be raster scanned to produce a fluorescence intensity map of the surface.

Emission from the sample at 570-700 nm is separated from the reflected pump beam by two long-pass dichroic mirrors with band edges around 550 nm and any remaining pump light is filtered out by a long-pass filter (transmitting $>$ 568 nm). An angle-tuneable band-pass filter is also used with bandwidth 20 nm and transmission variable from 560-630 nm (Semrock).

The emitted light is coupled into an optical fibre to be taken to the SPADs. For most experiments multimode fibre with a 50 μm core diameter is used to maximise the collection efficiency of single photons, however single mode fibre must be used to maintain a single spatial mode for experiments on HOM interference.

When the tuneable filter is rotated, the output beam walks-off the optic axis. To prevent this reducing the fibre coupling efficiency a compensating plate was added after the

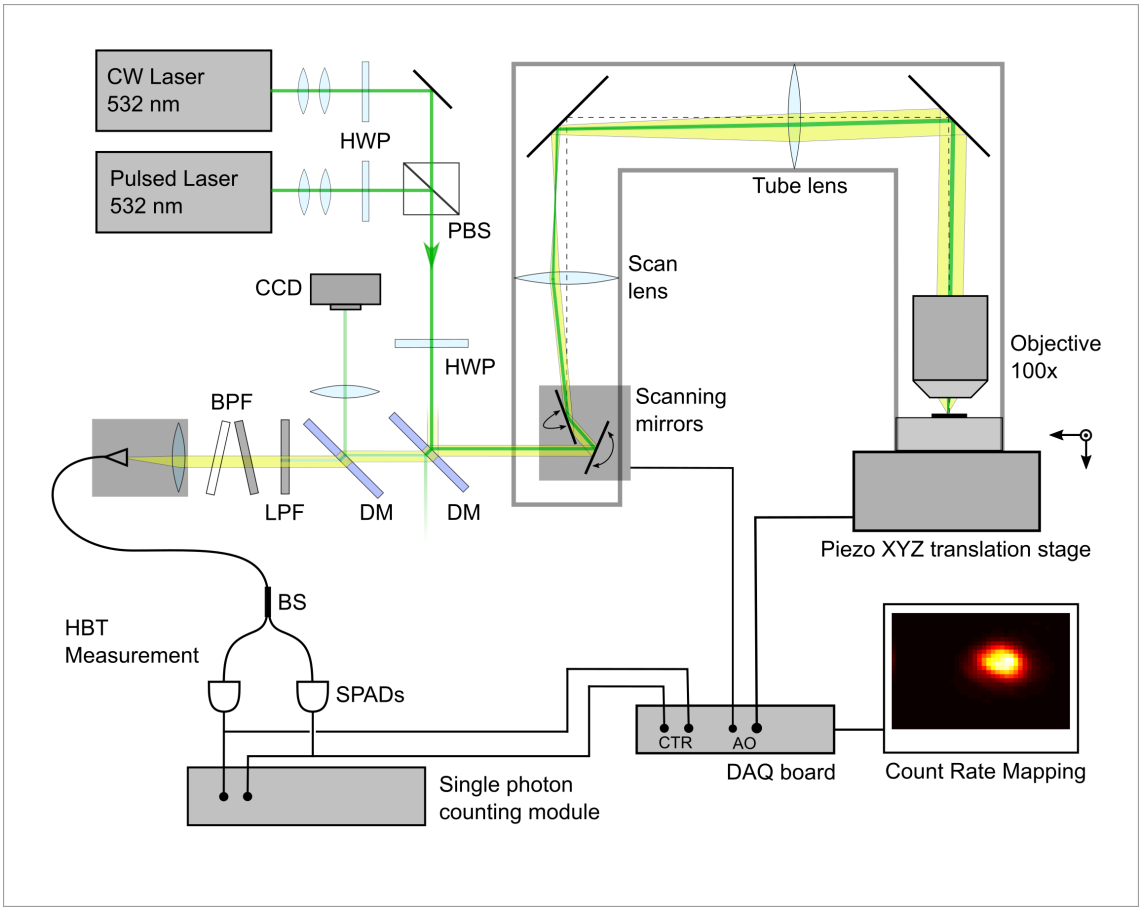

Figure 24: Custom confocal microscopy setup for studying hBN quantum emitters. DM: dichroic mirror transmitting > 550 nm; HWP: half wave-plate; PBS: polarising beamsplitter; BS: multimode fibre beamsplitter; LPF: longpass filter transmitting > 568 nm; BPF: tuneable bandpass filter with passband 20 nm; SPAD: single photon avalanche diode; DAQ: data acquisition board.

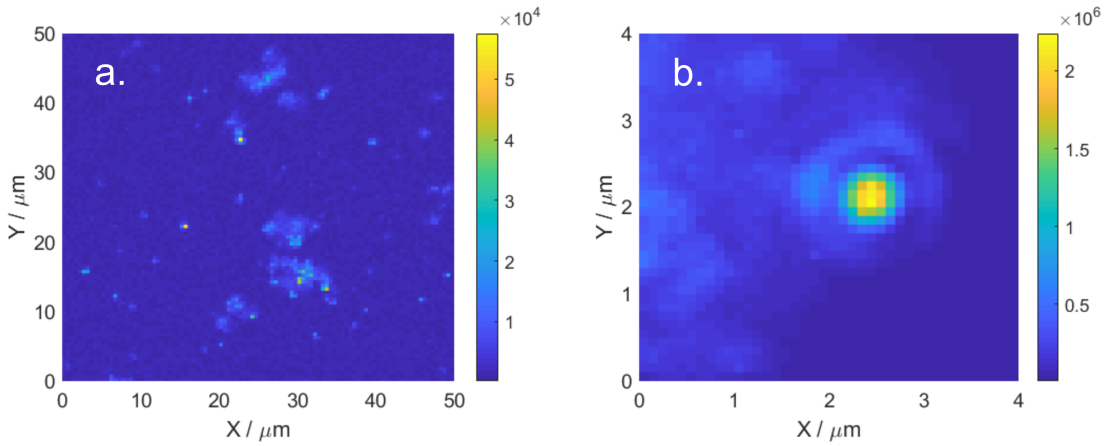

Figure 25: Fluorescence intensity maps of quantum emitters in hBN samples. (a) Standard large area scan over 50×50 μm area. (b) Standard high resolution scan zoomed in on a single emitter, 4×4 μm area. Colour maps show photon count rate in Hz.

filter which rotates in the opposite direction. Properly calibrated, the filter and compensating plate can be rotated by automated rotation mounts to produce a rough emission spectrum. This was included as a feature in the LabVIEW control VI for the experiment.

A typical experiment will first involve mapping an area of the hBN sample by scanning the piezo stage and recording the photon counts at each point over a short integration time (typically 10 ms). Defects appear as bright spots in the fluorescence intensity scan, typically 10-20 in a 50×50 μm scan area. Fig. 25 shows example fluorescence intensity maps of hBN samples. After identifying the location of a defect, the pump beam is steered to that location and the emission is split onto two SPADs (PDM Series, Micro Photon Devices) in the Hanbury Brown and Twiss (HBT) configuration. Around the wavelength of our filters, these SPADs have a detection efficiency of approximately 45%. The second order correlation ($g^{(2)}(\tau)$) function is measured to test the purity of single photon emission. This process is repeated for many emitters until one is found which satisfies the condition $g^{(2)}(\tau) < 0.5$, as explained in the next section.

3.4 Characterising Single Photon Emission

3.4.1 Second Order Correlation $g^{(2)}(\tau)$

In terms of creation and annihilation operators the second order correlation function is defined as [1]:

$$\begin{aligned} g^{(2)}(\tau) &= \frac{\langle \hat{a}_1^\dagger(t)\hat{a}_2^\dagger(t+\tau)\hat{a}_2(t+\tau)\hat{a}_1(t)\rangle}{\langle \hat{a}_1^\dagger(t)\hat{a}_1(t)\rangle\langle \hat{a}_2^\dagger(t+\tau)\hat{a}_2(t+\tau)\rangle} \\ g^{(2)}(0) &= \frac{\langle \hat{a}_1^\dagger\hat{a}_2^\dagger\hat{a}_2\hat{a}_1\rangle}{\langle \hat{a}_1^\dagger\hat{a}_1\rangle\langle \hat{a}_2^\dagger\hat{a}_2\rangle}. \end{aligned} \tag{90}$$

$\langle ... \rangle$ denotes averaging over time t. For a single photon source, the two modes 1 and 2 are made by splitting the single photon beam, and $g^{(2)}(\tau)$ quantifies correlations between detections in one mode at time t with detections in the other mode after a time delay τ.

The value of $g^{(2)}(0)$, indicates antibunched emission from a photon source if $g^{(2)}(0) < 1$. Intuitively, this indicates that photons are being detected on either one detector or the other, and that fewer coincidence detections are seen than expected for random photon arrivals. An n-photon number state has [1]:

$$g^{(2)}(0) = \frac{n-1}{n}. \tag{91}$$

So an ideal single photon state has $g^{(2)}(0) = 0$. The threshold normally taken for single photon emission is $g^{(2)}(0) < 0.5$. Since $g^{(2)}(0) = 0.5$ for the $n = 2$ number state then a lower value shows the largest contribution to the photon number distribution is from the single photon state.

To characterise the $g^{(2)}(\tau)$ function a HBT experiment was used, implemented using a fibre beamsplitter. The two outputs are taken to two fibre coupled SPADs. Electronic pulses triggered by single photon detections are delivered to two input channels of a single photon counting module (ID900 Time Controller, ID Quantique) which can assign timestamps to each detection at a resolution of up to 13 ps. The overall time resolution is limited to 50 ps by the detectors.

Experimentally, the $g^{(2)}(\tau)$ function corresponds to a histogram of time differences between photon arrivals at the two detectors. There are two approaches to building this histogram: a start-stop measurement or calculating $g^{(2)}(\tau)$ from the raw photon detection times. A start-stop measurement records the delay between a start pulse on one detector and the next stop pulse on the other detector. This is a fast method which can be done in real time using the Time Controller's FPGA hardware, however the histogram range is limited because it is biased to measuring short delays between detection times.

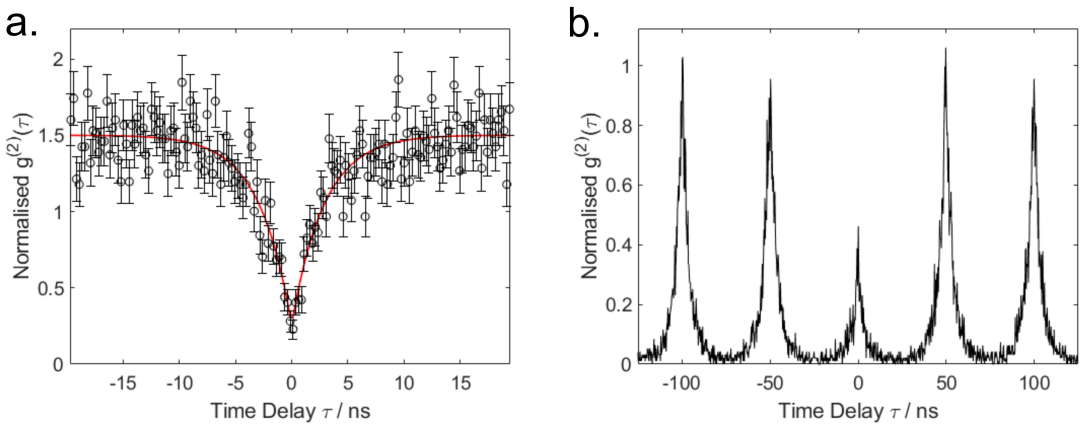

Figure 26: Second order correlation $g^{(2)}(\tau)$ functions for two different hBN emitters under (a) CW excitation 360 μW power, 600 s acquisition time; and (b) pulsed excitation with 168 μW mean power, 20.03 MHz repetition rate and 1200 s acquisition time. The error bars in the CW plot (a) were calculated using Equation 95, and the red line is a fit using the three-level model Equation 96. Both CW and pulsed measurements have $g^{(2)}(0) < 0.5$, indicating single photon emission: $g^{(2)}(0) = 0.23 \pm 0.06$ in (a) and $g^{(2)}(0) = 0.46 \pm 0.08$ in (b).

For $g^{(2)}(\tau)$ histograms over long timescales, the histogram must be calculated from the raw photon detection times or timestamps, recorded relative to the start of the measurement. The timestamps for each channel are arranged into two arrays with $N_{a,b}$ total timestamps from each channel: $\{t_{a1}, t_{a2} ... t_{aN_a}\}$, $\{t_{b1}, t_{b2} ... t_{bN_b}\}$. The differences between all times are calculated: $\{t_{a1} - t_{b1}, t_{a1} - t_{b2} ... t_{a2} - t_{b1}, t_{a2} - t_{b2} ...\}$. Keeping only time differences below the defined histogram window T, these time differences are plotted as a histogram with a bin width Δt. The resulting histogram corresponds to the *unnormalised* second order correlation function. The normalisation factor k_{norm} depends on the total detections from each channel, N_a and N_b, the total acquisition time T_{aq}, and the bin width Δt:

$$k_{norm} = N_a N_b \frac{\Delta t}{T_{aq}}. \tag{92}$$

When the histogram is re-scaled by $1/k_{norm}$ it is normalised to one for $|\tau| \to \infty$ and corresponds to the normalised second order correlation function $g^{(2)}(\tau)$. Figure 26(a) shows a normalised $g^{(2)}(\tau)$ function; note that the function decreases slowly to 1 beyond the range shown for τ, like in Figure 27.

There is also a correction for background counts due to stray laser light or background fluorescence. The signal to background ratio *SBR* is measured from the fluorescence intensity map of the emitter by taking the ratio between the peak fluorescence intensity and the average background. The normalised $g^{(2)}(\tau)$ is then corrected using the following

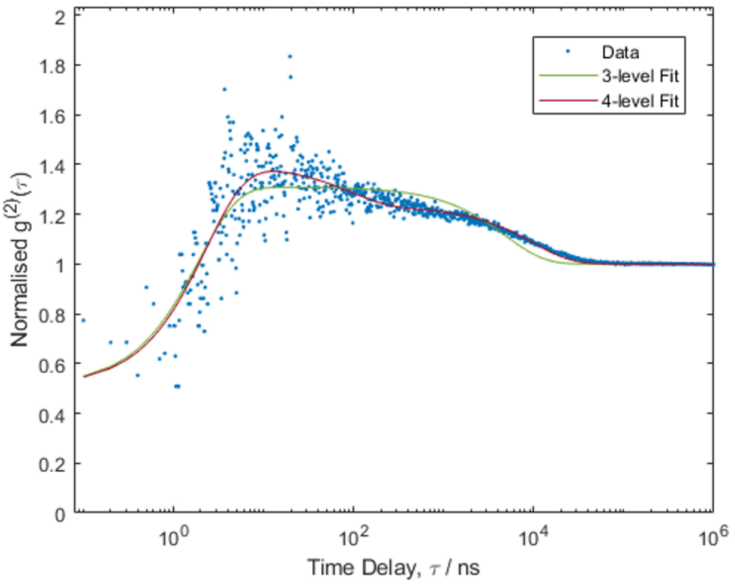

Figure 27: Second order correlation function $g^{(2)}(\tau)$ plotted over 7 orders of magnitude in delay time τ. Fits using three- or four-level models (Equations 96 and 97, respectively) are shown by green and red lines. For this emitter a four-level model with three timescales, one antibunching and two bunching timescales, is required to properly fit the data at long delay times.

transformation [85, 104]:

$$g^{(2)}_{corrected}(\tau) = \frac{g^{(2)}_{raw}(\tau) + \sigma^2 - 1}{\sigma^2} \tag{93}$$

$$\sigma = \frac{SBR}{SBR+1}. \tag{94}$$

When using a multimode fibre and fibre beamsplitter at the output, there were sharp spikes in all $g^{(2)}(\tau)$ histograms at ± 18 ns; many times higher than the other points. When the length of multimode fibre was increased, the spacing of these spikes also increased, therefore these must be due to back reflections from the fibre connections. This effect was never seen when using single mode fibres since all single mode fibres had angled APC connections to prevent back reflections. The spikes were always far from the antibunching dip and so did not affect the results. These points were removed when fitting functions to the $g^{(2)}(\tau)$ data.

Assuming Poissonian statistics for the background noise, error bars are given by:

$$\Delta g^{(2)} = \frac{\sqrt{g^{(2)}_{raw}}}{k_{norm}}. \tag{95}$$

A function can be fitted to the experimental histogram using a three-level model for the emitter. This has four parameters: A, B (antibunching depth and bunching parameters),

τ_1 and τ_2 (two characteristic emission lifetimes):

$$g^{(2)}_{fit}(\tau) = 1 - (1+A)\exp\left(-\frac{|\tau|}{\tau_1}\right) + B\exp\left(-\frac{|\tau|}{\tau_2}\right). \quad (96)$$

An example of a $g^{(2)}(\tau)$ histogram for CW excitation of a hBN emitter including background correction, error bars and the fit using Equation 96 is shown in Figure 26(a). The emitter clearly passed the threshold of single photon emission with a value of $g^{(2)}(0) = 0.23 \pm 0.06$. This measurement was done at 360 μW excitation power with 600 s acquisition time.

Another approach to fitting a function to the $g^{(2)}$ data is to use the energy level model of the emitter in Equations 86-88. This method is described in [85], where at least a four-level system is needed to properly fit $g^{(2)}$ data. The populations of all four levels are expressed in a system of differential equations, and all six transition rates plus the signal to background ratio are found by fitting this model to several sets of $g^{(2)}$ data at different excitation powers. This method was used to extract the transition rates of the three-level model from $g^{(2)}$ data in the study presented in the next chapter.

For most of the $g^{(2)}(\tau)$ data presented in this thesis Equation 96 was used to obtain best fit values for $g^{(2)}(0)$ and the emission lifetimes $\tau_{1,2}$. When the $g^{(2)}$ function is plotted over many orders of magnitude in delay time, some emitters are better described by a four-level model which is obtained by adding another exponential term to Equation 96:

$$g^{(2)}_{fit}(\tau) = 1 - (1+A)\exp\left(-\frac{|\tau|}{\tau_1}\right) + B\exp\left(-\frac{|\tau|}{\tau_2}\right) + C\exp\left(-\frac{|\tau|}{\tau_3}\right). \quad (97)$$

Figure 27 shows the difference between fitting with three-level and four-level models: for this emitter particularly at high excitation power, there is another timescale in the $g^{(2)}$ data, indicating an additional decay path from the excited state to the ground state with a different transition rate.

So far only the CW $g^{(2)}$ function has been considered; under pulsed excitation the $g^{(2)}$ function is a series of peaks spaced at the repetition period of the pulsed laser, as shown in Figure 26(b). The central peak shows the $g^{(2)}(0)$ value since it is the correlation between detections from the same laser pulse on the two detectors. Comparing data for two emitters in Figure 26 (a) and (b), $g^{(2)}(0) = 0.46 \pm 0.08$ for pulsed excitation at 168 μW mean power compared with $g^{(2)}(0) = 0.23 \pm 0.06$ under CW excitation at 360 μW. The pulsed $g^{(2)}$ function was measured at a pulse repetition rate of 20.03 MHz. This repetition rate was a trade-off between high repetition rate / high count rate, and low repetition rate to prevent overlap between adjacent pulses in the $g^{(2)}$ function, the width of each peak being determined by the emission lifetime.

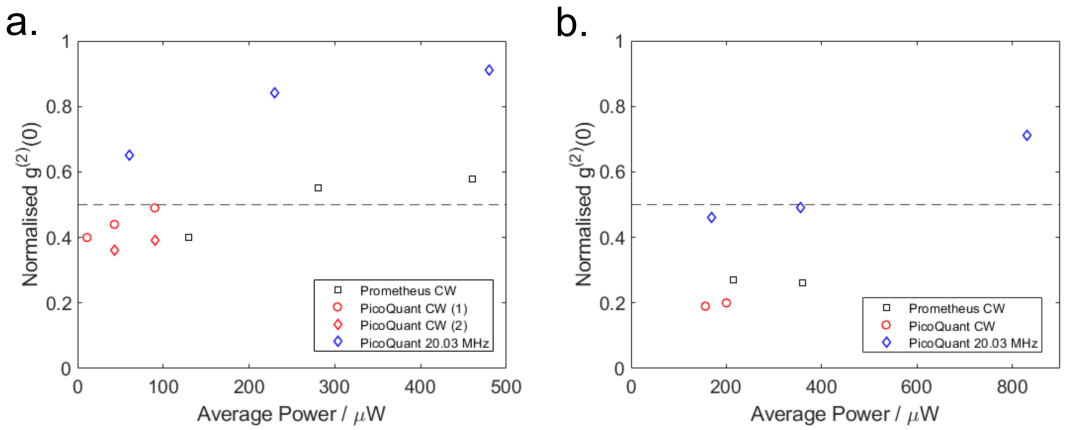

Figure 28: Comparison of $g^{(2)}(0)$ values for CW excitation with the Prometheus laser and excitation with the PicoQuant laser in CW or pulsed modes (pulse repetition rate 20.03 MHz). Data in (a) and (b) are for two different hBN emitters. In both cases, the $g^{(2)}(0)$ under pulsed excitation is dependent on the mean excitation power and consistently higher than with CW excitation from either laser.

For most emitters studied, the $g^{(2)}(0)$ value was consistently higher under pulsed excitation for all mean excitation powers. This is shown in Figure 28 which compares $g^{(2)}(0)$ values for two emitters under CW excitation from the Prometheus laser, the CW mode of the PicoQuant laser, and pulsed excitation at 20.03 MHz from the PicoQuant laser. Since the pulse length is 68 ps, the power experienced by the emitter during a pulse at 20.03 MHz is around 700$\times$ larger than the mean excitation power. The powers in Figure 28 reach hundreds of mW during a pulse, and the $g^{(2)}(0)$ values for the pulsed laser show a strong dependence on excitation power. Therefore, the minimum excitation power should be used for pulsed excitation. As discussed in the next section, the count rate collected from a hBN emitter under pulsed excitation was consistently lower than under CW excitation at the same mean power. These two factors together made it very difficult to obtain $g^{(2)}(0) < 0.5$ for pulsed excitation, because reducing the mean excitation power to improve $g^{(2)}(0)$ trades off with having a high enough count rate from the emitter to make measurements. The best pulsed measurement had $g^{(2)}(0) = 0.37 \pm 0.02$ for Emitter 6 which is studied further in the next chapter.

3.4.2 Lifetime Measurements

The fluorescence lifetime of the hBN emitters sets a limit on the maximum single photon count rate as the average time taken to complete one photocycle. In the three-level model shown in Figure 22, the emission lifetime is τ_{21}.

To measure the lifetime, the pulsed laser was used with a trigger pulse sent to the Time

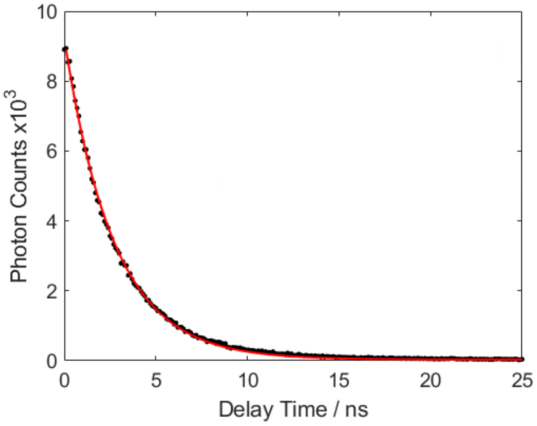

Figure 29: Lifetime measurement for a hBN emitter using pulsed excitation at 10 MHz repetition rate and 24 μW mean power. A single exponential fit repeated over 144 acquisitions of 100 s each gives a mean value for the emitter lifetime $\tau_{21} = 2.7 \pm 0.1$ ns.

Controller. Then a histogram was made of time delays between the trigger pulse and the detection of a photon from the hBN emitter. Figure 29 shows the lifetime histogram measured for Emitter 6 which is studied further in the next chapter, with mean power 24 μW and repetition rate 10 MHz. Histograms were made from 144 acquisitions each 100 s in length. Applying a single exponential fit to each lifetime histogram produced the mean lifetime $\tau_{21} = 2.7 \pm 0.1$ ns for this emitter. This agrees well with the range of literature values for hBN emitters.

3.4.3 Count Rate Saturation

The count rate for each emitter is maximised by adjusting the input polarisation (with the input HWP) and the focal spot z position (with the piezo stage z axis). The focusing must be optimised for each emitter because the substrates are always very slightly slanted, and also emitters could be at any height within a hBN flake. When coupling to multimode fibre, the emission count rate is typically $\sim 10^4$-10^6 cps. For a single mode output fibre, emission count rates are roughly an order of magnitude lower, but with the advantage that interference experiments can be done with single spatial modes.

hBN emitters show a saturation behaviour in their count rate I with increasing excitation power P, see Fig. 30. This can be described using four parameters: maximum count rate I_∞, saturation power P_{sat}, background fluorescence b, and constant background (dark counts) c [85].

$$I = \frac{I_\infty P}{P + P_{sat}} + bP + c. \tag{98}$$

The saturation behaviour of each emitter varies quite significantly, so it is important to

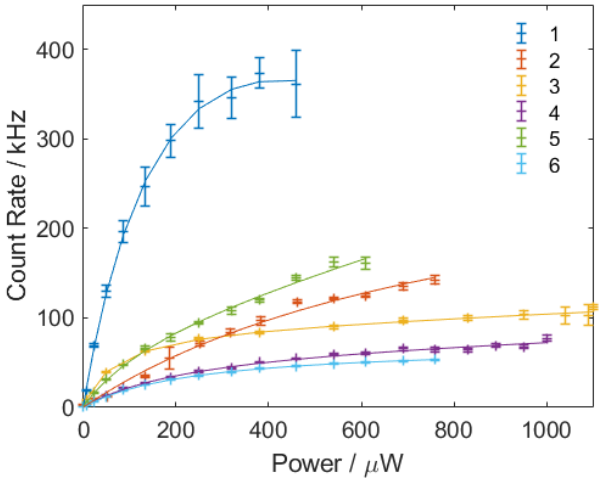

Figure 30: Saturation curves for hBN single photon emitters. Six emitters which are described in the following chapter. Measurements were all made under CW excitation and curves are fits to the data using Equation 98.

characterise the saturation for each emitter and quote excitation powers relative to P_{sat} for that particular emitter.

For making intensity maps of the sample powers around 300-500 μW are typically used. Once an emitter is being characterised, the excitation power can be reduced to improve the $g^{(2)}(0)$ value. In the end, the optimum power is a trade-off between low $g^{(2)}(0)$ and high count rate.

The count rate using pulsed excitation is lower than with CW excitation of the same mean power. This can be understood due to the duty cycle of the excitation light decreasing as the repetition rate is decreased. For our pulsed laser the pulse FWHM = 68 ps, this is much lower than the $\sim$ns lifetime of hBN emission, therefore even if the peak power is increased, emitters will rarely emit more than one photon per pulse. Fig. 31 compares the count rate from a single emitter with the average excitation power carefully calibrated to 215 μW for both CW and pulsed excitation.

3.4.4 Spectral Filtering

The output light was filtered using an angle tuneable bandpass filter. By filtering to pass only the peak of the emission spectrum, the $g^{(2)}(0)$ value was reduced. The bandpass filter (Semrock) has a 20 nm bandwidth, with a centre wavelength tuneable from 560-630 nm by rotating the filter from 60^o to normal incidence. This filter was mounted on a motorised rotation mount (Thorlabs) to precisely control the angle. When the filter is rotated, the beam is displaced slightly due to refraction. This effect is enough to misalign the beam from the output fibre coupler, even when using multimode fibre with a 50 μm

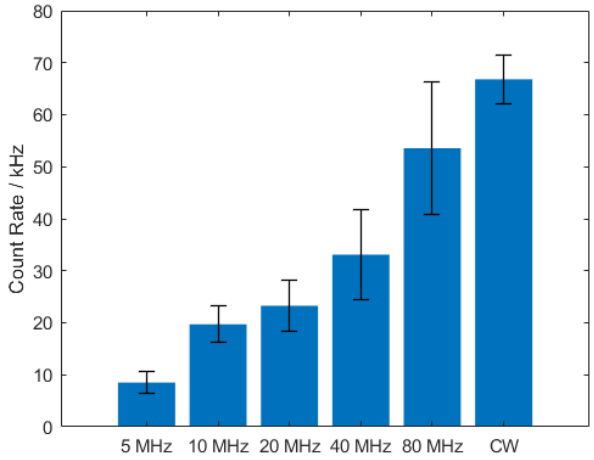

Figure 31: Comparison of single photon count rate under pulsed excitation with different repetition rates. Count rates for one hBN emitter using the PicoQuant laser in CW and pulsed modes with varying repetition rate, but at a constant mean excitation power of 215 μW. Error bars show one standard deviation of the count rate.

core diameter. A compensating plate of a high refractive index glass placed after the filter was used to correct the beam walk-off. The plate was also mounted on a motorised rotation mount rotating in the opposite direction, and its angle was calibrated to the angle of the filter as part of the LabVIEW control VI. In the final setup the bandpass wavelength of the filter could be scanned over the full 560-630 nm range without the beam walking-off from the output fibre. The filter angle was calibrated to centre transmission wavelength of the filter by measuring the transmission of a white LED through the filter on a spectrometer, see Figure 32.

In experiments on hBN emitters, the first scan to find emitters was done with the filter rotated to 90^o so it was out of the beam path. In this position, only the longpass 568 nm filter was in the path to block the excitation beam from reaching the detectors. After locating an emitter with a low $g^{(2)}(0)$ value, the filter was scanned to produce a rough emission spectrum (resolution around 20 nm, limited by the filter bandwidth). Some example filter spectra from hBN emitters are shown in Figure 33. Although this spectrum does not have the resolution to show individual peaks, i.e. the zero phonon line and phonon sidebands, it does show the filter angle with peak transmission. The $g^{(2)}(\tau)$ measurement was repeated with the filter at this maximum transmission angle, which generally improved (decreased) the $g^{(2)}(0)$. For example, for Emitter 6 which appears in the next chapter, the value was $g^{(2)}(0) = 0.56 \pm 0.10$ without the filter and $g^{(2)}(0) = 0.33 \pm 0.02$ with the filter at the peak transmission angle. Another example is Emitter 1, which had a value of $g^{(2)}(0) = 0.67 \pm 0.07$ without the filter and $g^{(2)}(0) = 0.45 \pm 0.08$ with the filter. Even the relatively wide 20 nm bandwidth filtering has a very significant effect on the $g^{(2)}(0)$ value,

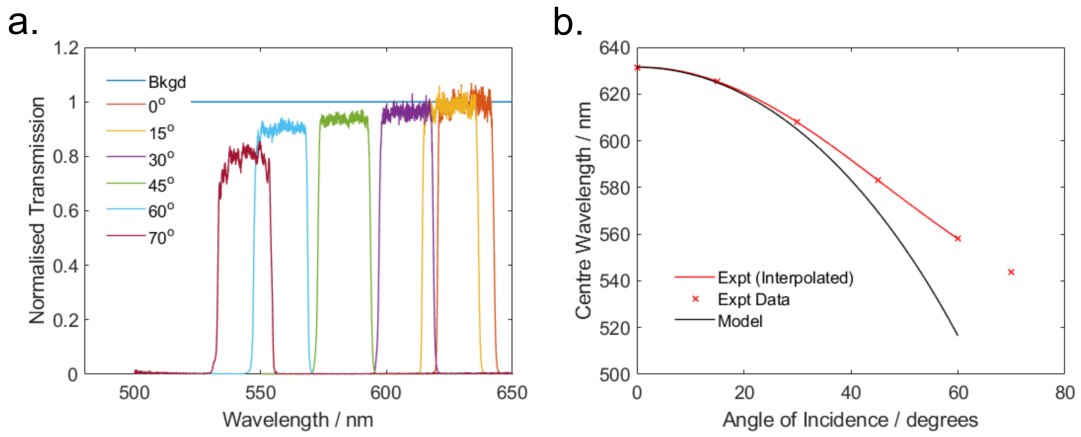

Figure 32: Calibration of spectra using angle tuneable filter. (a) Transmission spectra of the filter at different angles of incidence. Measured using a white LED transmitted through the filter and analysed on a spectrometer. All spectra are normalised by subtracting the LED spectrum measured with no filter. (b) Centre transmission wavelength as a function of filter angle of incidence. This calibration was used to convert filter angles to wavelengths in all following hBN spectra.

and it would often make the difference in emitters passing the threshold of $g^{(2)}(0) < 0.5$.

This method of filtering hBN emission brings an important improvement to the $g^{(2)}(0)$ value of emitters and gives some information on the peak emission wavelength of an emitter within the range 570 nm - 630 nm. This region was selected for filtering since a large proportion of hBN emitters prepared in the same way as our samples have ZPLs in this wavelength range. Although we could not obtain detailed spectral information about each emitter, this setup offers a cheaper alternative to filter the emission and get some information on the peak emission wavelength, instead of needing a single photon resolving spectrometer, or a monochromator that can be used with single photon detectors. Later in this thesis, I will show a custom built grating spectrometer using an EMCCD for measuring spectra using very low photon counts. This was done later than all the work presented on hBN and was also designed for a wavelength range around 780-820 nm, therefore it could not be used with the hBN emitters shown in this section.

3.5 Photon Indistinguishability Investigated by HOM Interference

In order to combine single photons to build entangled states for sensing applications, it was necessary to do HOM interference. Pairs of indistinguishable photons combined on a beamsplitter demonstrate the HOM effect: both photons leave the beamsplitter by the same output port. This output state is a two-photon N00N state, which has well known

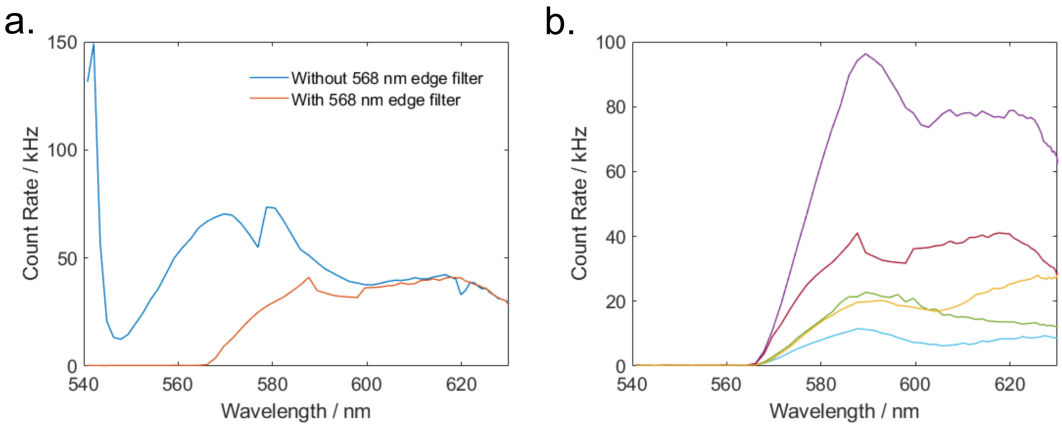

Figure 33: Spectra of hBN emission using angle tuneable filter. (a) Effect of longpass filter at 568 nm. Emission spectrum for one emitter is shown with and without the longpass filter in the optical path. (b) Emission spectra for five different hBN emitters, showing peak emission at slightly different wavelengths within the 570 nm - 630 nm range visible using the angle tuneable filter.

applications in quantum sensing experiments. To see the HOM effect, the photons must be indistinguishable in their polarisations, spectra, and arrival times on the beamsplitter. In this section I will discuss experiments trying to observe HOM interference using our hBN single photon emitters. This was not successful due to the problem of spectral diffusion, which was being discussed in other works while these experiments were being carried out. Eventually we moved to an alternative approach to generating N00N states using entangled photon pairs from a PPKTP crystal, described in later chapters.

For these experiments pulsed excitation was used to control the arrival time of single photons to within the radiative lifetime of the emitter ($\sim$ns). A fibre based HOM interference setup was added to the output of our setup, shown in Figure 34. This part of the setup was designed by Dr Samir Vartabi Kashanian. All the fibres were single mode (460Y, Thorlabs) and not polarisation maintaining. The count rates coupled into the single mode fibre were significantly lower than with multimode fibre. HOM interference from a single photon source requires the single photon beam to be split into two optical paths (two fibres in our case), then one of these optical paths must be delayed by one pulse period so that photons in the two paths arrive simultaneously on a beamsplitter. In our case the delay was implemented with an extra 10 m length of optical fibre. The relative arrival times of photons in the two paths was measured using a trigger pulse from the laser. The pulses in each path were overlapped to within 100 ps (the Time Controller time resolution in high speed mode) by tuning the laser repetition frequency to 20.03 MHz, as shown in Figure 35.

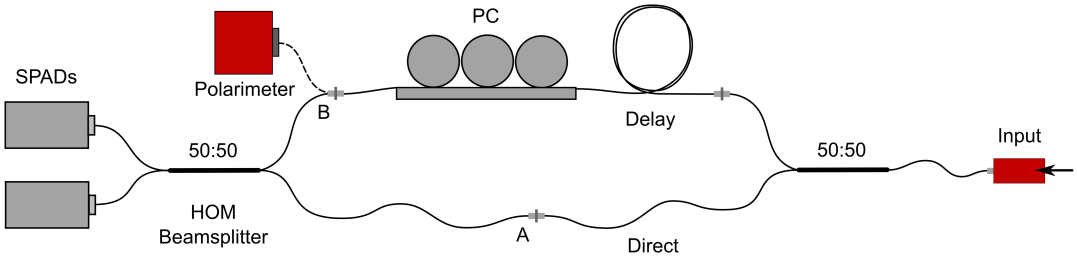

Figure 34: Fibre based HOM interference setup for pulsed single photon emission. The delay arm has 10 m extra fibre length to delay photons by one pulse period at 20.03 MHz pulse repetition rate. PC: fibre polarisation controller paddles, SPADs: single photon avalanche diodes. The polarimeter was connected to ports A and B to check the polarisation of the direct and delay paths, respectively.

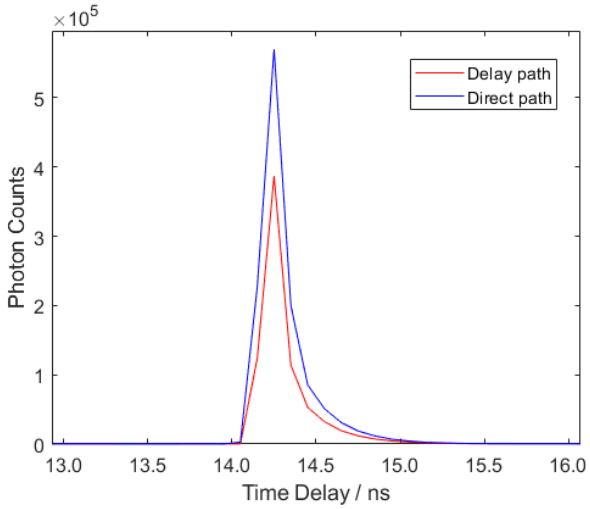

Figure 35: Histograms of photon arrival times through the direct (blue) and delay (red) paths in the fibre-based HOM setup. The input to the setup was an attenuated beam from the 532 nm pulsed laser. Time delays are relative to the trigger pulse from the pulsed laser. The pulse repetition rate of the laser was tuned until both pulses arrived simultaneously on the detectors, to within the time resolution of 100 ps, this happened at 20.03 MHz. The lengths of the fibres between the HOM beamsplitter and the detectors are the same, so we can also say the pulses arrive simultaneously on the beamsplitter.

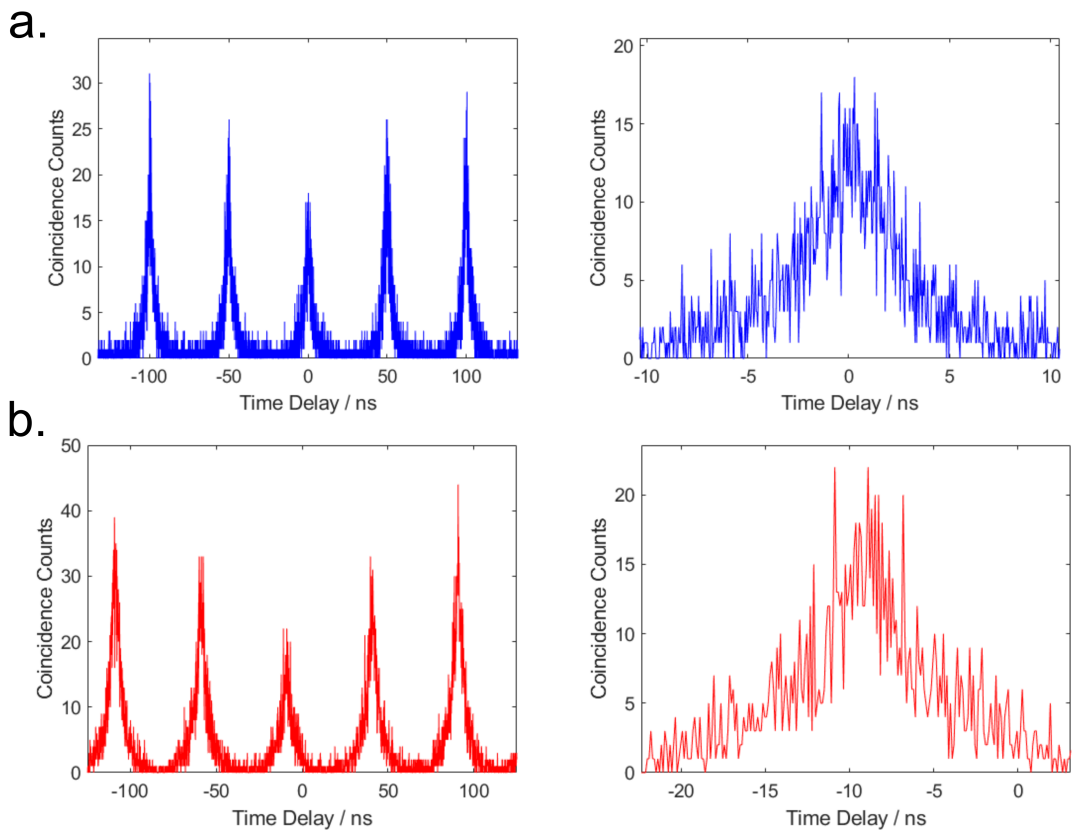

Figure 36: HOM measurements for two hBN emitters with pulsed excitation at 20.03 MHz repetition rate. (a) HOM histogram (left) and zoom in on the central peak (right). This emitter had $g^{(2)}(0) = 0.65$, 12 kHz count rate and was measured for 20 minutes. Average excitation power: 60 μW, histogram bin width: 13 ps. (b) An emitter with $g^{(2)}(0) = 0.46$, 12 kHz count rate, measured for 20 minutes. Average excitation power: 168 μW, histogram bin width: 108 ps. Neither measurement shows any sign of a HOM dip for this SNR and time resolution.

After confirming photons in the two paths arrived simultaneously, the polarisation of photons in the two paths also had to be matched. A linearly polarised calibration beam at 532 nm (split from the Coherent, Prometheus CW laser) was coupled to the input of the HOM setup and a polarimeter was used at each output to check the polarisation state. The fibre polarisation control paddles in the delay path were adjusted to make the polarisations of the two outputs either parallel or perpendicular. This calibration was performed before each HOM measurement on the hBN emitters to set the polarisation to parallel (interfering) or perpendicular (non-interfering). Care was taken to move the output fibres as little as possible when connecting them to the polarimeter, so the polarisation state of the output would not be affected significantly.

With the setup prepared in this way, the HOM measurement is a $g^{(2)}(\tau)$ measurement at the two outputs of the HOM beamsplitter. The HOM dip signal is expected to be a dip

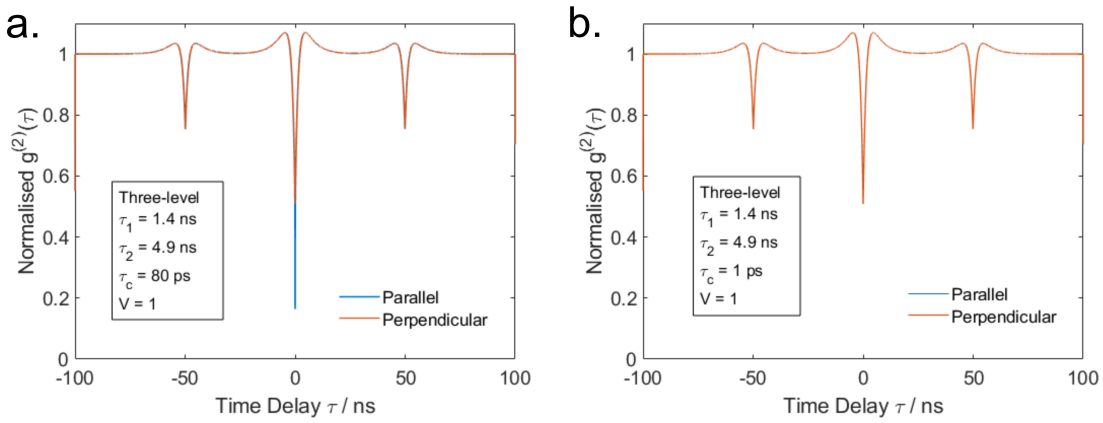

Figure 37: Modelled HOM signals with CW excitation. (a) Model for parallel (interfering) and perpendicular (non-interfering) polarisations with a three level emitter using lifetimes $\tau_1 = 1.4$ ns and $\tau_2 = 4.9$ ns, coherence time $\tau_c = 80$ ns and HOM visibility $V = 1$. There is a narrow HOM dip seen only for the parallel polarisation. (b) Model with coherence time $\tau_c = 1$ ps, close to the estimated coherence time for a hBN emitter at room temperature. The HOM dip is no longer resolved since the dip width is lower than the detector time resolution of 50 ps. The data were convolved with a Gaussian function FWHM = 50 ps and plotted with a bin width of 13 ps to model the time resolution of our experiment.

in the central ($\tau = 0$) peak of the $g^{(2)}(\tau)$ histogram, which is only visible with the polarisations of the interfering beams set to be parallel. This measurement was attempted with many different emitters. The main challenge was finding an emitter with $g^{(2)}(0) < 0.5$ under pulsed excitation. The two best HOM measurements (parallel polarisation) are shown in Figure 36. The first emitter had $g^{(2)}(0) = 0.65$, a detected count rate of around 12 kHz and was measured for 20 minutes. The bin width of the HOM coincidence histogram was 13 ps (the minimum available with the Time Controller). The second emitter had $g^{(2)}(0) = 0.46$, around 12 kHz count rate and was also measured for 20 minutes. Histogram bins were combined in this measurement to improve the SNR; the bin width on the plot is 104 ps. Neither of these coincidence histograms show any sign of a HOM dip, which suggests either the HOM visibility is much lower than the noise level of these measurements, or the dip is much narrower than the time resolution of these measurements.

One clear limitation in these measurements was the relatively high $g^{(2)}(0)$ values when using pulsed excitation. CW excitation would consistently produce lower $g^{(2)}(0)$ and a higher count rate. It is also possible to make HOM measurements on a CW source using the same setup. In the CW measurement, the HOM dip is superimposed on top of the $g^{(2)}$ dip due to antibunching. The expected coincidence histogram can be modelled using the

following expression [105]:

$$g_{\perp}^{(2)} = \frac{1}{2}g^{(2)}(\tau) + \frac{1}{4}\left[g^{(2)}(\tau+\Delta\tau) + g^{(2)}(\tau-\Delta\tau)\right] \tag{99}$$

$$g_{\parallel}^{(2)} = \frac{1}{2}g^{(2)}(\tau) + \frac{1}{4}\left[g^{(2)}(\tau+\Delta\tau) + g^{(2)}(\tau-\Delta\tau)\right]\left(1 - V\exp\left(-\frac{2|\tau|}{\tau_c}\right)\right). \tag{100}$$

The function $g^{(2)}(\tau)$ can be the three level model in Equation 96, $\Delta\tau$ is the time delay between the direct and delay paths through the HOM setup (in our measurements $\Delta\tau =$ 49.9 ns), τ_c is the emitter correlation time, and V is the HOM visibility, defined as [105]:

$$V_{HOM}(\tau) = \frac{g_{\perp}^{(2)}(\tau) - g_{\parallel}^{(2)}(\tau)}{g_{\perp}^{(2)}(\tau)}. \tag{101}$$

The expected CW HOM signal is shown in Figure 37 for a few example parameters. Both plots use a three level model for $g^{(2)}(\tau)$ with the lifetimes $\tau_1 = 1.4$ ns and $\tau_2 =$ 4.9 ns as example values from fitting to data from one hBN emitter and assuming perfect antibunching ($g^{(2)}(0) = 0$). The parallel and perpendicular HOM results were convolved with a Gaussian function with FWHM = 50 ps to model the detector time resolution, and plotted with the Time Controller's minimum time bin width of 13 ps. Figure 37(a) shows the model HOM signals with $\tau_c = 80$ ns, the value of the coherence time measured for a hBN emitter at 5 K by Sontheimer et al [106]. There is a HOM dip visible for the parallel measurement which goes below the dip due to photon antibunching. There was no literature value available for τ_c at room temperature, however this can be estimated using the spectral linewidth $\Delta\lambda$ [107]:

$$\tau_c = \frac{\lambda^2}{\pi c \Delta\lambda}. \tag{102}$$

A typical linewidth for the ZPL of hBN emitters at room temperature is $\sim$1 nm. The ZPL linewidth is broadened by spectral diffusion effects, as described in [107]. This gives a value of $\tau_c \simeq 0.4$ ps for emitters in the wavelength range of our tuneable filter (570 nm - 630 nm). Compared to the 50 ps time resolution of the detectors τ_c is expected to be two orders of magnitude smaller for a room temperature emitter. As shown in Figure 37(b), a HOM dip with $\tau_c = 1$ ps is not visible using our setup.

At this point it is clear that a HOM measurement is out of reach with our current setup. There are two main problems: the $g^{(2)}(0)$ under pulsed excitation is consistently higher than for CW excitation, but the time resolution of our measurement is around two orders of magnitude higher than the expected width of the HOM dip, so it would not be visible in the CW measurement. In order to see the HOM dip the coherence time of the emitters must be increased to greater than the detector time resolution 50 ps. This means reducing the ZPL linewidth, for example by using cryogenic temperatures or enclosing emitters in a high quality factor cavity.

Recently while preparing this thesis a HOM measurement using hBN emitters has been achieved [108]. Fournier et al. used emitters excited at 405 nm and measured at 4 K temperature. Their emitter was a so-called 'B centre', a class of emitters with a ZPL close to 436 nm which can be deterministically produced using an electron beam and have been shown to have good spectral stability and narrow linewidth. The linewidth of their emitter was limited by the spectrometer resolution 100 μeV (i.e. $<$ 15 pm) and it had $g^{(2)}(0) = 0.14 \pm 0.03$ under pulsed excitation. With these properties a corrected HOM visibility of 0.56 ± 0.11 was observed. This work shows the direction for indistinguishable single photon emission from hBN emitters lies in using cryogenic temperatures and fabricating a particular type of vacancy centre with an exceptionally stable spectrum such as the B centre.

3.6 Conclusions

In this chapter I presented experiments to develop and characterise single photon sources at room temperature using vacancy defects in hBN. The results showed reproducible single photon emission (having $g^{(2)}(0) < 0.5$) from emitters with a ZPL in the range 570 nm - 630 nm, with count rates routinely up to hundreds of kHz.

The results with pulsed excitation showed consistently higher $g^{(2)}(0)$ values and poorer single photon purity than CW measurements at the same average power. The count rate under pulsed excitation was also much lower at the same average power. Using a lower excitation power reduced the $g^{(2)}(0)$ value, however it also reduced the count rate. This trade off between low $g^{(2)}(0)$ and having a high enough count rate to effectively make measurements made it difficult to produce good single photon emission. Only a few emitters produced $g^{(2)}(0) < 0.5$ under pulsed excitation, and the only emitter found to be below 0.4 was Emitter 6 which was used for the study on the Mandel Q parameter presented in the next chapter.

Attempts to show HOM interference between our hBN single photons and characterise their indistinguishability were not successful. No HOM dip was observed with pulsed excitation, and the $g^{(2)}(0)$ value was always close to 0.5 in these measurements. The expected width of the HOM dip (assuming the room temperature spectrum of our emitters had a similar linewidth to emitters in the literature) was estimated to be $\simeq 0.4$ ps. This was around 100 times lower than the time resolution of our setup, therefore we would not expect to resolve the HOM dip without significantly reducing the linewidth of our emitters. HOM interference for hBN emitters at 4 K temperatures has since been demonstrated by Fournier et al. [108].

For sensing applications, I suggested at the start of this chapter that we could use HOM

interference to build path entangled states from our hBN single photons. The output state from HOM interference would be a two-photon N00N state which is well established in quantum-enhanced interferometry. Given HOM interference could not be reached with our setup another approach would have to be taken. As stated in the introduction, another property of single photon states is their low photon number variance, which is a form of intensity squeezing. A source which produces a very narrow photon number distribution could find applications in testing the single photon response of light sensitive biological systems [35], or even in metrology applications such as single photon detector calibration and defining the quantum candela [109]. The key property of our single photon emitters for these kinds of application would be their intensity stability and photon number distribution. In the next chapter I will present a study of these properties of single photon emission from hBN vacancy defects.

4 Photon Number Variance of hBN Single Photon Emission

4.1 Intensity Stability of Single Photon Emission

During these studies on hBN emitters, it became clear that the intensity stability of single photon emission would be critical to any application in sensing. The count rate from most emitters was very noisy; showing large fluctuations, step or spike-like blinking events, and sometimes bleaching permanently and unexpectedly. If these emitters were used as the input to a sensor, these noise events would be difficult to distinguish from real signals.

Changes or fluctuations in the emission count rate can be described as changes in the transition rates in the level scheme model of the emitters. Since non-radiative relaxation to the ground state is often a phonon-assisted process, we could expect that the temperature of the emitter can be coupled to the emission stability through the phonon modes in the hBN crystal. If so, stabilising temperature fluctuations or lowering the sample temperature may improve the intensity stability of the hBN emitter. To attempt to improve the stability of single photon emission, the setup was modified to control and stabilise the sample temperature near ambient temperature. This section shows the effect of temperature and excitation power on the single photon emission stability and the $g^{(2)}(0)$ value.

The setup was modified to control the temperature of the hBN sample holder with 1 mK precision. Figure 38 shows the sample holder section. A thermo-electric cooler (TEC) (Thorlabs) was mounted (on its cool side) to the base of the aluminium sample holder using a thin, even layer of thermal adhesive. The hot side of the TEC was attached to an aluminium box with heatsinks attached on several surfaces to provide a large surface area for heat dissipation. At first, this box was placed directly on top of the piezo stage. In the final design, a 3D printed frame in PLA (polylactic acid) was made to attach the sample holder plate to the piezo stage directly, with the heatsink suspended. This was to prevent thermal expansion of the heatsink moving the sample relative to the microscope objective. When the heatsink was attached directly to the piezo stage, thermal expansion moving the sample away from the excitation focal spot limited the time an emitter could be studied for. The PLA frame had sufficiently low thermal conductivity that it didn't affect the temperature stabilisation of the sample holder, and it significantly reduced the drift due to thermal expansion.

The complete temperature control system consisted of a temperature controller unit (Lightwave) driving the TEC, with feedback from a negative temperature coefficient (NTC) thermistor. The NTC thermistor was inserted into a hole drilled into the centre of

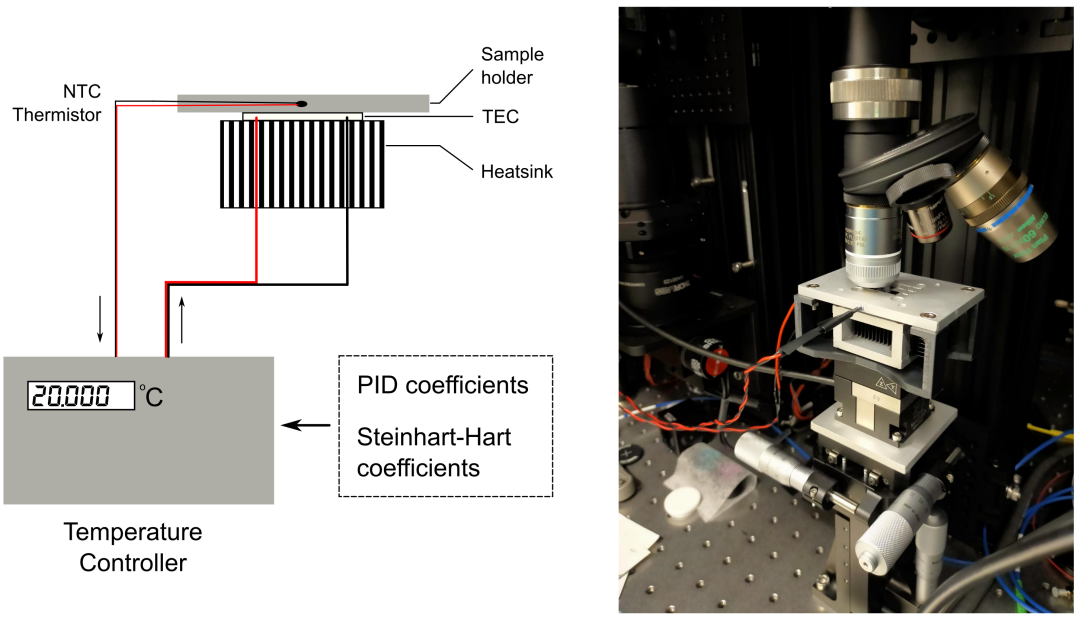

Figure 38: Temperature stabilisation system for the hBN sample holder.

the sample holder and surrounded by thermal conduction paste. The thermistor datasheet was used to calibrate the temperature controller by finding the Steinhart-Hart coefficients. An autotuning procedure in the temperature controller was used to find the optimum PID (proportional-integral-derivative) coefficients to achieve a stable temperature of the sample holder. Some trial and error was needed to find the correct size of heatsinks to reach a stable temperature when cooling below room temperature. The final system was capable of stabilising the sample holder temperature over the range 18-50^{o}C with a precision of 1 mK. The lower limit for cooling was 16^{o}C, however after a few minutes at this temperature the heatsink would overheat and the setup would go into thermal runaway.

In this section I will focus on data from six hBN emitters (numbered 1-6, see Table 1) which have raw timestamp data collected over long time periods under various excitation power and sample temperature conditions. From the raw timestamp data, both blinking events and $g^{(2)}(\tau)$ functions can be studied.

4.1.1 Blinking and Bleaching

Intermittent or fluctuating fluorescence emission can be observed from single fluorescent molecules, quantum dots, and vacancy centres such as those in diamond and hBN. The term 'blinking' is often used for this relatively long timescale $\sim$s emission intermittency, but in some fields blinking refers to the typically much faster transitions of a fluorescent emitter to a long lifetime shelving state [110]. In hBN both effects can be seen, so in this thesis I refer to blinking as long timescale step or spike-like transitions of an emitter between 'bright' and 'dark' states (i.e. states with higher and lower emission

Emitter #	P_{sat}/μW	P_{max}/μW	Blinking	Bleaching
1	250	135	Many *spikes*	×
2	890	760	Few small *steps*	×
3	66	320	Many large *steps*	×
4	250	550	Occasional *steps*	✓
5	160	320	Many large *steps*	×
6	240	760	No blinking	×

Table 1: Summary of the saturation power and blinking behaviour for six emitters discussed in this section.

count rates, respectively). There may also be more than two states that the emitter jumps between, each having a different fluorescence count rate. I will address the dynamics of transitions to a shelving state later in this chapter with the discussion of the Mandel Q parameter.

Blinking has been referred to frequently in the hBN literature [111, 85]. Martinez et al. show examples of step-like blinking, spike-like blinking, and no blinking for different emitters in the same hBN single crystal [111]. The blinking rates for each emitter vary significantly, showing a strong dependence of the photostability on the emitter environment within the same crystal. The suggested mechanism for this blinking is optically induced charge state conversion, due to electrons being exchanged with other emitters. Boll et al. show step-like blinking between three states with different photoluminescent intensities, rather than the more typical two states ('bright' and 'dark' states) [85]. The photon statistics are different in each blinking state: the lowest intensity state has higher bunching, and the emission lifetimes of the three states are different. There are examples of very similar blinking behaviours in other single photon emitters such as nitrogen vacancy centres [112], quantum dots [113], and single molecules [114]. As stated in Ref. [111], it is relatively uncommon to find single photon emitters with perfect photostability, i.e. no blinking, so the fact that a few hBN emitters do not blink is another benefit of using hBN as a single photon emitter.

4.1.1.1 Power dependence of blinking rate

Figure 39 shows some examples of blinking events in time traces from hBN emission. These types of blinking were characteristic of the blinking events seen for Emitters 1, 3 and 5. The blinking rate for these three emitters is dependent on the excitation power, shown in Figure 40. These three emitters were selected because they produced many blinking events which could be analysed. To analyse the data, raw timestamps were binned into 10 ms intervals to produce a timetrace. Blinking events were counted using MATLAB codes which set thresholds above and below the average count rate. For spike

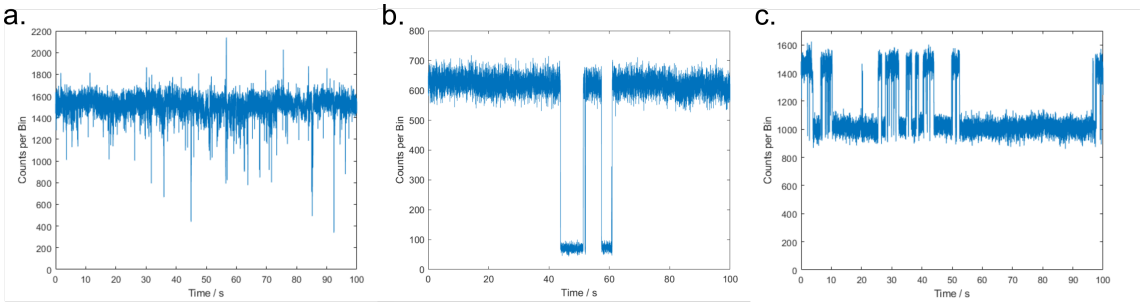

Figure 39: Timetraces showing examples of hBN emitter blinking. Timetraces are plotted in 10 ms intervals. (a) Emitter 1: rapid spike-like blinking. (b) Emitter 3: step-like blinking from a bright to a dark state. (c) Emitter 5: step-like blinking from a dark to a bright state showing smaller amplitude blinking events.

events (Emitter 1), the thresholds were set at 6σ above and below the mean count rate, where σ is the standard deviation of a Poisson distribution with the same mean count rate as the data. This was chosen to exclude the fluctuations around the mean count rate not due to blinking events in a way which scales with the mean count rate between different measurements. For step events (Emitters 3, 5), the data were first passed through the 'diff' function to give the differences between successive points. The edges of steps were then identified as spikes in the resulting time trace in the same way, using a threshold of 8σ to correctly exclude fluctuations in the count rate.

In Figure 40 the blinking rate generally increases with excitation power for Emitters 1, 3 and 5. However, for all three emitters the blinking rate decreases at the highest excitation power. For Emitters 1 and 3 the difference is relatively small and could be because the highest power was sampled fewer times than the next highest power: Emitter 1 had 14 samples at 50 μW and only 5 at 135 μW, and Emitter 3 had 40 samples at 250 μW and 5 at 320 μW. For Emitter 5 there were 15 samples for both 250 μW and 320 μW and the blinking rates at 320 μW are still significantly lower. This could be a sign of a permanent change in the blinking behaviour which happened for Emitter 5 at the highest excitation power. This is explained further in the next section.

The blinking rate is clearly minimised by reducing the excitation power. This suggests there is some blinking onset power at which an emitter starts blinking as the power is increased. Emitter 1 blinked at all excitation powers, constraining the onset power to $< 3\%$ of P_{sat}. Emitter 3 has an onset power $> 36\%$; $< 76\%$ of P_{sat}. Emitter 5 has an onset power $> 31\%$; $< 54\%$ of P_{sat}.

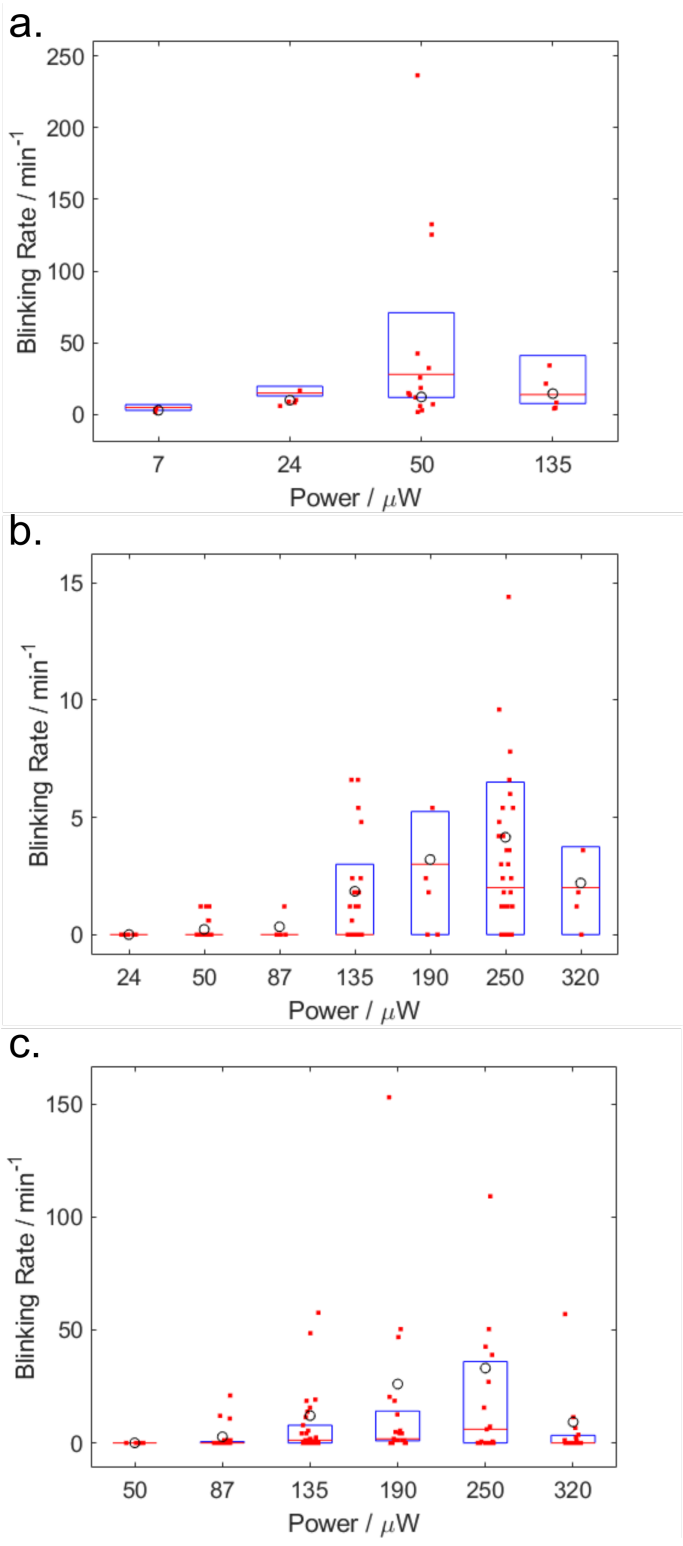

Figure 40: Blinking rate as a function of power. (a) Emitter 1 ($P_{sat} = 250\ \mu W$). (b) Emitter 3 ($P_{sat} = 66\ \mu W$). (c) Emitter 5 ($P_{sat} = 160\ \mu W$). Individual blinking rates for 100 s timetraces are plotted as red dots, with some horizontal scatter added to show points more clearly. Blue boxes show the inter-quartile range with red lines at the median value. Mean values are shown by black circles.

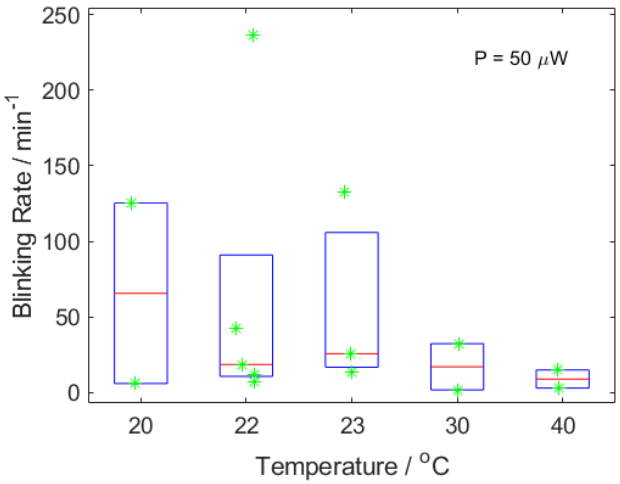

Figure 41: Blinking rate as a function of sample temperature for Emitter 1 at 50 μW. Each green point is the blinking rate for one 100 s timetrace, some horizontal scatter has been added to make points more visible. Blue boxes show the inter-quartile range, and red lines show the median value.

4.1.1.2 Temperature dependence of blinking rate

As for the effect of temperature, the dependence of blinking rate on the temperature of the sample is less clear. The largest data sets for temperature at constant excitation power were for Emitter 1 at 50 μW (Figure 41), and Emitter 3 at 135 μW and 250 μW (Figure 42). Emitter 5 only had data for 18-26^{o}C.

The data in Figure 41 suggest that the blinking rate decreases as sample temperature increases for Emitter 1 at 50 μW. However, there are only two samples each at 20, 30 and 40^{o}C. Another interpretation is that the room temperature measurement (22^{o}C), which did not have the temperature control running, has a higher maximum blinking rate. This could suggest a slightly decreased blinking rate when the sample temperature is being stabilised.

For Emitter 3, Figure 42, there is no clear trend in the blinking rate with temperature. Again, the lowest blinking rates occur at the highest sample temperatures. The room temperature blinking rates (at 21.4 and 21.5^{o}C) are not significantly higher than the blinking rates where the temperature is stabilised. The highest mean blinking rates are for 16^{o}C. As stated earlier, the temperature control system was only stable for a few minutes at this temperature, and the position of the emitter would drift causing the mean count rate to change over time. This may have caused more points to go outside the threshold values in the procedure for counting blinking events.

Overall, from Figures 41 and 42 the blinking rate was not reduced by stabilising the temperature or by decreasing it slightly below room temperature, as suggested earlier. None of the near-ambient temperature control conditions tested here suppressed the emit-

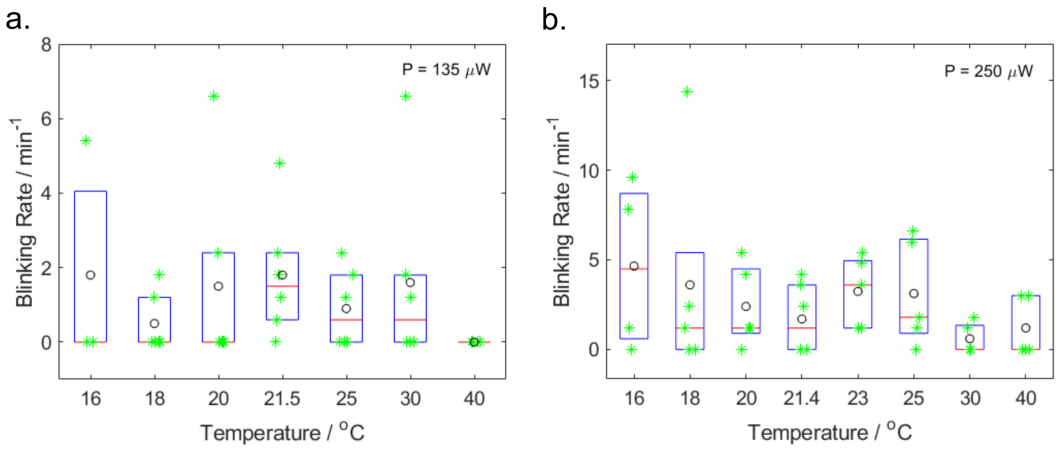

Figure 42: Blinking rate as a function of sample temperature for Emitter 3. (a) Excitation power 135 μW. (b) Excitation power 250 μW. Each green point is the blinking rate for one 100 s timetrace, some horizontal scatter has been added to make points more visible. Blue boxes show the inter-quartile range, and red lines show the median value. Mean values are shown by black circles.

ter blinking rate in a way that would useful in practical applications of hBN single photon emitters. Interestingly, the lowest blinking rates were obtained with the sample temperature increased to 40^{o}C.

4.1.1.3 Emitter bleaching

Fluorescence bleaching is another effect commonly seen when studying single fluorescent emitters. In the case of fluorescent molecules, bleaching can occur within seconds and often limits their use as single photon sources [115]. In this way, hBN emitters are particularly stable since they can be excited continuously for long time periods: tens of hours in the experiments in this thesis.

Some emitters however did bleach suddenly after a few hours of excitation. An example is Emitter 4, which bleached under an excitation power of 540 μW as shown in Figure 43, i.e. at a high power relative to $P_{sat} = 250$ μW. The fluorescence intensity of the emitter dropped to around 20% of the original value in around 7 s. Lowering the excitation power or leaving the emitter for a day didn't bring back the emission, so a permanent change had been made to the emitter, most likely induced by high excitation power. Although it did not often stop characterisation measurements on emitters, in any practical application bleaching would be an issue.

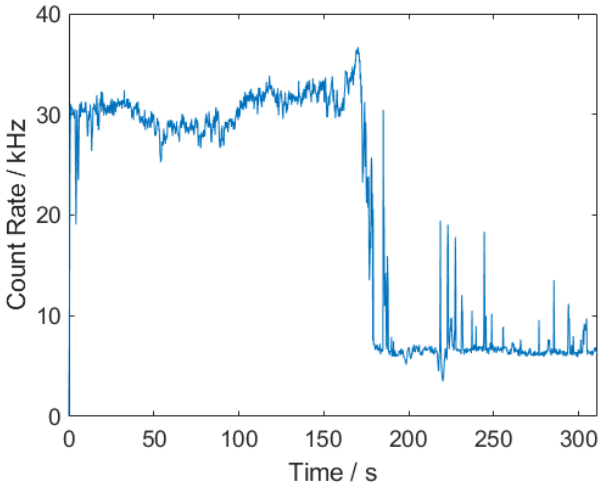

Figure 43: Fluorescence bleaching event for Emitter 4. The fluorescence intensity from Emitter 4 under an excitation power of 540 μW dropped permanently to approximately 20% of the original intensity. The decrease in intensity took around 7 s.

4.1.2 Power and Temperature Dependence of $g^{(2)}(0)$

Apart from the stability of the single photon count rate, the $g^{(2)}(0)$ value must also be optimised. If controlling the sample temperature and excitation power can improve (decrease) $g^{(2)}(0)$, this would be of major importance for practical applications of hBN single photon emitters.

4.1.2.1 Power dependence of $g^{(2)}(0)$

In the literature there are examples both of $g^{(2)}(0)$ being excitation power dependent, and of no power dependence. Our emitters also showed these different behaviours, as shown in Figure 44. For Emitter 3, the power was increased up to 4.8 times P_{sat} and the $g^{(2)}(0)$ value increased with power. In all other measurements with CW excitation, there was no clear power dependence of $g^{(2)}(0)$. It should be noted that measurements on Emitter 3 went up to the highest power relative to P_{sat}, so it is possible that power dependent effects for the other emitters would only become apparent at higher excitation powers.

For pulsed excitation, $g^{(2)}(0)$ showed a consistent power dependence, possibly due to the significantly higher pump laser intensity at the peaks of laser pulses. It was difficult to observe $g^{(2)}(0) < 0.5$ because as the excitation power was decreased the count rate generally became too low to practically measure $g^{(2)}(\tau)$ before the single photon condition was reached.

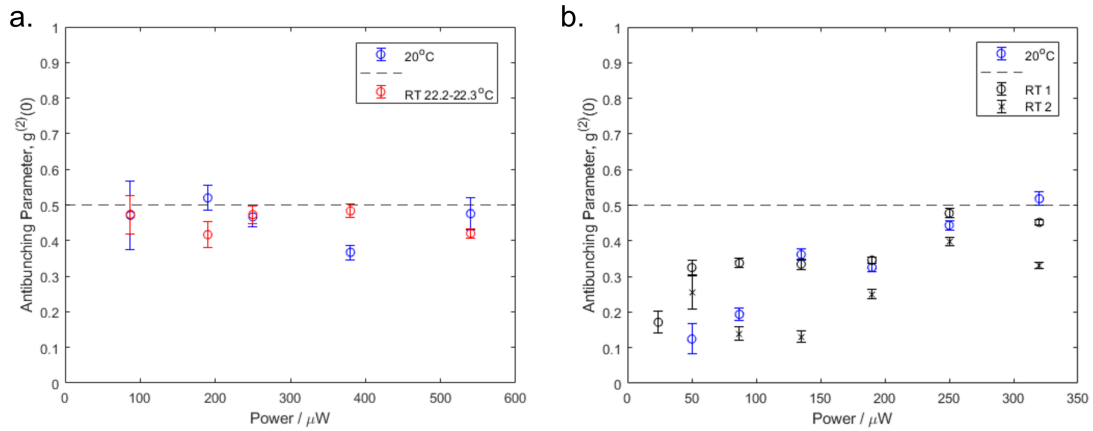

Figure 44: Normalised $g^{(2)}(0)$ or antibunching parameter as a function of excitation power. (a) Emitter 4: $g^{(2)}(0)$ as a function of power at 20^{o}C (blue) and room temperature (RT, red), showing no clear power dependence. (b) Emitter 3: $g^{(2)}(0)$ increases with power for two measurements at room temperature (black) and one at 20^{o}C.

4.1.2.2 Temperature dependence of $g^{(2)}(0)$

As for temperature dependence of $g^{(2)}(0)$, only one measurement could be found in the literature, which suggested that $g^{(2)}(0)$ increases with temperature when measured from 10 K, increasing sharply by around 0.2 at 200 K [116]. Our study focused on near-ambient temperatures since this is where hBN emitters would be operated as room temperature single photon sources in technological applications.

Firstly, there was no significant difference between $g^{(2)}(0)$ with or without temperature stabilisation when the temperature controller was set equal to room temperature. For almost all emitters studied there was no consistent trend in the fitting parameters of the $g^{(2)}(\tau)$ function when the sample temperature was varied over the range 16-40^{o}C. However, one Emitter 6 did show a weak temperature dependence of $g^{(2)}(0)$ which was seen on two temperature sweeps from 20-32^{o}C, with control measurements at 22^{o}C before and after each temperature sweep (see Figure 45).

In order to distinguish between temperature or power effects and the variance of the measurement, the repeatability of the $g^{(2)}(0)$ measurement was studied. The standard deviation of six repeated $g^{(2)}(0)$ measurements for this particular emitter at 22^{o}C and 250 μW power was 0.05, the range was 0.14. In comparison, the ranges of $g^{(2)}(0)$ values for the two temperature series were 0.13 and 0.14. Considering this, the evidence for temperature dependent $g^{(2)}(0)$ looks much weaker.

In a practical application of single photon emission, we would want to cool the emitter slightly (still near room temperature) in order to improve $g^{(2)}(0)$. However, if the

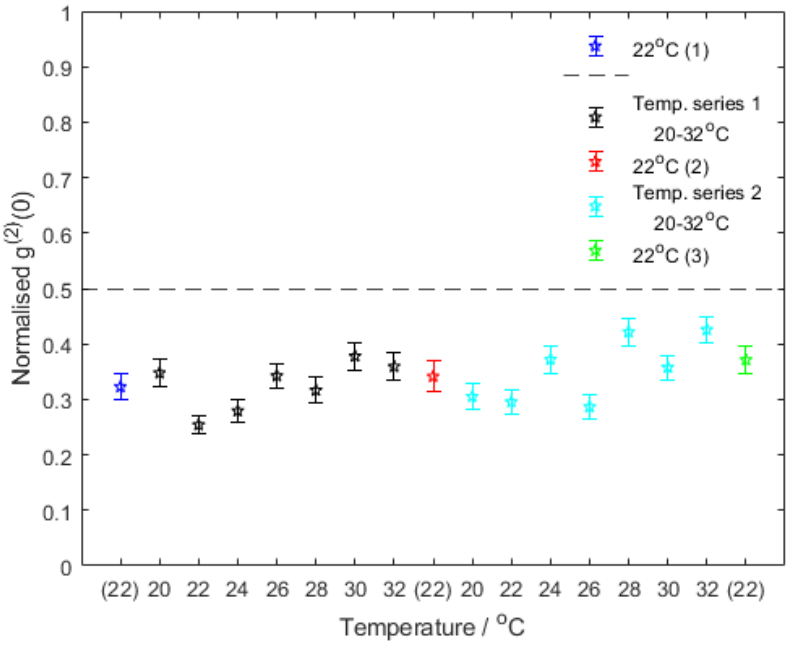

Figure 45: Normalised $g^{(2)}(0)$ as a function of temperature for Emitter 6. The temperature was increased from 20^{o}C to 32^{o}C twice (black and cyan points). Before and after each temperature sweep there was a control measurement at room temperature (22^{o}C).

improvement in $g^{(2)}(0)$ is not higher than the variance between measurements then we do not see any advantage from temperature control of the sample.

4.1.2.3 Relationship between blinking and $g^{(2)}(0)$

Emitter 5 showed an interesting behaviour during the temperature and power dependence study, see Figure 46. The excitation power was increased repeatedly up to 2.0 times P_{sat} at different sample temperatures. On the third power series, at 22^{o}C, the $g^{(2)}(0)$ value suddenly increased by around 0.2. The $g^{(2)}(0)$ stayed at this higher value permanently until the end of the measurement. At the same time, a change in the blinking behaviour was observed. This emitter showed occasional spike-like blinking from a dark state to a bright state. During the measurement where $g^{(2)}(0)$ increased, there was a step-like blinking event after which the emitter was mostly in the bright state, occasionally dropping down into the dark state. Therefore, there appeared to be a permanent change in both the $g^{(2)}(0)$ value and the blinking behaviour. Since this happened at the highest power measured and after several power increases this permanent change in the emitter's behaviour may have been power-induced.

The $g^{(2)}(0)$ and blinking change in Emitter 5 was only observed once, however it is another example alongside fluorescence bleaching of apparently irreversible changes to hBN emitters which tend to occur at higher excitation power. It is clear that the mini-

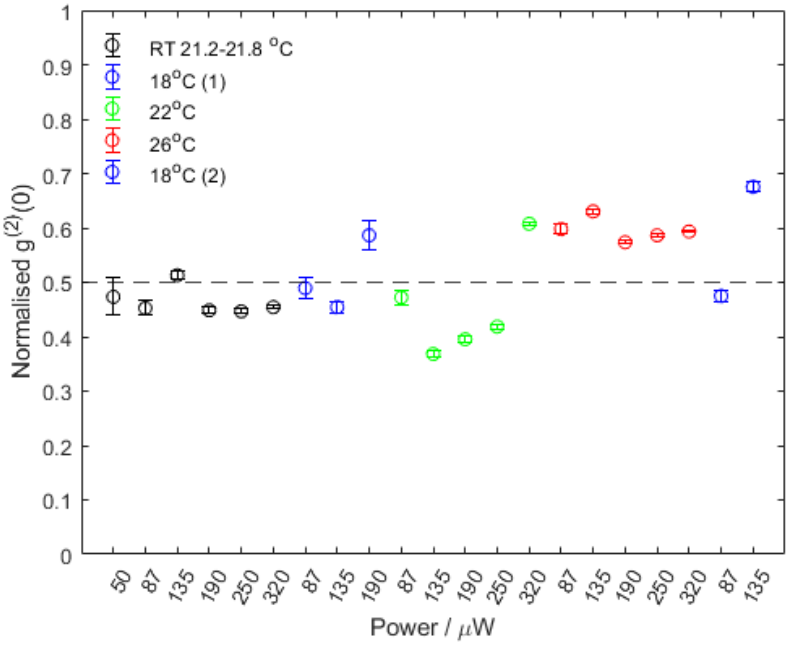

Figure 46: Normalised $g^{(2)}(0)$ for Emitter 5. The power was increased up to 320 μW at four different temperatures. $g^{(2)}(0)$ values are plotted in the order the measurements were taken. At the 22^{o}C, 320 μW measurement (final green point), the $g^{(2)}(0)$ suddenly increases by around 0.2, and remains permanently higher even when the power and temperature are changed. This change in $g^{(2)}(0)$ coincided with a change in the blinking behaviour as described in the main text.

mum possible excitation power should be used for a given application. Since these power induced changes can be permanent, even briefly increasing the excitation power during characterisation may be risky. There was no indication in our measurements that the saturation measurement, which has to go above P_{sat} to properly measure the saturation curve, caused any change to $g^{(2)}(0)$.

4.2 Time-dependent Mandel Q parameter analysis for a hexagonal boron nitride single photon source

This section deals with the single photon emission dynamics of a stable hBN emitter which did not show any blinking events during experiments. This was Emitter 6 in the previous section. When there are no blinking events we can ask what limits the intensity stability of single photon emission over various timescales? The fluctuations in the emission count rate without any blinking were studied using the photon number variance as a function of integration time. A convenient measure of the variance is the Mandel Q parameter. This section describes experiments to measure the time-dependent Mandel Q parameter of a hBN emitter, and the measurement artefacts which must be avoided. The following was adapted from a paper published in Optics Express [54]:

Callum Jones, Jolly Xavier, Samir Vartabi Kashanian, Minh Nguyen, Igor Aharonovich, and Frank Vollmer, "Time-dependent Mandel Q parameter analysis for a hexagonal boron nitride single photon source," Opt. Express 31, 10794-10804 (2023).

The supplementary material document accompanying this paper is included in Appendix A.

4.2.1 Time-dependent Mandel Q Parameter

A key component of quantum optical technologies is the single photon on demand (SPoD) source: a source which can deliver deterministic single photon pulses at high count rates [117, 110]. These sources may find applications in QKD [118], optical quantum computing, radiometry [119, 120], or even in probing the single photon response of biological systems [35]. For a quantum emitter such as those in hBN to be used as a SPoD source, it must have a photon number distribution as close as possible to the single photon number state. In other words, both multiphoton and zero photon pulses must be suppressed so that the photon number variance is reduced. The range of timescales over which this small photon number variance is preserved is a measure of the intensity stability of the source. Quantifying this stability is our motivation to measure the time-dependent Mandel Q parameter for a quantum emitter in hBN.

The time-dependent Mandel Q parameter is defined as the variance over mean minus one for the photon number N measured from a source during integration time T [110, 121, 122]:

$$Q(T) = \frac{\langle \Delta N^2 \rangle_T}{\langle N \rangle_T} - 1. \tag{103}$$

$\langle ... \rangle_T$ denotes averaging over the integration time T. The photon number for a coherent state follows a Poisson distribution, therefore $\langle \Delta N^2 \rangle_T = \langle N \rangle_T$ and $Q(T) = 0$. The expected result for a single photon source is a negative Q parameter, which indicates the photon number distribution is narrower than a Poisson distribution and so is an indication of intensity squeezing. An ideal single photon source detected with no losses has $Q = -1$.

In previous works Q(T) has been used to characterise single photon emission from a single molecule triggered single photon source [110]. Other more varied applications outside quantum information technologies include the use of Q(T) for single molecule measurements, for example the detection of singlet oxygen or the fast recognition of single dye molecules [123, 124]. We note that the abstracts in Refs. [125, 126] mention observations of negative Q(T) on timescales of $\sim$10 ns for hBN emitters, therefore this topic demands a full study.

In Ref. [54] we present the characterisation of a stable quantum emitter in hBN, focusing on the time-dependent Mandel Q parameter. With the help of data simulated by Monte Carlo methods, we show that the effect of the detector deadtime prevented us from observing antibunching in the Q parameter under CW excitation. However, for pulsed excitation with appropriate parameters, a negative Q parameter was found when integrating over one pulse period (100 ns). Finally, we discuss the use of Q(T) to complement other measures in the complete characterisation of photon statistics for hBN quantum emitters. While the absolute value of the Q parameter depends on the collection efficiency of single photons, we propose that the crossover time at which the photon statistics change from sub- to super-Poissonian is a robust and useful measure of the emitter's intensity stability.

4.2.2 Methods

4.2.2.1 Emitter characterisation

Individual quantum emitters were located by scanning the sample piezo stage to produce PL maps of the surface under CW excitation, see Figure 47(b). All the following measurements were carried out on one emitter (previously referred to as Emitter 6) which was exceptionally stable. No blinking was observed for this emitter under any excitation power we used over hours of measurement. The blinking we refer to here is a transition between a bright and dark state of the emitter (common to the literature on hBN [111, 85]),

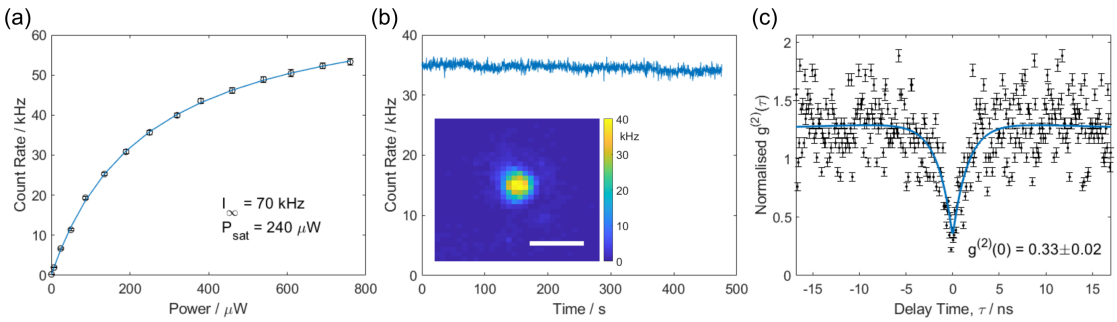

Figure 47: (a) Photoluminescence (PL) count rate saturation curve for our hBN quantum emitter. The saturation power P_{sat} is 240 μW. (b) PL count rate over time with 250 μW CW excitation showing stable emission rate. The emitter showed no blinking events under any of the conditions studied; this is also shown by the small error bars in the saturation curve. Inset: PL map (photon count rate in kHz) of the quantum emitter. Scale bar: 1 μm. (c) Second order correlation histogram for 250 μW CW excitation. A two-exponential fit was applied to obtain $g^{(2)}(0) = 0.33 \pm 0.02$, confirming single photon emission.

not the transition to a long-lived shelving state as the term blinking is used in Ref. [110]. Emitters showing fluorescence blinking have different transition rates when they are in their bright and dark states [85]; we expect our emitter to be free from this effect.

The emitter was characterised using the methods described in Chapter 3. The count rate saturation, time trace of fluorescence emission and CW $g^{(2)}(\tau)$ measurement are shown in Figure 47.

4.2.2.2 Mandel Q parameter calculation

To measure the intensity stability of our emitter, the time-dependent Mandel Q parameter Q(T) was calculated according to Equation 103. This was calculated using the same raw photon arrival times, or timestamps, used for $g^{(2)}(\tau)$ measurements. Timestamps were collected in acquisition times of 100 s for all measurements.

To calculate Q(T), timestamps from both detectors were combined into one array, sorted, and split into K time windows of length T using a MATLAB script (Ref. [127]). Unless stated otherwise, $K = 10^8$ time windows were used (or the maximum allowed by the 100 s acquisition time for a given T) to calculate the variance and mean of the photon number per window $\langle \Delta N^2 \rangle_T$ and $\langle N \rangle_T$, and hence Q(T). For pulsed excitation the T values were all multiples of the pulse repetition rate. Error bars were calculated by repeating the analysis over many acquisitions.

This analysis was carried out on timestamps from both CW (see Section 4.2.3) and

pulsed (see Section 4.2.4) excitation. In addition to the procedure above, pulsed timestamps were also filtered using the trigger pulse from the laser, as in [110]. Only timestamps occurring within a window starting from the arrival of the laser pulse were kept. The optimum filter width was found to be 5 ns; this is discussed further in the Supplemental Document (Appendix A).

4.2.2.3 Modelling hBN energy levels

In order to offer a comparison to experimental data for Q(T) and better understand the photodynamics of our hBN emitter, we simulated timestamp data using Monte Carlo methods. MATLAB scripts are given in Appendix B. We used a three-level system as a simplified model for the emitter, defined by four transition lifetimes (see Figure 48(b)). Although other works have found some emitters require four energy levels [85, 86], we found that models with three and four energy levels fit our $g^{(2)}(\tau)$ data equally well.

Timestamps were simulated based on the method detailed in [104]. In each excitation cycle, the four lifetimes for each transition are drawn from exponential distributions to determine whether a photon is emitted (is the cycle radiative or non-radiative), and at what time. Losses are modelled by removing photon detections based on a binomial distribution, the detections are split 50:50 into two channels to model the beamsplitter in the HBT setup, afterpulses are added at random after some detections (see Appendix A), and finally the detector deadtime is modelled by removing any detections less than the deadtime (80 ns for our SPADs) after the previous detection. The resulting timestamps are in an identical format to our experimental data, so the same data analysis for $g^{(2)}(\tau)$ and Q(T) was applied.

To run this simulation we needed to know appropriate transition lifetimes to set as mean values in the Monte Carlo model. We determined these parameters by fitting the three-level model to experimental $g^{(2)}(\tau)$ data plotted on a log scale over the time interval 100 ps – 10 μs by a procedure described in [85]. For a three-level system, the populations of the energy levels $\rho_i(t)$ are described by a system of coupled differential equations listed in Equations 86-88 (in Chapter 3).

The transition rates k_{ij} are used as fitting parameters for this model, which is related to the normalised $g^{(2)}(\tau)$ by the solution to the differential equations for $\rho_2(\tau)$, with the initial conditions $\rho_1(0) = 1$, $\rho_{2,3}(0) = 0$ [87] by Equation 89. This model will always have $g^{(2)}(0) = 0$, therefore to include the effect of the background counts we used the background correction Equation 93 to include σ as a fitting parameter. The model was fitted to experimental data using the parameters k_{ij}, which are the reciprocals of the transition lifetimes τ_{ij} represented in Figure 48(b).

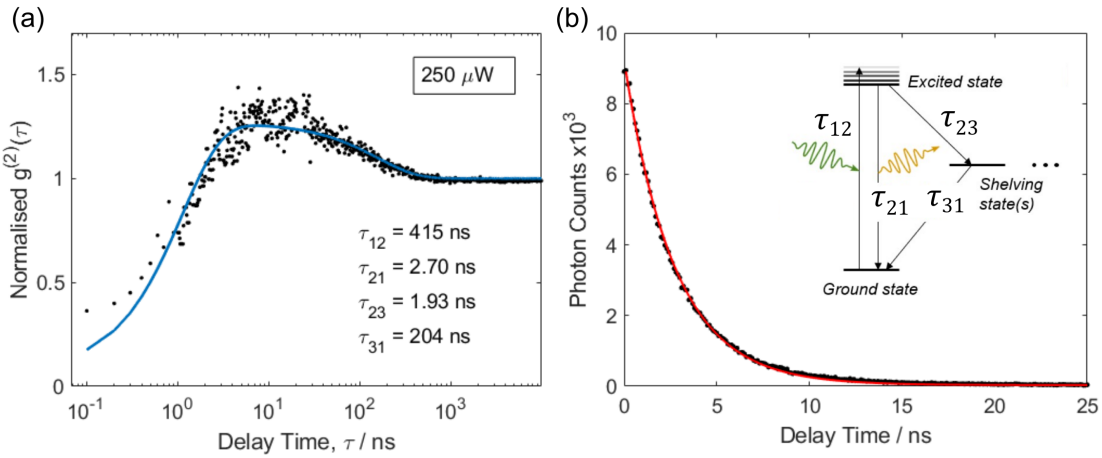

Figure 48: (a) Fitting a three-level model to $g^{(2)}$ data for CW excitation at 250 μW. The best fit transition lifetimes τ_{ij} are shown; lifetimes for the 540 and 760 μW are in Table 1. (b) Radiative lifetime measurement made using pulsed excitation at 10 MHz and 24 μW mean power; data is shown for one 100 s acquisition. Fitting a single exponential to all 144 acquisitions of timestamp data gives a mean value of $\tau_{21} = 2.7 \pm 0.1$ ns. Inset: Schematic of the three-level model for the emitter showing the transition lifetimes τ_{ij} between levels.

Power / μW	τ_{12} / ns	τ_{21} / ns	τ_{23} / ns	τ_{31} / ns	σ
250 ($1.0P_{sat}$)	415	2.70	1.93	204	0.962
540 ($2.3P_{sat}$)	189	2.83	1.85	195	0.722
760 ($3.2P_{sat}$)	135	2.86	1.81	125	0.811

Table 2: Fitting parameter for $g^{(2)}(\tau)$ data.

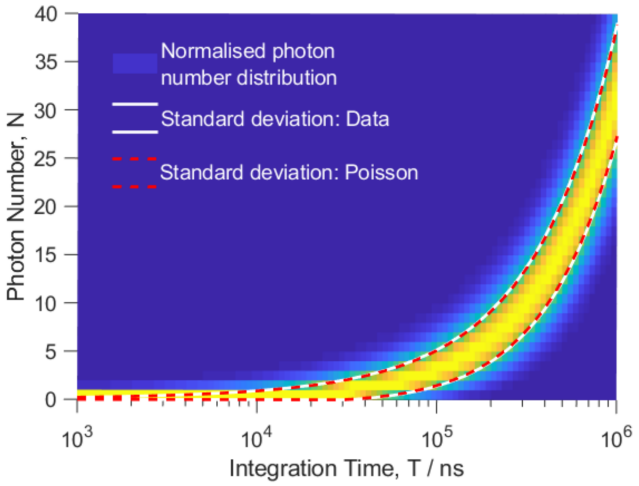

Figure 49: Photon number distribution for CW emission under 250 μW excitation. Along the y axis is a histogram of photon number per time bin, as a function of the time bin width or integration time, T. Each histogram height is normalised to one so the widths of the distributions can be compared. Curves indicate one standard deviation for the data (white), and a Poisson distribution with the same mean photon number (red). The data and Poisson deviations overlap almost exactly on this scale.

Additional constraints were needed to fit the four parameters τ_{ij}: the radiative lifetime, τ_{21}, was measured directly using pulsed excitation at 10 MHz and 24 μW mean power. A single exponential fit to the lifetime curve in Figure 48(b) gave $\tau_{21} = 2.7 \pm 0.1$ ns. In addition, the excitation lifetime τ_{12} was assumed to be linearly proportional to the power (as in [85]) and measurements at 250, 540 and 760 μW were used to constrain τ_{12}. The best fit parameters τ_{ij} and σ at the three powers are given in Table 2, these were used as the initial parameters for the Monte Carlo simulated timestamps.

4.2.3 Results - CW Mandel Q parameter

First, we examined the photon number distribution of our emitter for 100 s of timestamp data under CW excitation at 250 μW, see Figure 49. The single photon emission follows a distribution very close to a Poisson distribution over integration times from 1 μs to 1 ms. The photon number variance across these integration times is therefore almost the same as that of a coherent state. Since $g^{(2)}(\tau)$ clearly shows antibunching over ns timescales (e.g. in Figures 47(c), 48(a)), we would expect that as the integration time is decreased further the photon number variance will become significantly smaller than that of a Poisson distribution. The difference between the data and Poisson distribution variances is better visualized over several orders of magnitude in integration time using the Mandel Q parameter Q(T).

The Mandel Q parameter was calculated for CW excitation at three powers: 250, 540 and 760 μW, see Figure 50(a). We see that above approximately 100 ns the photon number distribution is wider than a Poisson distribution. Below this integration time there is a small negative value; the minimum is $Q = -(1.4 \pm 0.3) \times 10^{-3}$ for 540 μW, but Q(T) approaches zero at lower T. The measurement is limited at low integration times because the mean photon number per time bin tends to zero. At integration times $<< 1/I$, where I is the emitter count rate, most time bins contain no photons. This is also illustrated by Figure 49. For 250 μW excitation, $I = (34 \pm 3)$ kHz, therefore the average photon number is less than one below $T = 29 \pm 3$ μs.

Q(T) for simulated timestamp data can reproduce a similar form to the experimental data using the three-level Monte Carlo model described in Section 4.2.2. In Figure 50(b) we compare the result for a two-level and three-level emitter, in which the transition lifetimes for the first two levels are kept the same (red and blue points, respectively). The transition lifetimes found in Table 2 were optimized to match the simulated Q(T) more closely to experiment and to have the same acquisition time as the experimental data. The final simulation parameters were: $\tau_{12} = 205$ ns, $\tau_{21} = 1.60$ ns, $\tau_{23} = 1.40$ ns, $\tau_{31} = 420$ ns, and $\eta_{model} = 0.248$. The two-level model uses only τ_{12} and τ_{21}, and η_{model} is the fraction of photons detected in the model.

Figure 50(b) illustrates that the positive Q(T) values are a consequence of adding a metastable shelving state. For a two-level emitter with only a ground and excited state (red points), the antibunched photon statistics and negative Q(T) are maintained as the integration time is increased. However, adding a shelving state (blue points) introduces a non-radiative decay path causing fluctuations in the single photon count rate. These become significant for integration times higher than the shelving state lifetime, which was $\tau_{31} = 420$ ns in this case. Detector afterpulsing was included in the simulated data in Figure 50(b) and also causes Q(T) to become more bunched for T greater than the detector deadtime; see Appendix A.

An important factor that must be considered is the detector deadtime. When the deadtime is artificially removed from the simulated timestamp data, Q(T) becomes positive for all integration times, i.e. the negative value disappears (cyan points in Figure 50(b)). The deadtime introduces an artificial antibunching effect since there is a decreased probability of two photon detections within the deadtime period of around 80 ns. Therefore, the negative points in Figure 50(a) are likely due to the detector deadtime only, especially considering the minimum value of Q(T) occurs near 80 ns. As discussed in Refs. [110, 128], pulsed excitation with a repetition period longer than the deadtime must be used to avoid the deadtime artefact.

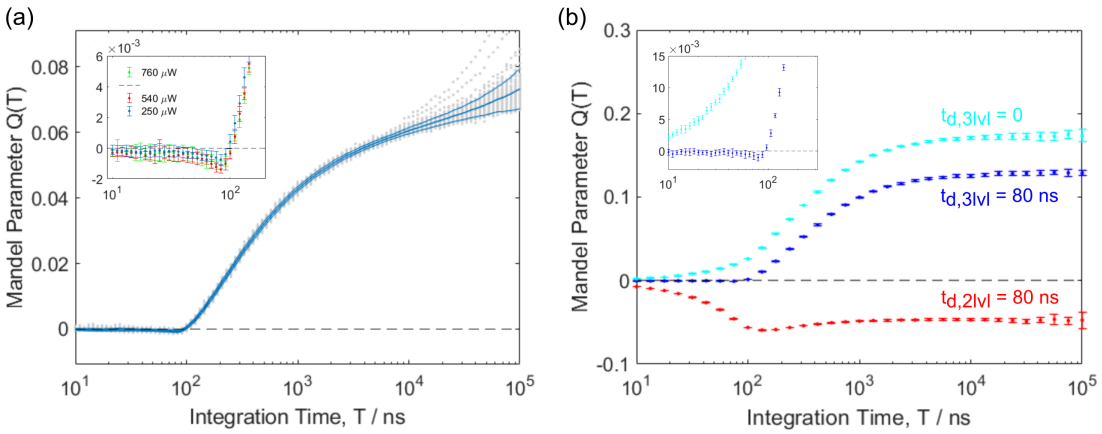

Figure 50: (a) Experimental Mandel Q(T) for CW excitation at 250 μW. Blue lines show mean values over 99 separate 100 s acquisition times, plus and minus one standard deviation. Inset: zoom-in showing small negative values for all three powers 250, 540 and 760 μW. (b) Simulated CW Mandel Q(T) from Monte Carlo model. Blue (cyan) points were simulated using a three-level model with (without) modelling the 80 ns detector deadtime t_d. Red points are from a two-level model with the detector deadtime. Removing the deadtime effect makes all Q(T) values more positive, and for the three-level simulation removing the deadtime removes all negative values (inset). Comparing the two- and three-level simulations we can see that adding a metastable shelving state causes Q(T) to become positive at long integration times.

4.2.4 Results - Pulsed Mandel Q parameter

For pulsed excitation, a 10 MHz repetition rate was used so that the repetition period of 100 ns was longer than the detector deadtime of 80 ns. A mean power of 24 μW (pulse energy 2.4 pJ) produced a $g^{(2)}(0)$ value of 0.37 ± 0.02 (Figure 51(a)) with a count rate of 2.8 kHz; increasing the power to 82 μW and 160 μW increased $g^{(2)}(0)$ above 0.5 (see Appendix A). The timestamps were filtered using a trigger pulse from the laser: only timestamps within 5 ns of the pulse start were used, i.e. approx. $2\times$ the radiative lifetime. Four hours of timestamps at 24 μW measured in 100 s acquisitions were used to produce the $g^{(2)}(\tau)$ and Q(T) plots in Figure 51.

We found a negative value at $T = 100$ ns of $Q = -(1.4 \pm 0.8) \times 10^{-4}$. As for the CW case, Q(T) is positive for integration times greater than 100 ns. This negative value is very small; the magnitude of Q(T) depends on the total detection efficiency of the measurement. The expected value for integration over one pulse period T_p is [128]:

$$Q(T_p) = \eta \left(\frac{g^{(2)}(0)}{2} - 1 \right) \tag{104}$$

where η is the total photon detection efficiency (i.e. including both the collection efficiency of photons and the detector efficiency). From our experimental values we can estimate $\eta = (2 \pm 1) \times 10^{-4}$. To measure a more negative value and a stronger signature of photon antibunching would require both a higher total detection efficiency and lower $g^{(2)}(0)$. We note that several works on hBN emitters have achieved low $g^{(2)}(0)$ values (as low as 0.07) under pulsed excitation [129, 96, 97, 92]. In our experiments we found a difficult trade-off in the pulsed excitation power between low $g^{(2)}(0)$ improved by low power and achieving a sufficiently high count rate to make our measurements.

Comparing with state-of-the-art quantum dot single photon emitters, approximate values for the Quandela source of $\eta = 0.4$, $g^{(2)}(0) = 0.02 - 0.04$ (only including optical losses from the source and fibre coupling to single mode fibre, not including detection efficiency) the single pulse Q parameter could be around $Q(T_p) = -0.4$ [67]. With this Q parameter we expect the variance in a photon number measurement to be approximately 60% of the shot noise level, with count rates up to 200 MHz. By using a planar antennae for efficient photon collection from a single molecule single photon source, Chu et al. [130] measured a single pulse Q parameter $Q(T_p) = -0.64$ and intensity squeezing down to 62% of the shot noise level. This source has a detected count rate of around 12 kHz and the noise was measured over an interval of $T = 1$ ms. These examples demonstrate how significant intensity squeezing can be seen with currently available single photon emitters, which can reduce the noise in intensity measurements at low ($\sim$10 kHz-100 MHz) count rates.

Simulated timestamp data was compared with or without the deadtime modelled in Figure 51(c). The data were simulated with the method described in Section 4.2.4 using the parameters: $\tau_{12} = 100$ ps, $\tau_{21} = 2.70$ ns, $\tau_{23} = 2.40$ ns, $\tau_{31} = 420$ ns, and total detection efficiency $\eta_{model} = 2.54 \times 10^{-3}$.

There is no significant difference in Q(T) when the deadtime is removed for pulsed excitation at 10 MHz, and crucially, the negative value at $T = 100$ ns remains. Therefore, we conclude that the experimental Q(T) data for 24 μW pulsed excitation shows evidence of antibunching at $T = 100$ ns and bunching at longer integration times. As in the case of CW excitation, the bunching is attributed to the presence of a metastable shelving state.

The lifetime of the shelving state can be estimated by fitting the model from [128] to the pulsed excitation Q(T) data, expressed in terms of the shelving/deshelving lifetimes τ_{23}, τ_{31}, the integration time $T = k\tau_{rep}$ (k is an integer number of pulse repetition periods τ_{rep}), and the total detection efficiency η:

$$Q(k\tau_{rep}) = \eta \left[\frac{\tau_{31}}{\tau_{23} + \tau_{31}} \left(\frac{2-\beta}{\beta} - \frac{2(1-\beta)}{k} \frac{1-(1-\beta)^k}{\beta^2} \right) - 1 \right] \tag{105}$$

where $\beta = \tau_{rep}(1/\tau_{23} + 1/\tau_{31})$.

A simplified form of this model was used to fit data from the single molecule triggered single photon source in [110] by assuming that $\tau_{rep}/\tau_{23} << 1$; $\tau_{rep}/\tau_{31} << 1$ is satisfied. Our hBN emitter does not meet these criteria: $\tau_{rep}/\tau_{23} = 0.67$ and $\tau_{rep}/\tau_{31} = 0.14$, therefore we use the full expression Equation 105 to fit to our Q(T) data (shown in Figure 51(b) inset). This yields values of $\tau_{23} = 153$ ns and $\tau_{31} = 665$ ns.

We note that in comparison with the single molecule fluorophore in [110] (having $\tau_{23} = 3.85$ ms and $\tau_{31} = 250$ μs), the hBN emitter has a much shorter shelving state lifetime. This makes the window of observable negative Q(T) values, between a typical detector deadtime and the transition to $Q(T) > 0$, narrower and more difficult to observe.

The crossover time at which $Q(T) = 0$ is a useful metric as it gives a measure of the stability of a single photon source over long timescales. Our single photon emitter had a crossover between 100 and 200 ns. A perfect single photon source, such as an ideal two-level system, would have $Q(T) < 0$ for all integration times.

For certain applications of hBN single photon sources the photon number distribution will be critical, for example SPoD sources or in probing the single photon response of biological systems [35]. In these cases, we need to not only confirm single photon emission using $g^{(2)}(\tau)$, but also quantify the single photon variance over timescales which will be relevant to the chosen application. The Mandel Q parameter provides a measure of the

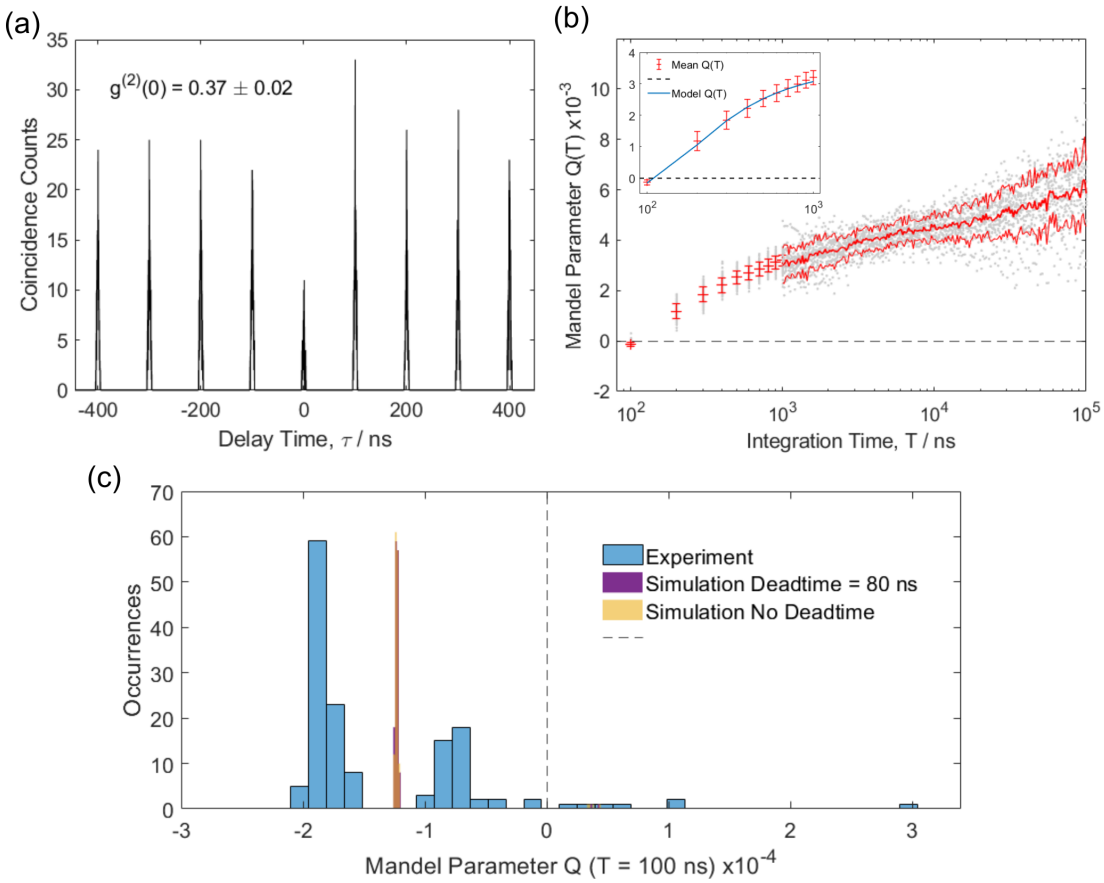

Figure 51: (a) Second order correlation function $g^{(2)}(\tau)$ for 10 MHz pulsed excitation at 24 μW mean power. $g^{(2)}(0) = 0.37 \pm 0.02$ was calculated using the relative area of the peak at zero delay time. Note that the timestamp data was filtered keeping only detections within 5 ns of the laser trigger pulse. (b) Mandel Q(T) for pulsed excitation at 24 μW showing positive Q(T) for integration times greater than 100 ns. Red lines show mean values +/- one standard deviation. Inset: fit to data using Equation 105. (c) Histogram of Q(T) values at T = 100 ns (integrating over one pulse period, blue bars). Values are compared over 144 acquisitions of 100 s each. The mean value is $Q = -(1.4 \pm 0.8) \times 10^{-4}$. The purple and yellow bars are Q(T) histograms from simulated timestamp data with comparable parameters, with/without modelling the detector deadtime. The distribution of Q(T) does not change when the simulated deadtime is removed, confirming that the detector deadtime has no effect on Q(T) when the pulse repetition period is greater than the deadtime.

photon variance, provided that artefacts due to the detector deadtime are avoided properly. While the absolute value of Q(T) is influenced by detection efficiency, the crossover time at which the photon statistics transform from sub- to super-Poissonian could be taken as a measure of long-term stability of photon antibunching from a single photon source.

Further improvements to hBN emitters for technological applications could look to improving the stability of emission over longer timescales. Currently, photon bunching seems to be inevitable over $\sim$100 ns timescales due to the presence of a metastable shelving state. However, hBN quantum emitters with different chemical structures have significantly different energy level structures and shelving state lifetimes [79]. An emitter with a longer shelving state lifetime and higher preference for radiative decay should offer better single photon antibunching stability.

4.3 Conclusions

I showed in this chapter that many of the hBN emitters exhibited fluorescence blinking. The blinking rate was not highly sensitive to the sample temperature near room temperature, so stabilising the sample temperature was not effective in improving the intensity stability of our emitters. Reducing the excitation power did consistently reduce the blinking rate, so the minimum possible excitation power should be used that gives a sufficient count rate for the measurement. Some permanent changes to emitters were also observed: fluorescence bleaching and a permanent increase in the $g^{(2)}(0)$ value. These changes occurred under relatively high excitation power, showing that using high excitation powers during characterisation can be risky since the properties of the emitter can be permanently changed.

A few rare hBN emitters did not show any blinking behaviour whatsoever, in particular Emitter 6. In the publication included in this chapter we measured the time-dependent Mandel Q parameter for Emitter 6. The photon number distribution for this emitter showed antibunching only below integration times of 100-200 ns. An antibunched photon number distribution over longer timescales could be achieved by improving the $g^{(2)}(0)$ value and total collection efficiency of photons. For now, we are far from having a very narrow photon number distribution over the timescales of a useful measurement for exploiting intensity squeezing, in comparison to sources with Q parameters down to -0.64 [130]. However, we have shown how the Mandel Q parameter can be a useful characterisation method to find the crossover time at which the photon statistics of a single photon source change from antibunched to bunched.

Overall, the previous two chapters have highlighted some challenges in using single photon emitters in hBN for quantum sensing applications. These are: achieving highly

indistinguishable single photons to do high visibility HOM interference and generate entangled states, fluorescence blinking and permanent damage induced in emitters by high excitation power, and producing single photon states with a very narrow photon number distribution for applications that demand intensity squeezing. In this thesis I have focused on the single photon emission from hBN vacancy defects, while an emerging area of interest is on defects with magnetically addressable spins. These will provide another approach to hBN quantum sensors for magnetic fields, or other physical quantities which can be coupled to the spin states.

In the next part of this thesis I will move onto a different approach to generating quantum optical states for sensing: producing entangled photon pairs using a nonlinear optical interaction in a PPKTP crystal.

Part III - Generating Entangled Photon Pairs Towards Applications in Quantum-Enhanced Biosensing using Tapered Fibres and WGM Interferometers

5 Entangled Photon Pairs from a PPKTP Sagnac Loop

5.1 Introduction

To develop sensing schemes using entangled photon states, we need a source of photon pairs which can be separated into two modes and which are generated in an entangled state of some degree of freedom, such as polarisation. Entangled photon pairs should be generated with high fidelity and with high photon pair generation efficiency, i.e. as high as possible a photon pair rate per unit pump power. When the photon pairs are projected into a basis in which they can interfere, they should also be degenerate in wavelength and indistinguishable, to give a high HOM interference visibility and efficiently produce N00N states. For sensing applications with an optical resonator such as a WGM microsphere, the ideal entangled photon source would have a spectral linewidth on the order of hundreds of MHz or lower and provide some wavelength tuning. A narrow spectral width means a broader temporal distribution and hence lower time resolution. However, this would not be an issue for WGM measurements since the sensing time resolution is not limited by the Fourier transform of the WGM spectral width. The highest time resolution achieved using a laser locked to the resonance wavelength was $\sim \mu$s [33], while the limit due to the resonance width is $\sim$ns. A source with these properties could be coupled directly to a WGM allowing the resonance wavelength shift of a WGM sensor to be read out using a quantum sensing scheme.

There are several approaches to generating entangled photon pairs: they can be produced by nonlinear optical processes, two-photon emission from trapped atoms [131], cascaded decay of biexcitons in quantum dots [132], and other emerging material systems. The nonlinear optics approach is most commonly using second order nonlinearity in a suitable nonlinear crystal to do spontaneous parametric down-conversion (SPDC). However, it is also possible to use third order nonlinearities to generate entangled photon pairs by four-wave mixing (FWM) [133]. For our experiments developing a entangled photon pair source for quantum sensing we chose second order nonlinearity and the SPDC process.

In this section I will present work on building and characterising a polarisation entangled photon pair source using a periodically-poled KTP (PPKTP) nonlinear crystal in a Sagnac loop configuration. PPKTP has a high second order susceptibility, producing an efficient SPDC process. The PPKTP Sagnac loop is now a well established setup for generating polarisation entangled photon pairs with a high pair generation rate per unit pump power [134]. We chose this as a high brightness source of photon pairs which can be separated into two output modes even when the photons are degenerate in wavelength using their orthogonal polarisations. This kind of source is ideal for two-photon interference and building two-photon N00N states which can be applied to sensing schemes.

The following sections provide more information on the SPDC process for generating photon pairs, and a summary of some previous experiments, particularly those involved in developing the PPKTP Sagnac loop experiment. Then I will present our experimental setup and present results characterising the entangled photon states: emission spectra from the PPKTP crystal, quantum state tomography to determine the state fidelity, and HOM interference.

5.1.1 Spontaneous Parametric Down-Conversion

Nonlinear optics is used as a method for producing photon pairs because it allows optical fields at different frequencies to be coupled to each other - this is required to convert one high energy photon into two lower energy photons. This coupling between optical fields is possible through the polarisation response of a suitable medium, usually a crystal with a carefully chosen structure. The electrons in the medium act like an array of antennae, absorbing and re-radiating optical fields. The polarisation response of the bulk medium can be expanded in powers of the incident E-field [135]:

$$P_i = \varepsilon_0 \chi^{(1)} E_i + \varepsilon_0 \chi^{(2)}_{ijk} E_j E_k + \varepsilon_0 \chi^{(3)}_{ilmn} E_l E_m E_n ... \tag{106}$$

where $\chi^{(n)}$ is the n^{th} order susceptibility, $i, j, k, l, m, n = 1, 2, 3$ are indices for fields along the three Cartesian axes, and repeated indices indicate a sum. The E-fields in each higher order term are allowed to be at different frequencies than the incident field. The first order term is the usual linear response of the medium, but all higher order terms represent nonlinear processes in which the incident field is converted into multiple output fields at different frequencies. The higher order susceptibilities of most materials are extremely small, and since the nonlinear terms depend on powers of the E-field, nonlinear effects are highly power dependent. At sufficiently high powers and in a medium with a high nonlinear susceptibility, nonlinear processes become significant and can be used for optical frequency conversion.

SPDC is the nonlinear conversion of a pump field into two signal and idler fields at lower frequencies. The process only takes place efficiently in a nonlinear medium with a sufficiently large second order susceptibility $\chi^{(2)}$, and provided the phase matching conditions on energy and momentum conservation are met. Depending on the polarisations of the pump, signal and idler fields there are different types of SPDC. For Type-I SPDC, the signal and idler modes have parallel polarisations, and are orthogonally polarised to the pump mode. The energy and momentum conservation conditions are [135]:

$$\omega_p = \omega_s + \omega_i \tag{107}$$

$$\vec{k}_p(n^e_p) = \vec{k}_s(n^o_s) + \vec{k}_i(n^o_i). \tag{108}$$

Here p, s, i label pump, signal and idler modes and n^e, n^o are the extraordinary and ordinary refractive indices of the nonlinear crystal medium. This condition can be met in KTP since it is a negatively birefringent medium ($n_e - n_o < 0$) and the input and output modes experience different refractive indices.

In contrast, Type-II SPDC produces orthogonally polarised signal and idler output modes. Modern Type-II SPDC generation commonly uses periodically poled nonlinear crystals, such as potassium titanyl phosphate (PPKTP). The nonlinearity of a crystal depends on the orientation of the pump, signal and idler E-field vectors relative to the principal axes of the crystal. In general the susceptibility $\chi^{(2)}$ is a tensor, which can be simplified for a given crystal structure to a set of nonlinear coefficients d_{ij} [135]. For a given crystal geometry and polarisations of the pump, signal and idler fields, only one of these d_{ij} are needed to describe the strength of the nonlinear response. PPKTP is chosen for its high d_{24} coefficient [136].

Periodic poling is a process in which voltage pulses of several kV/mm are applied across a nonlinear crystal by a periodic pattern of electrodes [137]. This permanently reverses the crystal polarity in a periodic pattern and tuning the poling period Λ provides an additional degree of freedom for achieving nonlinear phase matching. This technique, called 'quasi-phase matching', allows nonlinear interactions not otherwise possible with conventional birefringent phase matching and in particular allows the highest nonlinear coefficients of a given crystal to be accessed. The phase matching conditions for Type-II quasi-phase matching are [135]:

$$\omega_p = \omega_s + \omega_i \tag{109}$$

$$\vec{k}_p(n_p^e) = \vec{k}_s(n_s^e) + \vec{k}_i(n_i^o) + \frac{2\pi}{\Lambda}\hat{x}. \tag{110}$$

Periodic poling also makes it possible to achieve phase matching with the pump, signal and idler modes all polarised along the same crystal axis in a process called Type-0 phase matching [136, 138].

In experiment the temperature of the crystal can be tuned in order to change the signal and idler wavelengths which meet the energy conservation condition, and also the angles of emission from the optic axis which meet the momentum conservation condition. At one critical temperature the signal and idler modes are degenerate in wavelength. This temperature dependence changes the phase matching conditions because the refractive indices of the crystal are temperature dependent and change at different rates. The refractive index is described by the Sellmeier equations, with parameters which have been found empirically for different nonlinear materials, including PPKTP. For a PPKTP crystal cut orthogonal to the principal crystal axes, the refractive indices in the y and z directions

n_y						
	A_1	A_2	$A_3/\mu m^2$	$A_4/\mu m^{-2}$		
	2.09930	0.922683	0.0467695	0.0138404		
n_z						
	A	B	$C/\mu m^2$	D	$E/\mu m^2$	$F/\mu m^{-2}$
	2.12725	1.18431	5.14852×10^{-2}	0.6603	100.00507	9.68956×10^{-3}

Table 3: Sellmeier coefficients for PPKTP determined in Refs. [139] and [140].

(perpendicular to the optic axis) are given by the Sellmeier relations:

$$n_y^2(\lambda) = A_1 + \frac{A_2}{1 - A_3/\lambda^2} - A_4\lambda^2 \tag{111}$$

$$n_z^2(\lambda) = A + \frac{B}{1 - C/\lambda^2} + \frac{D}{1 - E/\lambda^2} - F\lambda^2. \tag{112}$$

Here λ is in μm, and the coefficients for PPKTP are determined empirically in Refs. [139] and [140], shown in Table 3.

The temperature dependence comes in through the thermal expansion coefficient of the crystal and the temperature dependent refractive index. Thermal expansion affects the poling period Λ: the crystal length L at temperature T is [141]:

$$L(T) = L(25^\circ C)[1 + \alpha(T - 25^\circ C) + \beta(T - 25^\circ C)^2] \tag{113}$$

where $\alpha = (6.7 \pm 0.7) \times 10^{-6\circ} C^{-1}$ and $\beta = (11 \pm 2) \times 10^{-9\circ} C^{-2}$ from Ref. [141]. The refractive index change due to temperature is given by:

$$\Delta n(\lambda, T) = n_0(\lambda)(T - 25^\circ C) + n_1(\lambda)(T - 25^\circ C)^2 \tag{114}$$

$$n_i(\lambda) = \sum_{j=0}^{3} \frac{a_{ij}}{\lambda^j}. \tag{115}$$

The coefficients a_{ij} are again determined empirically in Ref. [141] and are shown in Table 4.

Bringing everything together, the temperature dependent refractive indices are the values at $25^\circ C$ given by the Sellmeier equations, plus the refractive index change at temperature T. The poling period also changes with thermal expansion. The final expressions are:

$$n_y(\lambda, T) = \left(A_1 + \frac{A_2}{1 - A_3/\lambda^2} - A_4\lambda^2\right)^{\frac{1}{2}} + \left(\sum_{j=0}^{3} \frac{a_{0j}^{(y)}}{\lambda^j}(T - 25^\circ C) + \sum_{j=0}^{3} \frac{a_{1j}^{(y)}}{\lambda^j}(T - 25^\circ C)^2\right) \tag{116}$$

Δn_y				
	a_{i0}	a_{i1}	a_{i2}	a_{i3}
$i=0$ (10^{-6})	6.2897	6.3061	-6.0629	2.6486
$i=1$ (10^{-8})	-0.14445	2.2244	-3.5770	1.3470
Δn_z				
	a_{i0}	a_{i1}	a_{i2}	a_{i3}
$i=0$ (10^{-6})	9.9587	9.9228	-8.9603	4.1010
$i=1$ (10^{-8})	-1.1882	10.459	-9.8136	3.1481

Table 4: Temperature dependence coefficients for the refractive index of PPKTP determined in Ref. [141].

$$n_z(\lambda,T) = \left(A + \frac{B}{1-C/\lambda^2} + \frac{D}{1-E/\lambda^2} - F\lambda^2\right)^{\frac{1}{2}} + \left(\sum_{j=0}^{3} \frac{a_{0j}^{(z)}}{\lambda^j}(T-25^\circ C) + \sum_{j=0}^{3} \frac{a_{1j}^{(z)}}{\lambda^j}(T-25^\circ C)^2\right) \quad (117)$$

$$\Lambda(T) = \Lambda(25^\circ C)[1+\alpha(T-25^\circ C)+\beta(T-25^\circ C)^2]. \quad (118)$$

Another factor to consider is the spatial profile of the signal and idler modes at the output side of the nonlinear crystal. We have to decide where to collect the signal and idler photons to get the desired output state. There are two main cases: collinear, in which the signal and idler mode wavevectors are both along the optic axis and have zero divergence angle, or non-collinear, in which signal and idler photons are emitted at a non-zero angle from the optic axis, resulting in a cone-shaped spatial mode. The emission cones for signal and idler photons overlap at small divergence angles, however in the strongly non-collinear case the emission cones can be at an angle to the optic axis.

The simplest case to calculate is the collinear case, since all wavevectors are along the optic axis and the phase matching condition reduces to a scalar equation. Assuming collinear emission, we can calculate the crystal temperature at which the signal and idler modes are degenerate, T_{deg}. At this temperature, the signal and idler modes on the optic axis are degenerate and become non-degenerate away from the optic axis. If the temperature is now decreased below T_{deg}, the degenerate condition is met at an increasing angle from the optic axis. If the emission was imaged at the output of the crystal through a narrowband (few nm) interference filter, for example on an EMCCD, then the emission profile would change from a single peaked distribution on the optic axis at T_{deg} to a ring

with increasing radius as the temperature is decreased. Note that without spectrally filtering the emission the ring shape will be obscured by non-degenerate photon pairs which meet their phase matching conditions at different angles. As described in the next section, only the collinear case will be relevant to the experimental setup developed in this thesis.

So far this description has all been in terms of classical nonlinear optics. To describe entangled photon pair generation we consider the case where the pump power is relatively low. Interpreting the SPDC process in terms of photons, down-conversion is the conversion of one high energy pump photon into a pair of lower energy signal and idler photons. These signal and idler photons must have energies that sum to the energy of the original pump photon, and their transverse momenta must be equal and opposite to conserve momentum. This gives rise to the phase matching conditions. The output state from the SPDC process can be written in the photon number basis as:

$$|\psi_{SPDC}\rangle = \sqrt{1-\varepsilon}|0\rangle_s|0\rangle_i + \sqrt{\varepsilon}|1\rangle_s|1\rangle_i \tag{119}$$

where $|\rangle_{s,i}$ are the signal and idler modes, and $\varepsilon \ll 1$. In other words, the output state is a vacuum state except for a small fraction of pump photons which are converted into a pair of single photons in the signal and idler modes. This occurs with a small probability ε.

The SPDC process is termed 'spontaneous' parametric down-conversion because the signal and idler modes are initially (at the input side of the nonlinear crystal) in the vacuum state. The annihilation of a pump photon and the creation of signal and idler photons in the nonlinear medium is a spontaneous process which is a consequence of the signal and idler vacuum states having zero-point energy fluctuations. The more general case of parametric down-conversion has input seed fields in the signal and idler modes, so the nonlinear process occurs between optical modes that are already populated with photons. Another case is the optical parametric oscillator (OPO), in which the nonlinear medium is enclosed in an optical cavity so that the input signal and idler modes at both ends of the crystal are already populated with photons. These schemes can be used to produce entangled photon pair sources and are also widely used for sources of squeezed light. The next section will provide more details on the experimental setup required to produce an entangled photon state from a PPKTP crystal by Type-II SPDC.

5.1.2 Entangled Photon Sources using Type-II SPDC

A number of different experimental schemes have been devised for extracting entangled photon pairs from Type-II SPDC in $\chi^{(2)}$ crystals. Since the signal and idler modes have orthogonal polarisations it is possible to make a polarisation entangled state. The signal and idler modes must be separated into two spatial modes such that each output mode has an equal probability of containing a horizontally (H) or vertically (V) polarised

photon from each photon pair. The photons must also be temporally indistinguishable, i.e. there must be no time delay between H and V photons. The birefringence of the PPKTP crystal immediately presents a problem, because H and V polarised photons experience different refractive indices which introduces a time delay between them, and this must be compensated somehow. For HOM interference, the photon pairs must also be spectrally indistinguishable to achieve high interference visibility, for which we must tune the SPDC phase matching conditions to the degenerate condition $\omega_s = \omega_i = \omega_p/2$ using the crystal temperature.

Before describing different experimental schemes for producing polarisation entangled photon pairs, we need metrics for comparing the performance of different entangled photon sources. Common figures of merit for polarisation entangled states are *i.* the two-photon HOM interference visibility, *ii.* coincidence visibility as a function of polarisation analyser angle, *iii.* quantum state fidelity to the target entangled state, and *iv.* entanglement measures such as the *tangle* or *concurrence*. Note there are two different visibilities discussed in the literature: the HOM visibility is the usual two-photon interference visibility, the coincidence visibility is a different quantity which does not involve interference. When the polarisation analyser in one output beam is rotated, the coincidence rate of photon pairs will change sinusoidally. The visibility of these coincidence rate fringes is the coincidence (or correlation) visibility discussed in many papers.

As described in the previous section, the output modes from SPDC may be emitted in either a collinear or non-collinear configuration. In the non-collinear case, output photons are emitted in cones at an angle to the optic axis depending on their momentum. The signal and idler modes can be collected from two points diametrically opposite each other on the output cones since these photons have opposite transverse momenta and orthogonal polarisations. This method allows signal and idler modes to be separated spatially, however has the disadvantage of only using a fraction of the down-converted photons.

Early experiments to produce polarisation entangled states typically used beta-barium borate (BBO) crystals with a Type-II SPDC process in which the signal and idler emission cones are at different angles from the optic axis [142]. This produces two rings at a given wavelength, and photons must be collected from the two points where the rings overlap in order to obtain the polarisation entangled state. Experiments using a non-collinear scheme with PPKTP crystals have demonstrated high quality polarisation-entangled states and high visibility two-photon interference [143, 144, 145]. Jeong et al. [144] achieved a photon pair detection rate of 7 kHz mW^{-1} (91 kHz mW^{-1}) and HOM interference visibility 97.8% (93.6%) for single mode fibre (multimode fibre) coupled output modes. This experiment showed that a broadband multimode diode laser could be used as the pump laser and still demonstrate two-photon interference. The temporal distinguishability of

photon pairs introduced by the crystal birefringence is compensated using a 'universal Bell state synthesizer' scheme, using a prism delay line, a half-waveplate (HWP) in one output mode, and combining the two output modes on a polarising beamsplitter (PBS). Lee et al. [145] achieved a pair detection rate of 4.2 kHz mW^{-1} and HOM interference visibilities >96%, depending on the pump power. This work also uses a delay line, HWP, and PBS to compensate for the temporal distinguishability between photon pairs.

Using a collinear configuration, signal and idler photons are emitted along the pump beam axis. This allows all the generated photons to be collected, however, the signal and idler modes can no longer be separated spatially. Kuklewicz et al. [146] used a 50:50 beamsplitter to separate the signal and idler photons, with a four detector setup to post-select photon pairs. However, this approach loses half of the photon pairs which are not split into the two output modes on the beamsplitter.

One solution to the problem of separating signal and idler modes in the collinear configuration is to put the crystal in a polarising Sagnac loop [147, 148, 134, 149]. The crystal is pumped from both sides with H-polarised pump beams to produce H and V polarised photon pairs travelling clockwise and anticlockwise. A HWP inside the loop rotates the clockwise photon pair from H, V to V, H. A PBS then separates each photon pair into two output modes, with each output mode containing either H or V polarised photons depending on whether they propagated clockwise or anticlockwise around the loop. In this scheme, the temporal distinguishability between photon pairs is erased because clockwise and anticlockwise propagating photon pairs have opposite temporal delays due to the HWP in the loop. In the output modes there is still a time delay between the photons in each pair, but this delay does not provide any information on the polarisation state of the photons.

In Ref. [134], Fedrizzi et al. demonstrate a wavelength tuneable and narrowband emission version of the Sagnac loop scheme. Using a polarising beamsplitter, the clockwise and counterclockwise propagating signal and idler modes in the Sagnac loop can be separated into signal and idler modes at the output, which are in a polarisation entangled state. This setup demonstrates a high photon pair generation rate of 273 kHz $mW^{-1}nm^{-1}$ (82 kHz $mW^{-1}nm^{-1}$ detected) coupled into single mode fibres, and high coincidence visibility over a wide tuning range of signal and idler wavelengths (>97.5% over $\sim$50 nm). It is also possible to use the Sagnac loop setup with non-collinear phase matching, as shown in Ref. [138] where Type-0 quasi-phase matching is used to make co-polarised photon pairs.

These experiments on the Sagnac loop setup are the basis for our entangled photon pair source, which I will describe in the next section. We also use Type-II SPDC in a 25 mm

long PPKTP crystal with a 405 nm pump beam to produce output modes at 810 nm which are tuneable in wavelength. The polarising Sagnac loop setup is particularly well suited to our proposed application to sensing since it is a relatively straightforward setup to develop from scratch (no active stabilisation of optical cavities for example), the signal and idler spectral widths are relatively narrow due to the use of a long crystal, the pair generation rate is high, it is possible to do HOM interference and make two-photon N00N states with degenerate signal and idler photons, and the wide wavelength tuning would be useful for any application involving coupling to a WGM resonator.

Strictly speaking, we do not require a polarisation entangled photon pair state to make N00N states for sensing via HOM interference; a source of indistinguishable photon pairs which can be interfered on a beamsplitter would be sufficient. We developed the Sagnac source firstly to compensate the temporal delay between H and V polarised photons, as an alternative to using a delay line for one polarisation (as discussed above). Secondly, we were able to optimise the purity of the polarisation entangled state before proceeding to HOM interference to increase confidence in our results and in order to develop the methods for characterising quantum optical states in our lab.

5.2 Experimental Setup - Sagnac Loop

Polarisation entangled photon pairs were produced using Type-II SPDC with a 25 mm PPKTP crystal in a Sagnac loop setup. A schematic of the setup is shown in Figure 52. Professor Jolly Xavier designed the setup and sourced all the parts. I built the setup and made any necessary changes as it developed with guidance from Professor Jolly Xavier. Some stages of development are shown in Figure 53.

5.2.1 Description of the Setup

The pump laser is a 405 nm tuneable external cavity diode laser (Toptica) with a linewidth $\sim$ 100 kHz and a power of 20-25 mW after passing through a single mode polarisation maintaining fibre, which also cleans the spatial mode. An optical isolator was added at the input (> 32 dB isolation) because when the Sagnac loop is properly aligned, the pump beam comes back down the optic axis to the laser. The laser power is controlled with a HWP / PBS combination, and the polarisation state is set before each measurement using a QWP and HWP, and measured with a polarimeter. The polarisation angle should be 45° to split the pump beam 50:50 on the Sagnac loop PBS, and the ellipticity is adjusted to change the phase between the two parts of the polarisation entangled state at the output.

The Sagnac loop itself is a triangular loop in the optical path made by a PBS and

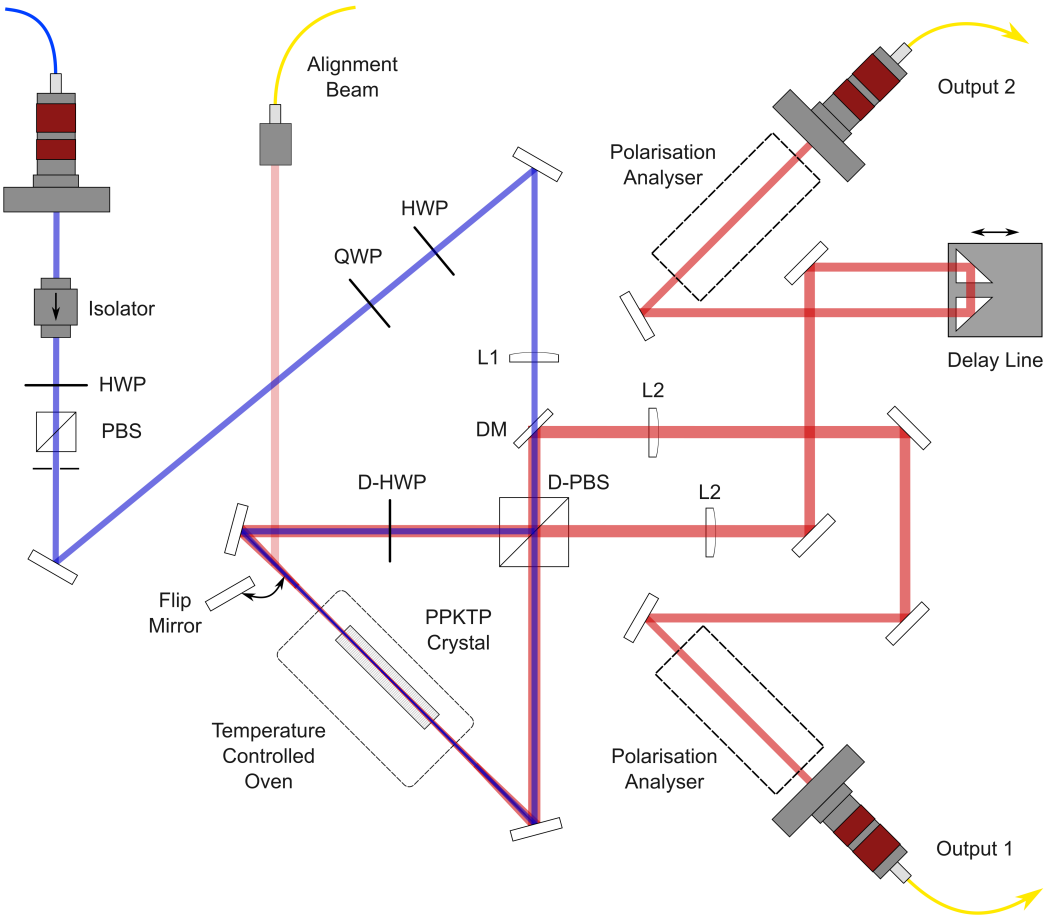

Figure 52: The PPKTP Sagnac loop setup. Input beam is at 405 nm delivered to the setup with a polarisation maintaining single mode fibre. Outputs 1 and 2 are collected into non-polarisation maintaining single mode fibre. Components in the Sagnac loop are coated with dual-band antireflection coatings for 405 nm and 810 nm. HWP: half waveplate, QWP: quarter waveplate, L1,2: f = 300 mm lenses, DM: dichroic mirror, PBS: polarising beamsplitter, D-PBS: dual-wavelength polarising beamsplitter, D-HWP: dual-wavelength half waveplate.

two mirrors. The PBS is a custom-made component which is dual-band anti-reflection coated for 405 nm and 810 nm. The PPKTP crystal ($1\times2\times25$ mm^3, Raicol Crystals) inside a temperature controlled oven is placed inside the Sagnac loop. The pump beam is focused into the centre of the crystal by lens L1 (plano-convex, f = 300 mm). A HWP in the loop (also dual-band anti-reflection coated for 405 nm and 810 nm) is set to rotate polarisations H→V and V→H. In the input beam there is a dichroic mirror (DM) (transmitting < 650 nm) such that the pump beam is transmitted but the down-converted modes at 810 nm will be reflected. When the pump beam enters the loop there are two modes: a clockwise H polarised mode and an anticlockwise V polarised mode. These two modes propagate as follows:

Clockwise mode. The H polarised pump beam produces H and V polarised signal and idler modes (H_s, V_i), respectively. These are rotated by the HWP to V_s, H_i. The signal mode is reflected at the PBS and DM to enter output 2. The idler mode is transmitted at the PBS to enter output mode 1.

Anticlockwise mode. The V polarised pump beam is rotated to H polarisation by the HWP. This produces signal and idler modes V_s, H_i. The signal mode is reflected at the PBS to enter output mode 1. The idler mode is transmitted at the PBS and reflected by the DM to enter output mode 2.

Therefore output mode 1 contains only signal photons of either H or V polarisation, and output mode 2 contains only idler mode photons of either H or V polarisation. We also see that the remaining pump beams in both the clockwise and anticlockwise modes pass back into the input beam path and are blocked by the optical isolator. Since the PBS and DM do not have a perfect extinction ratios, some of the pump beam enters outputs 1 and 2 and must be blocked by notch filters for 405 nm (OD > 6, Semrock).

The output modes are collected by two plano-convex lenses, L2 (f = 300 mm) and zoom fibre collimators to couple the modes into two single mode optical fibres. Each output beam has a polarisation analyser consisting of a QWP, HWP, and linear polariser. Output mode 2 has a delay line made with two anti-reflection coated corner prisms mounted on a translation stage. This is to control the optical path delay between the two modes which is essential for HOM interference. A 1D piezo stage was added to the delay line to enable fine control.

The output fibres are connected to two fibre coupled single photon detectors. The detectors for this setup are the same single photon avalanche diodes (SPADs) used for the hBN setup. At the expected down-conversion wavelength of 810 nm their detection efficiency is approximately 15%. The ID900 Time Controller is used for time-to-digital

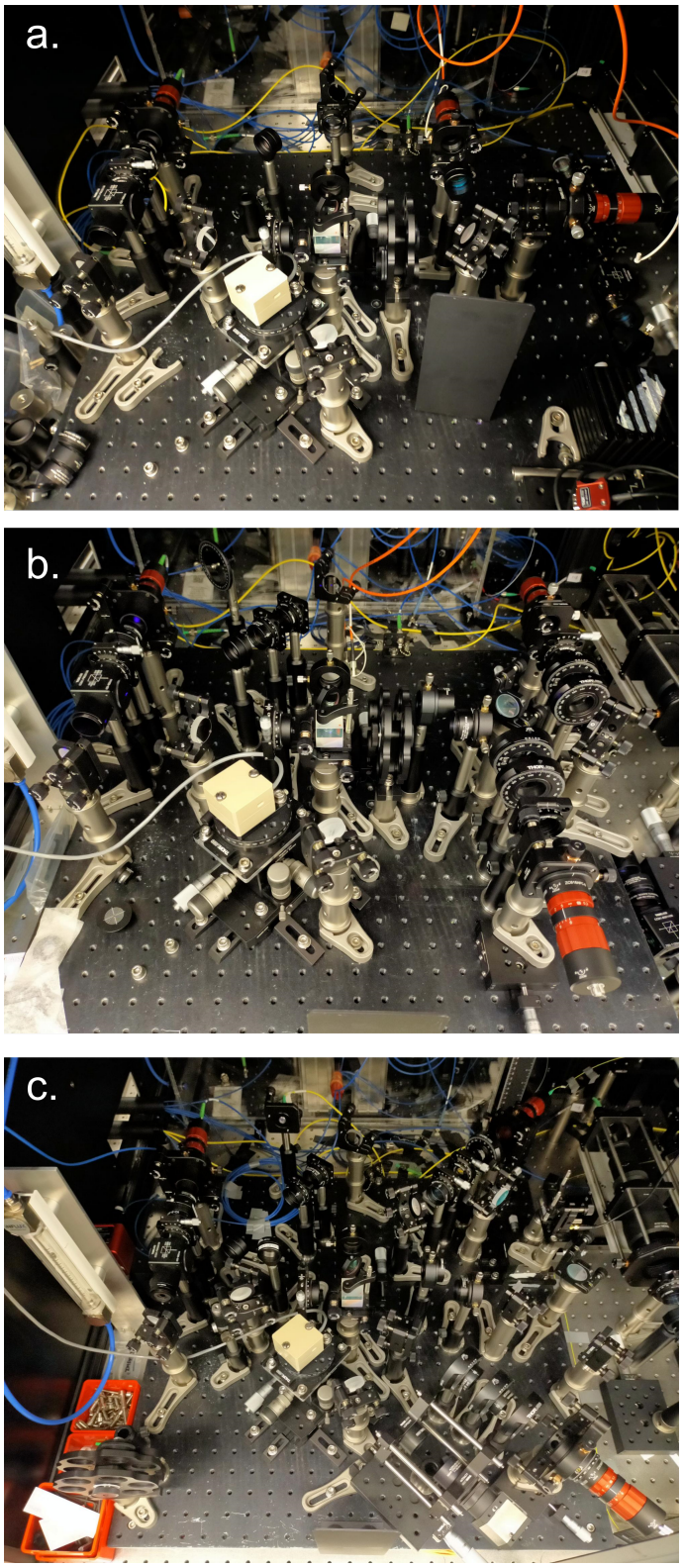

Figure 53: Stages of developing the PPKTP setup. (a) Basic setup to collect signal and idler modes into multimode fibres. (b) Addition of lenses (L2) to the collection optics and polarisation analysers (QWP, HWP, linear polariser) in each output beam. (c) The final setup including a delay line for HOM interference measurements.

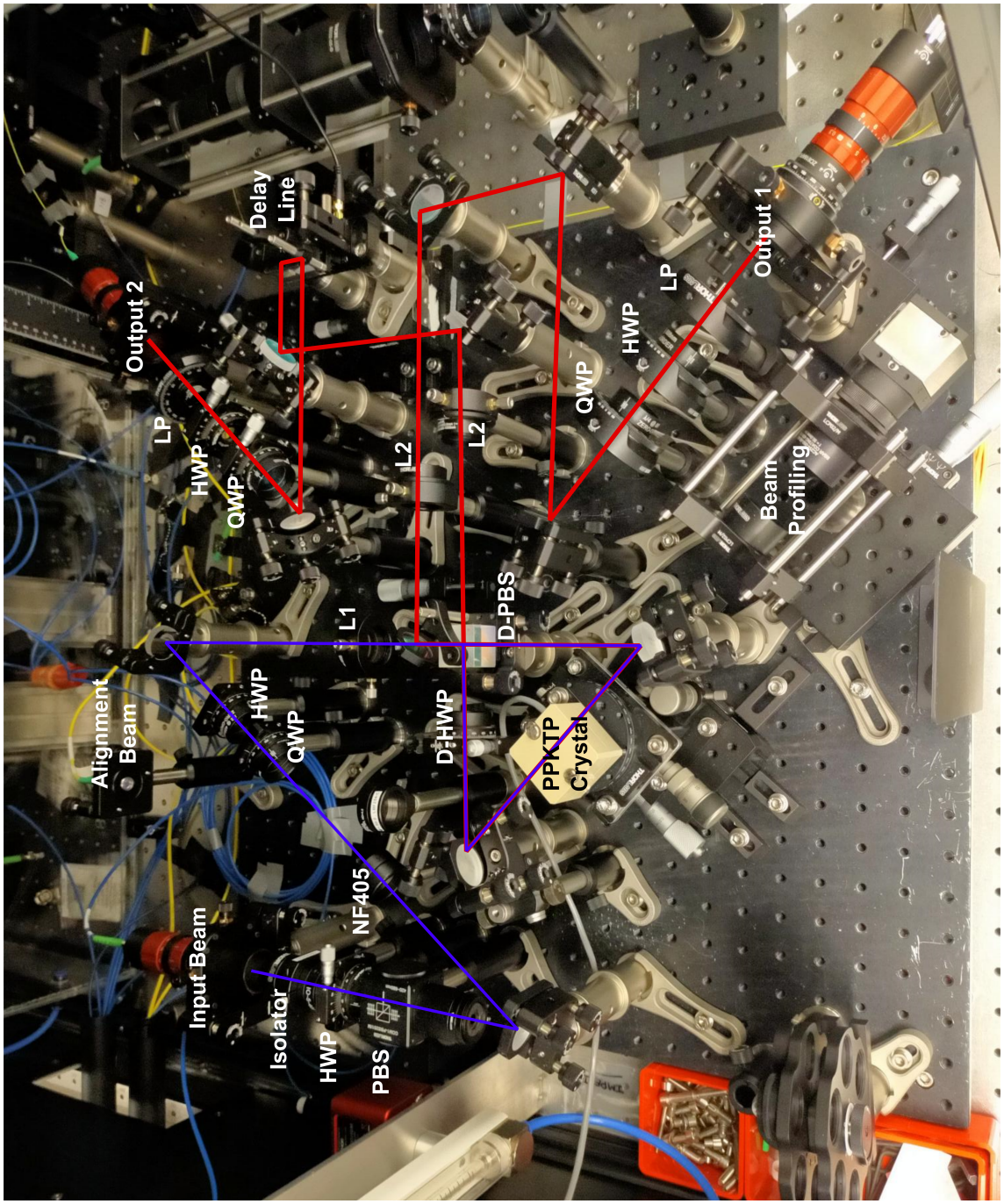

Figure 54: The final PPKTP setup showing the beam paths and components. Components in the Sagnac loop are coated with dual-band antireflection coatings for 405 nm and 810 nm. HWP: half waveplate, QWP: quarter waveplate, L1,2: f = 300 mm lenses, DM: dichroic mirror, PBS: polarising beamsplitter, D-PBS: dual-wavelength polarising beamsplitter, D-HWP: dual-wavelength half waveplate, BP400: bandpass filter at 400 nm. There are also notch filters blocking 405 nm before the two output fibre couplers to prevent any remaining pump beam going to the detectors.

conversion of photon detections and photon correlation measurements.

A photo of the final setup with the beam paths and components marked is shown in Figure 54. The alignment beam is from an 810 nm laser and was added for experiments on HOM interference which are discussed later in this chapter. A flip mirror in the Sagnac loop is used to direct the alignment beam onto outputs 1 and 2 to test the interference visibility at 810 nm.

5.2.2 Beam Profiles and Focusing Conditions

Efficient SPDC in the collinear configuration requires the optimum focusing conditions for the pump beam and the collection optics. Fedrizzi et al. have made a thorough investigation of the optimum focusing conditions for a PPKTP crystal in the Sagnac loop setup [134]. For our 25 mm long crystal the pump beam should have a waist radius of 26 μm to maximise the efficiency of producing photon pairs. The optimum beam waist radius is a trade-off between having a high optical intensity at the focus to increase the SPDC efficiency, and using a larger volume of the crystal for the SPDC process.

The optics collecting the signal and idler beams should also be focused on the middle of the PPKTP crystal. The focusing conditions of the output beams can be found by propagating a laser beam at 810 nm back through the output paths and into the crystal. These output beams have an optimum waist radius of 32 μm for maximum collection efficiency [134].

The beam profiles of the pump beam and 810 nm beams back-propagated through output modes 1 and 2 were measured using a 2f imaging setup with a CCD camera. This is shown in Figure 54. By removing one mirror from the Sagnac loop and moving the PPKTP crystal out of the beam path, the image plane of the beam profiler is at the position of the crystal and can be moved 26 mm with a translation stage. The intensity profile of the beam on the CCD is fitted using a 2D Gaussian function at each z position along the beam path to find the beam radius $w(z)$.

The beam profile is then fitted with the function:

$$w(z) = w_o \sqrt{1 + \frac{(z - z_o)^2}{z_R^2}} \tag{120}$$

where w_o is the beam waist radius, z_o is the z-position of the beam waist, and z_R is the Rayleigh range. For each beam the beam waist position was adjusted by moving the f = 300 mm lens (L1 or L2 in Figure 54), and the beam waist radius by changing the beam size using the zoom fibre collimators. The beams produced from the single mode

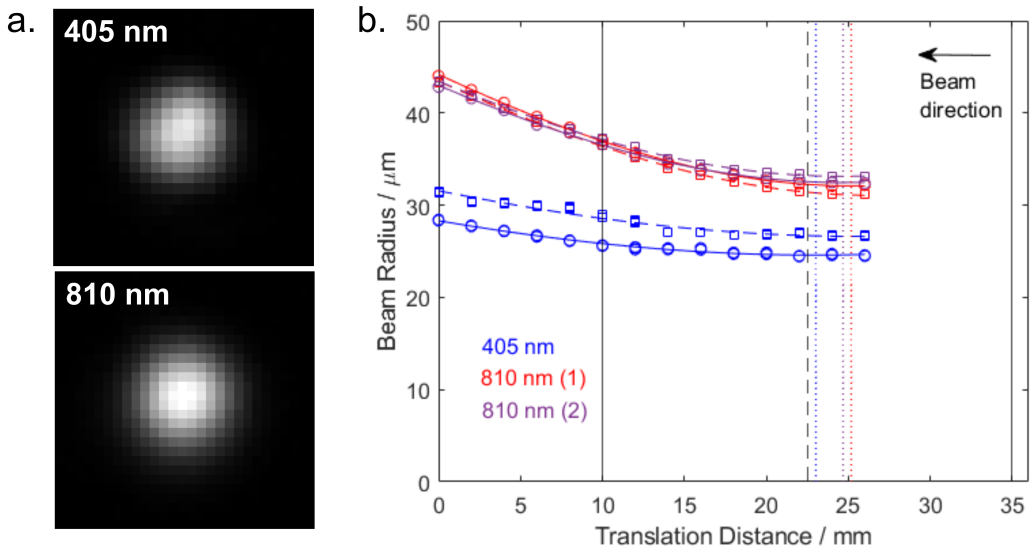

Figure 55: Beam profiles in the PPKTP crystal. (a) CCD images of the 405 nm and 810 nm beams showing a symmetric Gaussian shape. (b) Beam profiles against translation distance of the beam profiler, fitted with a Gaussian beam profile. Blue points are the beam radii of the pump beam (405 nm), and red and purple for the output beams (810 nm). The radii along the x direction are the circles and solid lines, y radii are the squares and dashed lines. There is a small amount of ellipticity for the pump beam: the difference between x and y beam radii is $< 8\%$.

optical fibres were very clean, however the optical isolator introduced some distortion to the pump beam which had to be corrected by slightly moving the isolator position until the intensity profile was Gaussian. The beam profiles for each beam along the optic axis z are shown in Figure 55. The final beam waist radii were $w_x = 24.6\ \mu$m and $w_y = 26.6\ \mu$m for the pump beam, $w_x = 32.1\ \mu$m and $w_y = 31.1\ \mu$m for output 1, and $w_x = 32.4\ \mu$m and $w_y = 33.1\ \mu$m for output 2. These radii are close to the target values of 26 μm for the pump beam and 32 μm for the output beams.

The beam profiles measured in free space are not the same as the profiles when the PPKTP crystal is placed in the optical path due to the high refractive index of the crystal. In a dielectric medium, the focal position is displaced in the propagation direction as described by Nemoto [150]. However, the beam waist radius is unchanged so that our measured beam waist radii and the target values from [134] are the same in free space and inside the PPKTP crystal.

5.2.3 Custom Grating Spectrometer using EMCCD

The count rate of the down-converted light from our crystal was far below the noise level of our optical spectrum analyser (OSA). To measure the spectra of the output modes, we built a custom fibre-coupled spectrometer using a diffraction grating and an electron multiplying charge coupled device (EMCCD) camera (Andor iXon Ultra 888, Oxford Instruments). The setup is shown in Figure 56. I worked together with Dr Samir Vartabi Kashanian to design and build the spectrometer.

A beam from a single mode fibre is collimated onto a diffraction grating and the first order diffracted beam is focused onto the EMCCD pixel array. We selected a diffraction grating with 1200 lines mm^{-1} and a blaze wavelength of 750 nm, to give high diffraction efficiency at the target wavelength 810 nm. The maximum possible beam width was used to fill a large area of the grating.

The spectrometer was calibrated using a highly attenuated beam from a tuneable external cavity diode laser at 765-815 nm. The laser beam was focused onto one EMCCD pixel with an f = 30 mm lens. As the laser wavelength is tuned, the focused beam scans across the EMCCD sensor because the diffraction grating angle is fixed. By measuring the wavelength precisely using a wavemeter, the EMCCD pixel position was calibrated to wavelength with a precision of $\sim$0.1 nm. The pixel-wavelength relation was very close to linear over a range of 800-815 nm; an example calibration plot is shown in Figure 57.

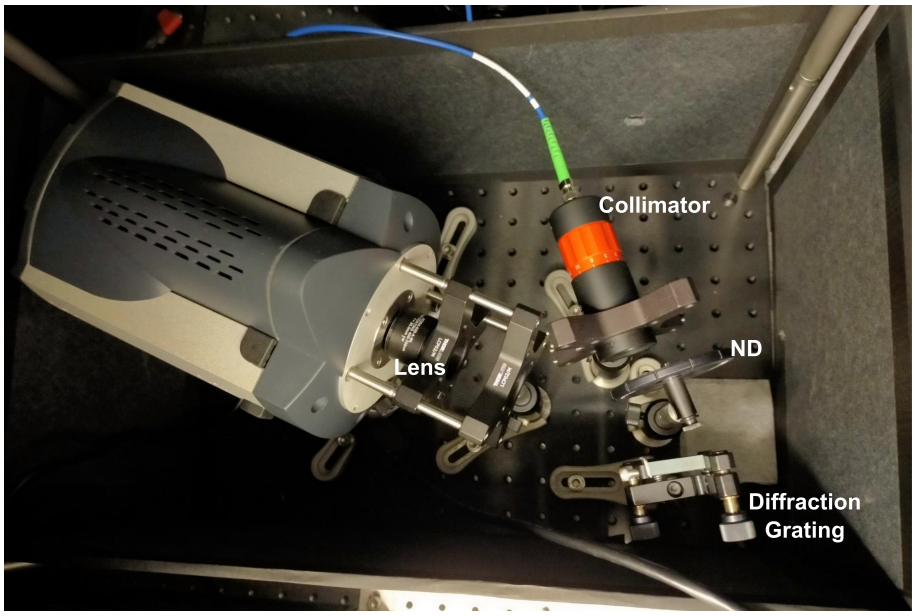

Figure 56: Diffraction grating spectrometer using EMCCD. A beam from a single mode optical fibre (in the final design this was not polarisation maintaining) is collimated onto a diffraction grating (1200 lines mm^{-1}, blaze wavelength 750 nm) and the first order diffracted beam is focused onto an EMCCD pixel array. ND: variable neutral density filter, Lens: f = 30 mm.

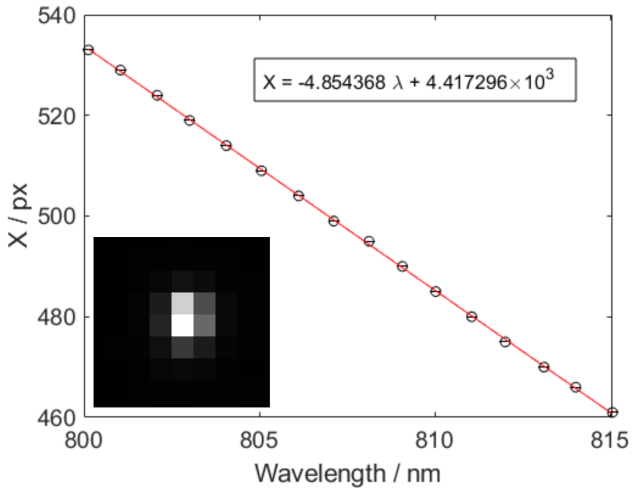

Figure 57: Calibration plot of EMCCD pixel number X to laser wavelength λ. The calibration was done with a highly attenuated tuneable laser over the range 800-815 nm. Inset: EMCCD image of the laser beam showing it is focused onto one pixel by the f = 30 mm lens.

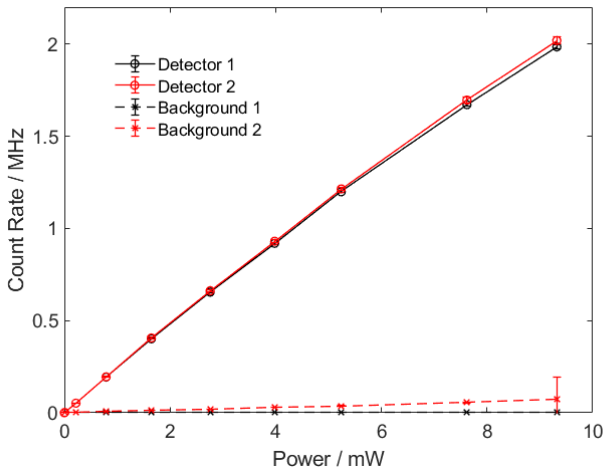

Figure 58: Count rates against pump power using multimode fibre to collect the output modes. Black and red solid lines are the count rates on detectors 1 and 2, dashed lines are the background counts due to the pump beam leaking into the outputs, measured using a bandpass filter at 400 nm, bandwidth 40 nm.

5.3 Photon Pairs from SPDC Process

5.3.1 Count Rate and Coincidence Rate

The first task was to detect down-converted photons from the PPKTP crystal on the single photon detectors, while filtering out the strong pump beam. Initially a basic setup was used with no polarisation analysers in the output beams and the outputs coupled to multimode fibres with 50 μm core diameter (e.g. Figure 53(a)). Notch filters blocking 405 nm with a bandwidth of 10 nm and optical density OD > 6 (Semrock) were placed in each output beam to block the remaining pump light from the crystal. In this configuration up to 2 MHz count rates were recorded on the detectors for the maximum pump power of 9.3 mW. The count rate against pump power is shown in Figure 58. To confirm these counts are from down-conversion and not the pump beam leaking through the filters, a bandpass filter at 400 nm with 40 nm bandwidth was added to each output. This is the 'background' count rate in Figure 58. Less than 4% of the counts were transmitted by the bandpass filter and therefore due to the pump beam, so we can conclude that the MHz count rates detected are down converted photons coming from the SPDC process in the PPKTP crystal.

Now we must confirm that the down-converted photons arrive as photon pairs at the detectors. The cross-correlation function $g^{(2)}(\tau)$ between the two detectors was measured using the ID900 Time Controller. Coincidence histograms are shown in Figure 59. The large peak at $\tau = 0$ shows that photon arrival times in the two output modes are correlated within around 400 ps. The smaller peaks near ± 50 ns are due to reflections in the multi-

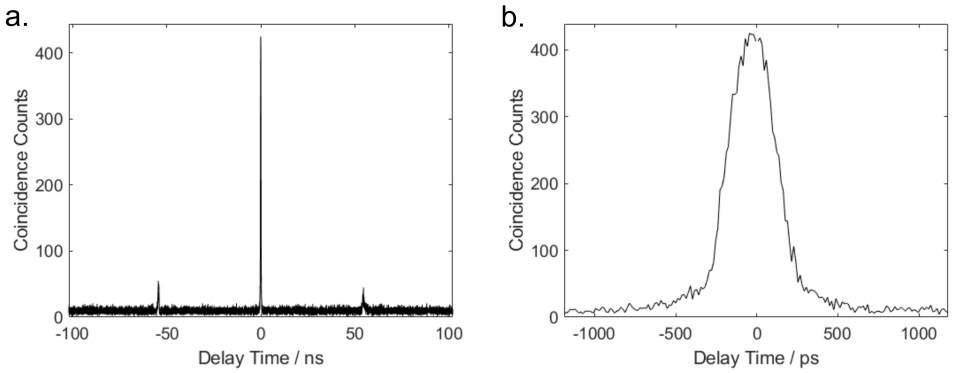

Figure 59: Cross correlation function $g^{(2)}(\tau)$ between the two output modes collected through multimode fibres. (a) $g^{(2)}(\tau)$ showing large peak at $\tau = 0$ due to correlated arrival times of photon pairs, and smaller peaks near ± 50 ns due to reflections in the multimode fibre. (b) Zoom-in of the central peak showing photon pairs arrive simultaneously to within 400 ps.

mode fibres, as in the experiments on hBN. The detected coincidence rate, or photon pair detection rate, is found by integrating the coincidence counts in the peak of the $g^{(2)}(\tau)$ function.

In the final version of the setup (as in Figures 53(c) and 54), the output beams were coupled to single mode fibres (Thorlabs, SM780Y, APC connectors). The count rates were significantly lower through single mode fibre, however these fibres maintain a single spatial mode which is essential for HOM interference later. Also, the APC connectors eliminate the back reflections seen in multimode fibre. The $g^{(2)}(\tau)$ function using single mode fibres is shown in Figure 60(a). This was also measured after the pump laser diode was replaced, resulting in a narrower pump spectrum. Compared to the multimode case, the $g^{(2)}(\tau)$ peak width is narrower at around 100 ps.

The output fibre couplers had to be very carefully aligned to couple the maximum photon pair rate while balancing the rates of $|HV\rangle$ and $|VH\rangle$ states. Figure 60(b) shows the count rates at each output and the coincidence rate in the $|DD\rangle$ basis (i.e. diagonal polarisation: projecting both parts of the entangled state), after optimising the output coupling with single mode fibres. Note that the maximum pump power was lower in this measurement because the optical isolator had been adjusted to improve the pump laser beam profile at the expense of the transmission efficiency.

5.3.2 Emission Spectrum and Temperature Tuning

Using the custom built grating spectrometer introduced earlier, the spectra of the signal and idler modes could be measured to a resolution of 0.1 nm. The output modes were

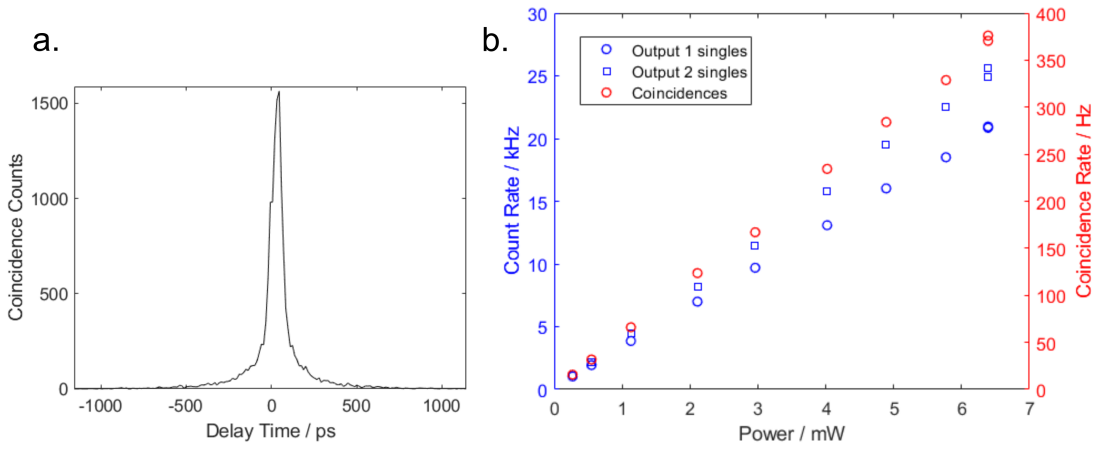

Figure 60: Coincidence rate of photon pairs using the final version of the setup with single mode fibres. (a) $g^{(2)}(\tau)$ function between the two output modes measured in the $|HV\rangle$ basis. (b) Singles count rate for outputs 1 and 2 (blue circles and squares, respectively), and coincidence rate (red circles) as a function of the total pump power, measured in the $|DD\rangle$ basis.

connected to the spectrometer with single mode optical fibres. Typical count rates in each mode were around 30 kHz, this was easily visible on the EMCCD in the spectrometer, with typical parameters being EM gain 300, acquisition time 0.5 s, and with the sensor cooled to -60°C. The output mode would be focused onto a line of pixels, which were converted from pixel number in the x direction to wavelength using the calibration procedure described earlier in this chapter. The spectrometer was always calibrated using the same single mode fibre used to measure spectra to avoid changing the alignment of the spectrometer setup.

The initial results for temperature tuning the signal and idler modes are shown in Figure 61. At this point in the experiments, the pump laser spectrum was multimode with four peaks over a width of around 0.6 nm. This produced multiple peaks in the signal and idler modes seen in Figure 61(b). For later experiments the pump laser diode was replaced and the laser was returned to proper single mode emission. Still, taking the peak wavelength for each output mode, the wavelength change with temperature is linear as expected. The output modes are degenerate at 26°C, so this temperature was used for all measurements in the first attempt at HOM interference.

After replacing the pump laser diode and ensuring its spectrum was single mode, the output spectra of the signal and idler modes were as shown in Figure 62. The spectra are now single peaked with an average FWHM linewidth of 0.8 nm, and the two modes are degenerate at 31.0^{o}C. Figure 62 shows good overlap between the signal and idler spectra at 31.0^{o}C. Note that the pump wavelength was slightly increased to 405.0 nm which in-

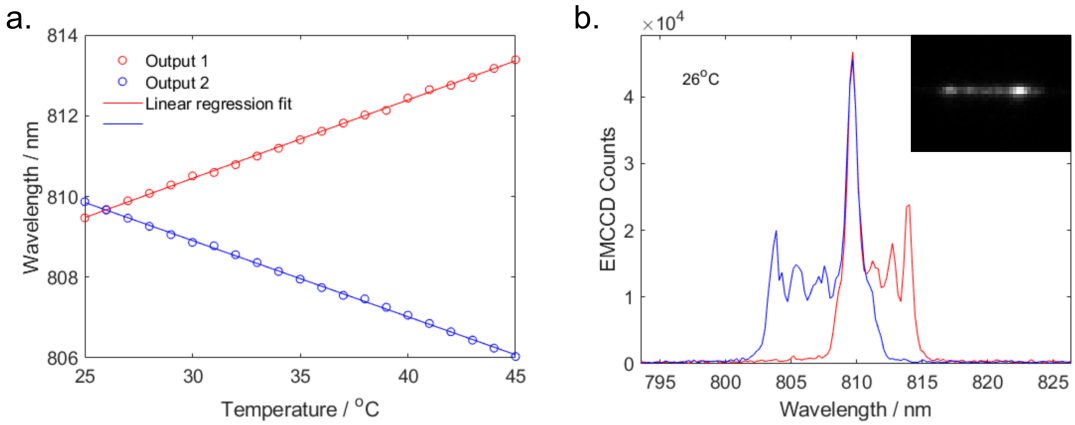

Figure 61: Temperature tuning the signal and idler mode wavelengths. (a) The maximum wavelengths from outputs 1 and 2 are tuned by changing the PPKTP crystal temperature. The output modes are degenerate at 26°C. (b) Spectra from outputs 1 and 2 measured on the EMCCD spectrometer at 26°C. There are multiple peaks in the spectrum over a range of more than 5 nm due to the broad multimode spectrum of the pump laser at the time of this measurement. The peak wavelength is the wavelength shown in the left panel. Inset shows the spectrum for one output mode as seen on the EMCCD.

creased the degenerate temperature compared to the measurement in Figure 61.

5.4 Quantum State Tomography on Polarisation Entangled Photon Pairs

To completely determine the output state from our setup we need to do quantum state tomography. This is the process by which the density matrix of the state in a given basis is reconstructed from a set of coincidence rate measurements. From the density matrix the quantum state can be uniquely determined, in this case in the two-photon polarisation basis. In this section I follow the method for quantum state tomography described by James et al. [151].

I will discuss two approaches, so called linear tomography and maximum likelihood tomography. Linear tomography is instructive for understanding how the experimental measurements are transformed into a density matrix, however experimental errors can cause this method to produce density matrices that are unphysical. The maximum likelihood approach starts with a density matrix that is physically allowed by construction, then fits this density matrix to the experimental data by maximising a suitable likelihood function.

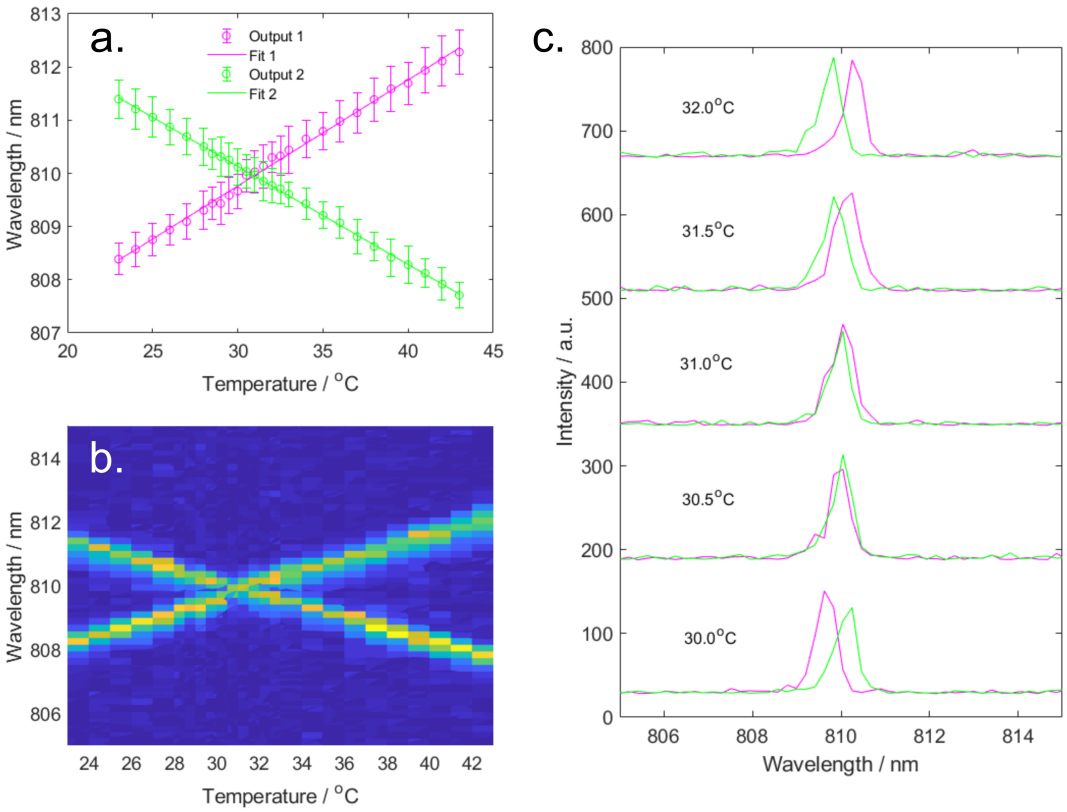

Figure 62: Temperature tuning of the signal and idler mode wavelengths after improving the pump laser spectrum. (a) Central wavelengths at outputs 1 and 2 as a function of crystal temperature, error bars indicate standard deviation of Gaussian fit to the spectral peak. Linear regression fit shows the wavelengths are degenerate at 31.0^{o}C. (b) Surface plot showing the measured spectra at each temperature. (c) Comparison of output 1 (magenta) and output 2 (green) spectra around the degenerate temperature, showing complete overlap.

Firstly the measurements: tomography requires a complete set of projection measurements on the polarisation states of the photon pairs. The basis for our density matrix will be the horizontal and vertical polarisation states for the signal and idler modes:

$$\begin{pmatrix} |H\rangle \\ |V\rangle \end{pmatrix}_s \otimes \begin{pmatrix} |H\rangle \\ |V\rangle \end{pmatrix}_i = \begin{pmatrix} |H\rangle_s|H\rangle_i \\ |H\rangle_s|V\rangle_i \\ |V\rangle_s|H\rangle_i \\ |V\rangle_s|V\rangle_i \end{pmatrix}. \tag{121}$$

The resulting 4×4 density matrix requires a minimum of 16 projection measurements to form a complete set. There is no unique set of measurements, the 16 measurements used in this thesis are the ones used in Ref. [151]. For each measurement basis the coincidence counts are measured for a fixed time. The measurement basis is chosen using the polarisation analysers in each output beam. The projection measurements are listed in Table 5 with the half waveplate ($h_{s,i}$) and quarter waveplate ($q_{s,i}$) angles required for each measurement. Superpositions of the H and V polarisation states are also used: diagonally polarised $|D\rangle = (|H\rangle + |V\rangle)/\sqrt{2}$, right circular polarised $|R\rangle = (|H\rangle - i|V\rangle)/\sqrt{2}$, and left circular polarised $|L\rangle = (|H\rangle + i|V\rangle)/\sqrt{2}$.

The measurement gives us 16 coincidence counts n_ν ($\nu = 1,2...16$) which are related to the density matrix by:

$$n_\nu = N\langle\psi_\nu|\hat{\rho}|\psi_\nu\rangle \tag{122}$$

where N is a constant containing the photon pair emission rate and detection efficiency. Following the derivation for linear tomography in Ref. [151], the density matrix can be reconstructed from n_ν by a weighted sum of a set of 4×4 matrices $\hat{M}_\nu$:

$$\hat{\rho} = \frac{\sum_{\nu=1}^{16} \hat{M}_\nu n_\nu}{\sum_{\nu=1}^{4} n_\nu}. \tag{123}$$

The matrices $\hat{M}_\nu$ are listed in the Appendix B in Ref. [151][4]. The density matrix is normalised by the constant $N = \sum_{\nu=1}^{4} n_\nu$. Using Equation (123) we can quickly estimate the density matrix from the experimental data. However, as stated earlier the resulting density matrix is not necessarily physical due to experimental errors, i.e. the matrix may not be positive semidefinite as required for a physical density matrix. To ensure the density matrix is physical, we must instead fit a model for the density matrix to the data using a maximum likelihood method.

The maximum likelihood method begins with constructing a parameterised density matrix which is positive semidefinite, normalised, and Hermitian by construction. The

[4]Note that there are typos in $\hat{M}_2$ and $\hat{M}_{14}$. In $\hat{M}_2$, row 4, column 2 should be $-(1-i)$. In $\hat{M}_{14}$, row 2, column 3 should be $(1-i)$ and row 3, column 2 should be $(1+i)$. These matrices can be checked against Equation (B3) in the Appendix of James et al. [151].

ν	State $\lvert\psi_\nu\rangle$	h_s	q_s	h_i	q_i
1	$\lvert H\rangle_s\lvert H\rangle_i$	45°	0	45°	0
2	$\lvert H\rangle_s\lvert V\rangle_i$	45°	0	0	0
3	$\lvert V\rangle_s\lvert V\rangle_i$	0	0	0	0
4	$\lvert V\rangle_s\lvert H\rangle_i$	0	0	45°	0
5	$\lvert R\rangle_s\lvert H\rangle_i$	22.5°	0	45°	0
6	$\lvert R\rangle_s\lvert V\rangle_i$	22.5°	0	0	0
7	$\lvert D\rangle_s\lvert V\rangle_i$	22.5°	45°	0	0
8	$\lvert D\rangle_s\lvert H\rangle_i$	22.5°	45°	45°	0
9	$\lvert D\rangle_s\lvert R\rangle_i$	22.5°	45°	22.5°	0
10	$\lvert D\rangle_s\lvert D\rangle_i$	22.5°	45°	22.5°	45°
11	$\lvert R\rangle_s\lvert D\rangle_i$	22.5°	0	22.5°	45°
12	$\lvert H\rangle_s\lvert D\rangle_i$	45°	0	22.5°	45°
13	$\lvert V\rangle_s\lvert D\rangle_i$	0	0	22.5°	45°
14	$\lvert V\rangle_s\lvert L\rangle_i$	0	0	22.5°	90°
15	$\lvert H\rangle_s\lvert L\rangle_i$	45°	0	22.5°	90°
16	$\lvert R\rangle_s\lvert L\rangle_i$	22.5°	0	22.5°	90°

Table 5: Set of projection measurements used for quantum state tomography, and the corresponding half waveplate and quarter waveplate angles of the signal (s) and idler (i) output polarisation analysers. Based on the projection measurements chosen in Ref. [151].

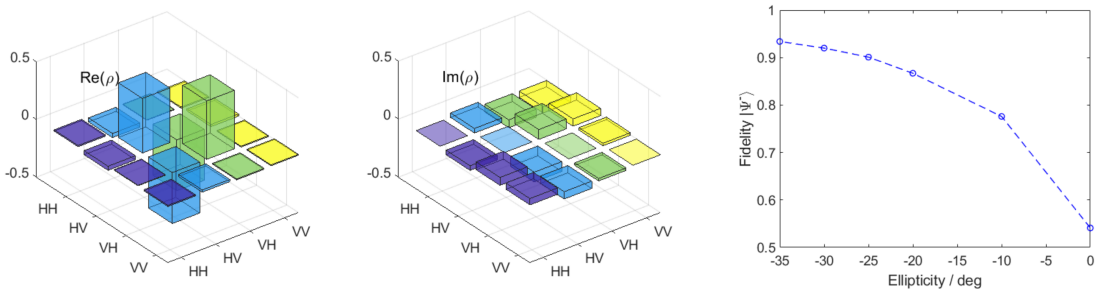

Figure 63: Real and imaginary parts of the density matrix from the PPKTP entangled photon pair source. The pump beam was polarised at 45° with an ellipticity -35° (left elliptical polarisation). The right panel shows the fidelity compared with the quantum state $|\psi^-\rangle$ increases as the pump beam is made more elliptical.

physical density matrix $\hat{\rho}_p$ satisfies these conditions if it is defined as:

$$\hat{\rho}_p(t) = \frac{\hat{T}^\dagger(t)\hat{T}(t)}{\mathrm{Tr}\{\hat{T}^\dagger(t)\hat{T}(t)\}} \tag{124}$$

where the matrix $\hat{T}(t)$ is parameterised by $t = (t_1, t_2 ... t_{16})$:

$$\hat{T}(t) = \begin{pmatrix} t_1 & 0 & 0 & 0 \\ t_5 + it_6 & t_2 & 0 & 0 \\ t_{11} + it_{12} & t_7 + it_8 & t_3 & 0 \\ t_{15} + it_{16} & t_{13} + it_{14} & t_9 + it_{10} & t_4 \end{pmatrix}. \tag{125}$$

By assuming the error in the measured data is Gaussian distributed, a likelihood function can be defined for the likelihood that the physical density matrix $\hat{\rho}_p(t)$ produces the measured data $\{n_1, n_2 ... n_{16}\}$. After taking the logarithm of the likelihood function, maximising the likelihood is equivalent to minimising the function $L(t)$ with respect to the parameters $t = (t_1, t_2 ... t_{16})$ [151]:

$$L(t) = \sum_{v=1}^{16} \frac{[N\langle\psi_v|\hat{\rho}_p(t)|\psi_v\rangle - n_v]^2}{2N\langle\psi_v|\hat{\rho}_p(t)|\psi_v\rangle}. \tag{126}$$

The minimum of $L(t)$ was found using the MATLAB *fminsearch* function. The initial values of the parameters t were taken from the linear tomography density matrix by inverting the matrix using the relation given in Ref. [151].

There was generally only a very small discrepancy between the density matrix results using the linear tomography and maximum likelihood methods. However, the maximum likelihood method was always used for final results since it always gives a physically allowed density matrix.

The main measure we will use to assess the quality of the output polarisation entangled state is the quantum state fidelity F. The fidelity for comparing a measured density matrix $\hat{\rho}_{expt}$ with the target state $|\psi_{target}\rangle$ is given by:

$$F = \langle \psi_{target} | \hat{\rho}_{expt} | \psi_{target} \rangle. \tag{127}$$

So that the fidelity is 1 (or 100%) when the density matrix perfectly matches the target state. The polarisation entangled state generally has a phase difference θ between the two terms:

$$|\psi(\theta)\rangle = \frac{1}{\sqrt{2}} \left(|H\rangle|V\rangle + e^{i\theta} |V\rangle|H\rangle \right). \tag{128}$$

In our experiment we aimed for the Bell states $|\psi^{\pm}\rangle$:

$$|\psi^{\pm}\rangle = \frac{1}{\sqrt{2}} \left(|H\rangle|V\rangle \pm |V\rangle|H\rangle \right). \tag{129}$$

Figure 63 shows the real and imaginary parts of the density matrix for a polarisation entangled state with $F = 93.4\%$ ($|\psi^{-}\rangle$). The density matrix can be tuned by varying the pump beam polarisation. The polarisation azimuth should ideally be along 45° to put equal optical power in the clockwise and anticlockwise pump beams, but the ellipticity changes the phase θ between the two terms of the entangled state. However, we found that when the output couplers were aligned to maximise coincidence counts in the diagonal basis ($|DD\rangle$), there was generally an imbalance in coincidence counts in the $|HV\rangle$ and $|VH\rangle$ bases. This could be compensated by rotating the pump beam polarisation azimuth to change the relative power in the clockwise and anticlockwise pump beams.

As an example, in the experimental run shown in Figure 63, the fidelity was maximised for an ellipticity of -35° (left elliptical polarisation). Both the $|\psi^{-}\rangle$ and $|\psi^{+}\rangle$ states were realised with different settings of the input beam polarisation, as shown in Figure 64, with fidelities of $F = 94.7\%$ for $|\psi^{-}\rangle$ and $F = 98.9\%$ for $|\psi^{+}\rangle$. Note that the polarisation required for each state also depends on the exact alignment of the output fibre couplers, so the polarisation was optimised for a given state after each time the alignment was changed.

5.5 HOM Interference

The main aim of developing the PPKTP polarisation entangled photon pair source was to produce path entangled photon states, i.e. two-photon N00N states. To do this we need to interfere photon pairs using the HOM effect.

A schematic of the HOM setup at the output of the entangled photon pair source is shown in Figure 65. The two output modes in single mode fibres are coupled to a 50:50 single mode fibre beamsplitter, then fibre coupled to the SPAD detectors. One of the

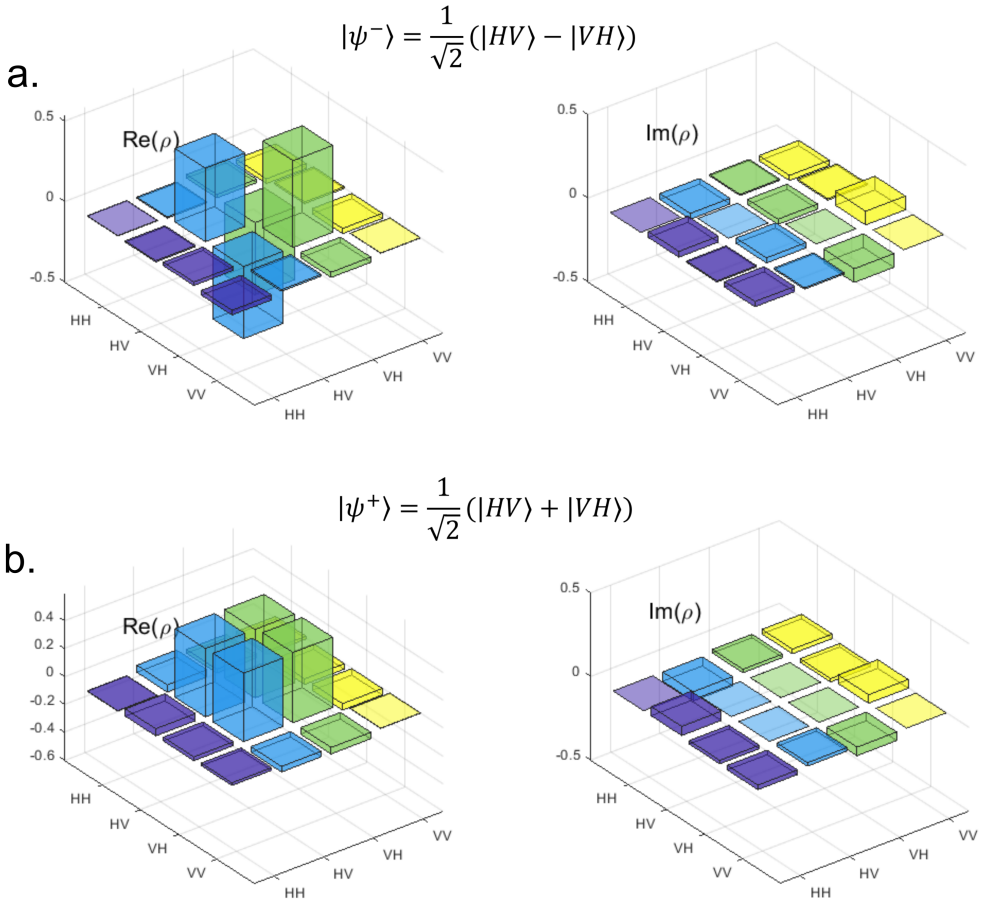

Figure 64: Examples of density matrices produced from the PPKTP entangled photon pair source. (a) Real and imaginary parts of the density matrix for the $|\psi^-\rangle$ state with fidelity $F = 94.7\%$. (b) Density matrix for the $|\psi^+\rangle$ state with fidelity $F = 98.9\%$. These two different polarisation entangled states were achieved by changing the polarisation angle and ellipticity of the input pump beam.

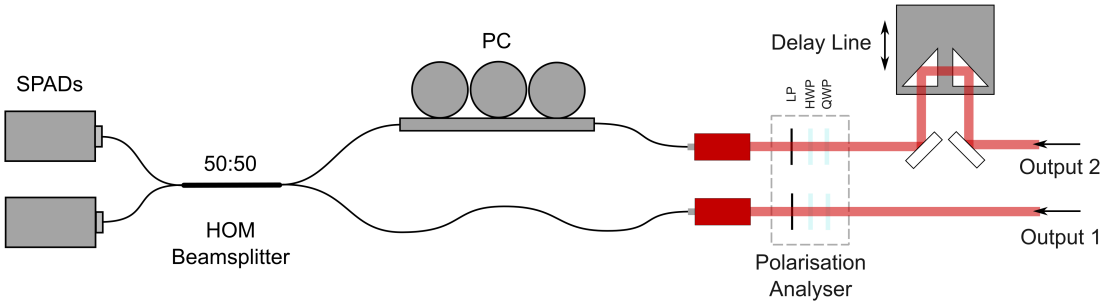

Figure 65: Schematic of the setup for HOM interference at the output of the PPKTP polarisation entangled photon pair source. Outputs 1 and 2 represent the two outputs shown in Figure 52. A polarisation analyser in each output beam is made up of a quarter waveplate (QWP), half waveplate (HWP), and linear polariser (LP). PC: polarisation controller, SPAD: single photon avalanche diode.

output fibres is in a fibre polarisation controller (PC), so that the polarisations of the two modes can be matched before the HOM beamsplitter. The delay line in the output 2 beam path controls the time delay between photons arriving at the beamsplitter.

For the first attempt at the HOM measurement, the photon pairs were prepared in the $|\psi^+\rangle$ state. This was confirmed by doing a tomography measurement just before the HOM beamsplitter, with fidelity $F = 96.8\%$. The polarisation analysers were set to the diagonal basis $|DD\rangle$ so that both parts of the entangled state were projected onto the fixed vertical polarisation at the linear polarisers. In this basis, we are selecting the product state $|DD\rangle$ so that the photons interfering at the HOM beamsplitter are ideally indistinguishable and show HOM interference.

To see HOM interference, the two output modes must be brought together with zero path length difference, parallel polarisation states, and well matched optical spectra. The polarisations between the interfering modes were then set roughly to parallel using the alignment beam at 810 nm (shown in Figure 52) and measuring the polarisation state in each mode using a polarimeter. This was an approximate method because the polarimeter available was for the visible range and calibrated up to 700 nm but it provided a starting position for the fibre polarisation controller. The polarisation could be optimised later by minimising the coincidence rate at the expected position of the HOM dip. To overlap the spectra of the two modes, the crystal temperature was set to 31.0°C, as found earlier in this chapter using the EMCCD spectrometer.

The results from the first HOM attempt are shown in Figure 66. The coincidence rate was measured (120 s per point) as the position of the delay line was varied around zero

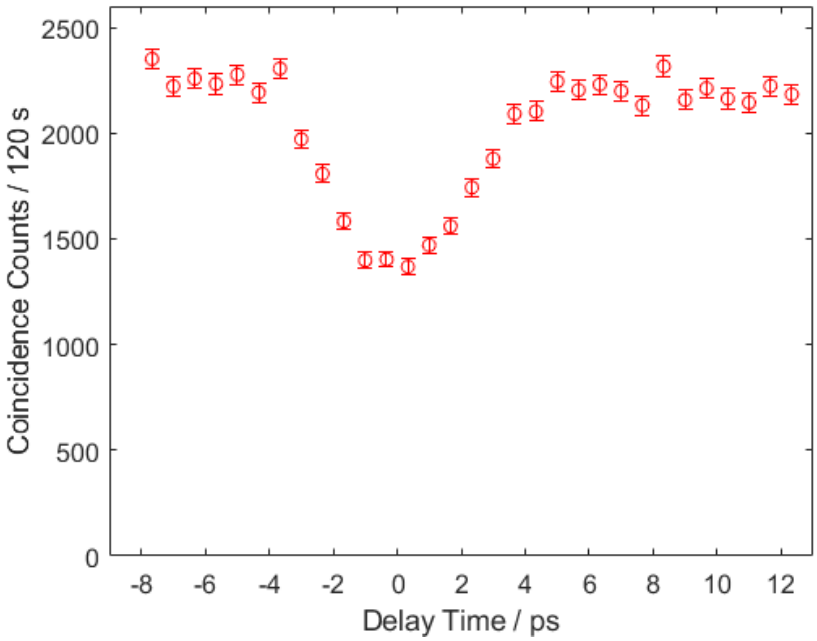

Figure 66: Initial HOM interference measurement. Coincidence counts as a function of delay line position, converted to delay time, showing a HOM dip. The output modes were set to the $|DD\rangle$ basis for this measurement and the polarisation states were roughly matched using a fibre polarisation controller. Coincidences were counted for 120 s per point.

path length difference. There is a dip in the coincidence rate near 6 mm on the delay line which is consistent with HOM interference. To convert from the delay line displacement d to the delay time τ:

$$\tau = \frac{2d}{c} \tag{130}$$

where $d = 0$ is taken as the centre of the HOM dip. Error bars were calculated as the square root of the coincidence count, assuming the counts are Poisson distributed.

When the outputs were being measured in the $|DD\rangle$ basis, the HOM signal was highly sensitive to the alignment of the fibre couplers in the two output beams. It was only possible to see a HOM dip as clear as in Figure 66 once, despite many attempts varying the output fibre coupler alignment and the polarisation controller settings.

A more successful approach to see HOM interference was to completely remove the linear polarisers from the output beams so that both the horizontal and vertically polarised components of each output mode were coupled into the single mode fibres. With this input state, the HOM measurement was repeated with the output polarisation analysers set to no rotation (parallel), and with the polarisation in one beam rotated 90° (perpendicular). An advantage of this approach is that the coincidence rates are increased by removing the linear polarisers, which are expected to block 50% in each output mode. Also, by mea-

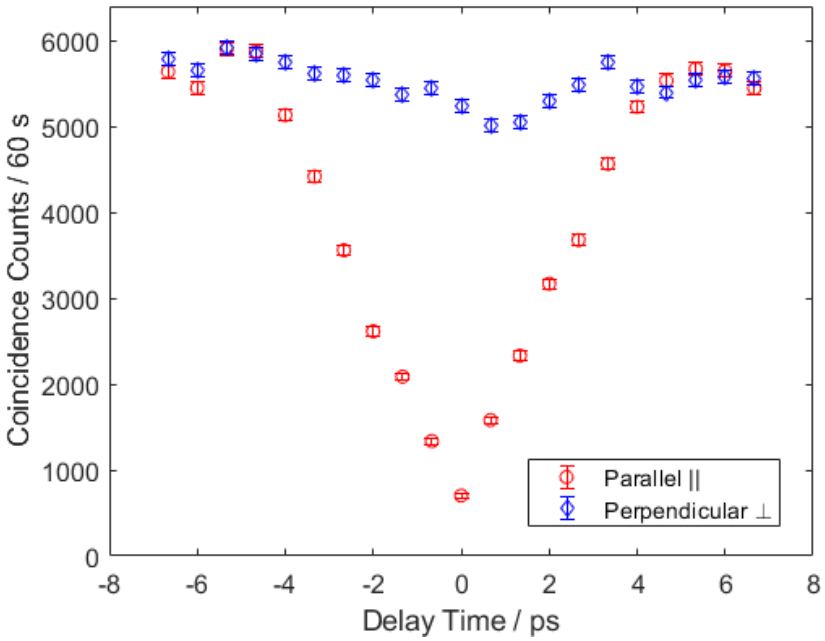

Figure 67: HOM interference measurement. Coincidence count rate as a function of delay line position, converted to delay time. This measurement was done with the linear polarisers removed from the output modes. The red points (parallel) are with no rotation to the output mode polarisation; blue points (perpendicular) are with one output mode polarisation rotated 90°. Coincidence counts were measured for 60 s per point.

suring both the parallel and perpendicular polarisation settings, we obtain a background measurement for the coincidence count rate from which we can measure the HOM interference visibility.

A HOM dip measured without the linear polarisers is shown in Figure 67. The parallel measurement is with polarisation analysers set to no rotation, and perpendicular is with the polarisation in one beam rotated 90°. Note that the half waveplates were in the output beams at all times (for both polarisation settings). We see a HOM dip for the parallel measurement and no dip for the perpendicular measurement. The fibre polarisation controller was adjusted to maximise the HOM dip visibility for the parallel measurement. The HOM interference result could now be achieved consistently. After optimising the polarisation controller position and crystal temperature a HOM visibility of up to 89% could be achieved.

To understand why we see a HOM dip with these experimental settings, we need to consider the effect of the HOM beamsplitter on the Bell states $|\psi^+\rangle$ and $|\psi^-\rangle$. For the $|\psi^+\rangle$ state, the output state has no coincidences on the two detectors, so we predict to see a HOM dip in this case. For the $|\psi^-\rangle$ state, the output state has only coincidences, and we

predict a HOM peak. This behaviour of entangled Bell states combined on a beamsplitter is demonstrated in Ref. [152]. Now if we rotate the polarisation of one mode by 90° in the $|\psi^+\rangle$ state, the coincidence terms again cancel and we expect a HOM dip. This does not agree with the results in Figure 67 if we do actually have the $|\psi^+\rangle$ state at the input to the HOM beamsplitter.

The results in Figure 67 are what we would expect for a product state of photons: when the two photons are polarised parallel they produce a HOM dip, and when they are polarised perpendicular there is no HOM dip (50% coincidences and 50% single counts).

It should be noted that removing the linear polarisers misaligns the output beams from the fibre couplers. The outputs were realigned to maximise the coincidence count rate for the HOM setup. It appears that after realigning the output couplers before the HOM measurement, we no longer have the polarisation entangled state in the two output modes. If instead we have a product state after realignment then we expect to see the HOM signals shown in Figure 67.

We confirmed this by measuring the HOM dip, then immediately replacing the linear polarisers and measuring the density matrix via tomography, without changing the output fibre coupler alignment. The density matrix in this case showed the main contribution to the state was the product state $|HV\rangle$, with near-zero contributions from the other two-photon polarisation basis states. The fibre polarisation controller then rotates the polarisation of one mode resulting in $|HH\rangle$ at the input to the beamsplitter for the parallel case, and $|HV\rangle$ for the perpendicular case, consistent with the HOM signals we see.

This highlights that polarisation entanglement is not required to achieve high visibility HOM interference; we instead need indistinguishable photon pairs to demonstrate HOM and produce two-photon N00N states.

5.6 Conclusions

In this chapter I presented work on building and characterising a source of polarisation entangled photon pairs using a PPKTP crystal in a Sagnac loop setup. This setup is intended to produce entangled photon pairs at degenerate wavelengths which can show two-photon interference via the HOM effect and can be applied in quantum-enhanced sensing schemes.

The final setup was able to achieve quantum state fidelities of up to 94.7% and 98.9% for the $|\psi^-\rangle$ and $|\psi^+\rangle$ polarisation entangled Bell states, respectively. HOM interference was also demonstrated with visibility up to 89%. The background coincidence count rate

in these HOM measurements was around 100 Hz, meaning that two-photon N00N states were being produced at almost 90 Hz rates. These states are directly applicable in quantum sensing schemes using a MZI, as discussed in Chapter 2.

The photon pair production rate achieved here was relatively low compared to other similar experiments in the literature. The maximum coincidence rate recorded during measurements on the final setup was up to 380 Hz at 6.4 mW total pump power. Accounting for the spectral width of the photons which was 0.8 nm, the spectral pair detection rate was approximately 74 Hz mW^{-1} nm^{-1}. One reason for this is that the SPAD detectors have a quantum efficiency of at most 15% at 810 nm. For coincidence counts, this efficiency is squared: 2.3%, therefore the photon pair rate arriving at the detectors is approximately 3.3 kHz mW^{-1} nm^{-1}. Since this is still below the tens of kHz reported in the literature [134], this suggests our photon pair source could be improved significantly by optimising the focusing conditions and collection optics to minimise losses before coupling to the single mode fibres.

Overall, the work in this chapter was successful in developing a source of entangled photon pairs suitable for making quantum sensing experiments. The source is fibre coupled to single mode fibres so that it can be easily integrated with other setups, and as shown in the next chapter, coupled to tapered optical fibre sensors. The entangled photon pairs could be used in a MZI as discussed already, or the HOM signal itself could be used for sensing applications. In the next chapter we take the latter approach to demonstrate a basic refractive index sensing experiment in a tapered fibre sensor using the HOM interference phenomenon to encode small changes in optical path delay.

6 Towards Quantum-Enhanced Sensing with Tapered Optical Fibres and WGM Interferometers

Having built and characterised a source of polarisation entangled photon pairs and demonstrated HOM interference, we now turn to coupling these photons to a sensor setup. Tapered optical fibres are a convenient way to couple the entangled photon pairs to an aqueous environment for sensing purposes, since we can keep the photons in-fibre all the way from the outputs of the PPKTP setup to our single photon detectors. Tapered fibres can then be used to couple photons to a WGM resonator.

First I will introduce the fabrication process for tapering fibres over a gas flame, then show results from inserting tapered fibres into the fibre-coupled HOM setup. By inserting a tapered fibre before the HOM beamsplitter, it is possible to detect changes in the refractive index around the tapered region as a shift in the HOM dip position. This is our first demonstration of a quantum optical sensing mechanism using the entangled photon pair source.

In the last sections of this chapter, I will show a demonstration of tapered fibre coupling to WGM microspheres, and how the WGM resonance wavelength can be controllably tuned by changing the temperature of the WGM resonator and the aqueous medium around it. These are some essential ingredients for coupling entangled photon pairs to the microsphere. However, coupling entangled photons from our source to a WGM resonator is still a major experimental challenge due to the large mismatch between the entangled photon spectral width (0.8 nm) and the typical WGM linewidths used for sensing ($\sim$100 fm). I will discuss how these challenges could be overcome in future experiments in order to investigate WGM quantum sensing schemes such as the Mach-Zehnder scheme presented in theory in Chapter 2.

6.1 Tapering Optical Fibres

Tapered fibres were made by stretching optical fibres over a propane/oxygen flame. The setup is shown in Figure 69, this was built with Dr Samir Vartabi Kashanian and Dr Rithvik Gutha, based on an earlier setup from Dr Eugene Kim [153]. The conditions needed for making low-loss tapered fibres are discussed in Refs. [154, 155]. We used a gas flow ratio of 36:100 of C_3H_8:O_2 to produce a sufficiently hot blue flame, shown in the inset of Figure 69.

Single mode fibre (SMF-28) was used for tapering since large quantities of telecommunications fibre are easily available. A 20-30 mm length of fibre is stripped of the

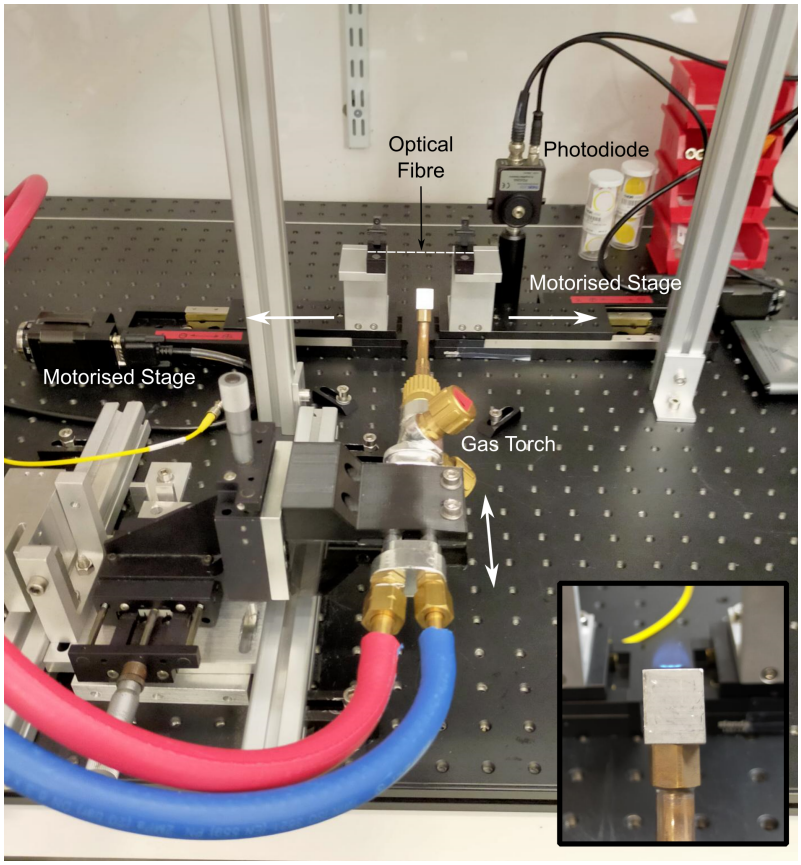

Figure 68: Photograph of the fibre tapering setup. Inset shows the blue propane/oxygen flame used to soften the optical fibre while it is being stretched by the two motorised stages.

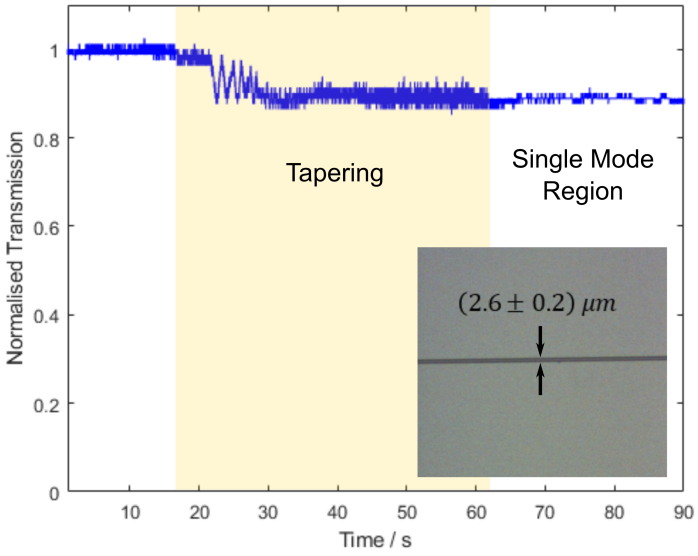

Figure 69: Transmission through optical fibre during tapering process. The fibre has reached the single mode condition once the interference fringes stop. Inset shows a tapered fibre viewed through a 10X objective, with a waist diameter of (2.6 ± 0.2) μm.

coating and cleaned with isopropanol. This section of fibre is clamped to two motorised stages above the gas flame and stretched by moving the stages apart a controlled rate with a LabVIEW control program. A 780 nm laser beam was coupled though the fibre and the transmission was monitored on a photodiode to track the tapering process. A typical transmission signal during tapering is shown in Figure 69. While the fibre is being stretched, interference fringes are seen as the cladding and core of the fibre are fused together and the fibre becomes multimode. When the fringes in the transmission stop, the tapered region has become single mode again.

Completed tapered fibres were attached to a holder using UV curing glue to move them to the PPKTP entangled photon pair setup. Fibres are typically $\sim$2 μm in diameter at the fibre waist, with a tapered region 5-10 mm long. The ends of the SMF-28 tapered fibre were fusion spliced to two single mode fibres for 780 nm with APC connectors in order to couple to the other 780 nm fibres used in the PPKTP setup. We found that splicing telecommunications fibre to 780 nm fibres did not cause excessive photon losses, and as shown in the next section, adding a tapered fibre to the fibre coupled HOM setup only slightly decreased the detected coincidence rate.

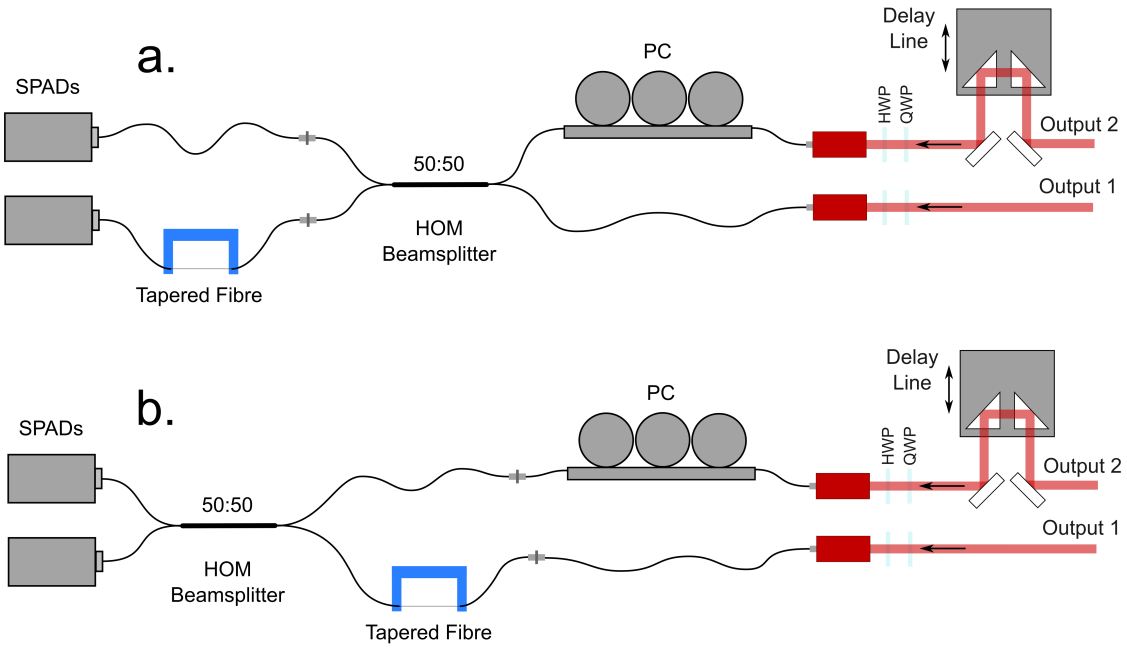

Figure 70: Schematic of HOM setup including a tapered fibre (a) after the HOM beamsplitter, and (b) before the HOM beamsplitter. In case (b), a change in the refractive index in the evanescent field around the tapered fibre causes a shift in the HOM dip due to the change in optical delay.

6.2 Detecting Refractive Index Changes in a Tapered Fibre Sensor using HOM Interference

Two configurations were used for HOM measurements including tapered fibres, as shown in Figure 70. Configuration (a) has a tapered fibre at one output of the HOM beamsplitter and another single mode fibre of approximately the same length at the other output. Configuration (b) has a tapered fibre before the HOM beamsplitter, at one of the inputs. In this case the single mode fibre in the other output must be closely matched in length in order to still have photon pairs arriving simultaneously on the beamsplitter and observe HOM interference.

Figure 71 shows the HOM dip observed with the tapered fibre after the HOM beamsplitter. Parallel and perpendicular polarisations ($\parallel$ and $\perp$) are shown for the case of *i.* no tapered fibre, *ii.* a tapered fibre in air, and *iii.* a tapered fibre in water. The tapered fibre is inserted into water using a polydimethylsiloxane (PDMS) chamber with 300 μl of water contained by surface tension. When the fibre is lowered into this chamber, an 8 mm length of the tapered region is surrounded by water.

From Figure 71, we see that the HOM dip is at the same delay line position (i.e. the same optical delay) in all three cases. Adding the tapered fibre introduces some additional losses, decreasing the coincidence rate by around 15%. Putting the fibre in water

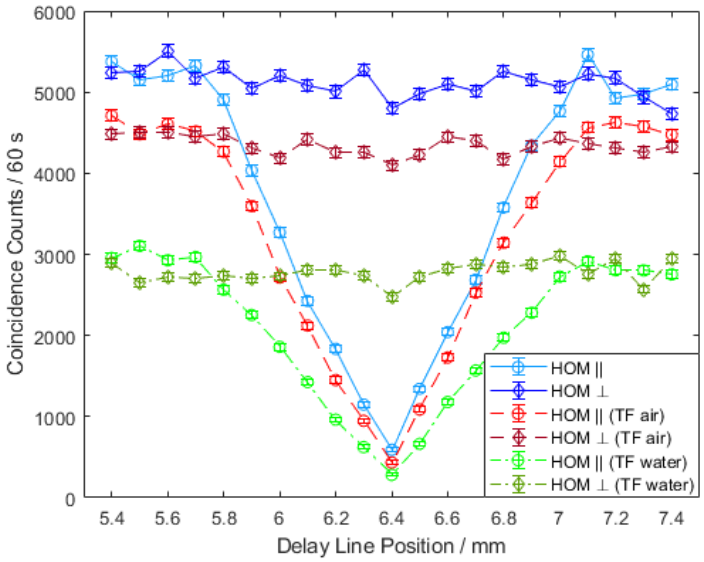

Figure 71: HOM dip measured with a tapered fibre inserted after the HOM beamsplitter. Measurements are shown without the tapered fibre, with the fibre in air, and with the fibre in water.

decreased the coincidence rate by a further 35%. Even after these losses, the HOM dip is easy to resolve measuring the coincidence counts for 60 s per point.

If the tapered fibre is instead put before the HOM beamsplitter, any change in refractive index around the tapered region does change the optical delay at which we see the HOM dip. First the tapered fibre was inserted at one of the inputs to the HOM beamsplitter (see Figure 70(b)) with a slightly longer length of fibre than the 5 m single mode fibre at the other beamsplitter input. Then the $g^{(2)}$ peak is measured at the outputs of the beamsplitter - the peak no longer occurs at zero time delay because of the additional length of fibre. The difference in the fibre lengths d can be calculated from the time delay where there is a peak in $g^{(2)}$, τ, if we assume the fibre has refractive index $n = 1.45$:

$$d = \frac{c\tau}{n} \tag{131}$$

where c is the speed of light in vacuum. Then, the fibre splices connecting the tapered fibre to the APC connectors are broken, a total length of fibre d is carefully removed and the fibres are spliced again. The tapered fibre should now be very close to 5 m and matched in length to the other beamsplitter input.

Figure 72 shows the HOM dip measured with the tapered fibre before the HOM beamsplitter, with the tapered region in air and in water. When the refractive index of the medium changes from 1.00 to 1.33, the HOM dip shifts by 0.67 ps in time delay. The fits applied in Figure 72 are of the form $y = A|\tau - \tau_o| + B$, where the HOM dip is at τ_o time

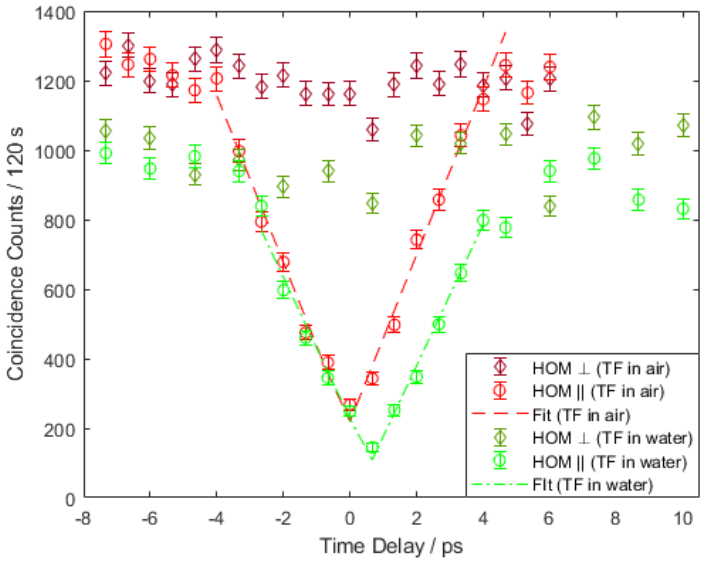

Figure 72: Change in refractive index around the tapered fibre detected by a shift in the HOM dip position.

delay. The time delay $\Delta\tau$ introduced by the tapered fibre can be modelled as:

$$\Delta\tau = \alpha\frac{L(\Delta n)}{c} \tag{132}$$

where L is the length of tapered fibre in the medium, Δn is the change in refractive index in the surrounding medium, and α is the fraction of the optical mode volume in the evanescent field, i.e. that experiences the change in refractive index. For the change between air and water in this experiment, $L = 8$ mm, $\Delta n = 0.33$, and $\Delta\tau = 0.67$ ps. This gives an estimate $\alpha = 8\%$. We could increase α and increase the refractive index sensitivity by making a narrower tapered fibre; although this typically increases the optical losses, it also extends the evanescent field around the fibre.

6.3 Tapered Fibre-Coupled WGM Resonators

Demonstrating the coupling of entangled photon pairs to tapered optical fibres was the first step towards experiments with entangled photon and WGM resonators, because we can use tapered fibres to couple photons to a WGM resonator. This method of coupling light to the resonator has a number of advantages: the setup is all in-fibre from the outputs of the PPKTP entangled photon pair source to the detectors to minimise photon losses, very high coupling efficiency can be achieved using tapered fibres, and the coupling reflection amplitude r (discussed in Chapter 2) can be varied by changing the sphere-fibre distance. Narrow tapered fibres with long evanescent fields can reach the critical and overcoupling conditions when brought very close to the resonator. In this section I will describe some experiments on tapered fibre coupling to a WGM microsphere and tuning

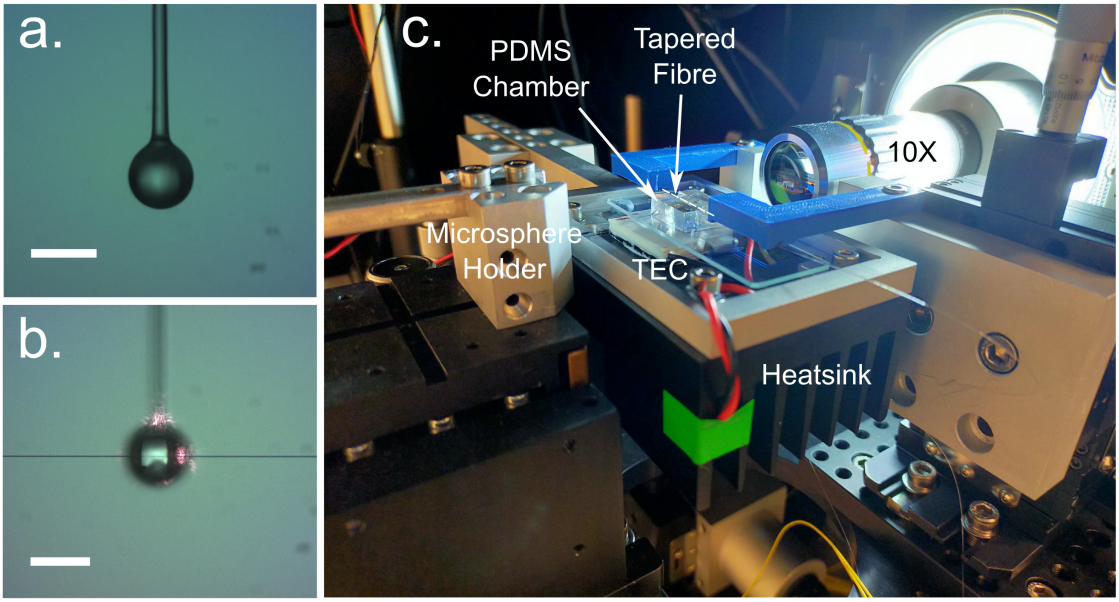

Figure 73: Photographs of tapered fibre coupling to WGM resonators. (a) WGM microsphere fabricated by melting the tip of an optical fibre (SMF-28), with diameter 89 μm. (b) Tapered fibre coupling laser light at 780 nm to the WGM microsphere. (c) Setup for coupling tapered fibres to WGM microspheres. The microsphere is inserted into the PDMS chamber from above. The chamber holds 300 μl of an aqueous sample. A TEC, heatsink and a thermistor which can be attached to the TEC surface allow the temperature of the aqueous sample and microsphere to be controlled. Scale bars in (a) and (b): 90 μm.

the WGM resonance wavelength by controlling the microsphere temperature.

Figure 73 shows the setup for immersing tapered fibre sensors in water and also for coupling light to WGM resonators. WGM microspheres are fabricated by melting the tip of a single mode optical fibre (SMF-28) with a high power IR laser (CO_2 laser, Synrad). Surface tension pulls the silica into a spherical shape as it melts to produce an optical resonator with a Q factor typically in the range 10^{6-7}. Figure 73(a) shows a WGM microsphere with 89 μm diameter, and (b) shows the same microsphere evanescently coupled to a 780 nm laser beam in a tapered fibre.

From the theoretical model in Chapter 2, we can characterise the WGM resonator by two main parameters: the amplitude transmission per round trip α, and the coupling amplitude reflection coefficient r. Transmission per round trip α is a property of the resonator and the surrounding medium since it has contribution from absorption in the microsphere, scattering from the surface of the sphere, and losses due to absorption or radiation to the external medium. The coupling condition with the tapered fibre is characterised by r, which depends on the evanescent field length of the tapered fibre, the mode

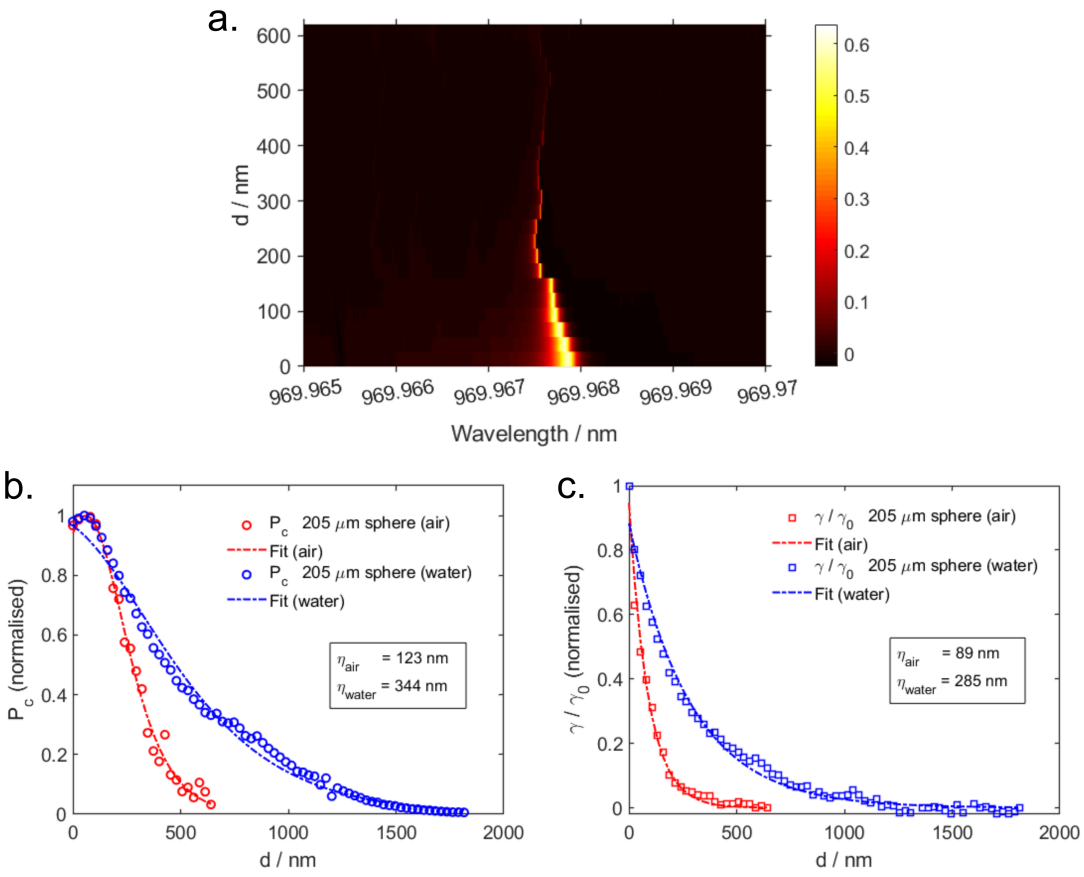

Figure 74: WGM microsphere coupled to a tapered fibre with varying tapered fibre-sphere distance. (a) Spectra for one WGM as the sphere-fibre distance d is varied. The colourmap shows the normalised optical power coupled to the resonance. (b) Circulating power in the WGM resonator P_c as a function of d for a sphere and fibre in air (red points) or water (blue points). Fits determine the values of the evanescent decay length η. (c) Linewidth plotted as ratio between extrinsic γ and intrinsic γ_0 linewidths, as a function of d. Single exponential fits determine η. Note that the data in (b) and (c) are normalised to the maximum values to compare between data sets.

matching between the fibre mode and the WGM modes, and the sphere-fibre distance d which is variable in the experiment.

To describe the effect of d on the WGM resonance in a microsphere, we can consider the power circulating in the resonator on resonance P_c, and the resonance linewidth γ. P_c is proportional to the WGM transmission on resonance T_0: $P_c = P_{in}(1-T_0)$. Following Ref. [156], we have the following expressions for the linewidth:

$$\frac{\gamma}{\gamma_0} = A \exp\left(-\frac{d}{\eta}\right) \tag{133}$$

and the circulating power:

$$\begin{aligned} P_c &= 1 - \left(\frac{1-\left(\frac{\gamma}{\gamma_0}\right)}{1+\left(\frac{\gamma}{\gamma_0}\right)}\right)^2 \\ P_c &= 1 - \left(\frac{1-A\exp\left(-\frac{d}{\eta}\right)}{1+A\exp\left(-\frac{d}{\eta}\right)}\right)^2 . \end{aligned} \tag{134}$$

The linewidth has two contributions: the extrinsic linewidth γ due to coupling losses, and the intrinsic linewidth γ_0 due to losses in the sphere, which experimentally was taken as the linewidth at the largest distance d. The parameter η is the evanescent decay length for the sphere and tapered fibre combined: $\eta = \eta_{sphere} + \eta_{fibre}$. This decay length can be determined by fitting data on WGM transmission and linewidth as a function of sphere-fibre distance to Equations 133 and 134.

Figure 74 shows the effect of varying the sphere-fibre distance d on the WGM coupling. To take this data I used an experimental setup and data analysis code by Dr Samir Vartabi Kashanian. The setup is similar to Figure 73 but has the tapered fibre mounted on a piezo stage so its position can be controlled precisely. The transmission spectrum is measured by sweeping the wavelength of the input laser (tuneable external cavity diode laser, Toptica) at 50 Hz and measuring the transmission on a photodiode with a trigger to each wavelength sweep. For this experiment a large 205 μm diameter sphere was used, which has the advantage of having many WGMs within a wavelength scan region. A laser near 980 nm was coupled to this sphere with a (2.1 ± 0.4) μm diameter tapered fibre. Figure 74(a) shows the WGM spectrum around one mode as the fibre was moved towards the sphere, with the fibre and sphere in air. The linewidth broadens, the resonance becomes deeper, and the resonance position generally redshifts as d decreases.

Fits to Equations 133 and 134 are shown in Figure 74(b, c) for a tapered fibre and sphere in air (red points) or in water (blue points). The fits for P_c and γ/γ_0 give different

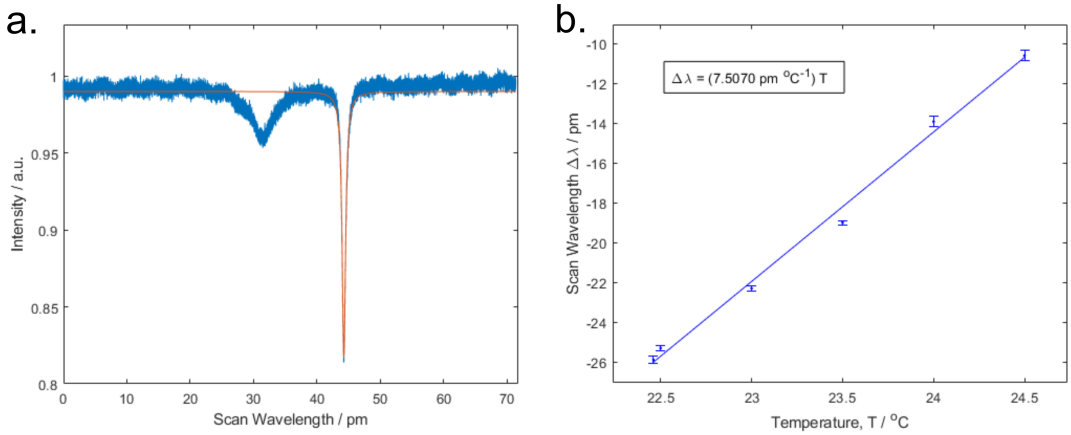

Figure 75: Temperature tuning of a WGM resonance. (a) Spectrum of WGM resonance with a Lorentzian fit applied to determine the resonance position. (b) Change in the resonance position $\Delta\lambda$ as the temperature of the water sample cell and microsphere is changed using the TEC.

values for the decay length η, but in both cases the evanescent decay length increases by approximately a factor of 3 when the sphere and fibre are submerged in water. Average values are $\eta_{air} = 106$ nm and $\eta_{water} = 315$ nm. Since the optical fibre refractive index is around 1.45, the index contrast between the fibre and surrounding medium is lower in water, hence the guided mode is less tightly confined. We can relate this result back to the tapered fibre HOM measurements in the previous section. When the medium around the tapered fibre sensor is changed from air to water the decay length of the evanescent field around the tapered fibre will increase as a consequence of the refractive index change.

An important point to note from Figure 74(b) is that P_c has a peak around $d = 50 \pm 10$ nm. This corresponds to the critical coupling condition, which in the theoretical model for WGM coupling is the condition $\alpha = r$. Therefore we can reach overcoupling using this tapered fibre for sphere-fibre distances less than 50 nm. The overcoupling regime was shown in Chapter 2 to be the optimum coupling condition for investigating effects due to entangled photon pairs coupled to WGM resonators in a MZI. As stated earlier in this section, the capability to reach critical and overcoupling is a major advantage to using tapered fibres to couple to microspheres.

In typical WGM coupling experiments, the laser source is widely tuneable and can be swept across individual resonances as well as tuned to different resonances. For example the laser used with the setup in Figure 73 is tuneable from 765-815 nm. Sources of entangled photons will generally be much harder to tune. For our PPKTP Sagnac source the pump laser is tuneable over 2 nm, but changing the pump wavelength causes the degenerate phase matching temperature to change making it challenging to use this as a practical tuning mechanism for the photon pairs. The other approach is to tune the wavelength of

WGM resonances. This can be achieved by changing the refractive index of the WGM microsphere by the thermorefractive effect: on our setup the temperature of the microsphere can be controlled using the TEC shown in Figure 73(c).

Figure 75 shows an experiment to demonstrate temperature tuning. A WGM microsphere was coupled with a tapered fibre in water and the temperature was changed from 22.5-24.5°C, waiting for around 10 minutes at each temperature for the microsphere and water to equilibrate with the TEC temperature. The resonance wavelength (determined by an inverted Lorentzian fit to the transmission spectrum) increases linearly with the temperature, with a gradient $\frac{d\Delta\lambda}{dT} = 7.5$ pm/°C. This system can control the temperature over at least a 30°C range for extended periods of time, so shifts of over 200 pm in the resonance wavelength are achievable.

6.4 Challenges in Coupling Entangled Photons to WGM Resonators for Quantum Sensing Schemes

The previous sections have presented some important experimental building blocks we need to do experiments with entangled photons coupled to WGM resonators: demonstrating HOM measurements through a tapered optical fibre and a basic refractive index sensor using a quantum optical effect of two-photon interference; showing tapered fibre coupling to a WGM microsphere on the same experimental setup; and temperature tuning WGM resonances with a view to tuning the resonance to the wavelength of an entangled photon pair source. Successfully coupling entangled photons to a WGM resonator would enable us to study the predicted entangled photon spectrum from Chapter 2 and investigate quantum sensing schemes with WGM biosensors. However, coupling to the resonator remains an experimental challenge. In this section I will discuss why, and how this could be done in future experiments.

WGM Linewidth. The typical linewidth in WGM resonators used for single molecule sensing is ∼100 fm, with microspheres of diameter 80-90 μm, although for short sphere-fibre distances we measured a linewidth of 2 pm. From Chapter 5, the spectral width of photon pairs produced in our PPKTP Sagnac source is 0.8 nm. This factor of $\sim 10^{2-3}$ mismatch in spectral width to WGM linewidth is the greatest challenge to coupling entangled photon pairs to a WGM resonator. From the computational study in Chapter 2, in order to properly resolve the features of the entangled photon WGM spectrum the ratio of photon spectral width to WGM linewidth should be $\Delta\lambda_{photon\ pairs}/\Delta\lambda_{WGM} \sim 0.1$. To achieve this we either make the photon spectrum narrower, the WGM linewidth broader, or both.

Decreasing the spectral width of the photon pairs could be achieved by filtering with

a Fabry-Perot cavity, although this would result in very high photon losses which affects the coincidence rate quadratically. Since the coincidence rate is currently up to around 400 Hz in experiments this does not seem feasible. Instead, the ideal approach would be to modify our photon pair source by putting the PPKTP crystal inside a Fabry-Perot cavity. Experiments on cavity-enhanced SPDC photon pair sources have demonstrated spectral widths of $\sim$10 MHz which enabled entangled photons to be coupled to atomic transitions [157]. This would be a major overhaul of the photon pair source. Incorporating the cavity into the Sagnac loop source is made complicated by the modes travelling both clockwise and anticlockwise - so we do not have separate input and output mirrors. Instead, it would be better to replace the Sagnac loop with a PPKTP crystal in a Fabry-Perot cavity pumped in one direction, or two PPKTP crystals in a bow-tie cavity. Alternatively, entangled photon pair sources using WGM resonators fabricated from nonlinear optical crystals can provide very narrow linewidth photons [158]. A problem with these sources is that so far only Type-I SPDC phase matching has been demonstrated. In this case both photons have the same polarisation so they must be detuned in wavelength to separate them into two spatial modes, which prevents HOM interference. Type-II SPDC in a WGM resonator is possible in principle but the phase matching between WGMs of different polarisations is challenging. Even after using cavity-enhanced SPDC, another ultra-narrowband filter may be required to cut out all except one of the transmitted modes.

Increasing the WGM linewidth is possible by making small microspheres (less than the typical 80-90 μm diameter). The broader WGM linewidth is not desirable for sensing, but it can make the condition $\Delta\lambda_{photon\ pairs}/\Delta\lambda_{WGM} \sim 0.1$ easier to achieve. From Chapter 2, the linewidth $\Delta\lambda \propto 1/R$ (R: microsphere radius) so it may be feasible to roughly double the WGM linewidth this way. The other way to increase the linewidth is to work in the overcoupled regime, which was also the best place to look for a potential SNR enhancement with entangled photons. This requires making thin tapered fibres which can reach overcoupling and bringing them into contact with the microsphere.

Wavelength Tuning. To match the wavelength of a WGM resonance to the photon pair wavelength at 810 nm requires the resonance and/or photon pairs to be tuned over a range of up to half the WGM free spectral range (FSR). Using the equation in Chapter 2, the FSR for 810 nm wavelength is $FSR = 1.6$ nm for a 90 μm diameter, increasing to $FSR = 2.9$ nm for a 50 μm diameter sphere.

As shown in the previous section, temperature tuning of the WGM resonance on our setup can provide at least 200 pm tuning range. This would be a coarse tuning method with a resolution around 1 pm based on the data in Figure 75.

If we used a cavity-enhanced photon pair source, the photon wavelength could be tuned over a small range (the FSR of the cavity) by tuning the cavity length. Since the SPDC bandwidth is relatively wide (0.8 nm for our 25 mm crystal) the photon pair count rate should not change significantly while the cavity transmission is tuned over a small

range. This fine control of the photon wavelength would potentially allow the WGM spectrum to be measured using entangled photon pairs.

Even with these fine and coarse methods for wavelength tuning, the WGM FSR is ~ 1 nm; it may be necessary to make many WGM microspheres to find one with a resonance within the temperature tuning range. Making larger resonators reduces the FSR and makes the wavelength matching easier, but also makes the linewidth narrower so there is a trade-off in the microsphere diameter between easier wavelength matching and linewidth matching.

Stability and Locking. The position of a WGM resonance inevitably drifts due to slow temperature and pressure changes. In an experiment with a tuneable laser, as long as the laser wavelength is swept over a wide enough range, the resonance will always remain in the wavelength scan range. Alternatively, the laser wavelength can be actively locked to the WGM resonance position using a Pound Drever Hall (PDH) locking scheme, for example [24, 33]. With an entangled photon pair source that is more difficult to tune in wavelength than the laser, and with photon counting measurements which may take a long period of time, slow drifts in the WGM wavelength are another challenge.

The first consideration to stabilise the WGM resonances is to stabilise the resonator temperature using the temperature control system shown in the previous section. Actively locking to the WGM resonance is more challenging in the photon counting regime. For example, PDH locking requires the input mode to the resonator to be frequency modulated. The modulation frequency is severely limited by the rate at which the photon number is sampled after the single photon detectors; the sampling rate should be sufficiently low to reduce shot noise in the photon number. A separate laser beam could be coupled to the resonator to produce a feedback PDH error signal, although this introduces a relatively high power classical beam. This approach could be useful for studying the entangled photon spectrum, but not for demonstrating a sensing advantage with entangled photons since the high power classical beam can be used to track the resonance instead of the comparatively very low power photon pairs.

Noise Sources in WGM Resonators. Finally, we consider the sources of noise in measuring the WGM resonance position. From Chapter 2, if the photon number per time bin $R\Delta t$ is sufficiently low, the change in the resonance position read off from the count rate on the side of the resonance is shot-noise-limited. It was also shown that this is the regime where entangled photon can potentially enhance the SNR in this measurement. However, we note that going to the low photon number regime always means increasing the noise in absolute terms compared to the classical WGM measurement. So it should be possible to make a proof-of-principle demonstration of SNR enhancement using entangled photons, but there is not an absolute improvement in measurement precision in this approach - unless the optical power used in the measurement has to be constrained to a low photon

count rate.

For more general quantum sensing schemes not necessarily using entangled photon pairs but instead squeezed light - as discussed further in the outlook in the following chapter - the noise sources currently limiting classical WGM sensing will become important. Instead of reducing the optical power until shot noise becomes larger than the other noise sources and demonstrating a reduction below this shot noise, quantum sensing schemes working at higher optical power need to overcome the usual noise limits first to reach and then go below the SNL. In current WGM sensing experiments, dominant noise sources include temperature and pressure variations over long timescales, laser frequency jitter [33], and fundamentally thermorefractive noise (fluctuations in the refractive index of the microsphere due to its temperature) [159, 160]. The shot noise level lies below these other noise sources.

Strategies to overcome these noise sources and reach a shot-noise-limited WGM measurement could include using a heterodyne detection scheme to move the signal to a frequency band with lower noise, as in Ref. [53], measurements using the relative positions of WGM split modes [161], or using a technique such as cavity ring-up spectroscopy (CRUS) which has been suggested to reach shot noise since it is a self-heterodyning measurement [162].

Despite these challenges, there is a strong motivation to improve the SNR of WGM biosensing measurements as argued in Chapter 1, especially in single molecule detection. The aim of demonstrating quantum sensing schemes using WGM biosensors provides an incentive to thoroughly characterise both classical and quantum noise sources in WGM measurements. Any improvement in the precision of these sensors whether using a classical or quantum measurement scheme could lead to new applications. The following chapter will summarise the work discussed in this thesis and give an outlook on future work and unanswered questions.

7 Conclusions and Outlook

In this thesis I have described the development of two quantum optics experiments to produce photon states for applications in quantum biosensing schemes: single photon emission from vacancy defects in hBN crystals, and polarisation entangled photon pairs produced by the nonlinear interaction SPDC in a PPKTP crystal. These photon sources were chosen to develop the capabilities for making quantum optics measurements in our lab and as promising light sources for quantum-enhanced biosensing schemes. Another aim of this thesis was to investigate quantum sensing schemes applied to WGM biosensors. By studying quantum sensing schemes we can explore the fundamental noise limits of measurements using these biosensors. Enhancements in the SNR of WGM biosensors could lead to important improvements and new capabilities in single molecule sensing in the future.

The hBN single photon emitters could not be used for biosensing in this study. The initial plan was to interfere successive single photons by HOM interference to generate path-entangled states suitable for quantum sensing schemes using MZI. However, I showed that with our experimental setup at room temperature we were unable to observe HOM interference due to the spectral diffusion of the single photon emission; HOM has been observed for hBN emitters at cryogenic temperatures recently [108]. Instead, we turned to studying the intensity stability and photon number variance of our hBN emitters, since another property of single photon emission which could potentially be used is a sub-Poissonian photon number variance (intensity squeezing). I characterised the fluorescence blinking and bleaching behaviours as a function of excitation power and sample temperature. This long timescale intermittency in the single photon emission would be disruptive to any application in sensing experiments, however a few emitters were found which did not show any fluorescence blinking. For one of these stable emitters, I measured the time-dependent Mandel Q parameter to quantify the photon number variance over different timescales. Despite showing clear single photon emission over nanosecond timescales, when the photon count rate was integrated for 200 ns or more the photon statistics became super-Poissonian due to the emitter having a transition to a shelving state. This meant that any intensity squeezing due to single photon emission was lost when integrating over any significant number of photons. We did however propose the time-dependent Mandel Q parameter as a useful measure of intensity stability in single photon sources as a result of this work [54].

To use entangled photon states and HOM interference for quantum sensing experiments, we turned next to the photon pair source using a PPKTP crystal in a Sagnac loop. I described the process of building and characterising this experiment which was able to produce polarisation entangled states with up to 98.9% fidelity, and HOM interference

with up to 89% visibility. Photon pairs were produced with degenerate wavelengths of 810 nm by controlling the temperature of the nonlinear crystal, and the spectral width was 0.8 nm. The rate of coincidence detections of photon pairs was up to 400 Hz in these experiments, which was limited primarily due to the efficiency of our single photon detectors at 810 nm. I demonstrated a basic quantum optical measurement scheme by adding a tapered optical fibre sensor to the all-fibre HOM experiment. The optical delay caused by a change in refractive index around the tapered fibre caused an observable shift in the HOM dip. For the refractive index change between air an water a 0.67 ps optical delay was measured. Although this is not a sensitive refractive index measurement, it is a proof-of-principle sensing scheme that uses a strictly quantum optical phenomenon to measure a sub-picosecond optical delay, and a demonstration of our entangled photon pair source being applied to a sensing experiment. The tapered fibre sensor setup also readily allows coupling to a WGM microsphere.

The main motivation of this work was to develop quantum optical light sources to investigate quantum sensing schemes with WGM biosensors. I showed some theoretical investigation into coupling entangled photon pairs to a WGM resonator in Chapter 2. For a WGM resonator coupled to one arm of a MZI with an entangled photon input state, it was shown that the transmission spectrum in photon coincidences has two dips, in comparison to the single Lorentzian dip for the classical case. This is a consequence of the double phase shift experienced by the entangled photon pair inside the interferometer. The spectrum changes with the WGM coupling conditions; the central peak of the spectrum is most visible in the overcoupled case and becomes extremely narrow near critical coupling. The higher gradient near the central peak compared to the gradient of the classical transmission spectrum suggests an enhancement in sensitivity when measuring a change in resonance position. I showed an example sensing scenario using a computational model to compare the noise in a resonance shift measurement between WGM sensing schemes with classical and entangled input states. Neglecting optical losses, a factor of two enhancement in the SNR was shown for an overcoupled WGM resonator at low optical powers where the measurement is shot-noise-limited. The model also showed that to observe this enhancement the entangled photon spectrum must be sufficiently narrow: ~ 0.1 WGM linewidths.

It was not possible to couple our PPKTP photon pair source to a WGM resonator in this study, primarily because of the large mismatch between the photon spectral width and the WGM linewidth. I discussed the challenges involved in coupling entangled photons to a WGM resonator at the end of Chapter 6, and suggested how these could be overcome in future experiments. This thesis has shown that the WGM-coupled MZI has an interesting transmission spectrum for entangled photon input states, if this can be confirmed experimentally. Using this entangled photon transmission spectrum there is the potential

to demonstrate a SNR enhancement over a classical measurement scheme for measurements at low optical power. These results give a strong motivation to develop experiments on coupling entangled photons to WGM resonators and to push the noise limits of WGM biosensors. I hope that the practical considerations discussed here on developing quantum optical light sources for sensing will inform these future experiments.

7.1 Outlook and Future Experiments

To close I will briefly discuss potential future experiments and some of the unanswered questions brought up during this thesis.

The next major step would be to couple entangled photons to a WGM resonator, which may require developing an entangled photon source using cavity-enhanced SPDC. With this setup it would be possible to investigate the transmission spectrum of a WGM-coupled MZI with an entangled photon pair input state, and to test the predictions from the theory in Chapter 2. This would also enable a test of the SNR enhancement in a WGM resonance shift measurement using entangled photon pairs. A further interesting research direction with this experiment would be to look for the HOM effect in a WGM resonator as described theoretically in Alsing et al. [62]. This would require a WGM resonator coupled to two tapered fibres in an 'add-drop filter' configuration, and entangled photon pairs coupled to the two fibres. The HOM experiment again requires an entangled photon pair source with a spectral width much narrower than the WGM linewidth, so the same tuneable and spectrally narrow entangled photon pair source would be ideal for both the MZI and HOM experiments.

A major theoretical question to investigate is how the WGM-coupled MZI behaves with different input states besides entangled photon pairs. In particular, what effects would we see with squeezed states: for example, one input mode having a coherent state and the other a squeezed vacuum state, or twin-beam squeezed states in the two input modes? Different geometries of optical cavities such as Fabry-Perot cavities could be added to the model since this could make our theoretical study relevant to a broader class of sensing experiments.

It was demonstrated recently by Belsley et al. [163] for an absorption or refractive index measurement of the medium around a WGM ring resonator, that a single-mode coherent input state maximises quantum Fisher information for this measurement, and that squeezed states would provide no advantage with the optimum experimental parameters. It would be critically important to make a connection with this work and determine whether coherent states can also provide the optimum sensing performance in the WGM-coupled MZI we considered here. Realistic experimental parameters for WGM biosensors

should also be added to the model, since it may be the case that squeezed light or other quantum optical states can provide a sensing advantage over coherent states in the *experimentally accessible* regions of the parameter space.

Finally, we can ask how these future experiments and theoretical studies could have applications in advancing WGM biosensors. Proof-of-principle demonstrations for enhanced measurements using quantum optics can be made by working at low optical power in the shot-noise-limited regime, however to provide practical improvements to WGM sensors these experiments need to reach comparable optical power to measurements made using classical light. Major goals in this direction are to (a.) theoretically determine quantum optical states which can provide SNR enhancements in WGM sensing, and (b.) move to using states with higher optical power, for example using squeezed states of light. Working at a similar optical power to classical WGM sensing means that first the noise that currently dominates in these measurements has to be reduced to reach the SNL. Then, quantum optics approaches to surpassing the classical noise limits could be investigated.

Potential strategies to overcome noise in WGM measurements include relative mode shifts using WGM split modes [161], self-heterodyning techniques such as cavity ring-up spectroscopy (CRUS) which has been suggested to be able to reach shot noise [162], or other heterodyne measurement schemes to move the WGM signal into a frequency band with lower noise [53]. All improvements in SNR have the potential to bring important advances in WGM biosensing, in particular in optoplasmonic WGM sensing for single molecule studies. As described in the introduction, signals from small molecules and enzyme turnover events are often close to the noise. Whether using quantum sensing approaches or by reducing existing classical noise sources, any improvement in the SNR of these measurements could enable yet smaller motions of enzymes or other biomolecules to be resolved in the future.

Appendix A - Time-dependent Mandel Q parameter analysis for a hexagonal boron nitride single photon source: Supplementary Information

The following is the supplementary information document for the work on measuring the time-dependent Mandel Q parameter of a hBN single photon emitter, which was presented in Chapter 4. This has been published with Ref. [54]. The MATLAB code I used to calculate the time-dependent Mandel Q parameter is available on the Zenodo repository [127].

1. Pulsed timestamp filter

A filter was applied to the pulsed timestamp data before analysing the $g^{(2)}(\tau)$ and Q(T) functions. Using the trigger pulse output of the pulsed laser, the time delay between each photon detection and the previous trigger pulse was available for all our data. A histogram of the delay time after the trigger pulse is shown in Figure 76. The filter was applied by keeping only the detections which arrive within a given time window after the trigger pulse; all filters begin from the peak of the pulse at 7 ns delay. The following describes the process of choosing the optimum filter settings to exclude background noise counts and measure Q(T) due to single photon emission counts only.

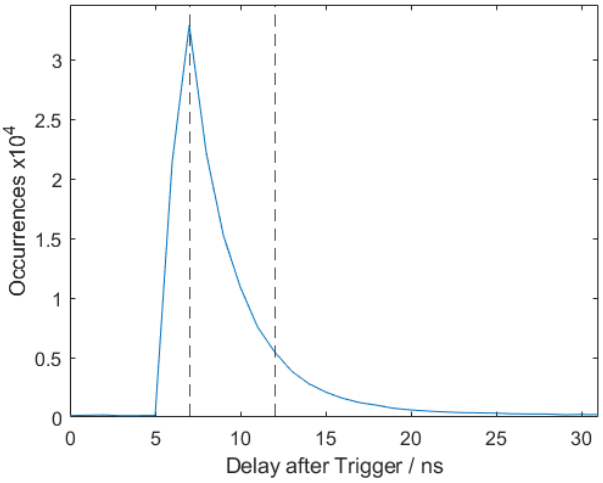

Figure 76: Lifetime curve showing 5 ns filter width applied to the data.

The filter width was varied from 1 ns to applying no filter, i.e. using the raw data. The distribution of Q parameter values for $T = 100$ ns integration time over all 144 data acquisitions is plotted as a function of filter width in Figure 77. The raw data is plotted at 100 ns filter width as this corresponds to the pulse period, i.e. maximum possible filter width.

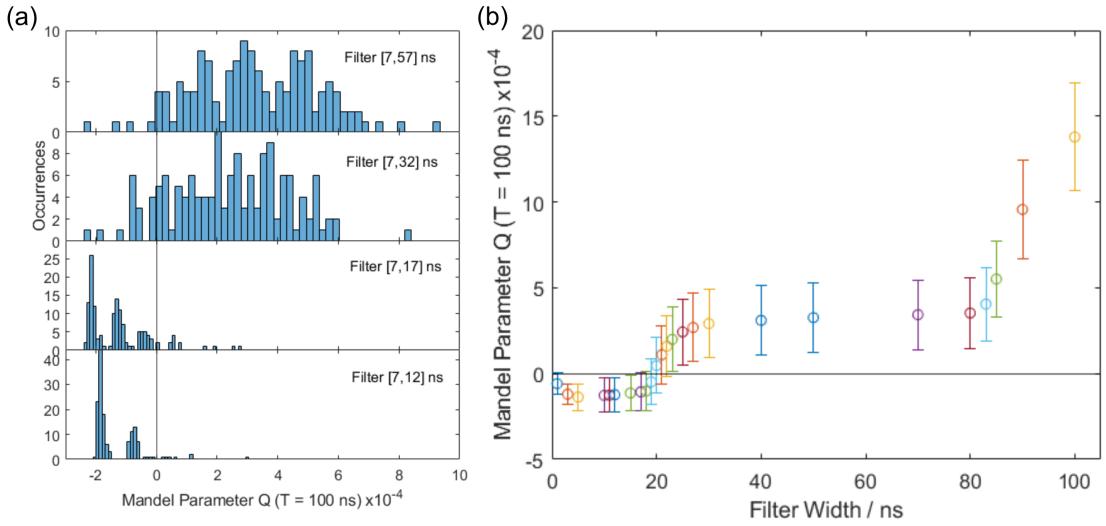

Figure 77: (a) Mandel Q parameter at 100 ns integration time (integrating over one pulse period). Histograms show Q parameter values over the 144 data acquisitions each 100 s long, for different filter widths. (b) Mean Q parameter as a function of filter width.

As the filter width goes to zero, Q(T) also goes to zero since the number of counts being used for the calculation decreases.

Between 5 ns and 18 ns filter width there is a stable negative Q(T). Above 18 ns however Q(T) increases sharply and becomes positive. There is another increase above 80 ns filter width.

The sudden increase in Q(T) above 18 ns filter width can be attributed to an artefact of our measurement seen in the raw $g^{(2)}(\tau)$ data, see Figure 78. There are additional peaks at ± 18 ns delay time in all $g^{(2)}(\tau)$ measurements. This only occurs when using multimode fibre to collect the output light from our setup, the delay time is always the same regardless of the light source being observed, and changing the length of multimode fibre at the output changes the delay time at which the peaks appear. Therefore we conclude these peaks are due to reflections from the end facets of our multimode fibre and as such we treat them as noise.

Using single mode fibres with angled (APC) connectors would solve this issue, however we use multimode fibre, which is widely used in other hBN experiments, in order to collect a high enough count rate under pulsed excitation to perform our measurements.

Note that for CW $g^{(2)}(\tau)$ measurements these peaks were still present, but since the peaks are narrow, they could be excluded from fitting procedures without significantly

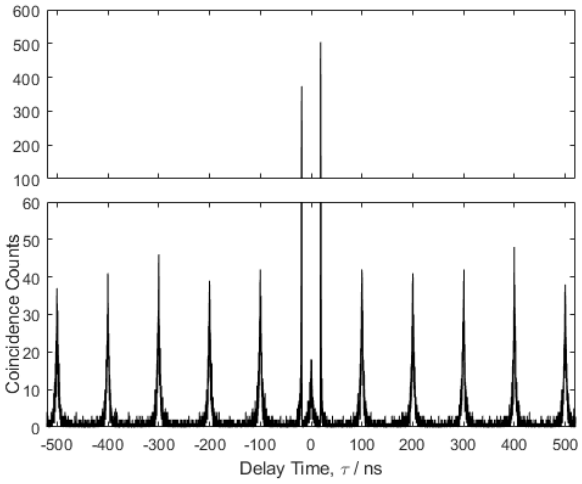

Figure 78: Raw $g^{(2)}(\tau)$ function for pulsed excitation with 24 μW mean power showing noise peaks at $\pm$18 ns due to reflections in the multimode fibre.

reducing the number of points used to fit models to the data.

The final choice of filter was 5 ns wide, i.e. over [7,12] ns delay time. This filter setting excludes the noise peaks at $\pm$18 ns in the $g^{(2)}(\tau)$ function while keeping enough photon counts to measure Q(T) due to single photon counts from our hBN emitter. A 5 ns filter also produces the most significant negative Q value. This filter width is approximately double the radiative lifetime of the emitter: $\tau_{21} = 2.7 \pm 0.1$ ns.

We can also test the effect of applying a filter to the simulated pulsed timestamp data. In Figure 79(a) we see that decreasing the filter width below $\sim$5 ns moves Q(T) closer to zero. Unlike the experimental data in Figure 77(b), Q(T) does not change significantly for filter widths above $\sim$5 ns because: a. the simulated data has no background noise, and b. the noise peaks at $\pm$18 ns delay are not present in the simulated data.

One clear difference between the simulated and experimental Q(T) histograms is that the simulation values are all clustered around a single value; the multiple peaks are only seen in the experimental data. We added noise to the simulation by adding uniformly distributed background counts to the simulated timestamps, with the same background count rate of 160$\pm$40 Hz per detection channel measured from experimental lifetime curves. With added noise, the simulated Q(T) histograms in Figure 79(b) do show multiple peaks and begin to resemble the experimental data more closely.

2. Detector deadtime measurement

The deadtime of our single photon avalanche diodes (SPADs) is nominally 77 ns. The

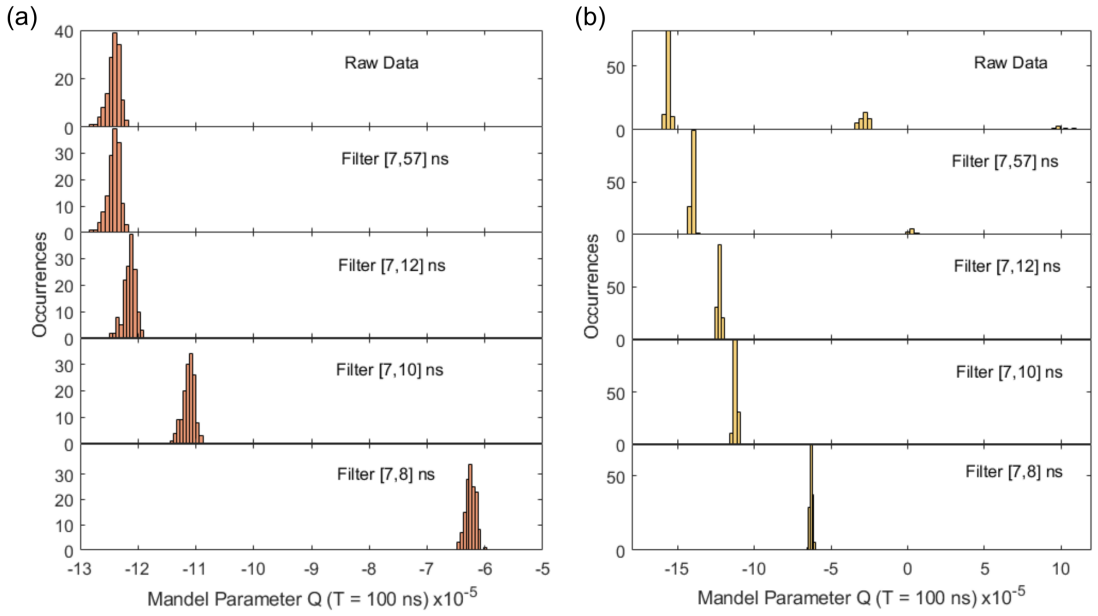

Figure 79: Mandel Q parameter for simulated pulsed timestamp data at 100 ns integration time. (a) Simulated Q parameter as a function of filter width. (b) Simulated Q parameter with uniformly distributed noise counts added to the simulated timestamp data.

deadtime must be known to choose an appropriate pulse repetition rate and to model the deadtime in Monte Carlo simulations. We measured the deadtime by detecting counts from room lights at around 4.4 MHz count rate, approaching the detector saturation count rate. The histogram of time delays between successive counts is shown in Figure 80.

The histograms show a sudden drop to zero for delays less than the deadtime. At large time delays the histograms slowly decrease to zero because we only accounted for the nearest-neighbour delays. Taking the deadtime to be the half-rise time of the curves gives values of $t_d = (81.35 \pm 0.10)$ ns for detector 1 and $t_d = (80.35 \pm 0.10)$ ns for detector 2. For the purposes of simulating timestamps we took the deadtime to be 80 ns for both detectors.

3. Detector afterpulsing

As well as a deadtime, SPADs can produce accidental electronic pulses after a photon detection. This artefact is known as afterpulsing.

Afterpulsing was characterised for our SPADs by measuring the histogram of delay times between trigger pulses and photon detections from the attenuated pulsed laser at 1 MHz repetition rate. Afterpulses are seen 80 ns after the pulse peak, and they decay with an exponential shape, see Figure 81(a). From this measurement the afterpulsing

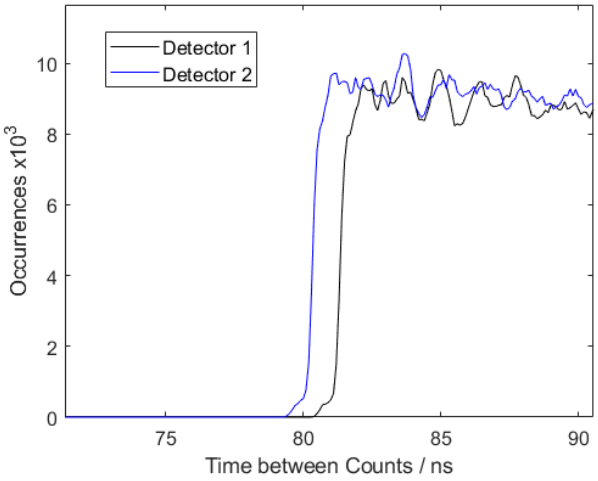

Figure 80: Detector deadtime measurement using a near saturation count rate from room lights. Histogram of delay times between successive photon detections, showing a sudden drop to zero below the detector deadtime. Taking the deadtime as the half rise time of the curves, detector 1 deadtime $t_d = (81.35 \pm 0.10)$ ns; detector 2 deadtime $t_d = (80.35 \pm 0.10)$ ns. At high time delays the histogram slowly decreases to zero because we only consider nearest-neighbour delays.

probability was determined to be 0.027, consistent with the datasheet value of <0.03. A single exponential with 52 ns width was fitted to the afterpulse peak.

Afterpulses were also added to the Monte Carlo model for generating simulated timestamp data using the parameters we measured: an afterpulsing probability 0.027, and an exponential probability distribution starting 80 ns after detections with a width of 50 ns. The simulated data in Figure 50(b) in the main text include these afterpulses. The effect of adding afterpulses is shown for two- and three-level emitters in Figure 81(b) including the 80 ns detector deadtime, and Figure 81(c) with no deadtime. In all cases afterpulsing causes more bunching in the Q(T) function above 80 ns. However, it is still clear that a three-level system is required to describe the extent of the bunching seen in experiment (Figure 50(a) in main text).

Due to the 5 ns filter applied to the pulsed timestamp data, most of the afterpulse counts are excluded from the Q(T) calculation. Only counts close to 100 ns (the pulse repetition period) after the pulse will be included, since they 'wrap around' and arrive at the same time as the next pulse. We estimate this effectively reduces the afterpulsing probability to 0.0017, i.e. the afterpulsing effect is more than an order of magnitude smaller for the pulsed timestamp data than the CW data.

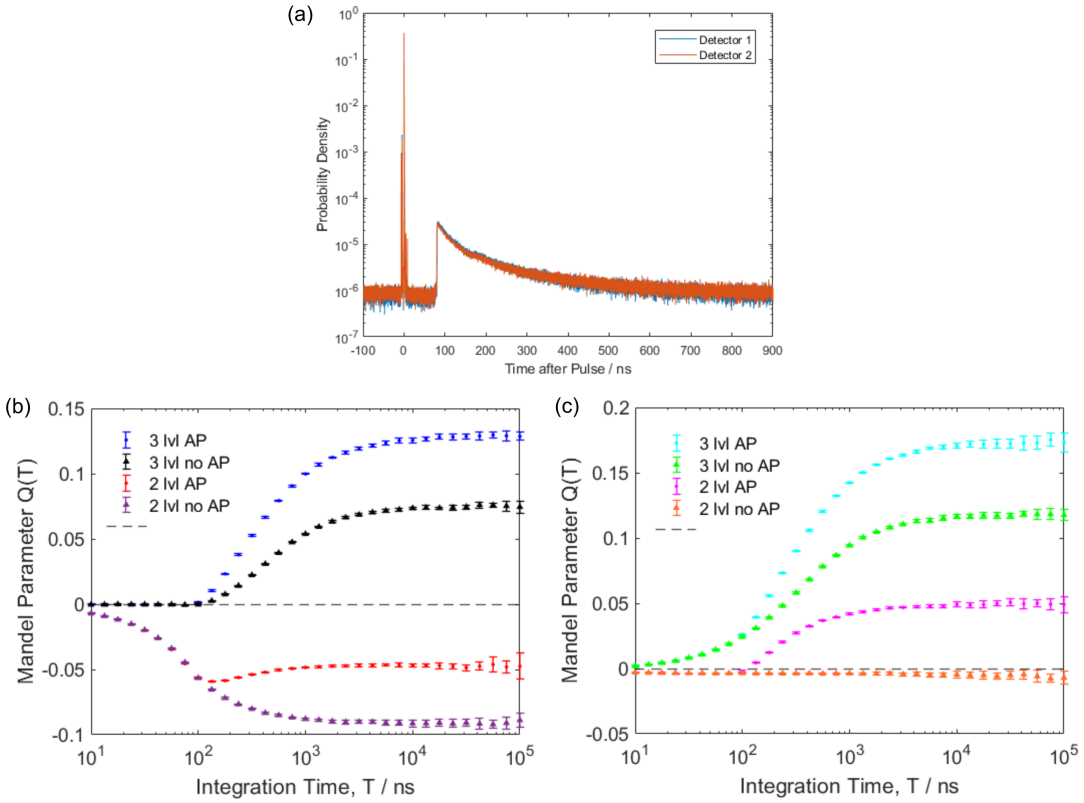

Figure 81: Detector afterpulsing. (a) Measurement of delay histogram between trigger pulses and photon detections using an attenuated pulsed laser at 1 MHz. An exponential shaped afterpulse is seen one deadtime after the pulse peak. (b) Simulated CW Mandel Q parameter with 80 ns deadtime, showing the difference between including afterpulsing (AP) in the model for two- and three-level emitters (2 lvl, 3 lvl). (c) Simulated CW Q parameter with no deadtime, with and without afterpulsing. Afterpulsing was modelled with a probability of 0.027 and an exponential probability distribution starting at 80 ns with 50 ns width.

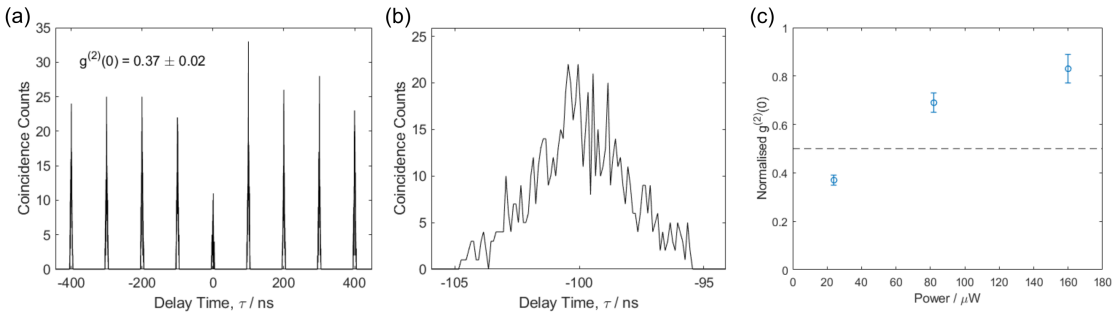

Figure 82: (a) $g^{(2)}(\tau)$ under pulsed excitation at 24 μW. The 5 ns width filter (over [7,12] ns delay after the trigger pulse) was applied to all timestamp data before calculating $g^{(2)}(\tau)$. (b) Zoom-in showing shape of $g^{(2)}(\tau)$ peaks after the filter was applied. (c) Power dependence of $g^{(2)}(0)$.

4. Pulsed $g^{(2)}$ as a function of power

Figure 82 shows the $g^{(2)}(\tau)$ function under pulsed excitation as a function of the mean incident power, at 24 μW, 82 μW and 160 μW. The data had a 5 ns wide filter applied (over [7,12] ns delay after the trigger pulse). The value $g^{(2)}(0)$ was calculated as the ratio between the $\tau = 0$ peak area and the mean area of the 18 next nearest peaks, and the error was estimated as the standard deviation of the peak areas. Values for $g^{(2)}(0)$ were: 0.37 ± 0.02 at 24 μW, 0.69 ± 0.04 at 82 μW, and 0.83 ± 0.06 at 160 μW.

We found that under pulsed excitation the $g^{(2)}(0)$ value was very sensitive to power and the low power needed to achieve $g^{(2)}(0) < 0.5$ meant that the count rate had to be reduced significantly: the count rate was 2.8 kHz at 24 μW mean power.

The background count rate was measured from a single exponential fit to the 24 μW lifetime curve as 160 ± 40 Hz per detection channel (Figure 48(b) in main text). This corresponds to only 0.04 coincidences per time bin in the 24 μW $g^{(2)}(\tau)$ histogram, therefore the background on the pulsed $g^{(2)}$ measurement was ignored. Note that the filtering process does remove background counts occurring outside the filter width.

5. Emitter spectral filtering

The output count rate as a function of tunable filter angle was converted into the spectrum in Figure 83. The tunable filter bandwidth is around 20 nm. All measurements were done with the filter set to the maximum count rate at 595 nm (at 38^o to optic axis).

The significance of using spectral filtering is to improve the $g^{(2)}(0)$ value for our emitter: without the filter (filter completely removed from optical path) $g^{(2)}(0) = 0.56 \pm 0.10$, with the filter set to peak count rate $g^{(2)}(0) = 0.33 \pm 0.02$ (see Figure 47(c) in main text).

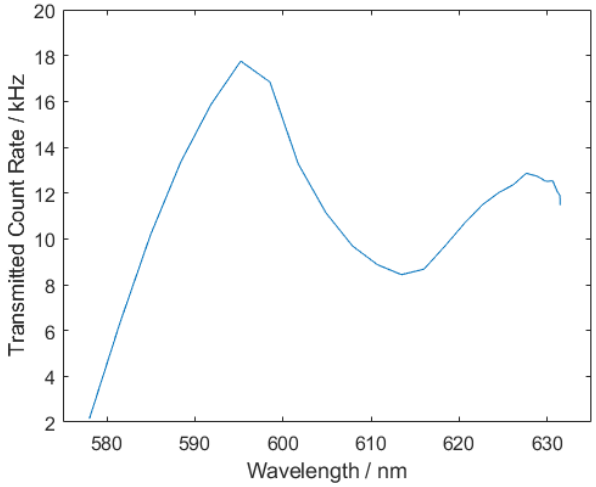

Figure 83: Emission spectrum from our hBN emitter measured by rotating the angle tunable bandpass filter at the output. The bandpass filter has a bandwidth of around 20 nm. Peak emission count rate occurs at 595 nm, corresponding to a filter angle of 38^o.

6. Analytical solution for CW Q(T)

There is an analytical relation between $g^{(2)}(\tau)$ and Q(T) in the continuous wave (CW) case, for integration time T and average photon count rate $\langle I \rangle$ this is given by [121, 117]:

$$Q(T) = \frac{2\langle I \rangle}{T} \int_0^T d\tau \int_0^\tau d\tau' \left(g^{(2)}(\tau') - 1 \right). \tag{135}$$

We can calculate this for a $g^{(2)}(\tau)$ function which is well described by a two-exponential fit with lifetimes t_1, t_2:

$$g^{(2)}(\tau') = 1 - (1+a)\exp\left(-\frac{|\tau'|}{t_1}\right) + a\exp\left(-\frac{|\tau'|}{t_2}\right). \tag{136}$$

For simplicity the bunching amplitude is described by one parameter a, so that $g^{(2)}(0) = 0$.

Substituting into Equation 135:

$$Q(T) = \frac{2\langle I \rangle}{T} \int_0^T d\tau \int_0^\tau d\tau' \left(-(1+a)\exp\left(-\frac{|\tau'|}{t_1}\right) + a\exp\left(-\frac{|\tau'|}{t_2}\right)\right) \tag{137}$$

$$Q(T) = \frac{2\langle I \rangle}{T} \int_0^T d\tau \left(-t_1(1+a)\left(1-\exp\left(-\frac{|\tau'|}{t_1}\right)\right) t_2 a \left(1-\exp\left(-\frac{|\tau'|}{t_2}\right)\right)\right) \tag{138}$$

$$\begin{aligned} Q(T) = \frac{2\langle I \rangle}{T} \Bigg(& t_1^2(1+a) - t_2^2 a - (t_1(1+a) - t_2 a)T \\ & - t_1^2(1+a)\exp\left(-\frac{T}{t_1}\right) + t_2^2 a \exp\left(-\frac{T}{t_1}\right)\Bigg). \end{aligned} \tag{139}$$

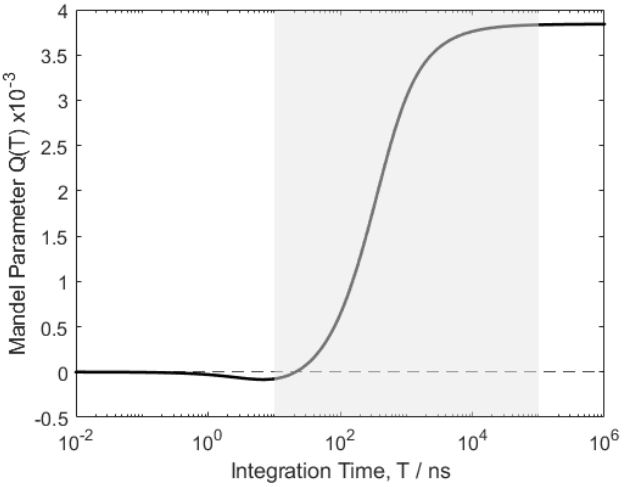

Figure 84: Analytical solution for CW Mandel Q parameter. The function in Equation 139 was plotted with parameters $a = 0.3$, $t_1 = 2.7$ ns, $t_2 = 200$ ns, and single photon count rate $\langle I \rangle = 34$ kHz. Shaded region shows the range plotted for experimental and simulated data in Fig. 4 of the main text.

Here we have an analytical expression for the CW Mandel Q parameter for an ideal ($g^{(2)}(0) = 0$) single photon emitter including bunching.

We can plot this function using values from CW $g^{(2)}(\tau)$ measurements under 250 μW excitation. In Figure 84 the analytical Q(T) expression is plotted for bunching parameter $a = 0.3$, antibunching and bunching times $t_1 = 2.7$ ns and $t_2 = 200$ ns, and single photon count rate $\langle I \rangle = 34$ kHz. Note that the count rate $\langle I \rangle$ already includes the total detection efficiency so accounts for losses in the optical path.

The shaded region indicates the range plotted for experimental and simulated Q(T) in Figure 50 of the main text. The limiting behaviour at high and low T is the same as that in the experimental data; in particular Q(T) tends to zero at low T. We also see that the crossover time from negative to positive Q(T) occurs at around 21 ns, much lower than the 100 ns seen in the experimental data. The analytical model does not include all transition lifetimes of the three-level emitter τ_{ij}, or the effect of detector deadtime.

It would also be possible to produce an analytical solution for the pulsed Mandel Q parameter. However, this would be more challenging because the pulsed $g^{(2)}(\tau)$ histograms are noisier due to the relatively low photon count rate under pulsed excitation. As such there are fewer constraints when choosing a function to use in Equation 135, with parameters which model pulsed $g^{(2)}(\tau)$ well.

Appendix B - MATLAB Code

The following code used in this thesis was written in MATLAB R2019a, with no additional packages.

Model for noise in WGM-coupled MZI

This is the code used to model the noise in an edge-of-resonance measurement of the resonance shift for a WGM resonator coupled to one arm of a MZI. The methods and results are in Chapter 2. Three cases are considered: transmission for a WGM coupled to a waveguide with a single classical mode (`class_trans`), transmission for a WGM-coupled MZI with one classical input mode (`class_mzi`), and transmission in terms of coincidence detections for a WGM-coupled MZI with a photon pair state in the two input modes (`entgl_mzi`).

The three following functions are called by the main script: `wgm_gradients`, `wgm_time_series_noise` and `wgm_mzi_func`.

```
function [max_slope,ind_slope] = wgm_gradients(a,r,n_r,R,w,w_o,MODE)
% Find WGM gradients %
% MODE: 1 classical transmission, 2 classical MZI, 3 entangled MZI %

if MODE == 0
    % Classical transmission spectrum
    I_class_trans = abs(t_wgm(a,r,n_r,R,w,w_o)).^2;
    diff_I_class_trans = diff(I_class_trans);
    [max_slope, ind_slope] = max(diff_I_class_trans);
end

if MODE == 1
    % Classical MZI spectrum
    I_class_mzi = (1/2 * abs(1 + t_wgm(a,r,n_r,R,w,w_o))).^2;
    diff_I_class_mzi = diff(I_class_mzi);
    [max_slope, ind_slope] = max(diff_I_class_mzi);
end

if MODE == 2
    % Entangled MZI transmission spectrum (coincidence counts)
    Prob_N00N = wgm_mzi_func(a,r,n_r,R,w,w_o);
    C_entgl_mzi = Prob_N00N(5,:);
    diff_C_entgl_mzi = diff(C_entgl_mzi);
    [max_slope, ind_slope] = max(diff_C_entgl_mzi);
end
```

```
end

%%%%%%%%%%%%%%%%%%%%%%%%%%%%%%%%%%%%%%%%%%%%%%%%%%%%%%%%%%%%%%%%%%%%%%%%%%%%%%%%

function [noise3sigma,t_series,t] = wgm_time_series_noise(K,M,a,r,n_r,R,lambda_o,
    c,w,t_step,ind_slope,max_slope,frac_noise,thermo_noise,MODE)
% Find 3 sigma noise in resonance shift measurement %
% MODE: 1 classical transmission, 2 classical MZI, 3 entangled MZI %
Itemp = zeros(K,M);
delt_Omega = zeros(K,M-1); % M-1 because we take diff() later
delt_w = w(2) - w(1);

for k = 1:K

    w_res = zeros(1,M);
    w_res = w_res + thermo_noise*randn(1,M);

    for m = 1:M

        if MODE == 0
            I = abs(t_wgm(a,r,n_r,R,w(ind_slope),w_res(m))).^2;
        end

        if MODE == 1
            I = (1/2 * abs(1 + t_wgm(a,r,n_r,R,w(ind_slope),w_res(m)))).^2;
        end

        if MODE == 2
            Prob_N00N = wgm_mzi_func(a,r,n_r,R,w(ind_slope),w_res(m));
            I = Prob_N00N(5,:);
        end

        I = I .* (1 + frac_noise(k).*randn(1));
        Itemp(k,m) = I;

    end

    delt_Omega(k,:)  = diff(Itemp(k,:))*delt_w/max_slope;

end

stdev_Omega = std(delt_Omega,0,2);
noise3sigma = 3*1e15*stdev_Omega*lambda_o^2/(2*pi*c);

t_series = Itemp;
t = zeros(K,M);

for m = 2:M
```

```
t(:,m) = t(:,m-1) + t_step';
end

end

%%%%%%%%%%%%%%%%%%%%%%%%%%%%%%%%%%%%%%%%%%%%%%%%%%%%%%%%%%%%%%%%%%%%%%%%%%%%%%%

function [Prob] = wgm_mzi_func(a,r,n_r,R,w,w_o)
% Detection probabilities for WGM-coupled MZI with photon pair input %
% WGM transmission amplitude t(w)
t = t_wgm(a,r,n_r,R,w,w_o);
tc= conj(t);
ta= abs(t);

% Expectation values of noise operator FFdag and noise operator squared F^2Fdag^2
E_F = (1 - ta.^2);
E_F2 = 2*(1 - 2*ta.^2 + ta.^4);

% Normalisaion factor A(w)
A = sqrt(1 ./ (2./(2*ta.^4) + 2*(E_F.^2)./ta.^4 + 2*(E_F2.^2)./(4*ta.^4)));

% Wavefunction amplitude for each state at the output of the MZI
% Photon numbers S_nm at detectors n and m
S_20 = (1i*sqrt(2)/4) * (A./tc.^2 - 1);
S_02 = (1i*sqrt(2)/4) * (1 - A./tc.^2);
S_11 = 0.5*(A./tc.^2 + 1);
S_10 = - 1i*A.*E_F ./ (sqrt(2)*tc.^2);
S_01 = - A.*E_F ./ (sqrt(2)*tc.^2);
S_00 = 1i*A.*E_F2 ./ (2*tc.^2);

% Probabilities for each detection outcome
P_20 = abs(S_20).^2;
P_02 = abs(S_02).^2;
P_11 = abs(S_11).^2;
P_10 = abs(S_10).^2;
P_01 = abs(S_01).^2;
P_00 = abs(S_00).^2;

Prob(1,:)  = P_00;
Prob(2,:)  = P_01;
Prob(3,:)  = P_02;
Prob(4,:)  = P_10;
Prob(5,:)  = P_11;
Prob(6,:)  = P_20;

end
```

The following is the main script. This script calculates the 3σ level noise in the res-

onance shift measurement for K values of the integration bin width t_step and P values of the coupling parameter r, the outputs for the three cases is in a $(3 \times K \times P)$ array delt_Omega_array. The photon detection rate is fixed at R, and the photon number per time bin is R*t_step. Noise is added to the transmission intensity and resonance position using pseudo-random samples from a Gaussian distribution. Final standard deviations are calculated from M = 10^3 repetitions of the measurement.

```
%% MAIN SCRIPT %%

%% Set Parameters %%

% Initial resonator params
a = 0.9997;
r = 0.9996;
n_r = 1.45;
R = 40e-6;
lambda_o = 810e-9;
c = 3e8;

% Spectrum params N_pts = 1e5; % number of points per spectrum
w_min = -2*pi*2e9; % WGM spectrum frequency points:  2 GHz above and below resonance
w_max = 2*pi*2e9;
w = linspace(w_min,w_max,N_pts);
delt_w = w(2) - w(1);
w_o = 0;

% Time series params
M = 1e3; % number of steps in time series
K = 20; % number of repeats of time series
t_min_log = -6;
t_max_log = 1;
t_step = logspace(-6,1,K); % Integration time per time series point

w_noise = 4.57e5; % Noise level (1sigma:  approx 1 fm)
thermo_noise = 2*pi*w_noise;

Rate = 1e6; % Default detection rate:  photon number per time bin is R*t_step

%% WGM time series and noise %%

% MODE: 1 classical transmission, 2 classical MZI, 3 entangled MZI

P = 1e3;
delt_Omega_array = zeros(3,K,P);
r_array = [0.999:1e-6:0.999999];

for p = 1:P
```

```
    r = r_array(p);

    Rate_int = Rate*t_step;
    frac_noise = sqrt(Rate_int)./Rate_int;

    [max_slope_class_trans,ind_slope_class_trans] =
       wgm_gradients(a,r,n_r,R,w,w_o,0);
    [noise3sigma_class_trans,t_series_class_trans,t] =
       wgm_time_series_noise(K,M,a,r,n_r,R,lambda_o,c,w,t_step,
       ind_slope_class_trans,max_slope_class_trans,frac_noise,thermo_noise,0);

    %%%%

    Rate_int = Rate*t_step;
    frac_noise = sqrt(Rate_int)./Rate_int;

    [max_slope_class_mzi,ind_slope_class_mzi] =
       wgm_gradients(a,r,n_r,R,w,w_o,1);
    [noise3sigma_class_mzi,t_series_class_mzi,t] =
       wgm_time_series_noise(K,M,a,r,n_r,R,lambda_o,c,w,t_step,
       ind_slope_class_mzi,max_slope_class_mzi,frac_noise,thermo_noise,1);

    %%%%

    Rate_int = Rate*t_step;
    frac_noise = sqrt(Rate_int)./Rate_int;

    [max_slope_entgl_mzi,ind_slope_entgl_mzi] =
       wgm_gradients(a,r,n_r,R,w,w_o,2);
    [noise3sigma_entgl_mzi,t_series_entgl_mzi,t] =
       wgm_time_series_noise(K,M,a,r,n_r,R,lambda_o,c,w,t_step,
       ind_slope_entgl_mzi,max_slope_entgl_mzi,frac_noise,thermo_noise,2);

    %%%%

    delt_Omega_array(1,:,p) = noise3sigma_class_trans;
    delt_Omega_array(2,:,p) = noise3sigma_class_mzi;
    delt_Omega_array(3,:,p) = noise3sigma_entgl_mzi;

end

%% Plotting %%
% Plot noise vs r, second index in delt_Omega_array selects the t_step value:
8 corresponds to R*t_step = 3.8e2 as in the results in the main text

y1(1,:)  = delt_Omega_array(1,8,:);
y2(1,:)  = delt_Omega_array(2,8,:);
```

```
y3(1,:)  = delt_Omega_array(3,8,:);

figure; semilogy(r_array,y1,'b-')
hold on; semilogy(r_array,y2,'r-')
hold on; semilogy(r_array,y3,'g-')
```

Time-dependent Mandel Q parameter calculation

The code used for calculating the Mandel Q parameter from pulsed and CW timestamp data is in the Zenodo repository: `https://doi.org/10.5281/zenodo.7644060` [127]. This is the code that was used in the data analysis for our publication 'Time-dependent Mandel Q parameter analysis for a hexagonal boron nitride single photon source' and the results presented in Chapter 4 [54].

Monte Carlo model for two- and three-level single photon emitters

The simulated timestamp data for CW and pulsed single photon detections used in our publication Ref. [54] and the results in Chapter 4 were generated using a Monte Carlo model for a two- or three-level emitter. This model was based on Python code by Bernd Sontheimer which can be found in the Appendix of Ref. [104]. The main idea is to draw a vector of transition lifetimes from pseudo-random exponential distributions for each transition in the energy level model and add them cumulatively to produce an ordered list of photon emission timestamps. The code was modified for MATLAB and extended to simulate timestamp data for CW and pulsed emission from two- and three-level systems, and also to model the effects of detector deadtime and afterpulsing which were important measurement artefacts in the Mandel Q parameter study.

Two-level emitter CW timestamps

The following function takes parameters `N`: number of excitation cycles, `t_ex`: excitation lifetime (τ_{12}), `t_rad`: radiative lifetime (τ_{21}), and `eta`: total photon detection efficiency. Times are in picoseconds. Within the function the afterpulsing and deadtime parameters are set: afterpulse time `pulse_time`, afterpulse tail length `tail_time`, afterpulsing probability `afterpulse_prob`, and detector deadtime `dead_time`. The outputs are two column vectors of photon detection timestamps in picoseconds. The detections are split 50:50 onto two output channels so that $g^{(2)}$ can be calculated; the functions in the Mandel Q parameter code take two input channels and combine them so they can use this simulated data directly.

```
function [arrival_time_0,arrival_time_1] = simulate_ts2lvl_func(N,t_ex,t_rad,eta)
```

```
% Timestamps for CW two-level emitter

% generate random delays for each excitation (picoseconds)
delay_ex = exprnd(t_ex,1,N);
delay_rad = exprnd(t_rad,1,N);

% sum all delays for radiative cycles
delay_tot = delay_ex + delay_rad;

% emission cycles must be sequential:  photon arrival times are the
% cumulative sum of total delays per excitation cycle
arrival_time = cumsum(delay_tot);

%%%%%%%%%%%%%%%%%%%%%%%%%%%%%%%%%%%%%%%%%%%%%%%%%%%%%%%%%%%%%%%%%%%%%%%%%%%%%%%

%%%% Enter loss and BS transmission %%%%
p_loss = 1 - eta;
BS_transmit = 0.5;

% lose a random set of photons
photon_lost = binornd(ones(1,length(arrival_time)),p_loss);
arrival_time = arrival_time(photon_lost == 0);

% split photons between channels 0 and 1
which_path = binornd(ones(1,length(arrival_time)),BS_transmit);
arrival_time_0 = arrival_time(which_path == 0);
arrival_time_1 = arrival_time(which_path == 1);

% afterpulses
pulse_time = 8e4;
tail_time = 5e4;
afterpulse_prob = 0.027;

afterpulse_happens_0 = binornd(ones(1,length(arrival_time_0)),afterpulse_prob);
afterpulse_happens_1 = binornd(ones(1,length(arrival_time_1)),afterpulse_prob);

N_afterpulse_0 = length(arrival_time_0(afterpulse_happens_0 == 1));
N_afterpulse_1 = length(arrival_time_1(afterpulse_happens_1 == 1));

afterpulse_times_0 = arrival_time_0(afterpulse_happens_0 == 1) + pulse_time +
    exprnd(tail_time,1,N_afterpulse_0);
afterpulse_times_1 = arrival_time_1(afterpulse_happens_1 == 1) + pulse_time +
    exprnd(tail_time,1,N_afterpulse_1);

arrival_time_0 = sort([arrival_time_0 afterpulse_times_0]);
arrival_time_1 = sort([arrival_time_1 afterpulse_times_1]);

% remove photons arriving within the detector deadtime
```

```
%%%% Enter deadtime %%%%
dead_time = 8e4;
last_detection = 0;
photon_dead_0 = ones(1,length(arrival_time_0));
photon_dead_1 = ones(1,length(arrival_time_1));

for i = 1:length(arrival_time_0)
    dt = arrival_time_0(i) - last_detection;
    if dt > dead_time
        last_detection = arrival_time_0(i);
        photon_dead_0(i) = 0;
    end
end

last_detection = 0;
for j = 1:length(arrival_time_1)
    dt = arrival_time_1(j) - last_detection;
    if dt > dead_time
        last_detection = arrival_time_1(j);
        photon_dead_1(j) = 0;
    end
end

% final arrival times at channels 0 and 1 (picoseconds)
arrival_time_0 = arrival_time_0(photon_dead_0 == 0);
arrival_time_1 = arrival_time_1(photon_dead_1 == 0);

t_acquisition = max([arrival_time_0 arrival_time_1])*1e-12
count_rate = numel([arrival_time_0 arrival_time_1])/t_acquisition

end
```

Three-level emitter CW timestamps

To use the three-level CW timestamp model, insert the following script before the line %%%... in the two-level code above. The new parameters are the shelving state lifetimes `t_shelf` (τ_{23}) and `t_deshelf` (τ_{31}), both in picoseconds.

```
function [arrival_time_0,arrival_time_1] = simulate_ts_func(N,t_ex,t_rad,
    t_shelf,t_deshelf,eta)

% generate random delays for each excitation (picoseconds)
delay_ex = exprnd(t_ex,1,N);
delay_rad = exprnd(t_rad,1,N);
delay_shelf = exprnd(t_shelf,1,N);
delay_deshelf = exprnd(t_deshelf,1,N);

% radiative cycle if t_rad < t_shelf i.e.  photon emitted
```

```
photon_emitted = zeros(1,N);
photon_emitted(delay_rad < delay_shelf) = 1;

% sum all delays for radiative and non-radiative cycles
delay_tot = zeros(1,N);
delay_tot(photon_emitted == 1) = delay_ex(photon_emitted == 1) +
    delay_rad(photon_emitted == 1);
delay_tot(photon_emitted == 0) = delay_ex(photon_emitted == 0) +
    delay_shelf(photon_emitted == 0) + delay_deshelf(photon_emitted == 0);

% emission cycles must be sequential:  photon arrival times are the
% cumulative sum of total delays per excitation cycle
arrival_time = cumsum(delay_tot);
arrival_time = arrival_time(photon_emitted == 1);

%%%%%%%%%%%%%%%%%%%%%%%%%%%%%%%%%%%%%%%%%%%%%%%%%%%%%%%%%%%%%%%%%%%%%%%%%%%%%%%
```

Three-level emitter pulsed timestamps

To use the three-level pulsed timestamp model, insert the following script before the line %%%. . . in the two-level code above. The pulse repetition period is set inside the function by `t_rep`, in picoseconds.

```
function [arrival_time_0,arrival_time_1] =
    simulate_ts_pulse_func(N,t_ex,t_rad,t_shelf,t_deshelf,eta)

% lifetimes for each transition (picoseconds)
t_rep = 1e5;

% generate pulse arrival times
pulse_times = ones(1,N)*t_rep;
pulse_times = cumsum(pulse_times);

% generate random delays for each excitation
delay_ex = exprnd(t_ex,1,N);
delay_rad = exprnd(t_rad,1,N);
delay_shelf = exprnd(t_shelf,1,N);
delay_deshelf = exprnd(t_deshelf,1,N);

% radiative cycle if t_rad < t_shelf i.e.  photon emitted
photon_emitted = zeros(1,N);
photon_emitted(delay_rad < delay_shelf) = 1;

% sum all delays for radiative and non-radiative cycles
delay_tot = zeros(1,N);
delay_tot(photon_emitted == 1) = delay_ex(photon_emitted == 1) +
    delay_rad(photon_emitted == 1);
delay_tot(photon_emitted == 0) = delay_ex(photon_emitted == 0) +
```

```
    delay_shelf(photon_emitted == 0) + delay_deshelf(photon_emitted == 0);

% emission cycles must be sequential:  photon arrival times are the
% cumulative sum of total delays per excitation cycle
arrival_time = pulse_times + delay_tot;
% remove any photons excited during the non-radiative decay of any previous
% cycle
index = find(photon_emitted);
window = 100;
for n = 1:window
    if arrival_time(index(n)) < max(arrival_time(1:index(n)-1))
        photon_emitted(index(n)) = 0;
    end
end
for n = window+1:length(index)
    if arrival_time(index(n)) < max(arrival_time(index(n)-window:index(n)-1))
        photon_emitted(index(n)) = 0;
    end
end
arrival_time = arrival_time(photon_emitted == 1);

%%%%%%%%%%%%%%%%%%%%%%%%%%%%%%%%%%%%%%%%%%%%%%%%%%%%%%%%%%%%%%%%%%%%%%%%%%%%%%%%
```

References

[1] M. Fox, *Quantum Optics An Introduction*. Oxford University Press, 2006.

[2] S. L. Braunstein and C. M. Caves, "Statistical distance and the geometry of quantum states," *Physical Review Letters*, vol. 72, no. 22, p. 3439, 1994.

[3] R. Demkowicz-Dobrzański, M. Jarzyna, and J. Kołodyński, "Quantum limits in optical interferometry," *Progress in Optics*, vol. 60, pp. 345–435, 2015.

[4] V. Giovannetti, S. Lloyd, and L. Maccone, "Quantum metrology," *Phys. Rev. Lett.*, vol. 96, no. 010401, 2006.

[5] M. Zwierz, C. A. Pérez-Delgado, and P. Kok, "Ultimate limits to quantum metrology and the meaning of the Heisenberg limit," *Physical Review A*, vol. 85, no. 4, p. 042112, 2012.

[6] V. Giovannetti, S. Lloyd, and L. Maccone, "Advances in quantum metrology," *Nature Photonics*, vol. 5, no. 4, pp. 222–229, 2011.

[7] R. Loudon and P. L. Knight, "Squeezed light," *Journal of Modern Optics*, vol. 34, no. 6-7, pp. 709–759, 1987.

[8] H. Vahlbruch, M. Mehmet, K. Danzmann, and R. Schnabel, "Detection of 15 dB squeezed states of light and their application for the absolute calibration of photoelectric quantum efficiency," *Physical Review Letters*, vol. 117, no. 11, p. 110801, 2016.

[9] M. Mehmet and H. Vahlbruch, "High-efficiency squeezed light generation for gravitational wave detectors," *Classical and Quantum Gravity*, vol. 36, no. 1, p. 015014, 2018.

[10] H. Yonezawa, K. Nagashima, and A. Furusawa, "Generation of squeezed light with a monolithic optical parametric oscillator: Simultaneous achievement of phase matching and cavity resonance by temperature control," *Optics Express*, vol. 18, no. 19, pp. 20143–20150, 2010.

[11] E. Lariontsev and I. Zolotoverkh, "Characteristics of bright-squeezed light produced in a below-threshold optical parametric oscillator," *Journal of Optics B: Quantum and Semiclassical Optics*, vol. 4, no. 1, p. 15, 2002.

[12] C. M. Caves, "Quantum-mechanical noise in an interferometer," *Physical Review D*, vol. 23, no. 8, p. 1693, 1981.

[13] J. Aasi, J. Abadie, B. Abbott, R. Abbott, T. Abbott, M. Abernathy, C. Adams, T. Adams, P. Addesso, R. Adhikari, *et al.*, "Enhanced sensitivity of the LIGO gravitational wave detector by using squeezed states of light," *Nature Photonics*, vol. 7, no. 8, pp. 613–619, 2013.

[14] J. P. Dowling, "Quantum optical metrology–the lowdown on high-N00N states," *Contemporary Physics*, vol. 49, no. 2, pp. 125–143, 2008.

[15] T. Nagata, R. Okamoto, J. L. O'brien, K. Sasaki, and S. Takeuchi, "Beating the standard quantum limit with four-entangled photons," *Science*, vol. 316, no. 5825, pp. 726–729, 2007.

[16] R. Okamoto, H. F. Hofmann, T. Nagata, J. L. O'Brien, K. Sasaki, and S. Takeuchi, "Beating the standard quantum limit: phase super-sensitivity of N-photon interferometers," *New Journal of Physics*, vol. 10, no. 7, p. 073033, 2008.

[17] S. Daryanoosh, S. Slussarenko, D. W. Berry, H. M. Wiseman, and G. J. Pryde, "Experimental optical phase measurement approaching the exact Heisenberg limit," *Nature Communications*, vol. 9, no. 1, p. 4606, 2018.

[18] B. L. Higgins, D. W. Berry, S. D. Bartlett, H. M. Wiseman, and G. J. Pryde, "Entanglement-free Heisenberg-limited phase estimation," *Nature*, vol. 450, no. 7168, pp. 393–396, 2007.

[19] S. Slussarenko, M. M. Weston, H. M. Chrzanowski, L. K. Shalm, V. B. Verma, S. W. Nam, and G. J. Pryde, "Unconditional violation of the shot-noise limit in photonic quantum metrology," *Nature Photonics*, vol. 11, no. 11, pp. 700–703, 2017.

[20] C. A. Casacio, L. S. Madsen, A. Terrasson, M. Waleed, K. Barnscheidt, B. Hage, M. A. Taylor, and W. P. Bowen, "Quantum-enhanced nonlinear microscopy," *Nature*, vol. 594, no. 7862, pp. 201–206, 2021.

[21] F. Vollmer and S. Arnold, "Whispering-gallery-mode biosensing: label-free detection down to single molecules," *Nature Methods*, vol. 5, no. 7, pp. 591–596, 2008.

[22] M. R. Foreman, J. D. Swaim, and F. Vollmer, "Whispering gallery mode sensors," *Advances in Optics and Photonics*, vol. 7, no. 2, pp. 168–240, 2015.

[23] S. Vincent, S. Subramanian, and F. Vollmer, "Optoplasmonic characterisation of reversible disulfide interactions at single thiol sites in the attomolar regime," *Nature Communications*, vol. 11, no. 1, p. 2043, 2020.

[24] S. Subramanian, H. B. Jones, S. Frustaci, S. Winter, M. W. van der Kamp, V. L. Arcus, C. R. Pudney, and F. Vollmer, "Sensing enzyme activation heat capacity

at the single-molecule level using gold-nanorod-based optical whispering gallery modes," *ACS Applied Nano Materials*, vol. 4, no. 5, pp. 4576–4583, 2021.

[25] J. Xavier, S. Vincent, F. Meder, and F. Vollmer, "Advances in optoplasmonic sensors–combining optical nano/microcavities and photonic crystals with plasmonic nanostructures and nanoparticles," *Nanophotonics*, vol. 7, no. 1, pp. 1–38, 2018.

[26] M. A. Santiago-Cordoba, S. V. Boriskina, F. Vollmer, and M. C. Demirel, "Nanoparticle-based protein detection by optical shift of a resonant microcavity," *Applied Physics Letters*, vol. 99, no. 7, 2011.

[27] S. Shopova, R. Rajmangal, S. Holler, and S. Arnold, "Plasmonic enhancement of a whispering-gallery-mode biosensor for single nanoparticle detection," *Applied Physics Letters*, vol. 98, no. 24, 2011.

[28] J. D. Swaim, J. Knittel, and W. P. Bowen, "Detection limits in whispering gallery biosensors with plasmonic enhancement," *Applied Physics Letters*, vol. 99, no. 24, 2011.

[29] M. D. Baaske, M. R. Foreman, and F. Vollmer, "Single-molecule nucleic acid interactions monitored on a label-free microcavity biosensor platform," *Nature Nanotechnology*, vol. 9, no. 11, pp. 933–939, 2014.

[30] E. Kim, M. D. Baaske, I. Schuldes, P. S. Wilsch, and F. Vollmer, "Label-free optical detection of single enzyme-reactant reactions and associated conformational changes," *Science Advances*, vol. 3, no. 3, p. e1603044, 2017.

[31] S. Frustaci and F. Vollmer, "Whispering-gallery mode (WGM) sensors: review of established and WGM-based techniques to study protein conformational dynamics," *Current Opinion in Chemical Biology*, vol. 51, pp. 66–73, 2019.

[32] M. D. Baaske and F. Vollmer, "Optical observation of single atomic ions interacting with plasmonic nanorods in aqueous solution," *Nature Photonics*, vol. 10, no. 11, pp. 733–739, 2016.

[33] S. Subramanian, *A whispering gallery mode based biosensor platform for single enzyme analysis*. PhD Thesis: University of Exeter, 2021.

[34] M. R. Foreman, W.-L. Jin, and F. Vollmer, "Optimizing detection limits in whispering gallery mode biosensing," *Optics Express*, vol. 22, no. 5, pp. 5491–5511, 2014.

[35] M. A. Taylor and W. P. Bowen, "Quantum metrology and its application in biology," *Physics Reports*, vol. 615, pp. 1–59, 2016.

[36] J. Xavier, D. Yu, C. Jones, E. Zossimova, and F. Vollmer, "Quantum nanophotonic and nanoplasmonic sensing: towards quantum optical bioscience laboratories on chip," *Nanophotonics*, vol. 10, no. 5, pp. 1387–1435, 2021.

[37] N. P. Mauranyapin, A. Terrasson, and W. P. Bowen, "Quantum biotechnology," *Advanced Quantum Technologies*, vol. 5, no. 9, p. 2100139, 2022.

[38] M. P. Landry, P. M. McCall, Z. Qi, and Y. R. Chemla, "Characterization of photoactivated singlet oxygen damage in single-molecule optical trap experiments," *Biophysical Journal*, vol. 97, no. 8, pp. 2128–2136, 2009.

[39] A. Blázquez-Castro, "Optical tweezers: Phototoxicity and thermal stress in cells and biomolecules," *Micromachines*, vol. 10, no. 8, p. 507, 2019.

[40] A. Crespi, M. Lobino, J. C. Matthews, A. Politi, C. R. Neal, R. Ramponi, R. Osellame, and J. L. O'Brien, "Measuring protein concentration with entangled photons," *Applied Physics Letters*, vol. 100, no. 23, 2012.

[41] J.-S. Lee, S.-J. Yoon, H. Rah, M. Tame, C. Rockstuhl, S. H. Song, C. Lee, and K.-G. Lee, "Quantum plasmonic sensing using single photons," *Optics Express*, vol. 26, no. 22, pp. 29272–29282, 2018.

[42] Y. Peng, Y. Zhao, X.-g. Hu, and Y. Yang, "Optical fiber quantum biosensor based on surface plasmon polaritons for the label-free measurement of protein," *Sensors and Actuators B: Chemical*, vol. 316, p. 128097, 2020.

[43] Y. Peng and Y. Zhao, "Microfiber quantum sensors for protein measurement with quantum N00N state," *Sensors and Actuators B: Chemical*, vol. 383, p. 133616, 2023.

[44] O. Varnavski, C. Gunthardt, A. Rehman, G. D. Luker, and T. Goodson III, "Quantum light-enhanced two-photon imaging of breast cancer cells," *The Journal of Physical Chemistry Letters*, vol. 13, no. 12, pp. 2772–2781, 2022.

[45] M. A. Taylor, J. Janousek, V. Daria, J. Knittel, B. Hage, H.-A. Bachor, and W. P. Bowen, "Biological measurement beyond the quantum limit," *Nature Photonics*, vol. 7, no. 3, pp. 229–233, 2013.

[46] M. A. Taylor, J. Janousek, V. Daria, J. Knittel, B. Hage, H.-A. Bachor, and W. P. Bowen, "Subdiffraction-limited quantum imaging within a living cell," *Physical Review X*, vol. 4, no. 1, p. 011017, 2014.

[47] R. C. Pooser and B. Lawrie, "Plasmonic trace sensing below the photon shot noise limit," *ACS Photonics*, vol. 3, no. 1, pp. 8–13, 2016.

[48] M. Dowran, A. Kumar, B. J. Lawrie, R. C. Pooser, and A. M. Marino, "Quantum-enhanced plasmonic sensing," *Optica*, vol. 5, no. 5, pp. 628–633, 2018.

[49] B.-B. Li, J. Bílek, U. B. Hoff, L. S. Madsen, S. Forstner, V. Prakash, C. Schäfermeier, T. Gehring, W. P. Bowen, and U. L. Andersen, "Quantum enhanced optomechanical magnetometry," *Optica*, vol. 5, no. 7, pp. 850–856, 2018.

[50] Z. Xu, K. Oguchi, Y. Taguchi, S. Takahashi, Y. Sano, T. Mizuguchi, K. Katoh, and Y. Ozeki, "Quantum-enhanced stimulated Raman scattering microscopy in a high-power regime," *Optics Letters*, vol. 47, no. 22, pp. 5829–5832, 2022.

[51] J. Liu, Q. Yang, S. Chen, Z. Xiao, S. Wen, and H. Luo, "Intrinsic optical spatial differentiation enabled quantum dark-field microscopy," *Physical Review Letters*, vol. 128, no. 19, p. 193601, 2022.

[52] T. Li, F. Li, X. Liu, V. V. Yakovlev, and G. S. Agarwal, "Quantum-enhanced stimulated Brillouin scattering spectroscopy and imaging," *Optica*, vol. 9, no. 8, pp. 959–964, 2022.

[53] N. Mauranyapin, L. Madsen, M. Taylor, M. Waleed, and W. Bowen, "Evanescent single-molecule biosensing with quantum-limited precision," *Nature Photonics*, vol. 11, no. 8, pp. 477–481, 2017.

[54] C. Jones, J. Xavier, S. Vartabi Kashanian, M. Nguyen, I. Aharonovich, and F. Vollmer, "Time-dependent Mandel Q parameter analysis for a hexagonal boron nitride single photon source," *Optics Express*, vol. 31, no. 6, pp. 10794–10804, 2023.

[55] L. Mandel and E. Wolf, *Optical coherence and quantum optics. Chapter 10: Quantization of the free electromagnetic field*. Cambridge University Press, 1995.

[56] H.-A. Bachor and T. C. Ralph, *A Guide to Experiments in Quantum Optics*. Wiley, 3rd ed., 2004.

[57] L. Mandel and E. Wolf, *Optical coherence and quantum optics. Chapter 12: Quantum correlations and photon statistics*. Cambridge University Press, 1995.

[58] P. G. Kwiat, "Hyper-entangled states," *Journal of Modern Optics*, vol. 44, no. 11-12, pp. 2173–2184, 1997.

[59] C.-K. Hong, Z.-Y. Ou, and L. Mandel, "Measurement of subpicosecond time intervals between two photons by interference," *Physical Review Letters*, vol. 59, no. 18, p. 2044, 1987.

[60] A. Yariv, "Universal relations for coupling of optical power between microresonators and dielectric waveguides," *Electronics Letters*, vol. 36, 2000.

[61] W. Bogaerts, P. D. Heyn, T. V. Vaerenbergh, K. D. Vos, S. K. Selvaraja, T. Claes, P. Dumon, P. Bienstman, D. V. Thourhout, and R. Baets, "Silicon microring resonators," *Laser Photonics Rev.*, vol. 6, pp. 47–73, 2012.

[62] P. M. Alsing, E. E. Hach, C. C. Tison, and A. M. Smith, "Quantum-optical description of losses in ring resonators based on field-operator transformations," *Phys. Rev. A*, vol. 95, p. 053828, 2017.

[63] R. Loudon, *Quantum Theory of Light*. Oxford University Press, 3rd ed., 2000.

[64] X. Ding, Y. He, Z.-C. Duan, N. Gregersen, M.-C. Chen, S. Unsleber, S. Maier, C. Schneider, M. Kamp, S. Höfling, C.-Y. Lu, and J.-W. Pan, "On-demand single photons with high extraction efficiency and near-unity indistinguishability from a resonantly driven quantum dot in a micropillar," *Phys. Rev. Lett.*, vol. 116, p. 020401, 2016.

[65] L. Hanschke, K. A. Fischer, S. Appel, D. Lukin, J. Wierzbowski, S. Sun, R. Trivedi, J. Vučković, J. J. Finley, and K. Müller, "Quantum dot single-photon sources with ultra-low multi-photon probability," *npj Quantum Information*, vol. 4, 2018.

[66] Sparrow Quantum. `https://sparrowquantum.com/product/`, Accessed: Nov 2023.

[67] Quandela, "Prometheus single-photon source." `https://www.quandela.com/prometheus/`, Accsessed: Nov 2023.

[68] M. Keller, B. Lange, K. Hayasaka, W. Lange, and H. Walther, "Continuous generation of single photons with controlled waveform in an ion-trap cavity system," *Nature*, vol. 431, p. 1075–1078, 2004.

[69] B. Lounis and W. E. Moerner, "Single photons on demand from a single molecule at room temperature," *Nature*, vol. 407, p. 491–493, 2000.

[70] L. Zhang, Y.-J. Yu, L.-G. Chen, Y. Luo, B. Yang, F.-F. Kong, G. Chen, Y. Zhang, Q. Zhang, Y. Luo, J.-L. Yang, Z.-C. Dong, and J. G. Hou, "Electrically driven single-photon emission from an isolated single molecule," *Nature Communications*, vol. 8, 2017.

[71] R. Brouri, A. Beveratos, J.-P. Poizat, and P. Grangier, "Photon antibunching in the fluorescence of individual color centers in diamond," *Opt. Lett.*, vol. 25, no. 17, pp. 1294–1296, 2000.

[72] C. Kurtsiefer, S. Mayer, P. Zarda, and H. Weinfurter, "Stable solid-state source of single photons," *Phys. Rev. Lett.*, vol. 85, pp. 290–293, 2000.

[73] P. Tonndorf, R. Schmidt, R. Schneider, J. Kern, M. Buscema, G. A. Steele, A. Castellanos-Gomez, H. S. J. van der Zant, S. M. de Vasconcellos, and R. Bratschitsch, "Single-photon emission from localized excitons in an atomically thin semiconductor," *Optica*, vol. 2, no. 4, pp. 347–352, 2015.

[74] A. Srivastava, M. Sidler, A. V. Allain, D. S. Lembke, A. Kis, and A. Imamoğlu, "Optically active quantum dots in monolayer WSe_2," *Nature Nanotechnology*, vol. 10, p. 491–496, 2015.

[75] T. T. Tran, K. Bray, M. J. Ford, M. Toth, and I. Aharonovich, "Quantum emission from hexagonal boron nitride monolayers," *Nature Nanotechnology*, vol. 11, pp. 37–41, 2015.

[76] J. Wrachtrup, "Single photons at room temperature," *Nature Nanotechnology*, vol. 11, pp. 7–8, 2016.

[77] M. Neumann, X. Wei, L. Morales-Inostroza, S. Song, S.-G. Lee, K. Watanabe, T. Taniguchi, S. Gotzinger, and Y. H. Lee, "Organic molecules as origin of visible-range single photon emission from hexagonal boron nitride and mica," *ACS Nano*, 2023.

[78] A. Sajid, J. R. Reimers, and M. J. Ford, "Defect states in hexagonal boron nitride: Assignments of observed properties and prediction of properties relevant to quantum computation," *Phys. Rev. B*, vol. 97, p. 064101, 2018.

[79] C. Cholsuka, S. Suwanna, and T. Vogl, "Tailoring the emission wavelength of color centers in hexagonal boron nitride for quantum applications," *Nanomaterials*, vol. 12, p. 2427, 2022.

[80] A. Sajid and K. S. Thygesen, "$V_N C_B$ defect as source of single photon emission from hexagonal boron nitride," *2D Materials*, vol. 7, no. 031007, 2020.

[81] N. Mendelson, D. Chugh, J. R. Reimers, T. S. Cheng, A. Gottscholl, H. Long, C. J. Mellor, A. Zettl, V. Dyakonov, P. H. Beton, S. V. Novikov, C. Jagadish, H. H. Tan, M. J. Ford, M. Toth, C. Bradac, and I. Aharonovich, "Identifying carbon as the source of visible single-photon emission from hexagonal boron nitride," *Nature Materials*, vol. 20, pp. 321–328, 2020.

[82] C. Jara, T. Rauch, S. Botti, M. A. L. Marques, A. Norambuena, R. Cotoa, J. E. Castellanos-Águila, J. R. Maze, and F. Munoz, "First-principles identification of single photon emitters based on carbon clusters in hexagonal boron nitride," *J. Phys. Chem. A*, vol. 125, no. 6, pp. 1325–1335, 2021.

[83] M. Mackoit-Sinkevičienė, M. Maciaszek, C. G. Van de Walle, and A. Alkauskas, "Carbon dimer defect as a source of the 4.1 eV luminescence in hexagonal boron nitride," *Applied Physics Letters*, vol. 115, no. 21, p. 212101, 2019.

[84] F. Hayee, L. Yu, J. L. Zhang, C. J. Ciccarino, M. Nguyen, A. F. Marshall, I. Aharonovich, J. Vučković, P. Naranga, T. F. Heinz, and J. A. Dionne, "Revealing multiple classes of stable quantum emitters in hexagonal boron nitride with correlated optical and electron microscopy," *Nature Materials*, vol. 19, pp. 534–539, 2020.

[85] M. K. Boll, I. P. Radko, A. Huck, and U. L. Andersen, "Photophysics of quantum emitters in hexagonal boron-nitride nano-flakes," *Opt. Express*, vol. 28, no. 5, pp. 7475–7487, 2020.

[86] R. N. Patel, D. A. Hopper, J. A. Gusdorff, M. E. Turiansky, T.-Y. Huang, R. E. K. Fishman, B. Porat, C. G. V. de Walle, and L. C. Bassett, "Probing the optical dynamics of quantum emitters in hexagonal boron nitride," *PRX Quantum*, vol. 3, p. 030331, 2022.

[87] J. Bernard, L. Fleury, H. Talon, and M. Orrit, "Photon bunching in the fluorescence from single molecules: A probe for intersystem crossing," *The Journal of Chemical Physics*, vol. 98, no. 2, pp. 850–859, 1993.

[88] P. Khatri, A. J. Ramsay, R. N. E. Malein, H. M. H. Chong, and I. J. Luxmoore, "Optical gating of photoluminescence from color centers in hexagonal boron nitride," *Nano Letters*, vol. 20, no. 6, p. 4256–4263, 2020.

[89] M. Kianinia, C. Bradac, B. Sontheimer, F. Wang, T. T. Tran, M. Nguyen, S. Kim, Z.-Q. Xu, D. Jin, A. W. Schell, C. J. Lobo, I. Aharonovich, and M. Toth, "All-optical control and super-resolution imaging of quantum emitters in layered materials," *Nature Communications*, vol. 9, no. 874, 2018.

[90] A. Dietrich, M. Bürk, E. S. Steiger, L. Antoniuk, T. T. Tran, M. Nguyen, I. Aharonovich, F. Jelezko, and A. Kubanek, "Observation of Fourier transform limited lines in hexagonal boron nitride," *Phys. Rev. B*, vol. 98, p. 081414, 2018.

[91] T. Vogl, R. Lecamwasam, B. C. Buchler, Y. Lu, and P. K. Lam, "Compact cavity-enhanced single-photon generation with hexagonal boron nitride," *ACS Photonics*, vol. 6, no. 8, pp. 1955–1962, 2019.

[92] C. Fournier, A. Plaud, S. Roux, A. Pierret, M. Rosticher, K. Watanabe, T. Taniguchi, S. Buil, X. Quélin, J. Barjon, J.-P. Hermier, and A. Delteil, "Position-controlled quantum emitters with reproducible emission wavelength in hexagonal boron nitride," *Nature Communications*, vol. 12, no. 3779, 2021.

[93] T. Vogl, G. Campbell, B. C. Buchler, Y. Lu, and P. K. Lam, "Fabrication and deterministic transfer of high-quality quantum emitters in hexagonal boron nitride," *ACS Photonics*, vol. 5, pp. 2305–2312, 2018.

[94] S. Choi, T. T. Tran, C. Elbadawi, C. Lobo, X. Wang, S. Juodkazis, G. Seniutinas, M. Toth, and I. Aharonovich, "Engineering and localization of quantum emitters in large hexagonal boron nitride layers," *ACS Appl. Mater. Interfaces*, vol. 8, no. 43, pp. 29642–29648, 2016.

[95] N. Mendelson, Z.-Q. Xu, T. T. Tran, M. Kianinia, J. Scott, C. Bradac, I. Aharonovich, and M. Toth, "Engineering and tuning of quantum emitters in few-layer hexagonal boron nitride," *ACS Nano*, vol. 13, no. 3, pp. 3132–3140, 2019.

[96] Ç. Samaner, S. Paçal, G. Mutlu, K. Uyanık, and S. Ateş, "Free-space quantum key distribution with single photons from defects in hexagonal boron nitride," *Advanced Quantum Technologies*, vol. 5, no. 9, p. 2200059, 2022.

[97] H. Z. J. Zeng, M. A. P. Ngyuen, X. Ai, A. Bennet, A. S. Solntsev, A. Laucht, A. Al-Juboori, M. Toth, R. P. Mildren, R. Malaney, *et al.*, "Integrated room temperature single-photon source for quantum key distribution," *Optics Letters*, vol. 47, no. 7, pp. 1673–1676, 2022.

[98] A. L. Exarhos, D. A. Hopper, R. N. Patel, M. W. Doherty, and L. C. Bassett, "Magnetic-field-dependent quantum emission in hexagonal boron nitride at room temperature," *Nature Communications*, vol. 10, no. 222, 2019.

[99] A. Gottscholl, M. Kianinia, V. Soltamov, S. Orlinskii, G. Mamin, C. Bradac, C. Kasper, K. Krambrock, A. Sperlich, M. Toth, I. Aharonovich, and V. Dyakonov, "Initialization and read-out of intrinsic spin defects in a van der Waals crystal at room temperature," *Nature Materials*, vol. 19, pp. 540–545, 2020.

[100] S. Baber, R. N. E. Malein, P. Khatri, P. S. Keatley, S. Guo, F. Withers, A. J. Ramsay, and I. J. Luxmoore, "Excited state spectroscopy of boron vacancy defects in hexagonal boron nitride using time-resolved optically detected magnetic resonance," *Nano Lett.*, vol. 22, no. 1, pp. 461–467, 2022.

[101] S. Kim, J. E. Fröch, J. Christian, M. Straw, J. Bishop, D. Totonjian, K. Watanabe, T. Taniguchi, M. Toth, and I. Aharonovich, "Photonic crystal cavities from hexagonal boron nitride," *Nature Communications*, vol. 9, no. 2623, 2018.

[102] M. Nonahal, C. Li, F. Tjiptoharsono, L. Ding, C. Stewart, J. Scott, M. Toth, S. T. Ha, M. Kianinia, and I. Aharonovich, "Coupling spin defects in hexagonal boron nitride to titanium dioxide ring resonators," *Nanoscale*, vol. 14, no. 40, pp. 14950–14955, 2022.

[103] K. Parto, S. I. Azzam, N. Lewis, S. D. Patel, S. Umezawa, K. Watanabe, T. Taniguchi, and G. Moody, "Cavity-enhanced 2D material quantum emitters deterministically integrated with silicon nitride microresonators," *Nano Letters*, vol. 22, no. 23, pp. 9748–9756, 2022.

[104] B. Sontheimer, *Characterization and Utilization of Novel Solid-State Quantum Emitters*. PhD Thesis: Humboldt Universitaet zu Berlin, 2020.

[105] R. B. Patel, A. J. Bennett, K. Cooper, P. Atkinson, C. A. Nicoll, D. A. Ritchie, and A. J. Shields, "Postselective two-photon interference from a continuous nonclassical stream of photons emitted by a quantum dot," *Phys. Rev. Lett.*, vol. 100, p. 207405, 2008.

[106] B. Sontheimer, M. Braun, N. Nikolay, N. Sadzak, I. Aharonovich, and O. Benson, "Photodynamics of quantum emitters in hexagonal boron nitride revealed by low-temperature spectroscopy," *Phys. Rev. B*, vol. 96, p. 121202, 2017.

[107] B. Spokoyny, H. Utzat, H. Moon, G. Grosso, D. Englund, , and M. G. Bawendi, "Effect of Spectral Diffusion on the Coherence Properties of a Single Quantum Emitter in Hexagonal Boron Nitride," *J. Phys. Chem. Lett.*, vol. 11, no. 4, p. 1330–1335, 2020.

[108] C. Fournier, S. Roux, K. Watanabe, T. Taniguchi, S. Buil, J. Barjon, J.-P. Hermier, and A. Delteil, "Two-photon interference from a quantum emitter in hexagonal boron nitride," *Phys. Rev. Appl.*, vol. 19, p. L041003, 2023.

[109] J. Cheung, C. Chunnilall, E. Woolliams, N. Fox, J. Mountford, J. Wang, and P. Thomas, "The quantum candela: a re-definition of the standard units for optical radiation," *Journal of Modern Optics*, vol. 54, no. 2-3, pp. 373–396, 2007.

[110] F. Treussart, R. Alléaume, V. Le Floc'h, L. T. Xiao, J.-M. Courty, and J.-F. Roch, "Direct measurement of the photon statistics of a triggered single photon source," *Phys. Rev. Lett.*, vol. 89, p. 093601, 2002.

[111] L. J. Martínez, T. Pelini, V. Waselowski, J. R. Maze, B. Gil, G. Cassabois, and V. Jacques, "Efficient single photon emission from a high-purity hexagonal boron nitride crystal," *Phys. Rev. B*, vol. 94, p. 121405, 2016.

[112] C. Bradac, T. Gaebel, N. Naidoo, M. J. Sellars, J. Twamley, L. J. Brown, A. S. Barnard, T. Plakhotnik, A. V. Zvyagin, and J. R. Rabeau, "Observation and control of blinking nitrogen-vacancy centres in discrete nanodiamonds," *Nature Nanotechnology*, vol. 5, pp. 345–349, 2010.

[113] A. Efros and D. Nesbitt, "Origin and control of blinking in quantum dots," *Nature Nanotechnology*, vol. 11, p. 661–671, 2016.

[114] R. M. Dickson, A. B. Cubitt, R. Y. Tsien, and W. E. Moerner, "On/off blinking and switching behaviour of single molecules of green fluorescent protein," *Nature*, vol. 388, pp. 355–358, 1997.

[115] S. Han, C. Qin, Y. Song, S. Dong, Y. Lei, S. Wang, X. Su, A. Wei, X. Li, G. Zhang, R. Chen, J. Hu, L. Xiao, and S. Jia, "Photostable fluorescent molecules on layered hexagonal boron nitride: Ideal single-photon sources at room temperature," *The Journal of Chemical Physics*, vol. 155, no. 24, 2021.

[116] M. Koperski, K. Nogajewski, and M. Potemski, "Single photon emitters in boron nitride: More than a supplementary material," *Optics Communications*, vol. 411, pp. 158–165, 2018.

[117] B. Lounis and M. Orrit, "Single-photon sources," *Reports on Progress in Physics*, vol. 68, no. 5, p. 1129, 2005.

[118] N. Sangouard and H. Zbinden, "What are single photons good for?," *Journal of Modern Optics*, vol. 59, no. 17, pp. 1458–1464, 2012.

[119] M. Oxborrow and A. G. Sinclair, "Single-photon sources," *Contemporary Physics*, vol. 46, no. 3, pp. 173–206, 2005.

[120] S. Scheel, "Single-photon sources–an introduction," *Journal of Modern Optics*, vol. 56, no. 2-3, pp. 141–160, 2009.

[121] R. Short and L. Mandel, "Observation of sub-Poissonian photon statistics," *Physical review letters*, vol. 51, no. 5, p. 384, 1983.

[122] Z. Xin-Zheng, W. Zhen-Hua, L. Hui, W. Qiang, T. Bai-Quan, G. Feng, and X. Jing-Jun, "Characterization of photon statistical properties with normalized Mandel parameter," *Chinese Physics Letters*, vol. 25, no. 11, p. 3976, 2008.

[123] S. Dong, T. Huang, Y. Liu, J. Wang, G. Zhang, L. Xiao, and S. Jia, "Fast recognition of single molecules based on single-event photon statistics," *Physical Review A*, vol. 76, no. 6, p. 063820, 2007.

[124] Y. Li, R. Chen, H. Zhou, Y. Shi, C. Qin, Y. Gao, G. Zhang, Y. Gao, L. Xiao, and S. Jia, "Observation of singlet oxygen with single-molecule photosensitization by time-dependent photon statistics," *The Journal of Physical Chemistry Letters*, vol. 9, no. 18, pp. 5207–5212, 2018.

[125] P. Jha, C. Parazzoli, H. Akbari, B. Capron, B. Koltenbah, and H. Atwater, "Room temperature photon statistics of hexagonal boron nitride quantum emitters," *APS March Meeting*, vol. Abstract: V51.00011, 2021.

[126] P. Jha, H. Akbari, C. Parazzoli, B. Capron, B. Koltenbah, and H. Atwater, "Photon statistics and coherence properties of hBN quantum emitters," *APS March Meeting*, vol. Abstract: B72.00005, 2022.

[127] C. Jones, "CallumHJones/MandelQ: MandelQ (v1.0)." https://doi.org/10.5281/zenodo.7644060, 2023.

[128] R. Alléaume, F. Treussart, J.-M. Courty, and J.-F. Roch, "Photon statistics characterization of a single-photon source," *New Journal of Physics*, vol. 6, no. 1, p. 85, 2004.

[129] G. Grosso, H. Moon, B. Lienhard, S. Ali, D. K. Efetov, M. M. Furchi, P. Jarillo-Herrero, M. J. Ford, I. Aharonovich, and D. Englund, "Tunable and high-purity room temperature single-photon emission from atomic defects in hexagonal boron nitride," *Nature Communications*, vol. 8, no. 1, pp. 1–8, 2017.

[130] X.-L. Chu, S. Götzinger, and V. Sandoghdar, "A single molecule as a high-fidelity photon gun for producing intensity-squeezed light," *Nature Photonics*, vol. 11, pp. 58–62, 2017.

[131] S. Ghosh, N. Rivera, G. Eisenstein, and I. Kaminer, "Creating heralded hyper-entangled photons using Rydberg atoms," *Light: Science and Applications*, vol. 10, no. 100, 2021.

[132] Y. Chen, M. Zopf, R. Keil, F. Ding, and O. G. Schmidt, "Highly-efficient extraction of entangled photons from quantum dots using a broadband optical antenna," *Nature Communications*, vol. 9, no. 2994, 2018.

[133] P. Kultavewuti, E. Y. Zhu, X. Xing, L. Qian, V. Pusino, M. Sorel, and J. S. Aitchison, "Polarization-entangled photon pair sources based on spontaneous four wave mixing assisted by polarization mode dispersion," *Scientific Reports*, vol. 7, no. 5785, 2017.

[134] A. Fedrizzi, T. Herbst, A. Poppe, T. Jennewein, and A. Zeilinger, "A wavelength-tunable fiber-coupled source of narrowband entangled photons," *Opt. Express*, vol. 15, no. 23, pp. 15377–15386, 2007.

[135] R. W. Boyd, *Nonlinear Optics*. AP, 3rd ed., 2008.

[136] H. J. Lee, H. Kim, M. Cha, and H. S. Moon, "Simultaneous type-0 and type-II spontaneous parametric down-conversions in a single periodically poled $KTiOPO_4$ crystal," *Applied Physics B*, vol. 108, p. 585–589, 2012.

[137] V. Y. Shur, E. V. Pelegova, A. R. Akhmatkhanov, and I. S. Baturin, "Periodically poled crystals of KTP family: a review," *Ferroelectrics*, vol. 496, no. 1, pp. 49–69, 2016.

[138] M. Jabir and G. Samanta, "Robust, high brightness, degenerate entangled photon source at room temperature," *Scientific Reports*, vol. 7, p. 12613, 2017.

[139] F. König and F. N. C. Wong, "Extended phase matching of second-harmonic generation in periodically poled KTiOPO4 with zero group-velocity mismatch," *Applied Physics Letters*, vol. 84, no. 10, pp. 1644–1646, 2004.

[140] K. Fradkin, A. Arie, A. Skliar, and G. Rosenman, "Tunable midinfrared source by difference frequency generation in bulk periodically poled KTiOPO4," *Applied Physics Letters*, vol. 74, no. 7, pp. 914–916, 1999.

[141] S. Emanueli and A. Arie, "Temperature-dependent dispersion equations for KTiOPO4 and KTiOAsO4," *Appl. Opt.*, vol. 42, no. 33, pp. 6661–6665, 2003.

[142] P. G. Kwiat, K. Mattle, H. Weinfurter, A. Zeilinger, A. V. Sergienko, and Y. Shih, "New high-intensity source of polarization-entangled photon pairs," *Phys. Rev. Lett.*, vol. 75, pp. 4337–4341, 1995.

[143] M. Fiorentino, C. E. Kuklewicz, and F. N. C. Wong, "Source of polarization entanglement in a single periodically poled KTiOPO4 crystal with overlapping emission cones," *Opt. Express*, vol. 13, no. 1, pp. 127–135, 2005.

[144] Y.-C. Jeong, K.-H. Hong, and Y.-H. Kim, "Bright source of polarization-entangled photons using a PPKTP pumped by a broadband multi-mode diode laser," *Opt. Express*, vol. 24, no. 2, pp. 1165–1174, 2016.

[145] S. M. Lee, H. Kim, M. Cha, and H. S. Moon, "Polarization-entangled photon-pair source obtained via type-II non-collinear SPDC process with PPKTP crystal," *Opt. Express*, vol. 24, no. 3, pp. 2941–2953, 2016.

[146] C. E. Kuklewicz, M. Fiorentino, G. Messin, F. N. C. Wong, and J. H. Shapiro, "High-flux source of polarization-entangled photons from a periodically poled KTiOPO4 parametric down-converter," *Phys. Rev. A*, vol. 69, p. 013807, 2004.

[147] T. Kim, M. Fiorentino, and F. N. C. Wong, "Phase-stable source of polarization-entangled photons using a polarization Sagnac interferometer," *Phys. Rev. A*, vol. 73, p. 012316, 2006.

[148] F. N. C. Wong, J. H. Shapiro, and T. Kim, "Efficient generation of polarization-entangled photons in a nonlinear crystal," *Laser Physics*, vol. 16, p. 1517–1524, 2006.

[149] Y. Li, Z.-Y. Zhou, D.-S. Ding, and B.-S. Shi, "CW-pumped telecom band polarization entangled photon pair generation in a Sagnac interferometer," *Opt. Express*, vol. 23, no. 22, pp. 28792–28800, 2015.

[150] S. Nemoto, "Waist shift of a gaussian beam by a dielectric plate," *Appl. Opt.*, vol. 28, pp. 1643–1647, May 1989.

[151] D. F. V. James, P. G. Kwiat, W. J. Munro, and A. G. White, "Measurement of qubits," *Phys. Rev. A*, vol. 64, p. 052312, 2001.

[152] Z.-F. Liu, C. Chen, J.-M. Xu, Z.-M. Cheng, Z.-C. Ren, B.-W. Dong, Y.-C. Lou, Y.-X. Yang, S.-T. Xue, Z.-H. Liu, *et al.*, "Hong-Ou-Mandel interference between two hyperentangled photons enables observation of symmetric and antisymmetric particle exchange phases," *Physical Review Letters*, vol. 129, no. 26, p. 263602, 2022.

[153] E. Kim, *Ensemble and Single Molecule Biosensing with Optical Microcavities*. PhD Thesis: Friedrich-Alexander Universitat Erlangen-Nürnberg, 2017.

[154] C. Lützler, *Fabrication of Optical Microfibers*. Masters Dissertation: Universitat Bonn, 2017.

[155] J. Ward, A. Maimaiti, V. H. Le, and S. Chormaic, "Contributed review: Optical micro-and nanofiber pulling rig," *Review of Scientific Instruments*, vol. 85, no. 11, 2014.

[156] Y. L. Li, *Cooling Sensing using Whispering Gallery Mode Resonators*. PhD Thesis: University College London, 2016.

[157] J. A. Zielińska, *Spontaneous parametric down-conversion sources for generation of atom-resonant quantum light*. PhD Thesis: ICFO - The Institute of Photonic Sciences, 2018.

[158] M. Förtsch, J. U. Fürst, C. Wittmann, D. Strekalov, A. Aiello, M. V. Chekhova, C. Silberhorn, G. Leuchs, and C. Marquardt, "A versatile source of single photons for quantum information processing," *Nature Communications*, vol. 4, no. 1, p. 1818, 2013.

[159] A. B. Matsko, A. A. Savchenkov, N. Yu, and L. Maleki, "Whispering-gallery-mode resonators as frequency references. I. Fundamental limitations," *JOSA B*, vol. 24, no. 6, pp. 1324–1335, 2007.

[160] N. Kondratiev and M. Gorodetsky, "Thermorefractive noise in whispering gallery mode microresonators: Analytical results and numerical simulation," *Physics Letters A*, vol. 382, no. 33, pp. 2265–2268, 2018.

[161] S. Subramanian, S. Vincent, and F. Vollmer, "Effective linewidth shifts in single-molecule detection using optical whispering gallery modes," *Applied Physics Letters*, vol. 117, no. 15, 2020.

[162] S. Rosenblum, Y. Lovsky, L. Arazi, F. Vollmer, and B. Dayan, "Cavity ring-up spectroscopy for ultrafast sensing with optical microresonators," *Nature Communications*, vol. 6, no. 1, p. 6788, 2015.

[163] A. Belsley, E. J. Allen, A. Datta, and J. C. Matthews, "Advantage of coherent states in ring resonators over any quantum probe single-pass absorption estimation strategy," *Physical Review Letters*, vol. 128, no. 23, p. 230501, 2022.